Seismic performance and fragility assessment of ductile light non-structural components in nonlinear structures: from peak demand factors to loss estimation

by

Majid MEHRJOO

MANUSCRIPT-BASED THESIS PRESENTED TO ÉCOLE DE TECHNOLOGIE SUPÉRIEURE IN PARTIAL FULFILLMENT FOR THE DEGREE OF DOCTOR OF PHILOSOPHY
PH.D.

MONTREAL, FEBRUARY 18, 2026

ÉCOLE DE TECHNOLOGIE SUPÉRIEURE
UNIVERSITÉ DU QUÉBEC

BOARD OF EXAMINERS

THIS THESIS HAS BEEN EVALUATED

BY THE FOLLOWING BOARD OF EXAMINERS

Ms. Rola Assi, Thesis Supervisor
Department of Construction Engineering at École de technologie supérieure

Ms. Martine Dubé, President of the Board of Examiners
Department of Construction Engineering at École de technologie supérieure

Mr. Ahmad Abo El Ezz, Member of the jury
Department of Construction Engineering at École de technologie supérieure

Mr. Lotfi Guizani, Member of the jury
Department of Construction Engineering at École de technologie supérieure

Mr. Derek Rodriguez, External Evaluator Independent
Research Associate at National Research Council Canada

THIS THESIS WAS PRESENTED AND DEFENDED

IN THE PRESENCE OF A BOARD OF EXAMINERS AND PUBLIC

ON DECEMBER 17, 2025

AT ÉCOLE DE TECHNOLOGIE SUPÉRIEURE

ACKNOWLEDGMENTS

I am deeply grateful to my supervisor, Professor Rola Assi, who has been an extraordinary mentor throughout my research journey. Her brilliant insights, patient guidance, and constant encouragement have shaped not just this thesis, but my entire approach to research. Her passion for excellence and ability to challenge my thinking while providing unwavering support have helped me grow immensely as a researcher.

My heartfelt appreciation extends to my beloved wife, Arefeh, whose unconditional love and support have been my anchor throughout this demanding academic pursuit. Your patience, understanding, and encouragement during the long hours of research and writing have made this achievement possible. Your belief in my abilities and your constant presence have been a source of strength and motivation that sustained me through every challenge.

I am profoundly grateful to my mother, Shahnaz, who has been the pillar of our family. After losing my father, Yadolah, when I was just a child, you raised my brother and me with unwavering determination and love. Your sacrifices, resilience, and lifelong emphasis on education have shaped who I am today.

To my brother Mohammad and his wife Nasim, your steadfast belief in my abilities and your constant support have been invaluable. Mohammad, you have been both brother and mentor, providing guidance and wisdom throughout my life. Your support through life's challenges, your example of dedication and hard work, and the sacrifices you made for my education have shaped who I am today. Nasim, you have been like a sister to me, bringing warmth, joy, and unconditional love into our family. Your encouragement, understanding, and the genuine care you have shown me throughout this academic journey have been deeply meaningful.

Though my father, Yadolah, is no longer with us, the values and principles that my family has carried forward in his memory continue to guide me. This work represents not only my dedication to academic excellence but also honors the legacy that my family has preserved.

Finally, I thank my colleagues and friends in the academic community for their support. I also gratefully acknowledge the financial support provided by the Natural Sciences and Engineering Research Council of Canada (NSERC) and Le Centre d'études interuniversitaire des structures sous charges extrêmes (CEISCE) through the research grants of Professor Rola Assi, which were instrumental in the completion of this research.

ÉVALUATION DE LA PERFORMANCE SISMIQUE ET DE LA FRAGILITÉ DES COMPOSANTS NON STRUCTURAUX DUCTILES LÉGERS DANS DES STRUCTURES NON LINÉAIRES : DES FACTEURS DE DEMANDE MAXIMALE À L'ESTIMATION DES PERTES

Majid MEHRJOO

RÉSUMÉ

Les pertes associées à la défaillance des composants non structuraux (CNS) lors des séismes représentent entre 70 à 85% de l'investissement total en construction, constituant ainsi la principale source de pertes économiques après un séisme. Malgré cette importance, les approches de conception conventionnelles ne tiennent pas adéquatement compte des différents niveaux de ductilité des ancrages et des dispositifs de fixation des CNS. Elles reposent généralement sur des facteurs empiriques simplifiés, sans considération explicite du comportement inélastique des composants. Afin de combler cette lacune, la présente thèse propose un cadre analytique en quatre volets visant à réduire simultanément les sollicitations sismiques et les coûts de réparation des CNS légers ductiles, au moyen de méthodologies de conception basées sur la performance et intégrant explicitement l'inélasticité des composants.
Dans un premier temps, des facteurs dépendants de la ductilité (A_r/R_P, IVR et IDR) sont dérivés et calibrés à partir d'analyses temporelles linéaires réalisées sur quatre portiques-types en béton armé à ductilité modérée (3, 6, 9 et 12 étages) soumis à 24 accélérogrammes ajustés au spectre de réponse d'aléa sismique uniforme de catégorie C de Montréal. Les résultats indiquent une diminution de 40 à 60% des accélérations, des vitesses et des déplacements de plancher lorsque la ductilité des CNS passe de $\mu = 1{,}0$ à $\mu \approx 2{,}0$ en régime de résonance.
Dans la deuxième étape, une Analyse Dynamique Incrémentale (IDA) est appliquée pour évaluer l'effet combiné de la non-linéarité structurelle et de la résonance avec les trois premiers modes structuraux (T_1, T_2, T_3) sur la fragilité des CNS. Les réponses inélastiques réduisent les accélérations de plancher médianes jusqu'à 110% par rapport aux prédictions élastiques et décalent les probabilités de dépassement d'état de dommage, définies selon les directives Hazus, vers des intensités plus élevées, en particulier pour les composants accordés sur le premier mode.
Dans la troisième étape, les courbes de fragilité sont intégrées dans le cadre de la méthodologie de la FEMA P-58 afin d'estimer les coûts directs de réparation de deux composants représentatifs : les plafonds suspendus installés en toiture et aux étages intermédiaires et les refroidisseurs installés en toiture. L'utilisation d'ancrages améliorés, notamment des contreventements multidirectionnels pour les plafonds et des dispositifs de retenue sismique pour les refroidisseurs, multiplie les seuils d'amorçage de dommage par 3 à 5 pour les plafonds et par 1,3 pour les refroidisseurs, réduisant les coûts de réparation attendus jusqu'à 95% et 17%, respectivement, à 1,5 g d'accélération de plancher. Les pertes sont concentrées en toiture où les coûts sont 30 à 60% plus élevés qu'aux étages intermédiaires; les plafonds affichent des ratios de perte de 1,5 à 2% de la valeur de remplacement du bâtiment, tandis que les refroidisseurs restent inférieurs à 0,55% de cette valeur, reflétant leur impact économique plus faible malgré leur importance fonctionnelle critique pour les opérations du bâtiment.

Dans la quatrième étape, les effets conjoints de la non-linéarité structurelle et du comportement inélastique des CNS sont évalués au moyen d′analyses temporelles non linéaires intégrant les déplacements de plastification des étages dérivés d'analyses pushover. Les résultats montrent des réductions d'accélération de plancher de 67 à 78% pour les CNS élastiques et de 9 à 64% pour les CNS ductiles par rapport aux prédictions obtenues pour les structures élastiques. Les facteurs de force des composants (S_P) proposés identifient une ductilité modérée ($\mu_{comp} \approx 1,5$) comme cible de conception optimale ($S_P = 3,4$ en toiture vs. 4,0 pour les ancrages élastiques), tandis que la comparaison avec les exigences du Code national du bâtiment du Canada 2020 (CNB 2020) révèle que les dispositions actuelles ainsi que leurs variantes (celles récemment approuvées du CNB 2025) sous-estiment les demandes en toiture jusqu'à 35% pour les bâtiments de hauteur moyenne à élevée.

Collectivement, ce cadre en quatre étapes fournit des outils de conception pratiques, des facteurs de modification basés sur la ductilité, et des fonctions de fragilité et facteurs de force des composants, permettant de réduire les sollicitations sismiques des CNS de 40 à 60% et les coûts de réparation jusqu'à 95% pour les plafonds suspendus et 17% pour les refroidisseurs, tout en comblant les lacunes critiques des dispositions actuelles du CNB pour les bâtiments de hauteur moyenne à élevée.

Mots-clés : composants non structuraux, inélasticité des ancrages, facteurs de modification de force basés sur la ductilité, analyse dynamique incrémentale, non-linéarité structurelle, fragilité sismique, évaluation des pertes selon la méthodologie de la FEMA P-58

SEISMIC PERFORMANCE ASSESSMENT OF DUCTILE LIGHT NON-STRUCTURAL COMPONENTS IN NONLINEAR STRUCTURES: FROM PEAK DEMAND FACTORS TO FRAGILITY AND LOSS ESTIMATION

Majid MEHRJOO

ABSTRACT

Losses resulting from the failure of non-structural components (NSCs) during earthquakes account for nearly 70–85% of total construction investment, representing the dominant share of post-earthquake economic losses.

Despite this significance, conventional design approaches fail to adequately represent the varying levels of ductility of NSC attachments, relying instead on simplified empirical factors that do not explicitly consider the complex inelastic behavior of these components.

To address this gap, the present thesis develops a four-step investigation aimed at simultaneously reducing seismic demands and repair costs for light ductile NSCs through performance-based design methodologies that explicitly account for component inelasticity.

In the first step, ductility-based peak component modification factors (A_r/R_P, IVR, and IDR) are derived and calibrated to quantify demand reductions attributable to NSC inelastic behavior. These factors are obtained from linear time-history analyses of four archetype moderately ductile reinforced concrete moment-resisting frames (3, 6, 9, 12 stories). These frames were subjected to 24 spectrally matched ground motions consistent with Montreal's Class C Uniform Hazard Spectrum. These results indicate 40–60% reductions in peak floor acceleration, velocity, and displacement demands when NSC ductility increases from $\mu = 1.0$ to $\mu \approx 2.0$ under resonant conditions.

In the second step, Incremental Dynamic Analysis (IDA) is employed to quantify the combined effects of structural nonlinearity and modal resonance with the first three structural modes (T_1, T_2, T_3) on NSC fragility. Results indicate that inelastic structural behavior reduces median peak floor accelerations by up to 110% relative to elastic predictions and shifts damage-state exceedance probabilities, defined per Hazus guidelines, toward higher intensity levels, particularly for components tuned to the first structural mode.

In the third step, fragility functions are coupled with the FEMA-P-58 loss assessment methodology to estimate direct repair costs for two representative components: suspended ceilings installed at the roof and intermediate floors, and rooftop chillers. Enhanced attachment details, specifically multi-directional bracing for ceilings and seismic restraint devices for chillers, raise damage initiation thresholds by factors of 3-5 and 1.3, respectively. These improvements reduce expected repair costs by up to 95% for suspended ceilings and 17% for chillers at peak floor accelerations of 1.5 g peak floor acceleration. Losses concentrate near the building rooftops, where repair costs are 30-60% higher than at mid-height, and ceiling loss ratios reach 1.5-2% of total building replacement value. Chiller loss ratios remain below 0.55% of building replacement value, reflecting their smaller relative economic impact despite their critical functional role in building operations.

In the fourth step, the combined effects of structural and NSC nonlinearity are investigated through nonlinear time-history analyses incorporating pushover-derived story yield

displacements. Building upon the elastic results from the first step, these analyses demonstrate reductions in floor acceleration demands of 67-78% for elastic NSCs and 9-64% for ductile NSCs relative to elastic structural predictions. Proposed component force factors S_P values identify moderate ductility ($\mu_{comp} \approx 1.5$) as the optimal design target ($S_P = 3.4$ at roof vs. 4.0 for elastic attachments). Comparison with NBC 2020 provisions reveals that both current and the recently approved NBC 2025 formulations underestimate roof-level demands by up to 35% for mid- to high-rise buildings.

Collectively, this four-step framework delivers practical performance-based design tools, including ductility-dependent modification factors, fragility functions, and component force factors that reduce NSC seismic demands by 40–60% and lower repair costs by up to 95% for ceilings and 17% for rooftop chillers, while addressing critical limitations in NBC 2020 provisions for mid- to high-rise buildings.

Keywords: non-structural components, component attachment inelasticity, ductility-based force modification factors, incremental dynamic analysis, structural nonlinearity, seismic fragility, FEMA P-58 loss assessment method

TABLE OF CONTENTS

PAGE

LIST OF TABLES

LIST OF FIGURES

Page

LIST OF ALGORITHMS

LIST OF ABBREVIATIONS AND ACRONYMS

ASCE	American Society of Civil Engineers
CAD	Canadian Dollar
CSA	Canadian Standards Association
CNB	Code National du bâtiment- Canada
CNS	Composants Non-Structraux
DS	Damage state
EDP	Engineering demand parameter
FEMA	Federal Emergency Management Agency
FFT	Fast Fourier Transform
FRS	Floor-response spectrum
FSD	Floor spectral displacement
FSV	Floor spectral velocity
HVAC	Heating, ventilation and air-conditioning
IDA	Incremental Dynamic Analysis
IDR	Inter-story Drift Ratio
IM	Intensity measure
IVR	Inelastic velocity ratio
MDOF	Multi-degree-of-freedom system
MLE	Maximum-likelihood estimation
NBC	National Building Code of Canada
NSCs	Non-structural components

OFC	Operational and Functional Components
PACT	Performance Assessment Calculation Tool
PEER	Pacific Earthquake Engineering Research
PFA	Peak floor acceleration
PGA	Peak ground acceleration
PSA	Peak spectral acceleration
RC	Reinforced concrete
SDOF	Single-degree-of-freedom
THA	Time-history analysis
UHS	Uniform-hazard spectrum

LIST OF SYMBOLS

Greek alphabet

Symbol	Definition	Units
α_s	Strain hardening ratio	dimensionless
κ	Residual strength ratio	dimensionless
μ_{comp}	Target ductility ratio of an NSC	dimensionless
θ_c	Capping rotation	radians (rad)
θ_p	Pre-capping rotation	radians (rad)
θ_{pc}	Post-capping rotation reserve	radians (rad)
θ_r	Residual rotation at which M_R is measured	radians (rad)
θ_u	Ultimate rotation capacity	radians (rad)
θ_y	Yield rotation	radians (rad)
ξ	Damping ratio	dimensionless

Latin alphabet

Symbol	Definition	Units
A_r	Component amplification factor	dimensionless
A_r/R_P	Ratio of amplification to response-modification factors	dimensionless
C_{AR}	Component resonance ductility factor	dimensionless
f_n	Undamped natural frequency of the component	Hz
K_o	Initial elastic stiffness of the component	N/mm or kN/m
m	Component mass	kg or $kN \cdot s^2/m$
R_P	Component response-modification factor	dimensionless
S(%)	Sensitivity index for damping variation	Percentage (%)
Sa(T)	5%-damped elastic spectral acceleration at period T	m/s^2 or g
S_{sed}	Peak spectral acceleration in the 0-0.5s period range	m/s^2 or g
T_1	Fundamental (first mode) period of the supporting structure	seconds (s)
T_2	Second-mode period of the supporting structure	seconds (s)
T_3	Third-mode period of the supporting structure	seconds (s)
T_{b1}	Building fundamental period (first mode)	seconds (s)
T_c	Natural period of the non-structural component	seconds (s)
Mc	Moment at capping rotation θ_c	N·mm or kN·m
M_R	Residual moment associated with θ_r	N·mm or kN·m
M_u	Ultimate moment at rotation θ_u	N·mm or kN·m
My	Yield moment of the component	N·mm or kN·m
Vs-30	Average shear-wave velocity in the top 30 m of soil	m/s

INTRODUCTION

0.1 Context and Problem Statement

Non-structural components (NSC)s typically represent 75-85% of the total building value and can account for 50-80% of post-earthquake repair costs, making their seismic performance critical for overall building resilience (Anwar et al., 2018; Goulet et al., 2007; Miranda & Taghavi, 2005; Zeng et al., 2016). Suspended ceilings, mechanical equipment, and building facades are consistently identified as among the most vulnerable NSC categories during seismic events. Business interruption costs associated with NSC damage frequently exceed direct repair costs, as failure of critical NSCs such as HVAC systems, fire protection systems, or building envelope components can render buildings unusable even when structural systems remain functional (Ghasemof et al., 2022; Mehrjoo & Aval, 2024).

Post-earthquake reconnaissance following major seismic events, including the 1994 Northridge, 1995 Kobe, and 2010-2011 Canterbury earthquakes, has repeatedly demonstrated widespread NSC damage despite minimal structural damage in code-conforming buildings, revealing significant inadequacies in current design approaches (Esper & Tachibana, 1998; Miranda et al., 2012; Naeim, 2004).

Current analytical approaches in the National Building Code of Canada (NBC) primarily focus on the elastic behavior of NSCs and supporting structures, thereby potentially overestimating seismic demands (NRC, 2020). The inadequacy of these code-based approaches within the Canadian context has been confirmed by recent research. Shayan and Assi (2023) demonstrated that current NBC provisions often fail to accurately capture NSC seismic demands in moderately ductile frame buildings. Similarly, Assi et al. (2024) highlighted the limitations of these empirical methods in accounting for structural nonlinearity in shear wall buildings. Furthermore, a recent evaluation by Fazileh et al. (2025) highlighted significant discrepancies in the code's empirical methods, emphasizing the need for improved design formulations that explicitly consider the inelastic behavior of NSCs.

Additionally, while codes incorporate component response modification factors (R_P) intended to account for ductility in NSC attachments, these constant R_P factors fail to differentiate between fundamentally different NSC types despite their distinct attachment systems and failure mechanisms. Moreover, current approaches use simplified component amplification and response modification factors (A_r/R_P) that may fail to accurately capture actual demands when component ductility and period tuning effects are most significant (Anajafi, 2018; ATC, 2018a; Villaverde, 2006; T. Wang et al., 2021).

To address these code limitations, research has generally pursued two paths: simplified analytical techniques and advanced numerical simulations (Anajafi, 2018; Villaverde, 2006). While analytical techniques provide computationally efficient solutions for developing design-oriented factors and understanding fundamental ductility effects (Filiatrault et al., 2018; Obando & Lopez-Garcia, 2018), and advanced numerical methods like Incremental Dynamic Analysis (IDA) enable detailed probabilistic fragility assessment (ATC, 2018a; Banerjee et al., 2016; D'Altri et al., 2020), a unified approach combining these methods is often absent in the literature.

Specifically, while ductility in structural components is well-studied, a comprehensive understanding of NSC attachment ductility remains lacking (ATC, 2018a). Most existing research treats suspended ceilings, mechanical equipment, and other NSCs as having similar ductility and frequency response characteristics, despite their fundamentally different attachment systems, dynamic properties, and failure mechanisms (Anajafi et al., 2020; T. Wang et al., 2021).

Consequently, there is a critical need for a comprehensive framework that quantifies the combined effects of NSC attachment ductility and structural nonlinearity on component seismic demands across different floor levels. This necessity is particularly acute in the Eastern Canadian seismic context. As demonstrated in a recent study (Mehrjoo & Assi, 2025a), the unique high-frequency spectral content of ground motions in this region generates acceleration demands that are not adequately captured by current semi-empirical code provisions.

0.2 General and Specific Objectives

The main objective of this research is to advance the performance-based seismic design of ductile non-structural component attachments in moderately ductile reinforced concrete (RC) moment-resisting frame buildings located in Eastern Canada. This purpose is detailed in the following specific objectives of the present manuscript-based thesis:

1. Developing reliable peak component factors and ductility-based modification factors for acceleration-sensitive NSCs using linear time history analysis with historical and synthetic ground motions matched to the Montreal Site Class C uniform hazard spectrum.
2. Quantifying the combined effects of structural nonlinearity and NSC attachment ductility on component seismic acceleration demands through incremental dynamic analysis and proposing fragility curves corresponding to damage states defined by Hazus guidelines for moderately ductile RC moment-resisting frame buildings.
3. Assessing seismic vulnerability and quantifying economic losses of ductile NSCs using the probabilistic FEMA P-58 methodology, and proposing repair costs, loss ratios, and repair ratios as functions of peak floor acceleration (PFA) for suspended ceiling and chiller systems in the Eastern Canadian seismic environment.
4. Quantifying the combined effects of structural nonlinearity and NSC attachment ductility on component force factors (S_P) and evaluating the adequacy of current design provisions in capturing these effects.

0.3 Methodology of the Research

For the first specific research objective, linear time-history analyses were performed on four archetype reinforced concrete moment-resisting frame buildings (3-, 6-, 9-, and 12-storey), whose structural properties and member dimensions are summarized in ANNEX I, using 24 ground motion records (12 historical records from PEER NGA-East database and 12 synthetics records from the Atkinson (2009) database). The records were matched to Montreal's Site Class C Uniform Hazard Spectrum (2% and 10% probability of exceedance in 50 years) as defined by the National Building Code of Canada 2020 (NBC 2020), corresponding to the 6th

Generation Seismic Hazard Model. The spectral matching was performed using the frequency-domain matching technique detailed in ANNEX VI. NSC seismic demands were evaluated using uncoupled analysis with iterative Newmark integration ($\gamma = 1/2$, $\beta = 1/6$, as described in ANNEX VII) in MATLAB (The MathWorks Inc., 2023) for four ductility levels: elastic behavior ($\mu = 1$), low ductility ($\mu = 1.25$), moderate ductility ($\mu = 1.5$), and high ductility ($\mu = 2$), modeled using bilinear elasto-plastic force-displacement relationships. Three ductility-based modification factors were determined: the component force modification factor (A_r/R_P), inelastic velocity ratio (IVR), and inelastic displacement ratio (IDR). These factors were calculated by comparing elastic and inelastic NSC responses at ground, intermediate, and roof levels, considering the first three building periods (T_1, T_2, T_3), which cumulatively capture more than 90% of the modal mass, to capture resonance effects. A sensitivity analysis on NSC damping ratio variations (1%, 2%, and 3%) relative to the base 5% damping ratio (Equation 2.1), validated the robustness of the proposed factors.

For the second specific research objective, incremental dynamic analysis (IDA) was used to evaluate both elastic and inelastic structural responses using the same 24 earthquake records matched to Montreal's 2% in 50 years hazard spectrum (as described in ANNEX VI), scaled incrementally from 0.1g to 4.0g; the resulting floor-by-floor IDA curves for all case study buildings are presented in ANNEX IV. NSC responses at the four ductility levels were assessed using uncoupled analysis with Newmark integration (ANNEX VII) at intermediate and roof levels, considering the first three building periods (T_1, T_2, T_3) to capture resonance effects. Fragility curves were developed using lognormal distribution parameters estimated through maximum likelihood estimation for four Hazus damage states (slight, moderate, extensive, and complete), yielding 16 fragility curves for each ductility-damage state combination to quantify the probability of exceeding specific limit states (the resulting median-based fragility curves are presented in Figure 3.5 and Figure 3.6.

For the third specific research objective, the FEMA P-58 loss estimation methodology was implemented using PACT software to assess the seismic vulnerability of acceleration-sensitive NSCs. Twelve NSC models with frequency characteristics ranging from 1.0 to 9.0 Hz and ductility ratios from $\mu = 1.34$ to 2.6 (with hysteretic response curves and backbone parameters documented in ANNEX III) were investigated as single-degree-of-freedom systems, classified

into four frequency ranges (Ranges I–IV: ~1.0 Hz to >3.0 Hz) and categorized by ductility level as low, moderate, or high. These models represented suspended ceiling systems (unbraced versus braced) and chiller systems (unrestrained versus seismically restrained anchorage) from the FEMA P-58 component library (with corresponding fragility curves shown in Figure-A V-1**)**. Using the same 24 earthquake records matched using the procedure in ANNEX VI, scaled from 0.1g to 4.0g, the analysis incorporated 200 Monte Carlo realizations at each intensity level, selected to ensure sufficient statistical convergence (Magsalay, 2025), to quantify repair costs, loss ratios, and repair ratios through convolution of fragility curves with consequence functions. Comparative assessments between conventional and enhanced attachment configurations quantified the damage initiation thresholds and reduced expected repair costs across PFA levels.

For the fourth specific research objective, nonlinear time-history analyses were conducted on the same four archetype buildings, incorporating pushover-derived story yield displacements (detailed hinge properties, target displacements, and pushover curves are provided in Figure-A II-1) to capture inelastic structural response. Using the same 24 earthquake records (spectral matching procedure described in ANNEX VI**)** for both hazard levels (2% and 10% in 50 years), NSC responses at the four ductility levels were evaluated using uncoupled analysis with step-by-step Newmark integration ($\gamma = 1/2$, $\beta = 1/6$) in MATLAB. This custom implementation was chosen to overcome the limitations of commercial software in modeling specific NSC attachment ductility and was validated against the numerical models developed by Mazloom (2023). The complete mathematical formulation and implementation details are provided in ANNEX VII. Component periods ranged from 0.01 to 2.0 seconds to capture resonance effects with building periods. Simplified bilinear elasto-plastic NSC models were validated against 12 detailed NSC models featuring advanced hysteretic behavior (documented in ANNEX III**)**, covering a frequency range of 1.0–9.0 Hz and ductility ratios (μ) of 1.34–2.6. Component force factors (S_P) were calculated as peak spectral acceleration to peak ground acceleration ratios, with design values proposed as mean plus one standard deviation. The analysis quantified how structural yielding and NSC attachment ductility simultaneously affect seismic force demands and evaluated the adequacy of current and alternative NBC 2020 provisions.

0.4 Original Contributions of the Thesis

According to the author's knowledge, the original contributions of this thesis include the following:

1. First comprehensive development of ductility-based peak component modification factors (A_r/R_P, IVR, IDR) specifically calibrated for acceleration-sensitive light NSCs in Eastern Canadian moderate seismicity conditions, addressing a significant gap in regional seismic design provisions.
2. Novel comprehensive assessment quantifying how structural nonlinearity and NSC attachment ductility simultaneously affect component seismic performance across multiple response parameters (acceleration demands, fragility curves, force factors, and economic losses), advancing beyond previous studies that examined these effects in isolation or under elastic building assumptions.
3. First identification and validation of optimal NSC attachment ductility ($\mu \approx 1.5$) as a design target through comprehensive fragility analysis spanning four damage states, providing quantitative design guidance for balancing seismic performance with practical constructability constraints.
4. Implementation of ductility-based fragility functions derived from this study within the FEMA P-58 loss estimation framework to establish quantitative relationships between NSC attachment ductility and repair cost reductions in nonlinear RC frame buildings, providing the first economic justification for ductile NSC design in moderate seismicity regions.
5. Development of revised component force factors (S_P) that explicitly quantify the combined influence of structural nonlinearity and varying levels of NSC attachment ductility, extending current code provisions by providing ductility-dependent design values for inelastic components.

0.5 Structure of the Thesis

This thesis is manuscript-based and organized into seven chapters, including an introduction, four core manuscript chapters, and a conclusion with recommendations:

- Chapter 0, the introduction, establishes the context, problem statement, research objectives, methodology, and original contributions of this thesis.
- Chapter 1 covers a literature review of design methods and existing research on ductile NSCs and the effect of their attachment ductility on seismic demands in reinforced concrete moment-resisting frame buildings.
- Chapter 2 presents the development of reliable peak component modification factors for ductile light NSCs subjected to horizontal ground motions in Eastern Canadian seismic conditions. According to the ductility-based modification factors obtained from the seismic demands of NSCs, reliable factors were proposed to accurately capture the effect of target ductility on floor acceleration, velocity, and displacement demands. The derived paper from this study was published in the Bulletin of Earthquake Engineering journal (Mehrjoo & Assi, 2024).
- Chapter 3 focuses on the probabilistic assessment of seismic acceleration demands of ductile NSCs in moderately ductile RC frame buildings. Thus, the combined influence of NSC attachment ductility and structural nonlinearity on component acceleration demands was investigated through incremental dynamic analysis and fragility curve development. The corresponding article of this study was published in the Journal of Engineering Structure (Mehrjoo & Assi, 2025a).
- Chapter 4 presents the seismic vulnerability assessment of ductile light NSCs, which was conducted using FEMA P-58 methodology. Subsequently, the economic quantification of repair costs, loss ratios, and repair ratios for suspended ceilings and chillers was proposed for performance-based design applications. Finally, the paper related to the studies of this section was submitted to the Journal of Urban Resilience and Earthquake Engineering (Mehrjoo & Assi, 2025b).
- Chapter 5 examines the combined influence of structural nonlinearity and NSC attachment ductility on component force factors (S_P) for acceleration-sensitive NSCs.

Through nonlinear time-history analyses, revised S_P values were investigated to assess the impact of ductility on design force demands. The corresponding conference paper was submitted to the 6th International Workshop on Seismic Performance of Non-Structural Elements (SPONSE 2026) (Mehrjoo & Assi, 2026).

- Chapter 6, the conclusion and recommendations, synthesizes the key findings from all objectives, presents the unified contributions to performance-based seismic design of NSCs, and provides recommendations for future research directions and code development.

Figure 0.1 illustrates the overall research framework and presents the interconnections between the main objective, the individual specific objectives addressed in the four scientific articles, the applied methodology, and the resulting research outcomes.

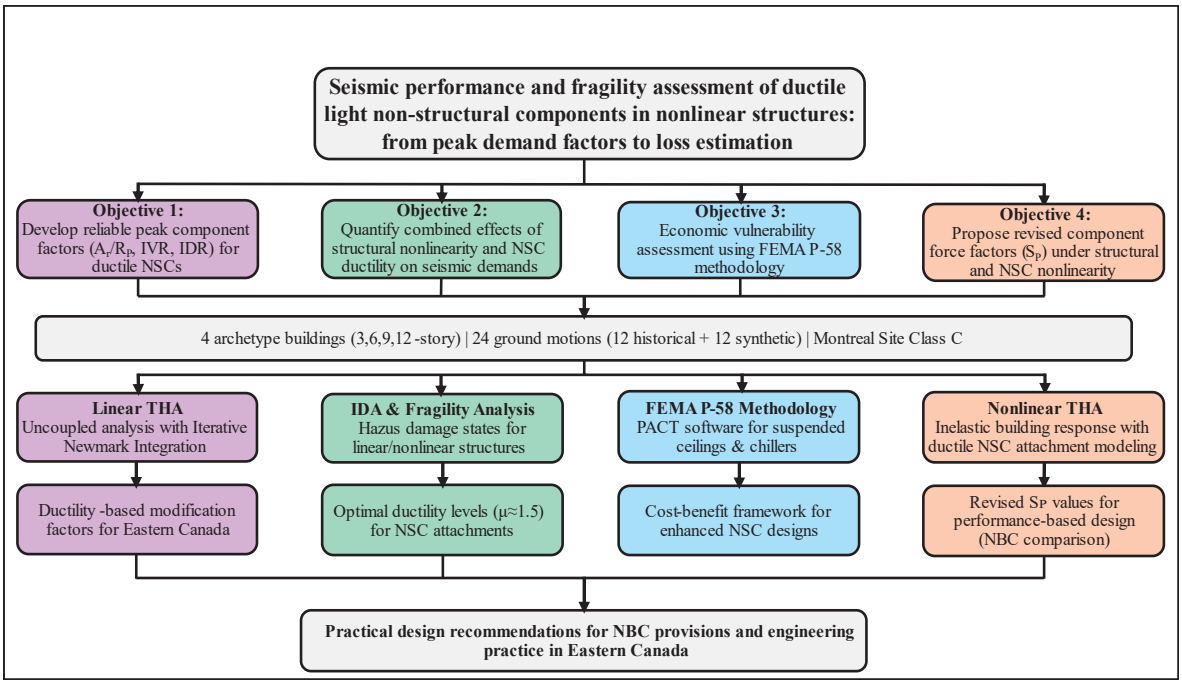

Figure 0.1 The research framework illustrating the links between objectives, methodology, and contributions.

CHAPTER 1

LITERATURE REVIEW

This chapter reviews the seismic performance assessment of acceleration-sensitive NSCs in reinforced concrete moment-resisting frame buildings, emphasizing ductility-based design approaches and probabilistic evaluation methodologies. The review synthesizes provisions from international seismic codes, specifically NBC 2020, ASCE/SEI 7-22, Eurocode 8-1, NZS 1170.5, and ATC NIST.GCR.18-917-43, and experimental and analytical investigations on component ductility effects. Advanced methods for estimating floor response spectra (FRS) and performing fragility analysis are reviewed to lay the foundation for subsequent chapters.

1.1 Introduction

NSCs account for the majority of building investment and are central to post-earthquake functionality; yet earthquake reconnaissance repeatedly shows that these components sustain damage even when primary structural systems remain essentially elastic. This damage pattern reflects a fundamental characteristic of acceleration-sensitive NSCs: their seismic demands are governed by building floor motions, not ground motions alone, and these floor accelerations can be significantly amplified through structural filtering, particularly when NSC periods coincide with the building fundamental periods.

This resonant amplification effect presents a significant challenge for seismic design, as the interaction between component and structural dynamic properties can produce substantial demand amplifications depending on period tuning and damping characteristics. Current seismic design procedures (e.g., NBC 2020) estimate NSC forces using simplified height amplification and component response modification factors (A_r/R_P), which are practical but may misrepresent actual demands when component ductility and period tuning effects are most significant. These limitations highlight the need for demand-consistent design factors that explicitly account for period ratios and component-structure interaction.

Despite extensive research on structural ductility effects, the combined influence of component attachment ductility and structural nonlinearity on NSC seismic demands, damage progression,

and economic losses remains insufficiently characterized. This gap is particularly critical for code-conforming buildings, where current design provisions may not adequately capture the demand reduction effects of ductile component attachments or the demand modifications induced by inelastic structural response. Addressing these limitations requires integrated analytical frameworks that couple probabilistic seismic demand assessment with component-specific fragility characterization and loss estimation, the central focus of this research.

Building on this premise, this chapter first establishes the context (Section 1.1), then classifies NSCs and examines their seismic importance (Section 1.2), reviews current code provisions for seismic force demands (Section 1.3), synthesizes research on ductility effects for acceleration-sensitive components (Section 1.4), examines vulnerability assessment and fragility analysis methodologies (Section 1.5), and concludes by identifying critical research gaps (Section 1.6).

1.2 Classification and Seismic Importance of Non-Structural Components (NSCs)

Building on the overview of NSC seismic challenges presented in the introduction, this section establishes a systematic framework for understanding NSCs through classification and examines their critical importance to building performance and seismic resilience. The Canadian standard CSA S832-14: R2019 (CSA 2014c) defines two primary groups of building components: structural components and NSCs which are also known as Operational and Functional Components (OFCs). NSCs are elements that are not part of the load-bearing system, such as plumbing, partition walls, electrical systems, equipment, and suspended ceilings. Figure 1.1 illustrates these components in a typical building, demonstrating that NSCs are essential to the facility's seismic performance objectives (ATC, 2017), as they provide the operational and functional requirements necessary for building operation.

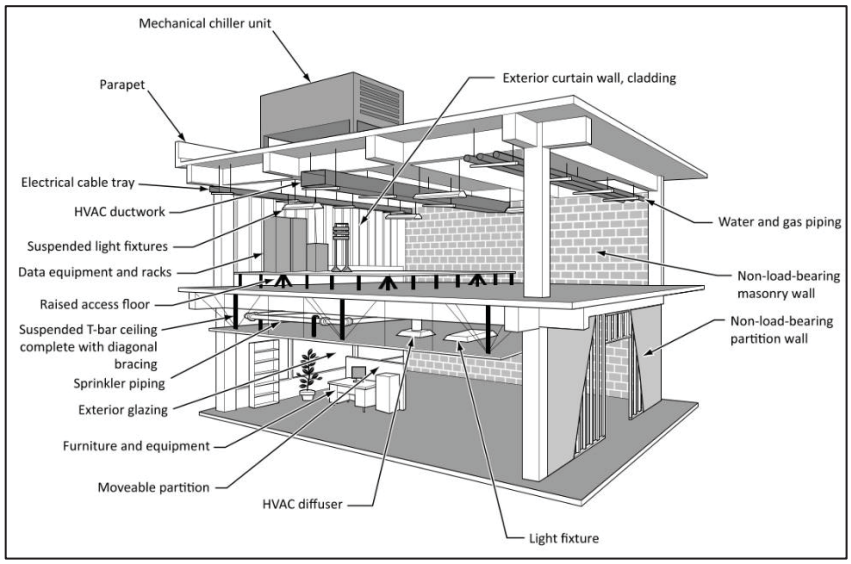

Figure 1.1 Operational and functional components of buildings
Taken from CSA S832-14 (2014c, p. 57)

NSCs can be classified into three main functional groups: (1) architectural components (e.g., suspended ceilings, external cladding, and partition walls), (2) building services components (e.g., mechanical, plumbing, electrical, and telecommunication devices), and (3) building contents (e.g., furniture and office equipment). Despite representing the majority of building investment, these components have proven to be particularly vulnerable during seismic events. The economic significance of NSCs is substantial as they represent 75%–85% of the original construction cost in buildings (Miranda & Taghavi, 2005; Taghavi & Miranda, 2003). Figure 1.2 illustrates the relative cost distribution between structural and non-structural components in three distinct building types, demonstrating the dominance of NSC investment across different facility types. Beyond their economic value, NSCs represent a crucial pillar of building operational capability (Retamales et al., 2013; Soroushian et al., 2015; T. Wang et al., 2021), as their failure can render structurally sound buildings non-functional.

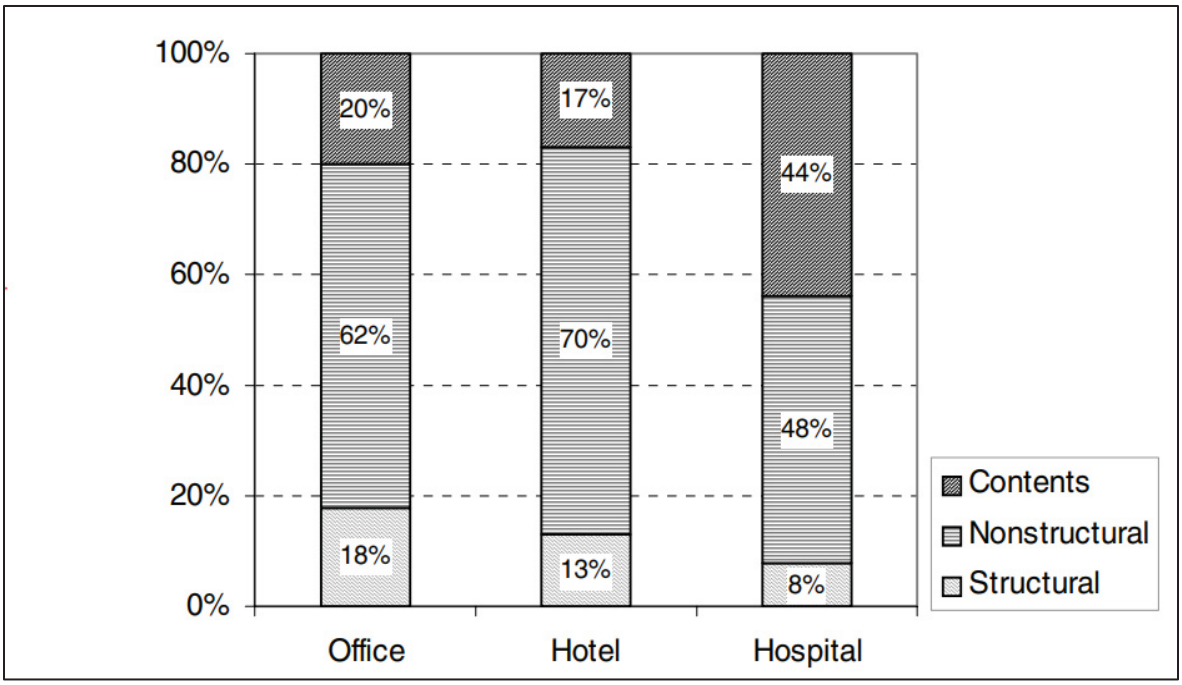

Figure 1.2 Relative components value for different building types
Taken from Taghavi and Miranda (2003, p. 64)

The seismic vulnerability of NSCs has been consistently documented through post-earthquake reconnaissance across major seismic events. Post-earthquake reconnaissance reports from major events, including the 1971 San Fernando (M_w 6.6), 1994 Northridge (M_w 6.7), 1995 Kobe (M_w 6.9), 2010 Maule (Chile) (M_w 8.8), and 2023 Turkey–Syria (M_w 7.8) earthquakes, consistently show that NSCs often sustain damage at lower ground-motion intensities than the primary structural system, resulting in occupant injuries, obstructed egress, and interruptions to critical services (Esper & Tachibana, 1998; Filiatrault et al., 2001; Lew et al., 1971; Miranda et al., 2012; Naeim, 2004; D. Perrone et al., 2019; Tapia-Hernández et al., 2025).

These failures are particularly consequential in critical facilities such as hospitals and fire stations, where NSC damage can compromise life-safety systems and emergency response capabilities.

During the 2010 Maule earthquake, numerous hospitals were partially or fully closed due to non-structural damage; similar life-safety issues linked to NSCs were reported after the 2008 Wenchuan (China) (M_w 7.9), 1988 Saguenay (Québec) (M_w 5.9), 2011 Tōhoku (Japan) (M_w

9.1) (Figure 1.3), and 2017 Ezgeleh (Iran) (M_w 7.3) (Figure 1.4) earthquakes (Alavi et al., 2018; Fan et al., 2018; Mitchell et al., 1989; D. Z. Wang & Dai, 2014).

Importantly, these losses occur even in code-compliant buildings, where NSC failure drives substantial repair costs and business interruptions (Goulet et al., 2007), underscoring that current design provisions may not adequately address NSC seismic demands.

Figure 1.3 Collapsed ceiling of the Kawasaki concert hall after the 2011 Tōhoku earthquake
Taken from Wang and Dai (2014, p. 1)

Figure 1.4 Imam Khomeini Hospital after the 2017 Ezgeleh (Kermanshah, Iran) earthquake
Taken from Zohrabi, ISNA News Agency (2017)

Beyond functional classification, NSCs can be categorized by their primary seismic response mechanism into three groups as defined in FEMA E-74 (ATC, 2012):

i) Acceleration-sensitive: seismic damage is primarily governed by floor accelerations and inertial forces. Suspended ceilings and mechanical equipment are typical examples of this category.
ii) Displacement-sensitive: seismic damage is primarily governed by building displacements or inter-storey drifts. Elevator cabs and windows are typical examples of this category.
iii) Both acceleration- and displacement-sensitive: a combination of building seismic inertial forces and displacements causes the damage. Partition walls, sprinklers, and stairs are examples of this category.

Both classification frameworks serve distinct purposes: functional categories organize components by their building role, while response-based categories identify the governing seismic demand parameters, forming the foundation for the provisions reviewed in the following section.

1.3 Review of Code Provision for Seismic Force Demand on NSCs

Seismic design codes worldwide primarily employ equivalent static force approaches to estimate NSC demands, though these methods differ significantly in how they account for building height amplification, component dynamic characteristics, and ductility effects. The following subsections examine each major international code's formulation in detail, highlighting key distinctions in their treatment of structural dynamics, component characteristics, and ductility provisions. A comparative analysis synthesizing these approaches is presented at the end of this section.

1.3.1 NBC 2020

The NBC 2020 (NRC, 2020) specifies Equation 1.1 and Equation 1.2 for calculating the lateral seismic design force:

$$F_p = 0.3S(0.2)I_E S_p W_p \quad (1.1)$$

$$Sp = C_p A_r A_x / R_p \quad (1.2)$$

(1.1Where $S(0.2)$ is the 5% damped spectral response acceleration, expressed as a ratio to gravitational acceleration, for a period of 0.2 s; I_E is the importance factor for the building; S_p is the seismic amplification factor of the component response, with a maximum value of 4.0 and a minimum value of 0.7; C_p is the seismic coefficient for the NSCs as recommended in the code; A_r is the Component Force Amplification Factor that accounts for the dynamic amplification of the non-structural component (depending on its flexibility and likelihood of resonance), with A_r = 1.0 for rigid components ($T_c \leq 0.06$ s) and A_r = 2.5 for flexible components ($T_c > 0.06$ s), where T_c is the component fundamental period; A_x is the height amplification factor at level x to account for the variation of response of mechanical/electrical equipment with elevation within the building, which equals $(1 + 2\, h_x/h_n)$; W_p is the weight of the component or element; and R_P is the element or component response modification factor, ranging from 1.0 to 5.0 (accounting for viscous damping, nonlinear behavior, and inherent over-strength).

The 2020 version of the NBC incorporates significant changes to seismic hazard definition, replacing separate site coefficients (F_a, F_v) with spectral acceleration values (S(T)) provided directly for each Site Class. Despite this update, critical parameters for accurate NSC design are still lacking, specifically the explicit consideration of component ductility capacity as introduced in evolving standards like ASCE/SEI 7-22 (ASCE, 2022).

1.3.2 NBC 2025 Provisions (Proposed Alternative Method)

To address these shortcomings, a refined formulation has been recommended for future NBC editions (CBHCC, 2024). While preserving the fundamental lateral force (F_P) and component response (S_P) definitions (Equation 1.1 and 1.2), this proposal introduces an enhanced height amplification factor (A_x) (Equation 1.3 that explicitly incorporates building dynamic characteristics.

$$A_X = \frac{1+\frac{1}{T_{ao}}\left(\frac{h_x}{h_n}\right)+\left(1-\left(\frac{0.4}{T_{ao}}\right)^2\right)\left(\frac{h_x}{h_n}\right)^{10}}{\sqrt{\frac{1.1R_{do}}{I_E}}} \quad (1.3)$$

Where:

- $\mathbf{T_{ao}}$ is the building's fundamental translational period
- $\mathbf{R_{do}}$ is the structural ductility-related modification factor for the building
- $\mathbf{I_E}$ is the importance factor for the building (1.0, 1.3, or 1.5)
- $\mathbf{h_x}$ is the height of the component attachment location measured from the base
- $\mathbf{h_n}$ is the total height of the building

The maximum and minimum values of S_P (4.0 and 0.7, respectively) remain unchanged, and C_P, A_r, and R_P are as defined in NBC 2020.

The proposed formulation offers several improvements over the current NBC 2020 method. It explicitly accounts for the building's fundamental period (T_{ao}), recognizing that dynamic amplification varies with building flexibility. The incorporation of R_{do} acknowledges that structures designed with higher ductility exhibit different dynamic characteristics that affect floor acceleration demands. Additionally, the formula includes both linear and tenth-power terms of (h_x/h_n), providing a more realistic representation of acceleration amplification over building height compared to the purely linear assumption in NBC 2020 (CBHCC 2024; Fazileh et al., 2025).

Despite these improvements, the proposed method has important limitations. It relies on empirical fundamental period formulas (such as those in NBC) for estimating T_{ao} that are calibrated to elastic structural behavior and do not account for the actual nonlinear response of structures under strong seismic loading. Furthermore, while the NBC 2020 and the NBC 2025 methods include a response modification factor (R_P) intended to capture nonlinear effects, they do not explicitly isolate the specific contribution of the NSC attachment ductility. Consequently, the current R_P values lack comprehensive calibration based on component performance, relying instead on engineering judgment.

Furthermore, a significant modification in the NBC 2025 is the inclusion of an alternative procedure that allows the use of FRS obtained from Non-Linear Time History Analysis (NLTHA). This approach permits the determination of seismic design forces for NSCs based

on more rigorous structural analysis. The code provides the following alternative equation 1.4 for this purpose:

$$V_p = S_{sed} I_E \left(\frac{C_p A_r}{R_p} \right) W_p \tag{1.4}$$

where S_{sed} is the maximum spectral acceleration value within the period range of 0 s to 0.5 s, determined from the mean 5%-damped floor spectral acceleration values by averaging the individual FRS at the centroid of the floor area at the floor level. It is important to note that recent evaluations by Fazileh et al. (2025) suggest this formulation may present an inconsistency when applying the component resonance factor (A_r) to spectral values (S_{sed}) that effectively already include dynamic amplification effects.

1.3.3 ASCE/SEI 7-22

ASCE/SEI 7-22 (ASCE, 2022) introduces additional refinement through its horizontal seismic design force equation presented in Equations 1.5 and 1.7, which explicitly accounts for structural ductility:

$$\mathrm{F_p} = 0.4\mathrm{S_{DS}I_pW_p}\left[\frac{\mathrm{H_f}}{\mathrm{R_\mu}}\right]\left[\frac{\mathrm{C_{AR}}}{\mathrm{R_{po}}}\right] \tag{1.5}$$

$$0.3\mathrm{S_{DS}I_pW_p} < \mathrm{F_p} < 1.6\mathrm{S_{DS}I_pW_p} \tag{1.6}$$

$$R_\mu = [1.1R/(I_e\Omega_0)]^{1/2} \geq 1.3 \tag{1.7}$$

Where F_P is the seismic design force; S_{DS} is the spectral acceleration at short periods; I_P is the component Importance factor; W_P is the component operating weight;

H_f is the height amplification factor determined based on the dynamic properties of the supporting structure. When the building fundamental period (T_a) is known, H_f is calculated using a polynomial formulation as described in Equation 1.8:

$$H_f = 1 + a_1(z/h) + a_2(z/h)^{10} \tag{1.8}$$

Where z is the attachment height; h is the structure height; a_1 and a_2 are period-dependent coefficients used as described in Equations 1.9 and 1.10:

$$a_1 = 1/T_a \leq 2.5 \tag{1.9}$$

$$a_2 = [1 - (0.4/T_a)^2] > 0 \tag{1.10}$$

When T_a is unknown, a simplified linear distribution is used as described in Equation 1.11:

$$H_f = 1 + 2.5\left(\frac{z}{h}\right) \tag{1.11}$$

Where C_{AR} is the component resonance ductility factor that converts the peak floor to the peak component acceleration; R_{po} is the component strength factor and R_μ is the structure ductility reduction factor defined in Equation 1.7.

In Equation 1.5, I_E, R, and Ω_0 represent the importance factor, response modification factor, and overstrength factor, respectively, for the supporting building or nonbuilding structure, all of which can be obtained from Table 12.2-1, 15.4-1, or 15.4-2 of this standard. The upper and lower bounds on F_P are specified in Equation 1.6.

One of the major improvements of the 2022 edition compared to previous versions and other standards is the introduction of R_μ, the structure ductility reduction factor shown in Equation 1.7, which explicitly reduces design forces based on the building's ductility capacity (R-factor), importance, and overstrength characteristics.

Furthermore, regarding component amplification, ASCE 7-22 (ASCE, 2022) no longer assigns a single value to flexible components. Instead, C_{AR} values are determined based on the component's ductility and its likelihood of being in resonance with the supporting structure. Values range from 1.0 to a maximum of 2.8, where the upper bound corresponds to low-ductility components ($\mu \approx 1.25$) likely to be in resonance.

1.3.4 ATC (NIST.GCR.18-917-43)

Building on observations from instrumented buildings, the Applied Technology Council (ATC, 2018a) has proposed Equation 1.12 that incorporates explicit floor amplification factors:

$$\frac{F_P}{W_P} = PGA\left[\frac{\left(\frac{PFA}{PGA}\right)}{R_{\mu bldg}}\right]\left[\frac{\left(\frac{PCA}{PFA}\right)}{R_{\text{Pocomp}}}\right]I_P \tag{1.12}$$

Where, PFA/PGA is the floor amplification factor and can be determined using Equation 1.13.

$$\frac{PFA}{PGA} = 1 + a_1[z/h] + a_2[z/h]^{10} \tag{1.13}$$

With;

$$a_1 = (1/T_{abldg}) \leq 2.5 \tag{1.14}$$

$$a_2 = \left[1 - \left(0.4/T_{abldg}\right)^2\right] > 0 \tag{1.15}$$

Where W_P is the component's weight, PGA is the peak ground acceleration, PFA is the peak floor acceleration, and $R_{\mu bldg}$ is the reduction factor for accounting for global structural ductility. R_{Pocomp} is the inherent component reserve strength margin factor, I_P is the component importance factor, and z is the height of the NSC in relation to the structure's base, while h is the overall height of the supporting structure. The fundamental translational period of the supporting structure, T_{abldg}, can be calculated using Equation 12.8-8 from ASCE/SEI 7-22 (ASCE, 2022). The term PCA/PFA represents the component amplification factor, where PCA (Peak Component Acceleration) is the maximum acceleration experienced by the component itself relative to the maximum floor acceleration (PFA). This ratio accounts for dynamic amplification due to resonance between the component's natural period and structural modal periods, varying from 1.4 to 4.0 depending on the location of the component inside the structure.

1.3.5 NZS 1170.5

The New Zealand standard (SNZ, 2004) provides an alternative formulation that explicitly incorporates both spectral shape effects and a piecewise height amplification approach distinct

from other international codes. The horizontal seismic design force of NSCs can be calculated using Equation 1.16 according to NZS 1170.5.

$$F_{Ph} = C_P(T_P)C_{Ph}R_P W_P \leq 3.6W_P \tag{1.16}$$

Where T_P is the component period; C_{Ph} is the horizontal response factor of the component; R_P is the component risk factor that changes depending on the component's failure consequences; and W_P is the component's weight. $C_P(T_P)$ is also the horizontal design coefficient of the component that can be calculated using Equation 1.17.

$$C_P(T_P) = C(0)C_{Hi}C_i(T_P) \tag{1.17}$$

As shown in Equation 1.18, the site hazard coefficient at T=0 can be obtained:

$$C(0) = C_h(0)ZRN(T, D) \tag{1.18}$$

Where C_{Hi} is the floor height coefficient for level i, calculated as the lesser value of the applicable expressions in Equation 1.19;

$$C_{Hi} = \begin{cases} 1 + \dfrac{h_i}{6}, & \text{for all } h_i < 12 \text{ m} \\ 1 + 10\dfrac{h_i}{h_n}, & \text{for } h_i < 0.2h_n \\ 3, & \text{for } h_i \geq 0.2h_n \end{cases} \tag{1.19}$$

Additionally, $C_i(T_P)$ is the spectral shape coefficient of the component for level i; $C_h(0)$ is the spectral shape factor at T = 0.2; R is the return period factor, which can range from 0.25 to 1.8 depending on the importance level of the supporting structure; and N is the near-fault factor. This upper-bound, piecewise-capped approach contrasts with the continuous amplification profiles in NBC and ASCE and can result in potentially higher design forces at upper building levels. While NZS incorporates site-specific factors such as return period and near-fault effects, it does not explicitly account for structural ductility or distinguish between elastic and inelastic building response within the height term.

1.3.6 Eurocode 8-1

Eurocode 8-1 (CEN, 2004) calculates the horizontal seismic design force F_a using Equation 1.20.

$$F_a = (S_a W_a \gamma_a)/q_a \tag{1.20}$$

Where; F_a is the horizontal seismic force, acting at the center of mass of the NSC in the most unfavorable direction; W_a is the weight of the element; S_a is the seismic coefficient applicable to NSCs defined in Equation 1.21; γ_a is the importance factor of the element; q_a is the behavior factor of the element.

$$S_a = \alpha \cdot S \cdot \left[\frac{3\left(1 + \frac{Z}{H}\right)}{1 + \left(1 - \frac{T_a}{T_1}\right)^2} - 0.5 \right] \geq \alpha S \tag{1.21}$$

Where: α is the ratio of the design ground acceleration on type A ground, a_g, to the acceleration of gravity g; S is the soil factor;T_a is the fundamental vibration period of the NSCs; T_1 is the fundamental vibration period of the building in the relevant direction; z is the height of the NSC above the level of application of the seismic action (foundation or top of a rigid basement); and H is the building height measured from the foundation or from the top of a rigid basement. The value of the seismic coefficient S_a may not be taken less than $\alpha \cdot S$.

The importance factor γ_a is typically assigned a value of 1.0 but should be increased for critical NSCs, including life safety systems and tanks/vessels containing hazardous materials (CEN, 2004). Unlike NBC and ASCE codes, Eurocode 8-1 explicitly incorporates both building and component periods (T_1 and T_a) in the amplification calculation, recognizing the potential for resonance effects between structural and non-structural elements.

It is important to note that the Second Generation of Eurocode 8 (currently in the final approval phase as prEN 1998) introduces significant modifications to the seismic design of non-structural components. As detailed by Kazantzi et al. (2024) and Fajfar and Vukobratović (2022), the new standards (prEN 1998-1-2: 2022a, prEN 1998-4: 2022b) propose a multi-tiered approach comprising three distinct design methods based on the available level of knowledge:

1. Method 1 (Detailed): A structure-specific approach that calculates the component force (F_{ap}) using floor response spectra (S_{ap}). This method explicitly accounts for the dynamic characteristics of both the supporting structure and the component, including period tuning effects (T_{ap}/T_1). It is the most accurate but requires detailed modal information of the building.
2. Method 2 (Simplified): A non-dissipative “period-agnostic” approach for cases where structural properties are unknown. It conservatively assumes the component is in

resonance with the building, applying a constant amplification factor (typically AMP = 7) to the PFA.

3. Method 3 (Dissipative): A new ductility-based approach that introduces a "sacrificial fuse" of verified ductility (μ_D) in the component anchorage. This method allows for reduced design forces by explicitly accounting for energy dissipation, linking the amplification factor directly to the fuse ductility.

These updates represent a shift towards more refined, performance-based definitions of component demand compared to the simplified formulations of the previous generation.

1.3.7 Comparative Analysis and Critical Limitations of Current Code Provisions

The preceding subsections have presented the individual formulations of major international seismic design codes for NSC force estimation. This section synthesizes these approaches through comparative analysis of their predicted floor acceleration amplification profiles, examines the historical evolution of component ductility provisions, and identifies fundamental limitations inherent to simplified code-based methodologies.

1.3.7.1 Height Amplification Factor Comparison

Figure 1.5 compares the resulting floor-acceleration amplification profiles (normalized to PGA) for a representative 12-story RC moment-resisting frame building (h = 36 m, T_1 = 1.1s). For NBC's new proposed method, building ductility parameters of Rdo = 2.5 and IE = 1.0 were assumed, while Eurocode 8-1 was evaluated for a rigid acceleration-sensitive component.

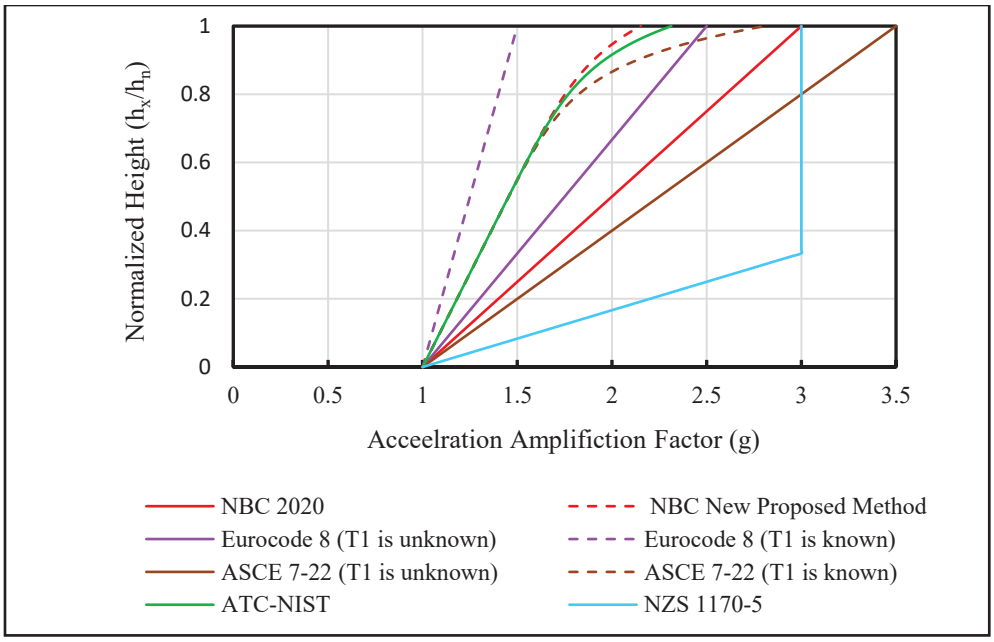

Figure 1.5 Comparison of height-wise acceleration amplification factors for different codes

As illustrated in Figure 1-5, substantial variations exist among code predictions. NBC 2020 employs a simplified linear formulation ($Ax = 1+2h_x/h_n$), yielding a roof amplification of 3.0×PGA. ASCE 7-22 (ASCE, 2022), when the building period is known ($T_a = 1.1$ s), uses the polynomial formulation $H_f = 1 + a_1(z/h) + a_2(z/h)^{10}$, yielding a lower roof amplification of approximately [2.8]×PGA. When the building period is unknown, ASCE 7-22 defaults to the simplified linear formulation $H_f = 1 + 2.5(z/h)$.

The ATC (NIST) approach predicts moderately high amplifications (2.3×PGA at the roof) with a pronounced nonlinear profile that reflects dynamic amplification behavior in elastic structures, though remaining lower than the upper-bound predictions of NZS 1170.5. NBC's new proposed method presents a fundamentally different approach by explicitly incorporating structural ductility effects through the $\sqrt{(1.1R_{do}/I_E)}$ reduction term, resulting in predictions of approximately 2.2×PGA at the roof. NZS 1170.5 employs a piecewise formulation for the height amplification factor (C_{Hi}). For the building considered ($h_n = 36$ m), this results in C_{Hi} reaching the maximum value of 3.0×PGA above 20% of the building height (7.2 m) and remaining constant thereafter, yielding one of the highest amplification factors among the codes examined rather than a simple linear profile. In comparison, Eurocode 8-1 yields predictions at the roof that vary with both structural and component dynamic characteristics.

When the building period is unknown, the formula simplifies to $S_a/(\alpha \cdot S) = 1 + 1.5(z/H)$ for a rigid component, yielding approximately 2.5×PGA at the roof. When the building period is known ($T_1 = 1.1$ s), the full expression (Equation 1.21) accounts for the ratio T_a/T_1, producing a different amplification profile that depends on the assumed component period. It should be noted that the second generation of Eurocode 8 ((prEN 1998-1-2: 2022a, prEN 1998-4: 2022b), as reviewed by Kazantzi et al., (2024) and Fazileh et al., (2025)) does not define a standalone height amplification factor comparable to A_x or H_f. Instead, the height effect is embedded within the floor response spectrum formulation through the modal participation factor (Γ_i) and mode shape value (φ_{ij}) at each floor, which requires building-specific modal properties. Consequently, a direct height-factor comparison in Figure 1.5 is not included for the second generation of Eurocode 8.

1.3.7.2 Historical Evolution of Component Ductility Provisions

Beyond height amplification methodologies, the provisions for component ductility and anchorage have evolved significantly in seismic codes, particularly in American design practice. The 1994 NEHRP regulations were the first to quantify performance criteria for NSCs, introducing the concept that components should possess ductile, energy-absorbing mechanisms through their anchoring systems (Drake & Bachman, 1994). However, quantifying anchor ductility presented significant challenges. The NEHRP 2003 Provisions (FEMA, 2003) introduced a 2.5 multiplier for anchor design when anchors are not governed by ductile steel yielding, requiring that anchor strength be at least 2.5 times the factored forces transmitted by the attachment. This approach was subsequently adopted by the International Building Code (IBC, 2012).

This approach evolved further with ACI 318 (ACI, 2019), implementing a 40% penalty on anchor capacity (50% for redundant anchorages), while ASCE 7 (ASCE, 2017) required a 130% multiplier on anchor forces plus additional multipliers based on anchor ductility capability. In current practice, ductile anchors allow design forces to be applied directly per ACI 318 (ACI, 2019), whereas brittle anchors require a 2.5 multiplier on component demand forces to maintain linear-elastic behavior and prevent premature failures.

1.3.7.3 Component Response Modification Factors in International Standards

Current international codes account for NSC ductility characteristics through component response modification factors, though with significant variations in their ranges and application. Unlike previous ASCE editions, which used a single factor (R_p) ranging from 1.0 to 12.0, ASCE 7-22 (ASCE, 2022) has decoupled this behavior into a Component Strength Factor (R_{po}) and a Component Resonance Ductility Factor (C_{ar}). In contrast, NBC uses more conservative R_P values from 1.0 to 5.0, while Eurocode 8 employs a behavior factor (q_a) to account for component ductility and energy dissipation capacity. Despite the widespread adoption of these provisions, the specific values for these factors across all standards were derived primarily from engineering judgment and observed performance rather than comprehensive experimental validation or numerical research. This gap between code provisions and rigorous empirical calibration has motivated extensive research into NSC dynamic behavior and ductility effects.

1.3.7.4 Fundamental Limitations of Simplified Code Approaches

Beyond these inter-code discrepancies, current international standards share several fundamental limitations that affect the accuracy of NSC seismic demand estimation. These limitations, which are inherent to simplified code-based approaches, include:

1. Higher mode contributions: Provisions neglect the effect of a building's higher frequency modes, which can be significant for high-rise buildings;
2. Torsional response: Provisions neglect the effect of the building's torsional motion on the seismic response of NSCs, which can be substantial for NSCs located away from the building's center of mass;
3. Height-wise variation: Several provisions, including NBC 2020, assume a linear variation of the floor acceleration over the building height, which is a simplified approximation, particularly for taller structures or those with irregularities. However,

newer provisions such as ASCE 7-22 and NBC 2025 have adopted nonlinear height-wise formulations that better capture dynamic amplification patterns.

Finally, arguably the most significant limitation of current simplified approaches is that the factors accounting for the non-linear response of NSCs, such as R_p in the NBC, C_{ar} in ASCE 7-22, and q_a in Eurocode 8-are not rigorously performance-based. As noted by recent studies (FEMA 2009; Daniele Perrone et al., 2022), these factors rely heavily on engineering judgment rather than comprehensive experimental testing, numerical modeling, or risk-based assessment. Consequently, they fail to provide a uniform probability of failure or a consistent reliability index across different component types. Calibrating these performance factors requires a complex process involving extensive numerical validation, which remains a critical gap in current seismic design provisions.

1.4 Ductility Effects on Seismic Demands of NSCs

Research on the seismic behavior of NSCs has evolved significantly over the past four decades, driven by observed performance in earthquakes and the recognized limitations of simplified code approaches. This section reviews the experimental and analytical investigations that have shaped our understanding of how component ductility influences seismic demands, establishing the foundation for the research presented in subsequent chapters.

Predicting accurate NSC seismic demands requires understanding how earthquake forces are modified as they propagate through building systems. Unlike ground-supported structures that respond directly to ground motions, NSCs experience seismic demands that are filtered twice: first through the primary building structure, and subsequently through the component's own dynamic characteristics. This dual filtering mechanism, illustrated in Figure 1.6, fundamentally governs NSC seismic response and necessitates careful consideration of both structural and component-level nonlinearity.

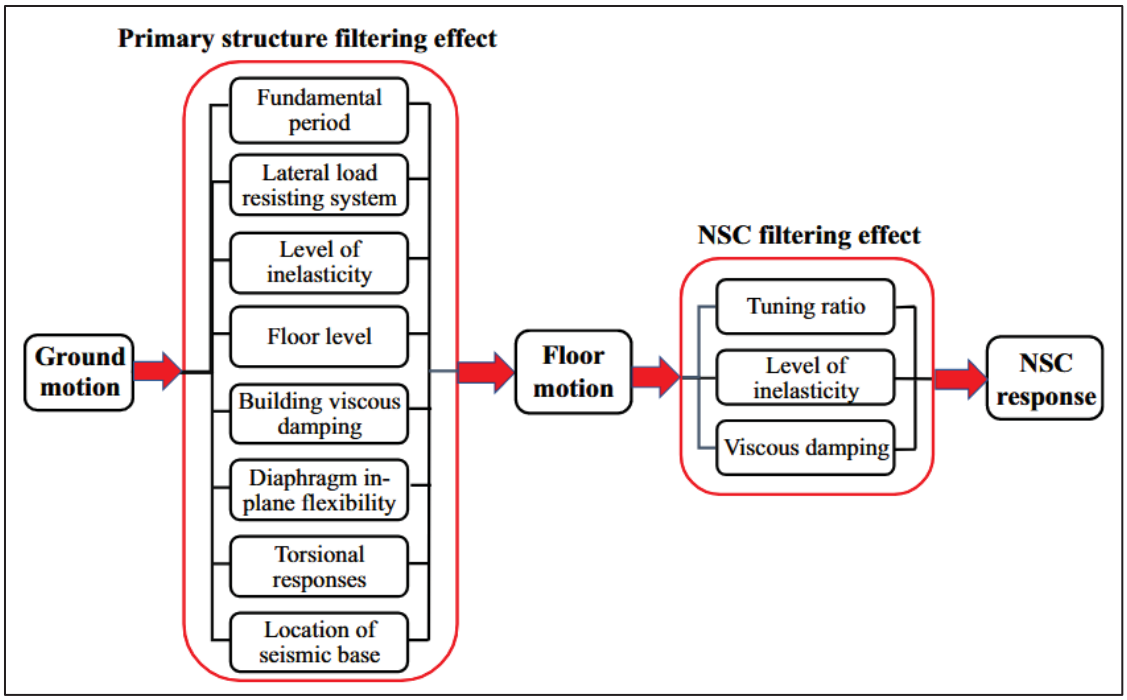

Figure 1.6 The two most prominent filters that determine NSC seismic reactions
Taken from Anajafi et al. (2020, p. 2117)

1.4.1 Experimental Investigations

Research has revealed significant gaps in conventional design approaches through experimental testing and field observations. The ATC-120 Project (ATC, 2018a) and experimental findings (Archila et al., 2012; Astroza et al., 2015; D. Watkins et al., 2009; D. A. Watkins, 2011) raise serious doubts about the validity of applying simplified empirical values universally across all NSC types. Notably, modal testing by Archila et al. (2012) on 11 NSCs in Vancouver hospitals showed damping ratios (ξc) ranging from 0.4-2.6% for pipe systems and below 0.4% for other NSCs, substantially lower than the assumed 5% default value. Low damping ratios result in high floor response spectra, particularly for NSCs with periods matching the supporting structure. These findings emphasize the need to incorporate component ductility effects more precisely.

1.4.2 Analytical Approaches for Modeling Inelastic NSC Response

Building on these experimental observations, previous analytical studies (Lin & Mahin, 1985; Lucchini et al., 2014; Medina et al., 2006; Sadeghzadeh-Nazari & Ghafory-Ashtiany, 2011; Soroushian et al., 2015; Sullivan et al., 2013) have established that secondary system damping critically affects floor acceleration demands, demonstrating that design approaches should accommodate damping ratios both above and below 5%. Researchers have developed various analytical methodologies to account for NSC nonlinearity, which can be categorized into three distinct approaches.

First, strength reduction methods have been employed to capture nonlinear effects. Villaverde (2006) employed strength reduction factors accounting for the nonlinear behavior of NSCs and their supporting frameworks. Igusa (1990) used random vibration analysis and equivalent linearization methods for two-DOF primary-secondary systems with minor nonlinearities, while Adam & Fotiu (2000) investigated SDOF oscillators on a four-story frame building. Chaudhuri & Villaverde (2008) extended this work to inelastic non-linear structures supported by moment-resistant frames.

Alternatively, equivalent damping methods offer another approach to modeling ductility effects. Vukobratović & Fajfar (2017) proposed accounting for ductile NSC inelastic behavior by increasing damping ratios when producing floor response spectra. Filiatrault et al. (2018) applied non-structural equivalent damping ratios to suspended piping systems, though this approach requires pseudo-static cyclic testing to determine appropriate values.

More recently, ductility-based design methods have emerged as a third approach. Miranda et al. (2018) designed anchors and connections as force-controlled components while allowing NSC attachments (bracings) to undergo inelastic actions, recognizing attachments as the weakest link influencing seismic demands. Using roof acceleration responses from instrumented California structures, they produced floor spectra for component ductility values of 1.0 (elastic), 1.5 (moderate), and 2.0 (high). These studies demonstrated that even such limited levels of nonlinearity can significantly reduce seismic demands.

1.4.3 Quantitative Benefits of Component Ductility

The analytical methodologies described above have been applied in numerous studies to quantify the seismic demand reductions achievable through component ductility. Kazantzi et al. (2018) showed that NSC inelasticity can reduce force and displacement demands by up to 50% at resonance and 20% for off-resonance conditions. Obando and Lopez-Garcia (2018) confirmed these findings for displacement-controlled components, particularly those tuned to the building's fundamental mode. Anajafi et al. (2020) further quantified the combined effects of ductility and damping, demonstrating that demand reductions are most pronounced for elastic-tuned components (up to 71%) but diminish for components with higher ductility levels (approximately 14% for $\mu = 3.0$).

1.4.4 Factors Influencing Ductility Benefits

Beyond these direct ductility effects, research has revealed that multiple factors influence the magnitude of ductility benefits. Recent studies (Anajafi et al., 2021; A. K. Kazantzi et al., 2020b; Surana et al., 2021) have demonstrated that NSC characteristics, particularly tuning condition and damping ratio, significantly affect acceleration response spectra, attachment ductility, and component nonlinearity. Aragaw & Calvi (2018) noted that damping effects on floor response spectra can be negligible when NSC periods are either very short or very long compared to the supporting structure, but remain important for most components. To further characterize these interactions, Anajafi & Medina (2019a) conducted a comprehensive examination using a damping modification factor (DMF), defined as the ratio between floor response spectra at a specific damping ratio versus 5% damping. Numerical calculations on code-conforming buildings revealed that both damping ratio and tuning period ratio (NSC period to building fundamental period) significantly affect DMF values, highlighting the complexity of ductility-damping interactions.

1.4.5 Implementation Challenges

Despite the demonstrated benefits of ductile behavior, practical implementation faces several challenges. Providing inelastic fuses presents practical challenges for many NSC types, including pipe networks, wall-anchored equipment, and components directly attached to structures without proper bracing systems. Nevertheless, various attachment configurations can provide ductile behavior; steel angles securing equipment to floors can dissipate significant energy through inelastic deformation, though such behavior is difficult to measure. The position (floor level) of NSC attachments, connection details, and dynamic properties of both building and component are often unknown during experimental testing (Anajafi, 2018), complicating performance verification. These implementation challenges and knowledge gaps motivate the comprehensive investigation of NSC ductility effects presented in this thesis.

1.5 Vulnerability Assessment and Fragility Analysis of NSCs

Having established the critical role of ductility in modifying NSC seismic demands, the next step toward performance-based design requires quantifying the probabilistic relationship between seismic demands and component damage. This quantification is achieved through vulnerability and fragility assessment.

1.5.1 Advanced Analytical Approaches for Demand Assessment

To address the nonlinear behavior of NSCs and their supporting structures, advanced analytical approaches have been developed that overcome the limitations of code-simplified methods. In particular, methods integrating seismic probabilistic assessment are necessary for a more comprehensive and accurate evaluation of NSCs' seismic demands. In this context, two prominent methodologies stand out: Incremental Dynamic Analysis (IDA) and Multiple-Stripe Analysis (MSA). IDA provides a comprehensive simulation framework to assess seismic demands across a continuous range of earthquake intensities by applying scaled accelerograms to the building model. MSA offers a complementary approach by analyzing structural response at discrete intensity levels using ground motion sets specifically selected for each intensity

level (Banerjee et al., 2016). In this study, IDA was selected as it enables the generation of continuous fragility curves to evaluate component performance corresponding to different damage states (D'Altri et al., 2020; D'Ayala et al., 2015; Roca et al., 2010).

1.5.2 Effect of Structural Nonlinearity on NSC Demands

A pivotal factor in these methodologies is the influence of structural nonlinearity on floor acceleration demands. Early studies by Lin and Mahin (1985) and Taghavi and Miranda (2012) demonstrated that inelastic structural responses can either amplify or attenuate floor accelerations compared to linear models, depending on factors such as building height, lateral system flexibility, and NSC period. Building on this understanding of structural effects, Clayton and Medina (2012) proposed a probabilistic method to estimate acceleration demands for NSCs in shear wall structures based on three NSC period ranges: rigid region ($T_C \rightarrow 0$), short-period region ($0 < T_C < 0.5T_{B1}$), and fundamental-period region ($0.5T_{B1} < T_C < 2.0T_{B1}$). IDA with site-specific ground-motion hazard data was used to develop hazard curves and component uniform hazard spectra (CUHS) considering various structural and NSC characteristics. The study found that component location, period ratios, and damping ratios are critical factors in estimating component responses, with components located at higher floors and those with period ratios near unity experiencing significantly amplified accelerations, while higher damping ratios provided substantial demand reductions. Recent work by Ruggieri and Vukobratović (2024) has further quantified this effect, showing that accounting for nonlinear behavior can reduce acceleration demands by up to 40% compared to elastic analysis predictions. Crucially, their findings indicate that the magnitude of this reduction is highly sensitive to the structural configuration and energy dissipation capacity.

1.5.3 Component Fragility Characterization

Translating these demand estimation approaches into damage prediction requires component-specific fragility characterization. D'Angela et al. (2024) conducted a comprehensive study of the seismic fragility of NSCs modeled as nonlinear single-degree-of-freedom systems. The research utilized IDA to evaluate the seismic response of a range of NSC frequencies, including

medical equipment, suspended ceiling systems, and museum objects. The various damage states and performance levels for each NSC category were evaluated in the analysis, which resulted in the production of fragility curves that are valuable in the seismic design and vulnerability assessment of NSCs. The results showed that as the rigidity of the NSCs increased, the probability of exceeding damage states tended to decrease. Similarly, the fragility dispersion (uncertainty) was found to decrease as the component rigidity increased. Gautam et al. (2021) investigated the seismic fragility of structural and NSCs in RC buildings in Nepal, using detailed vulnerability assessments of school buildings after the 2015 Gorkha Earthquake (Mw 7.8). This assessment provides insights into their seismic demands and highlights the urgent need for strengthening the NSCs and beam-column connections.

1.5.4 Economic Implications of Ductility in NSC Design

Building on these fragility analysis frameworks, performance-based design methodologies have evolved to incorporate economic loss assessment. Recent studies have shown that components with moderate to high attachment ductility consistently experience 40-60% less damage, and consequently lower repair costs, compared to components with elastic attachments, particularly under resonance conditions (ASCE, 2022; Lin & Mahin, 1985; Mehrjoo & Assi, 2024; NRC, 2015; Taghavi & Miranda, 2012). These quantified economic benefits have motivated both practical mitigation strategies and fundamental research into how component ductility effectively mitigates seismic damage.

Experimental and analytical investigations have identified several effective mitigation approaches for reducing NSC damage. Studies have demonstrated that measures such as additional bracing, internal gaps, and energy-dissipating connections can significantly reduce damage to components such as suspended ceilings and mechanical equipment (Bianchi et al., 2019; Brandolese et al., 2019; Ciurlanti et al., 2022; Dhakal et al., 2016; Gallo et al., 2018; Pürgstaller et al., 2020; Rojas et al., 2023; Ryu & Reinhorn, 2019). Collectively, these studies indicate that enhanced detailing can reduce seismic demands by approximately 30-40%, thereby significantly lowering failure probabilities.

1.6 Conclusion and Research Gaps

This literature review demonstrates that, although current codes provide a foundational approach for NSC seismic design and prior research has yielded valuable insights into NSC nonlinearity, significant gaps remain in translating these findings into practical performance-based design frameworks. Three critical analytical gaps limit the systematic implementation of ductility-based mitigation strategies:

First, while recent international studies have begun to address the combined effects of NSC attachment ductility and structural nonlinearity, these interactions have not been comprehensively quantified within the context of Canadian design practice. Specifically, the combined effects have not been evaluated across different building heights and seismic intensities characteristic of the Canadian hazard. This gap manifests as a lack of reliable, locally calibrated ductility-based factors for floor acceleration, velocity, and displacement demands that account for the interaction between structural behavior in the Canadian context and component response.

Second, the relationship between attachment ductility levels and component damage states remains insufficiently characterized within analytical frameworks. This limitation hinders the comprehensive assessment of how structural and NSC ductility jointly influence acceleration demands and associated damage progression.

Third, the translation of ductility-based damage reductions into economic metrics has not been systematically evaluated for diverse NSC types and building configurations. Without a clear economic valuation of ductile NSC vulnerability using a performance-based assessment, engineers cannot effectively quantify the cost-benefit trade-offs of different attachment detailing strategies or determine how these interactions influence component force factors for design.

Addressing these interconnected gaps is essential for developing evidence-based design guidelines that optimize NSC attachment detailing while balancing performance objectives and economic constraints. This thesis addresses these gaps through comprehensive numerical investigations spanning four archetype buildings, multiple ductility levels, and diverse NSC

types. The research establishes practical design tools that incorporate the benefits of component ductility within performance-based frameworks.

FOREWORD TO CHAPTER 2

To support the interpretation of the results presented in this chapter, it is important to clarify the selection of Engineering Demand Parameters (EDPs) and specific terminology. While the following manuscript primarily focuses on Peak Floor Acceleration (PFA) and Inelastic Displacement Ratio (IDR), consistent with standard practice for anchored components, the study also tracks the Inelastic Velocity Ratio (IVR).

This decision is grounded in the recognition that velocity demands govern the sliding, overturning, and swinging motions of unattached or freestanding NSCs (e.g., furniture and equipment) and suspended NSCs (e.g., ceilings and light fixtures) (Buccella et al., 2020; Pavlou & Constantinou, 2006). Although the specific components modeled in this chapter are anchored, the IVR metric is retained to ensure the generated demand data is sufficiently comprehensive to support future fragility assessments for these velocity-sensitive typologies.

Additionally, ten technical clarifications regarding the methodology are provided below:

1. Terminology (Section 2.1): The term 'elastic response spectra' is used to describe spectra computed for elasto-plastic NSCs. This should be interpreted as 'constant-ductility response spectra', as the spectra are derived for components with specified ductility levels.

2. Damping Model (Section 2.1.1): It is acknowledged that in nonlinear analyses, pure modal damping can theoretically introduce spurious high-frequency numerical noise in floor acceleration records. While this study utilized 5% modal damping, the inclusion of a small stiffness-proportional damping term is often recommended in practice to filter such non-physical high-frequency components.

3. Fundamental Period (Table 2.1): The fundamental period of the 3-story building is reported as 0.973 s. It is noted that this value exceeds standard empirical estimates (approx. 0.4–0.6 s) for a building of this height. Specifically, the NBC empirical formula $T_a = 0.075h_n^{(3/4)}$ yields 0.39 s, and the maximum permitted design period per NBC 2020 Section 4.1.8.11.3-d-i is $1.5 \cdot T_a = 0.585$ s. This model was adopted from Mazloom (2023) and designed according to NBC 2015 provisions. While the design forces were determined using the code-mandated upper limit for the period, the reported value of 0.973 s represents the computed period through numerical analysis. This increased flexibility is attributed to the specific

structural configuration, which features limited ductility moment-resisting frames and large 7-meter spans.

4. Definition of R_p Factor (Section 2.3.1.1): The component response modification factor (R_P) in this study is calculated as the ratio of elastic demand to the demand at a specific ductility level ($PSA_{elastic}/PSA_{\mu}$). It is important to clarify that this calculation isolates the ductility-based reduction (R_{μ}) and does not account for component overstrength (Ω_P), which is included in the NBC definition of R_P (where $R_P \approx R_{\mu} \times \Omega_P$). In this study, the component overstrength is assumed equal to unity ($\Omega_P = 1.0$), meaning that the computed R_P values represent the ductility reduction component (R_{μ}) solely. For full code implementation, it is recommended that these values be combined with appropriate overstrength factors inherent to specific component types.

5. Definition of A_r/R_P Ratio (Section 2.3.1.2): The text equates the ratio PSA/PFA to A_r/R_P. It is clarified that 'PSA' in this context refers to the Peak Spectral Acceleration of the inelastic component (PSA_{μ}). While standard definitions (e.g., NBC, ATC-120) define A_r specifically as the component *amplification* factor (equivalent to $PSA_{elastic}/PFA$), the ratio presented in this section (PSA_{μ}/PFA) inherently accounts for both the dynamic amplification (A_r) and the ductility reduction (R_P). Therefore, the term A_r/R_P is used to represent this combined effective design factor.

6. Data Averaging (Section 2.3.1.3 and Figure 2.4): It is clarified that the 'mean' values discussed in Section 2.3.1.3 and presented in Figures 2.4 through 2.7 represent the arithmetic mean calculated across the 24 ground motion records (12 historical and 12 synthetic) utilized in the time-history analyses.

7. Clarification of Figure 2.7 (PSA/PGA Ratios): It is important to clarify that Figure 2.7 presents the PSA/PGA ratios specifically for components mounted at the ground level. In this context, the Peak Floor Acceleration (PFA) is equivalent to the Peak Ground Acceleration (PGA). Therefore, the values presented represent the amplification of the component relative to the ground motion input, analogous to a standard ground response spectrum. This distinction explains why these ratios may appear lower than the PSA/PFA ratios for upper floors (Figures 2.4 and 2.5), where structural dynamic filtering can generate floor spectra with higher amplification peaks due to resonance effects.

8. Structural Linearity (Section 2.4): Supplementing the limitations discussed in Section 2.4, it is acknowledged that the supporting structures in this chapter were modeled as linear elastic systems. It is recognized that at the 2% in 50 years hazard level, structural nonlinearity is expected; however, this assumption allows for the isolation of component ductility effects and is consistent with standard methods for developing baseline component demands, but it neglects the influence of structural nonlinearity on floor spectral demands. This limitation is addressed in subsequent chapters (e.g., Chapter 3), where nonlinear structural behavior is explicitly incorporated.

9. Iterative Procedure for Target Ductility (Section 2.1): To achieve the specific target ductility levels reported in this chapter ($\mu = 1.0, 1.25, 1.5, 2.0$), an iterative numerical procedure was implemented. For each component and ground motion record, the yield strength (F_y) of the bilinear NSC model was iteratively adjusted until the calculated peak inelastic displacement (Δ_{max}) resulted in the target ductility ratio ($\mu = \Delta_{max} / \Delta_y$) within a specified convergence tolerance (tolerance of 1×10^{-4} on the target ductility ratio). This procedure ensures that the reported results represent true constant-ductility response spectra.

10. Clarification on Relative Yielding Intensities (Section 2.1): In the introduction, the statement "the yielding shear force of NSC attachments occurs at lower levels of seismic intensity, leading to nonlinearity in the supporting structure" is intended to express a comparison of intensity levels rather than a causal relationship. It should be interpreted as: the yielding of NSC attachments typically occurs at seismic intensities lower than those required to cause nonlinearity in the supporting structure. This distinction supports the decision to focus on NSC nonlinearity while modeling the structure as elastic for the specific range of intensities examined in this study.

11. Clarification on Seismic Hazard Model (Section 2.4): It is clarified that the seismic hazard model and Uniform Hazard Spectrum (UHS) utilized in this study correspond to the 6th Generation (NBC, 2020) of the Geological Survey of Canada, which determines the spectral shape of the selected records.

CHAPTER 2

PROPOSED RELIABLE PEAK COMPONENT FACTORS FOR DUCTILE LIGHT NSCS SUBJECTED TO HORIZONTAL GROUND MOTIONS

Majid Mehrjoo[a] and Rola Assi[b]

[a,b] Department of construction engineering, École de technologie supérieure (ÉTS), Montreal, Quebec, H3C 1K3, Canada

Paper published in Bulletin of Earthquake Engineering[1], December 2024

Abstract

This paper aims to propose reliable factors that accurately capture the effect of target ductility of non-structural components (NSCs) on floor acceleration, velocity, and displacement demands at both the ground level and the upper building floors.

A linear time history analysis (THA) was performed on four moment-resisting archetype buildings using historical and synthetic ground motions matched to the Montreal Site Class C uniform hazard spectrum (UHS) through frequency domain matching. The NSCs' seismic demands and ductility-based modification factors were determined using uncoupled analysis, in which the equations of motion were solved using the Iterative Newmark Integration approach implemented in MATLAB.

The seismic floor acceleration, displacement, and velocity demand amplitudes were reduced with increased NSC ductility, especially inside the resonance period range. The effect of ductility on the seismic acceleration demands was found to be significant near the resonance

---

[1] Mehrjoo, M., & Assi, R. (2024). Proposed Reliable Peak Component Factors for Ductile Light NSCs Subjected to Horizontal Ground Motions. Bulletin of Earthquake Engineering. **https://doi.org/10.1007/s10518-024-02081-x**

condition for the first three primary periods of the supporting structure. Conversely, the displacement and velocity demand were predominantly affected by the first primary mode. Specifically, for NSCs with moderate to high ductility levels, a 40%-60% decrease in demand was observed compared to NSCs exhibiting elastic behavior in the resonance condition. In contrast, the effect of ductility was minimal for out-of-resonance conditions and on ground-level seismic demands. Moreover, the sensitivity analysis on damping variations showed minimal impact on the proposed factors, further supporting their robustness. In conclusion, while ductility minimizes resonance effects on NSCs, a trade-off between the benefits of ductility and an acceptable damage level must be considered.

Keywords: non-structural components, ductile behavior, component attachments, newmark integration, dynamic analysis, peak component factors

2.1 Introduction

Non-structural components (NSCs) contribute significantly to the overall construction cost and functionality of buildings, typically accounting for 75% to 85% of the total construction cost (Miranda & Taghavi, 2005). However, these components frequently suffer extensive damage during earthquakes, posing serious threats to the safety and functionality of structures (Whittaker & Soong, 2003). This paper takes a deep dive into how the ductility of an attachment affects the seismic behavior of acceleration-sensitive NSCs, such as water heaters, chillers, antennas, chimneys, and parapets, in a bid to tackle the dearth of detailed research works on the subject (Adam & Fotiu, 2000; ATC, 2018a; Igusa, 1990; Toro et al., 1989; Villaverde, 2006; Vukobratović & Fajfar, 2017).

The work focuses primarily on the seismic floor acceleration demands that are influenced by the ductility of NSC attachments, which can have a substantial impact on the design of acceleration-sensitive NSC attachments (Chaudhuri & Villaverde, 2008; A. K. Chopra, 2011; Obando et al., 2022; Obando & Lopez-Garcia, 2018).

While focusing solely on accelerations may not provide a complete picture of the seismic demands imposed on NSCs, it is true that the displacement and velocity demands are also

influenced by the ductility of NSC attachments, and are crucial for characterizing the inelastic behavior of components under seismic ground motions (Anajafi et al., 2020; Filiatrault et al., 2004). Velocity demands govern the sliding, overturning, and swinging motions of unattached or freestanding NSCs (e.g., furniture and equipment) and suspended NSCs (e.g., ceilings and light fixtures) (Buccella et al., 2020; Pavlou & Constantinou, 2006). Displacement demands are equally important for the integrity and functionality of NSCs having a limited deformation capacity or that are sensitive to excessive movement, such as cladding and glazing systems (Filiatrault et al., 2018). These demands often govern the failure modes and damage levels experienced by different component types, underscoring their significance in seismic analysis and design processes (T. Wang et al., 2021).

Accurate assessments of these demands are not only vital for the seismic performance of the specific NSCs but also play a pivotal role in the broader context of fragility analyses (Ghasemof et al., 2022; Mehrjoo & Aval, 2024).

Various approaches have been adopted to study the effect of the ductile behavior of NSCs on their seismic performance. These methods can be broadly categorized into empirical code-based procedures, advanced numerical simulations, and simplified analytical techniques that balance accuracy and efficiency.

Empirical methods, such as those prescribed in seismic design codes, often rely on simplified equations and assumptions to estimate the seismic demand on NSCs (Anajafi, 2018; Villaverde, 2006). For instance, the National Building Code of Canada (NBC, 2020) proposes a force-based approach for designing NSCs to withstand seismic loads, relying on three key parameters: the peak horizontal floor acceleration (PFA), the component amplification factor (A_r), and the component response modification factor (R_P). The PFA accounts for the effects of input ground motion at above ground level, and A_r considers the amplification due to the flexibility of an NSC or its attachment (equal to 1 for NSC periods $T_{NSC} \leq 0.06$ seconds and 2.5 for $T_{NSC} > 0.06$ seconds), calculated by PSA/PFA = A_r/R_p; the R_P factor (1 to 5) is intended to account for the reduction in seismic demands due to the ductility of NSC attachments (Kawakatsu et al., 1979; Lin & Mahin, 1985; Soong et al., 1993; Viti et al., 1981). These empirical R_P factors, derived from reduction factors previously developed for primary systems,(Miranda & Bertero, 1994; Newmark & Hall, 1973; Obando et al., 2022) may not

accurately account for the variations in the ductile behaviors exhibited by NSC attachments under different earthquake intensities, leading to inaccurate estimations of NSC seismic demand (ASCE, 2017; Anajafi, 2018; ATC, 2018a; A. Kazantzi et al., 2018; Miranda et al., 2018; Villaverde, 2006; Vukobratović & Fajfar, 2017; T. Wang et al., 2021). The A_r/R_p ratio in the NBC to convert the peak floor acceleration into the peak component acceleration is calculated as the ratio of the peak spectral acceleration (PSA) over PFA. This ratio is analogous to the component resonance ductility factor (C_{AR}) in ASCE 7-22 (ASCE, 2022). The C_{AR} factor (1-2.8) is influenced by the NSC flexibility and its ductility. This approach, while practical for design purposes, may not capture the complex ductile behavior of NSCs and needs refinement to better represent the ductility across NSCs (ASCE, 2017; Anajafi, 2018; ATC, 2018a; A. Kazantzi et al., 2018; Miranda et al., 2018; Villaverde, 2006; Vukobratović & Fajfar, 2017; T. Wang et al., 2021). In addition, González et al. (2019) conducted a critical assessment of estimation procedures for floor acceleration demands in steel moment-resisting frames and found that existing empirical methods often failed to accurately predict the seismic demands experienced by NSCs, particularly when considering their inelastic behavior. This limitation was echoed by Anajafi and Medina (2019b), who noted that while modern seismic design techniques might have limited damage to primary structural elements, they often overlooked the extensive damage that could occur to NSCs during seismic events. Furthermore, Wang and Hutchinson (2024) pointed out that empirical code-based methods failed to adequately account for the variability in building-specific characteristics such as height, structural system, and nonlinearity, which resulted in conservative or inaccurate estimates of seismic demand on NSCs.

On the other hand, advanced numerical simulations, such as those employing finite element analysis, along with pushover and Incremental dynamic analysis (IDA), can provide a more accurate representation of the NSCs' seismic response while considering the ductile behavior of their attachments. However, these methods can be computationally expensive and require significant modeling effort, making them less practical for rapid assessment or design iterations.

Recent work by Ding et al. (2024) emphasizes the need for enhanced modeling techniques, particularly for inelastic NSCs, which behave differently than their elastic counterparts. Their

research proposes new equations that predict both displacement and acceleration responses, incorporating the inelasticity of both NSCs and primary structures.

Notably, while detailed analyses have been conducted to investigate the effect of ductility on structural components and to propose related response modifications (Abou-Elfath et al., 2018; Güner & Topkaya, 2020; Jamshidi Avanaki, 2019), similar comprehensive studies focusing on the ductility of NSC attachments are still lacking in the literature.

To bridge the gap between empirical methods and advanced detailed simulations, simplified analytical techniques have been proposed, aiming to capture the ductile behavior of NSCs while maintaining computational efficiency. These methods often involve assumptions regarding the NSCs' ductility and damping, establishing a balance between accuracy and practicality.

Regarding the last approach, Villaverde (2006) introduced a simplified procedure to estimate NSC seismic design forces by proposing strength reduction factors to account for the nonlinear behavior of both the NSCs and supporting structures. The application of this method requires knowledge of the NSC and the structure's geometric characteristics, the weight and target ductilities of NSCs, as well as the structure's fundamental natural period and the uniform hazard spectrum (UHS).

Anajafi et al. (2020) proposed dividing the elastic acceleration and displacement demands by the response modification factor (R_{CC}) and the inelastic displacement ratio (C_{CC}), respectively. Time history analysis was employed to quantify the effects of inelasticity in NSCs located at the roof level and modeled as single-degree-of-freedom (SDOF) systems with the target ductility. The yield strength of the system was iteratively adjusted based on the maximum elastic displacement observed in each analysis.

In addition, Kazantzi et al. (2020a) proposed simplified equations to estimate the component amplification factors for linear NSCs. Their approach was based on nonlinear regression analyses of floor motions recorded in instrumented buildings located in California during various seismic events. It was also revealed that amplification factors derived from floor motions differ greatly from those obtained from ground motions. This discrepancy was determined to be due to the substantial variations in frequency content between ground motions and floor motions.

Meanwhile, Obando and Lopez-Garcia (2018) conducted an in-depth examination of the ductile behavior of NSCs attached to various elastic building models. A regression formula was developed to estimate the inelastic displacement ratios (IDR) for NSCs at the roof level. It was also highlighted that the IDR demands for NSCs affected by floor accelerations differ from those impacted by ground accelerations.

Vukobratović and Fajfar (2017) proposed to account for the inelastic behavior of ductile NSCs by increasing the damping ratio (ξ) of the floor response spectra (FRS). In their investigation, the NSC target ductility was either 1.0 (elastic) or 1.5 (moderate ductile), and the NSC viscous damping ratio ranged from 1 percent to 7 percent. It was also found that NSC inelasticity can result in a significant reduction of the mean floor acceleration spectra (except for rigid NSCs) both in elastic and inelastic primary structure conditions.

Filiatrault et al. (2018) accounted for the ductile behavior of suspended piping systems using the non-structural equivalent damping ratio determined through a pseudostatic cycle test. Their displacement demand was shown to be decreased as the ductility of NSCs increases. Also, the study highlighted the need to address deformation limit states directly in the force-based design procedure to enhance the seismic performance assessment of NSCs. A key limitation of this method is its lack of well-defined yield and performance limit displacements for NSCs, which can compromise the accuracy of design assessments.

While previous research works primarily focused on roof level acceleration and often relied on limited case studies and local seismic events, the present study expands the scope to include acceleration, velocity, and displacement demands at various levels (roof, intermediate, and ground), and uses four multi-storey archetype reinforced concrete buildings subjected to 24 earthquake records matched to Montreal's UHS.

Therefore, this study follows analytical techniques to propose simplified ductility-based A_r/R_p, IDR, and IVR, through a numerical analysis approach implemented in MATLAB. The methodology involves performing multi-degree-of-freedom (MDOF) analysis employing linear time history analysis (THA) on linear elastic archetype-building models (A. K. Chopra, 2011; Obando & Lopez-Garcia, 2018). In addition, elastic response spectra are computed for elasto-plastic NSCs with the specified level of ductility(μ_{comp}). The process is repeated across

various NSC periods to study the effect of ductility on their responses, especially in the presence of a likelihood of resonance.

Given the variability in damping ratios and its impact on seismic demand estimations, a sensitivity analysis is conducted to investigate NSC response under varied damping conditions (1%, 2%, and 3%). The sensitivity of the proposed factors is quantified using a deterministic sensitivity index, calculated as a percentage variation from the base 5% damping ratio (Equation 2.1). This analysis assesses the robustness of the proposed factors across different damping scenarios, enhancing their reliability for NSC attachment design.

$$S(\%) = \frac{\partial Y/Y}{\partial X/X} * 100 \tag{2.1}$$

Where **Y** represents the seismic demand, and **X** is the damping ratio of the non-structural components. This index quantifies the relative change in seismic response due to changes in the damping ratio. The detailed process and analysis are elaborated in the following sections.

The choice of consideration of an elastic supporting structure boils down to the fact that a seismic assessment of NSCs is crucial in buildings that sustain minimal structural damage. In addition, the yielding shear force of NSC attachments occurs at lower levels of seismic intensity, leading to nonlinearity in the supporting structure (Obando & Lopez-Garcia, 2018). This consideration is particularly important as the continuity of post-earthquake operations depends on the serviceability of NSCs, which is acutely true for essential structures such as hospitals.

Although our study focuses primarily on the nonlinear behavior of NSCs, it is important to acknowledge that existing research has demonstrated the influence of the nonlinear behavior of supporting structures on floor seismic responses and, consequently, NSC performance. Studies by Lin and Mahin (1985) and Taghavi and Miranda (2012) have shown that inelastic structural responses can either amplify or reduce floor accelerations compared to linear structures, depending on various factors such as building height, flexibility, and NSC period. However, future research could incorporate the nonlinear behavior of supporting structures to enhance the accuracy of the results. The effort in the present study aims to further assist engineers in their design of NSC attachments with different ductilities by refining the A_r and R_P factors in NBC 2020.

2.1.1 Description of the Case Study Buildings and their Modeling Assumptions

For the purposes of this study, a series of 3-, 6-, 9-, and 12-floor symmetric and regular RC moment-resisting frame (MRF) buildings with limited ductility and the normal importance factor were selected. These structures represent typical low to mid-rise buildings in urban areas of Quebec, including Montreal, and were selected to conduct this analysis. The structures were designed in accordance with NBC 2015 (NRC, 2015) and CSA A23.3-14 (CSA, 2014a), and the design details can be found in the work of Mazloom and Assi (2022). The fundamental periods for these case studies are presented in Table 2.1. They were assumed to be constructed in Montreal, on stiff soil known as Site Class C.

Each building features a uniform layout with three bays, each extending 7 meters in both the north-south (N-S) and east-west (E-W) directions and having a consistent average floor height of 3 meters. As part of this study, these structures were idealized as stick-building models with a lumped mass and stiffness at each floor level. This allowed to conduct structural analyses by constructing mass, damping, and stiffness matrices, which represent the dynamic properties of the MDOF system. The flexural stiffnesses of individual storeys within the building model were determined using the box frame method (Hosseini & Imagh-e-Naiini, 1999; Vijayanarayanan et al., 2017). The governing equations of motion were solved using the step-by-step Newmark integration method implemented in a MATLAB script to obtain the building's floor acceleration, velocity, and displacement responses. Also, a 5% modal damping ratio was considered for this study.

Table 2.1 Fundamental periods of the case study buildings

Number of Storeys	$T_1(s)$	$T_2(s)$	$T_3(s)$
3	0.973	0.279	0.182
6	1.014	0.321	0.189
9	1.354	0.441	0.261
12	1.468	0.279	0.182

2.1.2 Description of the NSCs and their Modeling Assumptions

Light components with a small mass of 1 kg, less than 0.1% of the total mass of the supporting structure, were considered in this study. For such light NSCs, the effects of dynamic interaction between them and the structure can be neglected, allowing their seismic responses to be analyzed independently from the structure (ASCE, 2000; Amin et al., 1971; Cunha et al., 2014; A. Singh & Ang, 1974; Taghavi & Miranda, 2008). It is important to acknowledge that the interaction between the structural system and the NSCs can influence floor acceleration responses and, consequently, NSC seismic demands. Studies have shown that the presence of NSCs can alter the fundamental period and damping characteristics of buildings, which in turn affects the seismic demands placed on both structural and non-structural elements (Lima & Martinelli, 2018; Shakeel, 2019; Zhai et al., 2016). Future work could extend our findings by incorporating the interaction between the structural system and the NSCs.

Individual NSCs were represented by single-degree-of-freedom systems mounted on the top floors, intermediate floors, and at ground level, covering a range of periods going from 0.01 seconds to 2.0 seconds, to account for different NSC period ranges. A bilinear elastoplastic model, which neglects overstrength from strain hardening, was employed to model component behavior and calculate R_p. This allowed the efficient and accurate quantification of four considered ductility levels, including components with (μ_{comp}=1), corresponding to elastic behavior; (μ_{comp}=1.25), corresponding to low ductility behavior; (μ_{comp}=1.5), corresponding to moderate ductility behavior, and (μ_{comp}=2), corresponding to high ductility behavior. To simulate these ductility levels, the yield strength is defined as the maximum displacement of a bilinear elastoplastic system relative to its displacement at yield ($\mu_{comp}=u_m/u_y$). The behavior of the components across these ductility levels is then analyzed by developing a response spectrum using the floor time history responses obtained from the MDOF structural analysis. At each time step, the equations of motion for displacement, velocity, and acceleration are numerically solved. This numerical solution is obtained through the iterative application of the Newmark integration method (A. K. Chopra, 2011) (γ = 1/2, β = 1/6) in a MATLAB script, assuming a linear acceleration variation.

While considering stiffness degradation and yield limitations, equilibrium iterations are carried out to converge on the displacement responses at each time increment. The tangent stiffness is updated within the iterative solution to capture the transition from the elastic to the inelastic region. The approach for determining yield strength and ductility involves an iterative process and error matrix evaluation. This methodology aims to obtain values with the least error compared to the target ductility, addressing yield strength concerns while ensuring the highest level of accuracy in the final seismic demand spectra.

2.2 Selection and Scaling of Input Ground Motion Data

A total of 24 ground motion records comprising a suite of 12 historical ground motions and 12 synthetic ground motions are utilized in this study to reliably estimate the mean structural response quantities (ASCE, 2016; Hancock et al., 2008). Historical ground motions are utilized to provide insights into the actual seismic behavior observed during past earthquakes, while synthetic ground motions are employed to offer the flexibility needed to generate site-specific scenarios that may not be adequately represented in historical records (Panza et al., 2002). Frequency domain matching (Fahjan & Ozdemir, 2008) is employed in a MATLAB script to match the synthetic and historical earthquakes with the target UHS of Montreal corresponding to Site Class C, with a probability of exceedance of 2% per 50 years, and a damping ratio of 5%.

The intensity measure (IM) adopted for scaling the records was the spectral acceleration (Sa) at specific periods of the UHS for Montreal. Although using a Conditional Mean Spectrum (CMS) could better represent the variability in seismic responses, the UHS was chosen in accordance with the conservative design principles of the NBC. This ensures that the seismic demands are aligned with current design practices and that the NSCs are designed conservatively to withstand higher-bound seismic events. Consequently, this approach results in reduced dispersion in the seismic responses, as the records are closely matched to the UHS across all periods. Future studies could investigate the use of CMS for scaling ground motion records to provide a more realistic representation of seismic response variability while maintaining safety. This Frequency domain matching technique preserves the intrinsic

characteristics of seismic ground motions, closely matches the target spectrum, and optimizes the computation time required for the spectral matching process (Gascot & Montejo, 2014). This procedure entails the computation of the response spectrum for the existing accelerogram, identification of modification factors, and execution of frequency-domain amplitude adjustments, which are facilitated by the application of Fast Fourier Transform (FFT) techniques to minimize spectral discrepancies. An inverse FFT is then utilized to generate the scaled time history records.

2.2.1 Historical Ground Motions

A suite of 12 far-field ground motions drawn from the PEER NGA-East database was selected, as shown in Table 2.2 and Figure 2.1 according to the following criteria (FEMA, 2015; NRC, 2020; Reyes, 2009):

- The magnitude of earthquakes M_W is set to moderate, ranging between 3.5 and 6.
- The epicentral distance is set to cover far-field records ranging between 20 km and 100 km.
- The strike-slip type fault mechanism is chosen (Rosset & Chouinard, 2009).
- The average shear-wave velocity in the upper 30 meters of soil (Vs-30) ranges from 360 to 760 cm/sec, which corresponds to Site Class 'C' in accordance with the NBC 2020.

Table 2.2 Details of selected historical ground motions

No	Event/Station	Date/Time	Mw
1	Saguenay/Site 2, Quebec, PQ	1988-11-25	5.9
2	FtPayne_2003-04-29/Sewanee	2003-04-29 8:59	4.62
3	MtCarmel_2008-04-18a/Olney Central College Olney, IL	2008-04-18 15:14	4.64
4	MtCarmel_2008-04-18a/Univ. of Southern Indiana, Evansville, IN	2008-04-18 15:14	4.64
5	Slaughterville_2010-10-13/Jones High School	2010-10-13 14:06	4.36
6	Slaughterville_2010-10-13/Wilshire Boulevard- Harrah	2010-10-13 14:06	4.36
7	Arcadia_2010-11-24/Meyer Ranch, Chandler, OK	2010-11-24 22:48	3.96
8	Arcadia_2010-11-24/Bridge Creek, Tuttle, OK	2010-11-24 22:48	3.96
9	Sparks_2011-11-05/Pawnee, OK	2011-11-05 7:12	4.73
10	Sparks_2011-11-05/Meyer Ranch, Chandler, OK	2011-11-05 7:12	4.73
11	Sparks_2011-11-06/Jones High School	2011-11-06 3:53	5.68
12	Sparks_2011-11-06/Wilshire Boulevard- Harrah	2011-11-06 3:53	5.68

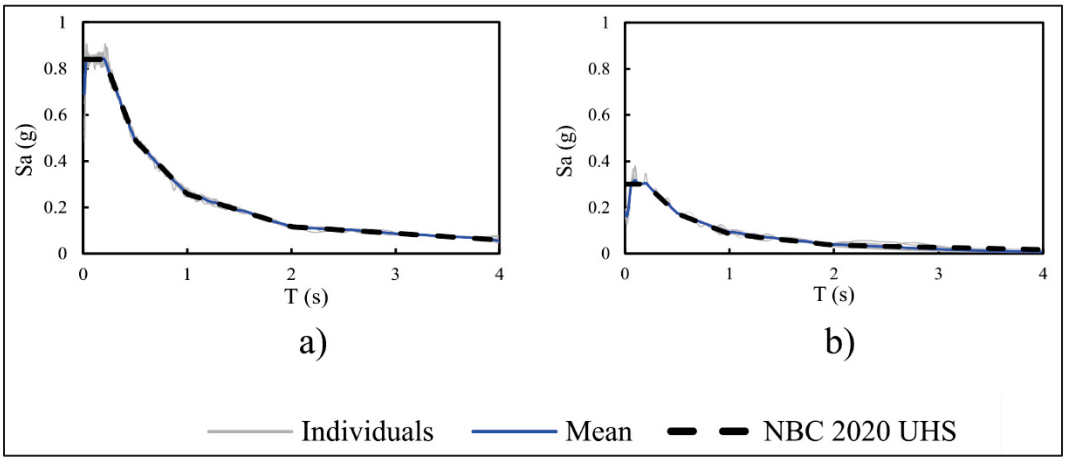

Figure 2.1 Mean and individual spectra of scaled historical ground motion and NBC 2020 UHS in Montreal: (a) 2% possibility of exceedance per 50 years, (b) 10% possibility of exceedance per 50 years

2.2.2 Synthetic ground motions

A suite of 12 synthetic accelerograms for the eastern region of Canada, as provided in the database by Atkinson (2009), were sourced from the Engineering Seismology Toolbox website (www.seismotoolbox.ca). For each magnitude-distance (M-R) scenario, a set of six ground motions was selected, ensuring compatibility with the Montreal UHS (Site Class C) for a 2475-year return period. The details of the selected accelerograms are presented in Table 2.3, and their response spectra and Montreal's UHS are shown in Figure 2.2.

Table 2.3 Details of the synthetic ground motions

M_w	R	Record	Duration(s)	Time Step(s)	PGA(g)
6.0	15	E6c1_43	43.598	0.002	0.607
		E6c1_4			0.368
		E6c1_21			0.493
	30	E6c2_17	47.530		0.522
		E6c2_37			0.419
		E6c2_15			0.338
7.0	25	E7c1_18	51.126	0.002	0.395
		E7c1_30			0.285
		E7c1_40			0.538
	100	E7c2_12	57.352		0.213
		E7c2_4			0.329
		E7c2_36			0.178

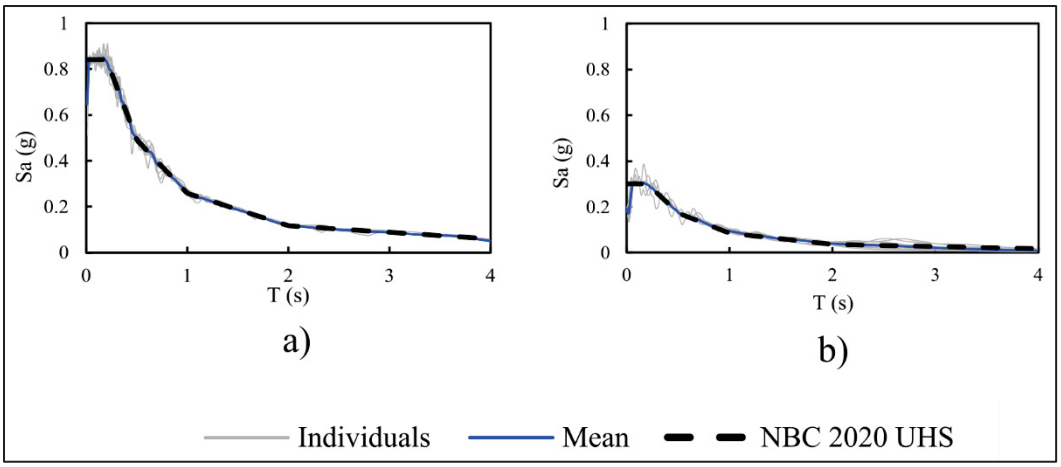

Figure 2.2 Mean, individual spectra of scaled synthetic records, and NBC 2020 UHS in Montreal: (a) 2% possibility of exceedance per 50 years, (b) 10% possibility of exceedance per 50 years

2.3 Computation of NSC Seismic Demands

This section presents the NSC seismic demands obtained at the roof, intermediate floors, and ground level using Historical and Synthetic ground motion data across all earthquake records scenarios with 2% and 10% probabilities of exceedance in 50 years. The intermediate floors of interest were level 6 of the 12-storey building, levels 4 and 5 of the 9-storey building, and level 3 of the 6-storey building.

2.3.1 Mean Acceleration Demands at Different Ductility Levels

The first subsection focuses on the R_P results obtained at different ductility levels. This allows to assess the influence of ductility on the response of NSCs. The second subsection investigates the effect of resonance on the PSA/PFA ratios. The third subsection investigates the effect of the ductility levels on the PSA/PFA. Finally, a sensitivity analysis investigates the effects of varying the damping ratios on the A_r/R_p and R_p values. Subsequently, Table 2.4 consolidates the mean values for the discussed factors at different ductility levels and component locations as well as the proposed values of A_r/R_P.

2.3.1.1 Component Response Modification Factor (R_p)

The component response modification factor R_p is determined by calculating the ratio, $PSA_{elastic_{comp}}/PSA_{\mu_{comp,}}$ with PSA representing the peak spectral acceleration corresponding to a damping ratio of 5%. The shown results in Figure 2.3 represent the values of $1/R_p$ for all case study buildings at three distinct levels (ground floor, intermediate floors, and the top floor). As a result, the correlation between seismic acceleration demands and ductility becomes more apparent, while the computed R_p factors presented in Table 2.4 are consistent with the NBC. Similarly, the corresponding values of combined historical and synthetic records are plotted to provide a comprehensive representation of the seismic behavior across the different building levels and input ground motions.

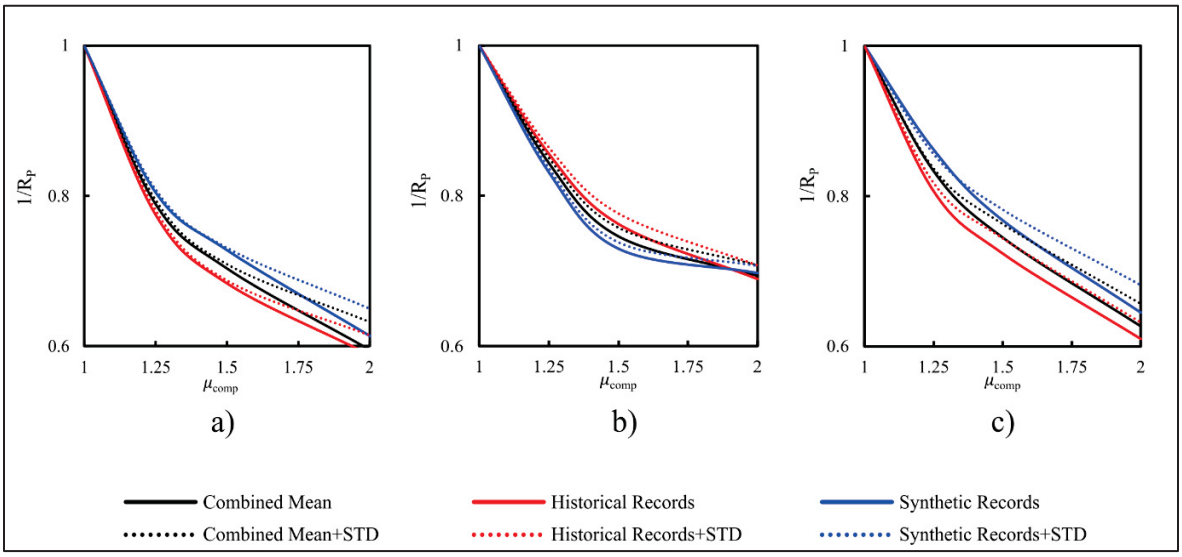

Figure 2.3 1/ R_P values for components with varying target ductility levels under historical and synthetic records at different building levels: a) roof, b) intermediate, and c) ground

A general decreasing trend in the $1/R_p$ factor as μ_{comp} values increase is identified, indicating that ductile components experience reduced seismic acceleration demands. Overall, as acceleration demands shift from elastic to highly ductile components, an average decrease of 35% is observed. Nevertheless, the effect of ductility is particularly pronounced at lower ductility levels, as evidenced by the steep decline in $1/R_P$ values when μ_{comp} increases from 1

to about 1.5. As ductility increases beyond $\mu_{comp} \approx 1.5$, the rate of decline in $1/R_P$ values diminishes. Thus, it is recommended to design non-structural components with moderate ductility levels. This approach ensures that the design remains practical and cost-effective. Moreover, a comparison between historical and synthetic records across earthquake scenarios (2% and 10% probabilities of exceedance in 50 years) shows that the synthetic input ground motion consistently results in slightly higher $1/R_P$ factors as compared to the historical input ground motions, although the discrepancy is relatively small. This observation aligns with the findings of Galasso et al. (2012), implying that the choice of ground motion input may have a limited impact on the seismic design and performance of NSCs, even at higher ductility levels. As a result, the mean results that are deemed to provide a sufficiently accurate representation of the two datasets will be used as the basis for the analyses presented in Figure 2.4 to Figure 2.7, as well as in Table 2.4.

2.3.1.2 Ratio of (A_r/R_P)

Figure 2.4 and Figure 2.5 represent the PSA/PFA, which corresponds to A_r/R_P for different NSC ductility levels, with the first three periods of the building shown. Additionally, by normalizing the NSC periods to the building's fundamental period, T_{b1}, the impacts of the building and their resonance on seismic demands are considered (A. K. Kazantzi et al., 2020a, 2020b; Miranda, 1991). Each of the four graphs (a, b, c, and d) depicts four curves, each corresponding to a distinct ductility level (μ_{comp}) ranging from 1 to 2.

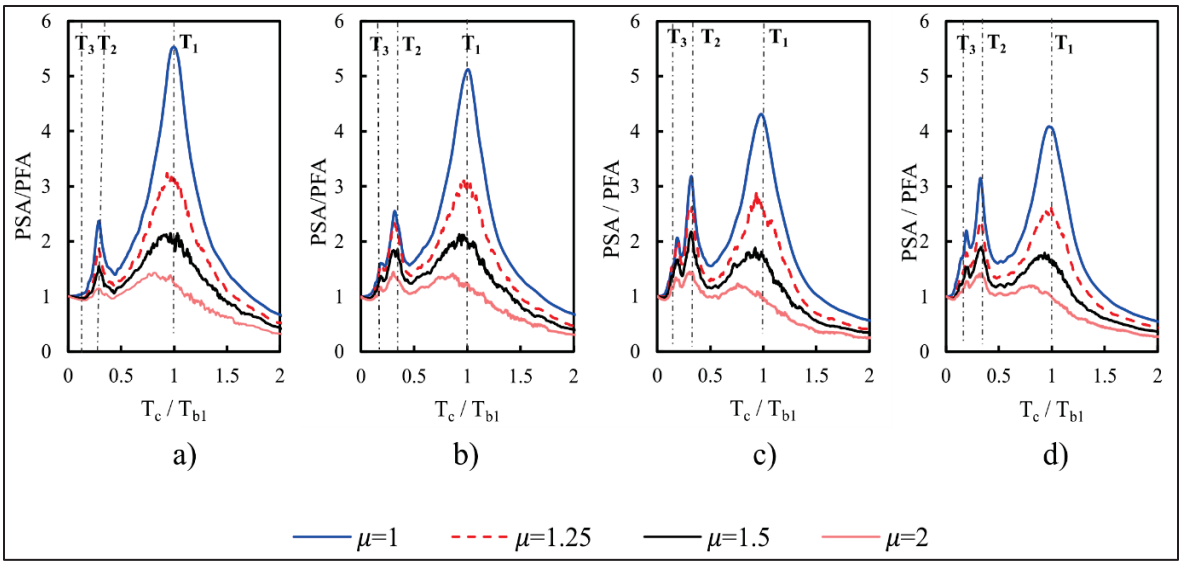

Figure 2.4 PSA/PFA values at intermediate floors of archetype buildings for various ductility levels: (a) 3-storey, (b) 6-storey, (c) 9-storey, (d) 12-storey

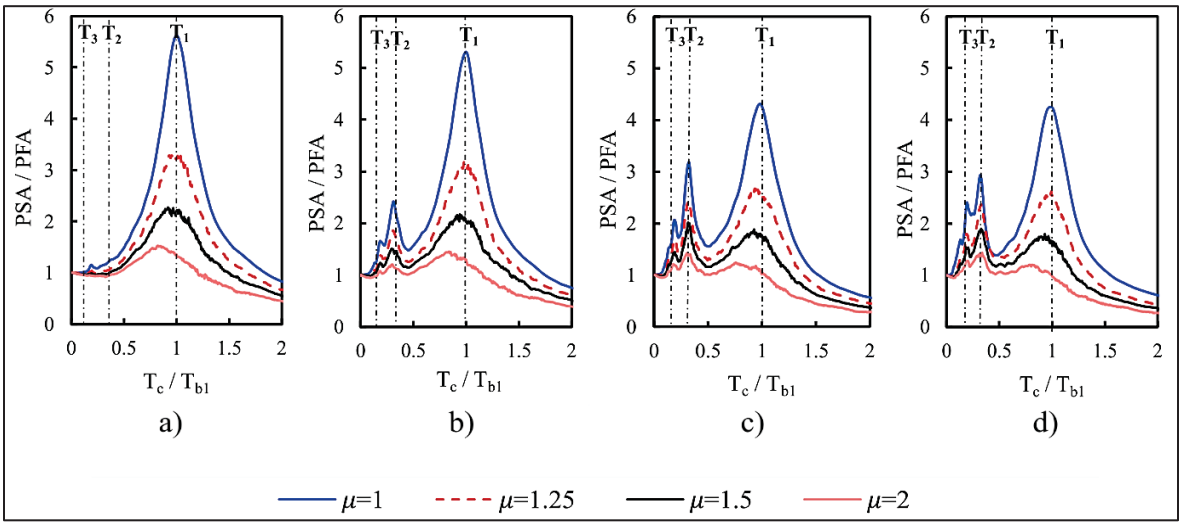

Figure 2.5 PSA/PFA values at the roof level of archetype buildings for various ductility levels: (a) 3-storey, (b) 6-storey, (c) 9-storey, (d) 12-storey

The PSA/PFA ratios are almost identical in terms of peaks, shapes, and values at the intermediate floors and roof level. Figure 2.4 and Figure 2.5 indicate that the impact of ductility on NSCs is a function of the tuning ratio between the NSCs and the main structure, especially within the $0.5 \leq T_c / T_{b1} \leq 1.5$ period range.

For components with $0.06 \leq T_c / T_{b1} \leq 0.5$ period range, the acceleration demands experience amplification exceeding twice the peak floor acceleration for elastic components. Also, it is noted that in this range, the acceleration peak values increase with the number of storeys. The PSA/PFA ratio for the second period (T_2) displays a steeper slope than other lines, suggesting an increased sensitivity to changes in the PSA/PFA ratio. In addition, the PSA/PFA ratio for the third period (T_3) becomes more noticeable in taller buildings, particularly those with 9 and 12 storeys. Overall, the PSA/PFA values exhibit a slight increase with height, but the incremental growth is minimal and could be considered insignificant. For components in the out-of-resonance range with a $T_c \leq 0.06$ or $T_c / T_{b1} > 1.5$ period range, the resonance is less likely to occur, and acceleration demands remain relatively unchanged.

2.3.1.3 Ductility Effect on A_r/R_P at Floor and Ground Levels

Figure 2.6 illustrates the computed mean ratio of PSA to PFA, for the considered ductility levels. Each graph in Figure 2.6, presents curves for roof and intermediate floor responses across all case studies and earthquake scenarios. Figure 2.6 also includes mean values accompanied by plus and minus standard deviations of the PSA/PFA ratios observed across the data.

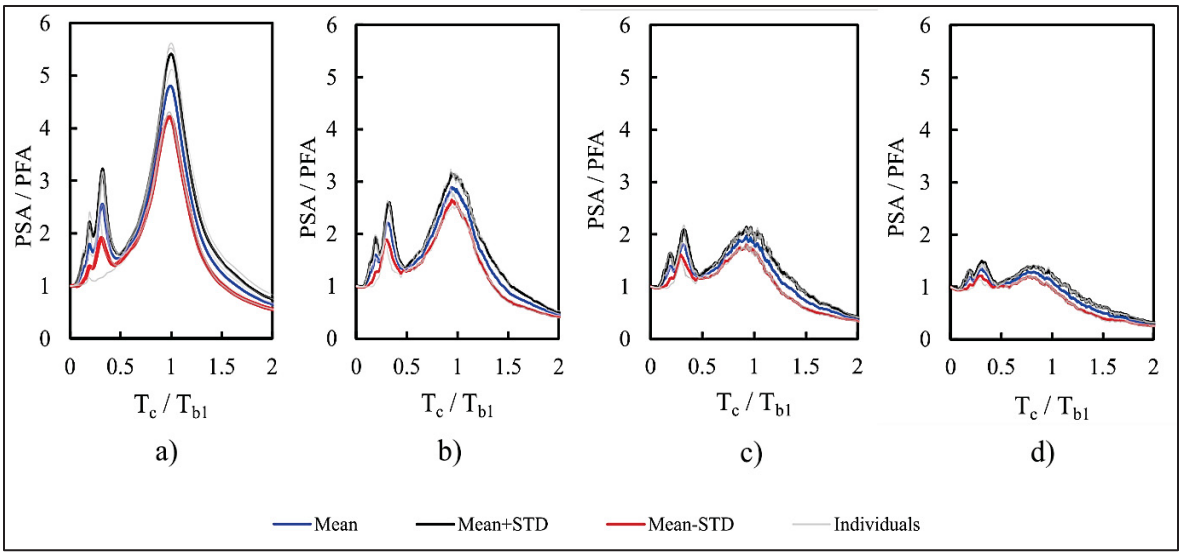

Figure 2.6 PSA/PFA floor values of archetype buildings for various ductility levels: (a) μ_{comp}=1, (b) μ_{comp}=1.25, (c) μ_{comp}=1.5, (d) μ_{comp}=2

One key finding of Figure 2.6 regarding the impact of the building height on the PSA/PFA is that it may not significantly influence the variability of PSA/PFA, as evidenced by the relatively small standard deviations observed in both the roof and intermediate floor responses. This observation aligns with the analysis presented in Figure 2.4 and Figure 2.5, which further supports this conclusion. When ductile NSCs are in resonance with the first fundamental period of a building, they experience a significant decrease in seismic demands with components having μ_{comp}=1.25, μ_{comp}=1.5, and μ_{comp}=2.0 experiencing an average of 20%, 25%, and 35% lower demands, respectively, compared to elastic components. Furthermore, it may be observed that for highly ductile components, the PSA/PFA ratios fall below 1, indicating that the component experiences lower accelerations than those corresponding to the supporting floor. The patterns observed in the floor-level graphs align with previous studies conducted by researchers such as Anajafi et al. (Anajafi et al., 2020; Anajafi & Medina, 2019b) and Shang et al. (2021), which similarly observed a reduction in seismic demands for ductile NSCs in resonance with the building's fundamental period, particularly for highly ductile components. Figure 2.7 illustrates the computed mean ratio of PSA to PGA (Peak component Acceleration to Peak Ground Acceleration), for the considered ductility levels. In Figure 2.7, each graph presents broadband spectra focusing on ground level responses across all earthquakes. Figure

2.7 also includes mean values accompanied by plus and minus standard deviations of the PSA/PGA ratios from the entire dataset.

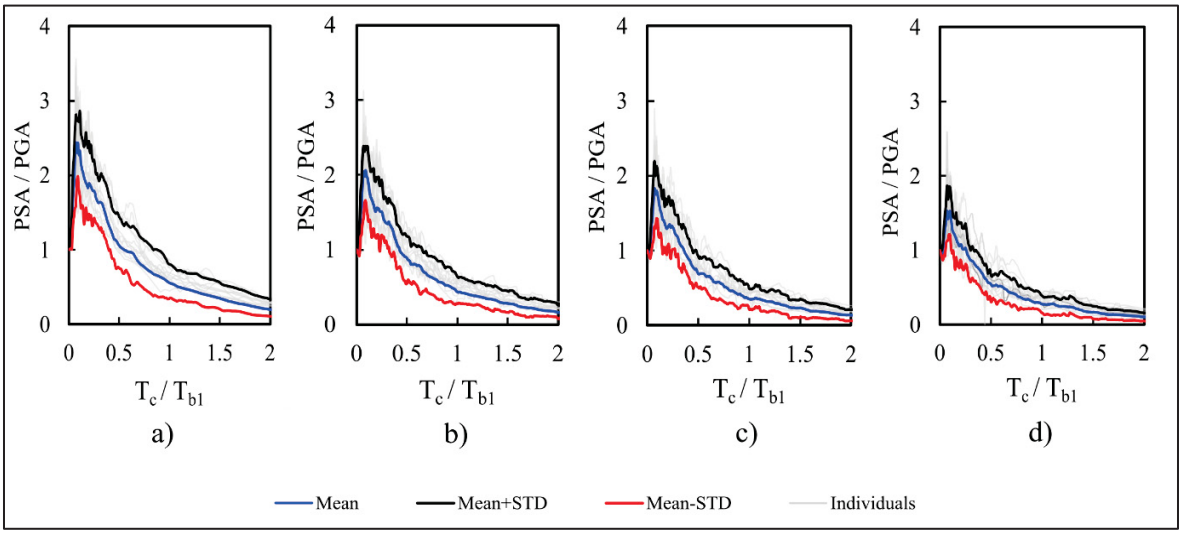

Figure 2.7 PSA/PGA ground values of archetype buildings for various ductility levels: (a) μ_{comp}=1, (b) μ_{comp}=1.25, (c) μ_{comp}=1.5, (d) μ_{comp}=2

Figure 2.7 shows that for very short periods (T_c / T_{b1} < 0.1), all components, regardless of ductility, experience resonance and high acceleration, with PSA/PGA ratios remaining above 1 until T_c / T_{b1} reaches about 0.5s. Beyond this point, all the ductility levels show PSA/PGA ratios below 1, indicating safer conditions for more flexible components.

Figure 2.7 highlights that the influence of ductility on the ground level is less pronounced in comparison to elevated floors. Consequently, the peak reductions in the PSA/PGA ratio are approximately 14%, 26%, and 40% for components exhibiting low, moderate, and high ductility levels, respectively. It is worth mentioning that, even though the components were in the resonance range, the mean PSA/PGA for elastic components was found to reach approximately 2.5, aligning with the NBC-specified value of 2.5, which is associated with an R_p of 1. These findings are consistent with the results reported by Aldeka (2015) and Anajafi et al. (2019b), which observed that the maximum PSA/PGA is generally below 2.5.

2.3.1.4 Proposed A_r/R_p Factors Based on Obtained Results

The sensitivity analysis presented in Figure 2.8 offers an in-depth analysis of the effects of varying damping ratios (1%,2%,3%, calculated using Equation 2.1 on the PSA/PFA and R_P ratios in comparison to the default 5%, thereby further validating the proposed PSA/PFA and R_P values.

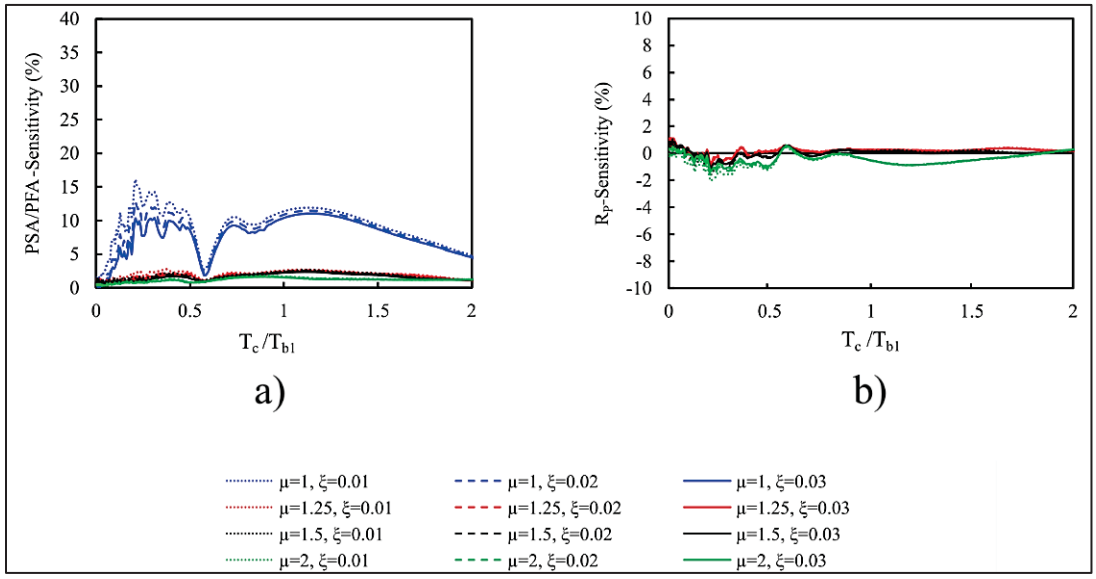

Figure 2.8 Sensitivity analysis of acceleration demands to damping ratios (1%, 2%, 3%) relative to the default 5%, averaged across roof, intermediate, and ground levels for earthquake scenarios with 2% and 10% probabilities of exceedance in 50 years: (a) PSA/PFA, (b) R_P

The maximum A_r/R_p and R_P values, derived from an analysis of all case studies for roof, intermediate, and ground levels, are presented in Table 2.4. The A_r/R_p values in Table 2.4 are obtained from Figure 2.6 and Figure 2.7, which illustrate the PSA/PFA ratio for each ductility level. These values are selected by considering the maximum value of the Mean curve for each ductility level across the entire period range; furthermore, the mean R_p values are obtained from Figure 2.3. Additionally, Table 2.4 includes proposed A_r/R_p values and the associated standard deviation (STD) values for floor and ground levels, which were obtained in Figure 2.6 and Figure 2.7. For proposed the A_r/R_p, the rounded maximum value of the Mean+STD

curve for each ductility level across the entire period range is considered to ensure a conservative design.

From Figure 2.8, it can be observed that ductility level $\mu = 1$ (elastic response) shows higher sensitivity to variations in damping from the default 5%, with an increase of 15% for certain periods. In order to generalize the proposed A_r/R_P values for $\mu = 1$, a 15% increase has been applied to the proposed values, considering this sensitivity as an additional standard deviation. In contrast, the sensitivity analysis for ductility levels μ_{comp}=1.25, μ_{comp}=1.5, and μ_{comp}=2 indicates negligible effects from changes in damping, suggesting that no further adjustments are necessary for these levels.

Similarly, for the R_p values, the sensitivity analysis shows negligible impact from changes in damping ratio for all ductility levels. Therefore, no modifications are required for the proposed R_p factors based on the results of the sensitivity analysis.

Table 2.4 Mean values of PSA/PFA (A_r/R_P), A_r, and R_P for elevated and ground level

			Values obtained from the equation (A. K. Chopra, 2011)	**Computed Mean Values**		**STD**	**Proposed Values**
Level of component	μ_{comp}	**Specific Location**	$R_P = (2\mu_{comp} - 1)^{1/2}$	R_P	A_r/R_P	A_r/R_P	A_r/R_P
Ground level	1		1	1	2.42	0.77	3.15
	1.25		1.22	1.22	2.05	0.48	2.6
	1.5		1.41	1.31	1.9	0.38	2.3
	2		1.73	1.58	1.52	0.33	2
Roof and elevated levels	1	Intermediate level	1	1	4.81	0.55	5.5
		Roof level	1	1	4.73		
	1.25	Intermediate level	1.22	1.19	2.83	0.22	3
		Roof level	1.22	1.23	2.85		
	1.5	Intermediate level	1.41	1.31	1.87	0.095	2
		Roof level	1.41	1.41	1.91		
	2	Intermediate level	1.73	1.41	1.21	0.149	1.5
		Roof level	1.73	1.59	1.24		

It is worth noting that the obtained component response modification factor (R_P) for both the ground level and elevated levels was found to be consistent with the theoretical formula from Chopra (2011), calculated as $R_p = \left(2\mu_{comp} - 1\right)^{1/2}$ at a 5% damping (ξ), with less than a 6% difference, thus confirming the accuracy of the R_P values in reflecting the measured ductility behavior.

The component modification factors (A_r/R_p) proposed in Table 2.4 are intended to provide engineers with a more refined understanding of how ductility influences the seismic acceleration demands of NSCs. These factors can complement the force-based approaches outlined in current seismic design codes, such as the NBC 2020, thereby improving both cost-efficiency and safety. Employing ductility-based factors for components exhibiting high ductility could lead to more economical anchorage designs, potentially reducing material consumption while ensuring the required seismic performance and preserving the intended ductility of NSC anchorage. This targeted approach helps protect acceleration-sensitive NSCs from excessive forces, reducing the risk of anchorage failure or component damage, ultimately contributing to more resilient buildings that can maintain critical functions following seismic events.

2.3.2 Mean Velocity Demands at Different Ductility Levels

The seismic velocity demand results are presented in this section and categorized into four parts. The initial part focuses on the Inelastic Velocity Ratio (IVR) factor, which is obtained by considering multiple component ductility levels and utilizing both Historical and Synthetic ground motion data. This part assesses the correlation between the ductility levels and their resulting impact on 1/IVR values. The second part investigates the floor spectral velocity (FS_V) response of NSCs across various periods. The third part examines the effect of the ductility levels on the FS_V responses across all earthquake records for the case study buildings. In the fourth subsection, a sensitivity analysis investigates the effects of varying damping ratios on the IVR values. Table 2.5 subsequently summarizes the IVR factors for different ductility levels and component locations.

2.3.2.1 Inelastic Velocity Ratio (IVR)

IVR values provide a measure of how ductility modifies NSCs' velocity responses under seismic loading. The IVR is computed as the ratio of the floor spectral velocity in an elastic system (μ_{comp} =1) to that of an inelastic system with a given μ_{comp} (Hatzigeorgiou & Papagiannopoulos, 2012) within the ($0.5 \leq T_c / T_{b1} \leq 1.5$) period range ratios. Figure 2.9 illustrates the floor spectral velocity as a function of the ductility of the components(1/IVR) at the roof, intermediate floors, and ground level of the studied buildings subjected to historical earthquakes, synthetic earthquakes, and combined records across earthquake scenarios (2% and 10% probabilities of exceedance in 50 years). Presenting the inverse values (1/IVR) clarifies the correlation between seismic velocity demands and ductility, while the IVR values are listed in Table 2.5. In addition, the mean values of all records along with the plus and minus standard deviations for these datasets are also presented.

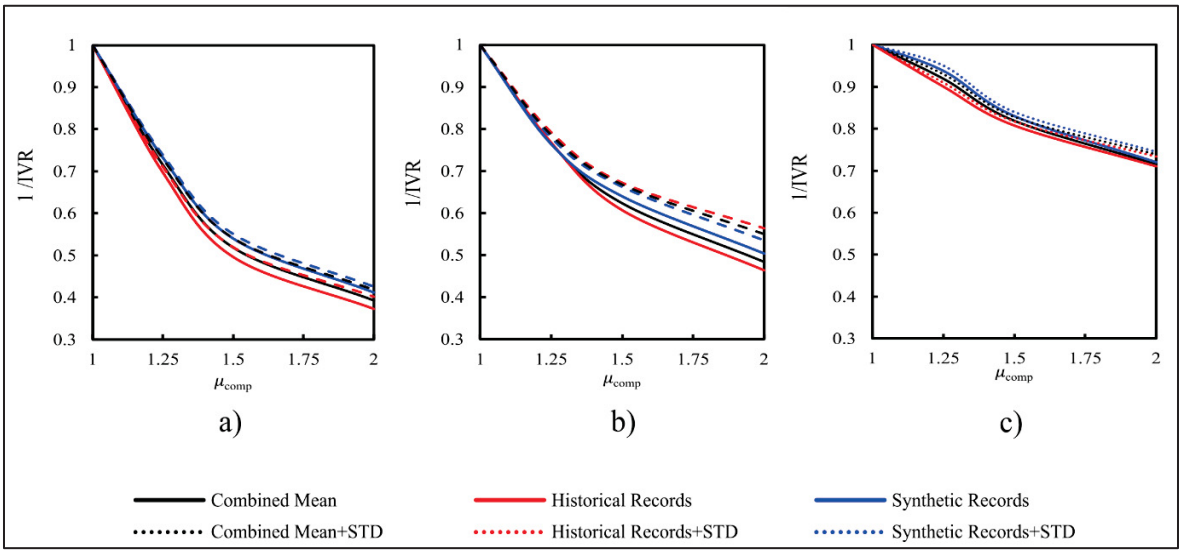

Figure 2.9 Reduction in Mean FS_V response for components with varying target ductilities at different levels: a) roof, b) intermediate, and c) ground

Figure 2.9 shows the tendency for components with higher ductility to exhibit decreased velocity demands, affirming the beneficial role the ductile behavior plays in decreasing the

seismic impact. The impact of ductility on the seismic response is less pronounced at the ground level than at higher elevations. Similar to its effect on acceleration responses, ductility significantly reduces 1/IVR values as μ_{comp} decreases from 1 to approximately 1.5.

Beyond $\mu_{comp} \approx 1.5$, the rate of decrease in 1/IVR values slows down. Therefore, it is advisable to use moderate ductility levels when designing velocity-sensitive components in order to enhance seismic performance while ensuring practical and cost-effective solutions. The alignment of historical and synthetic curves across all ductility levels in predicting FS_V reductions confirms the reliability of both datasets, as previously observed in acceleration responses.

Therefore, the mean ground motion results, offering a reliable depiction of both historic and synthetic datasets across earthquake scenarios (2% and 10% probabilities of exceedance in 50 years), served as the basis for the combined analysis presented in Table 2.5. For Figure 2.10 to Figure 2.17, the mean results of historic and synthetic datasets are presented separately, allowing for a direct comparison between the two types of ground motion inputs for both earthquake scenarios.

2.3.2.2 Floor Spectral Velocity (FSv) Response of NSCs

Figure 2.10 to Figure 2.13 illustrate the mean floor spectral velocity (FS_V) values at the roof and the intermediate level, with the first three periods of the building shown. Each of these four graphs (a, b, c, and d) has four curves, corresponding to a distinct ductility (μ_{comp}) ranging from 1 to 2, allowing for analysis of the floor spectral velocity response as a function of the component period (T_C) and ductility characteristics of NSCs.

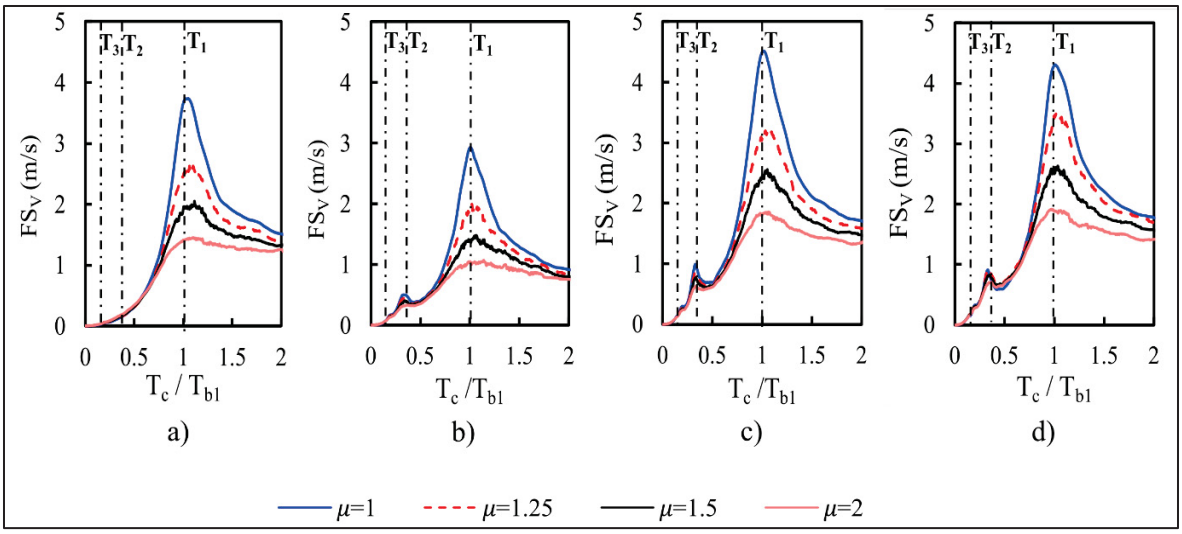

Figure 2.10 Mean Floor Spectral Velocity of the intermediate floors of archetype buildings for various ductility levels: (a) 3-storey, (b) 6-storey, (c) 9-storey, (d) 12-storey, considering an earthquake scenario with a 2% probability of exceedance in 50 years

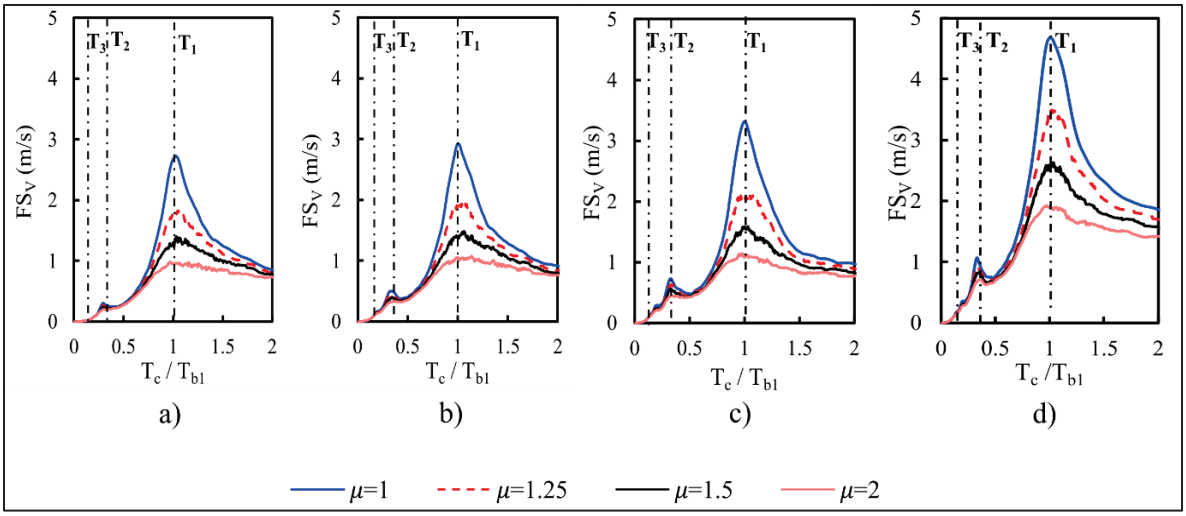

Figure 2.11 Mean Floor Spectral Velocity of the roof level of archetype buildings for various ductility levels: (a) 3-storey, (b) 6-storey, (c) 9-storey, (d) 12-storey, considering an earthquake scenario with a 2% probability of exceedance in 50 years

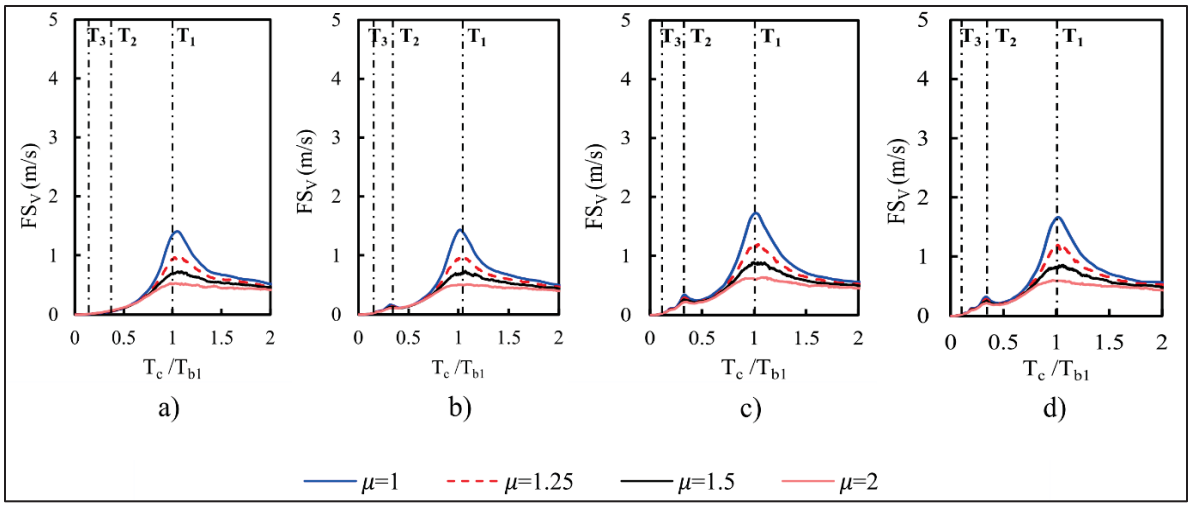

Figure 2.12 Mean Floor Spectral Velocity of the intermediate floors of archetype buildings at various ductility levels: (a) 3-storey, (b) 6-storey, (c) 9-storey, (d) 12-storey, considering earthquake scenarios with a 10% probability of exceedance in 50 years

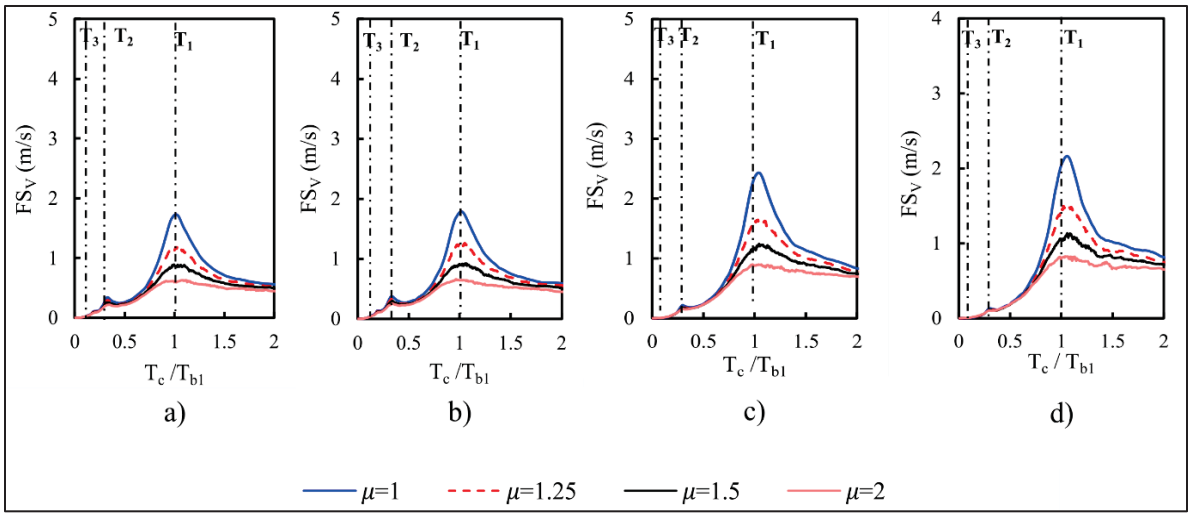

Figure 2.13 Mean Floor Spectral Velocity of the roof level of archetype buildings for various ductility levels: (a) 3-storey, (b) 6-storey, (c) 9-storey, (d) 12-storey, considering an earthquake scenario with a 10% probability of exceedance in 50 years

The Floor Spectral Velocity exhibits nearly identical peaks, shapes, and values at both the intermediate floors and roof levels. An analysis of Figure 2.10 to Figure 2.13 reveals that the effect of ductility on NSCs velocity demands depends on the tuning ratio between the NSCs and the main structure, especially within the $0.5 \leq T_c / T_{b1} \leq 1.5$ period range. Additionally,

the highest FS_V values are observed at the structure's first period (T_1), indicating that the first vibration mode is most critical. For components with a $0.06 \leq T_c / T_{b1} \leq 0.5$ period range, velocity demands have experienced a minor amplification at the second period (T_2), while the peak velocity values increase with the height of the building.

However, no amplification of FS_V values for the third period (T_3) was observed, regardless of ductility. For components in the out-of-resonance range within the $T_{comp} \leq 0.06$ or $T_c / T_{b1} > 1.5$ period range, resonance is less likely to occur, and velocity demands remain relatively unchanged.

2.3.2.3 Effect of Ductility on FSV Values at Floor and Ground Levels

Figure 2.14 and Figure 2.15 illustrate the FS_V values for roof and intermediate floor demands across all case studies and earthquakes, considering ductility levels of μ_{comp} = 1, 1.25, 1.5, and 2. Figure 2.14 and Figure 2.15 contain mean values with standard deviations of the FS_V values from the dataset used.

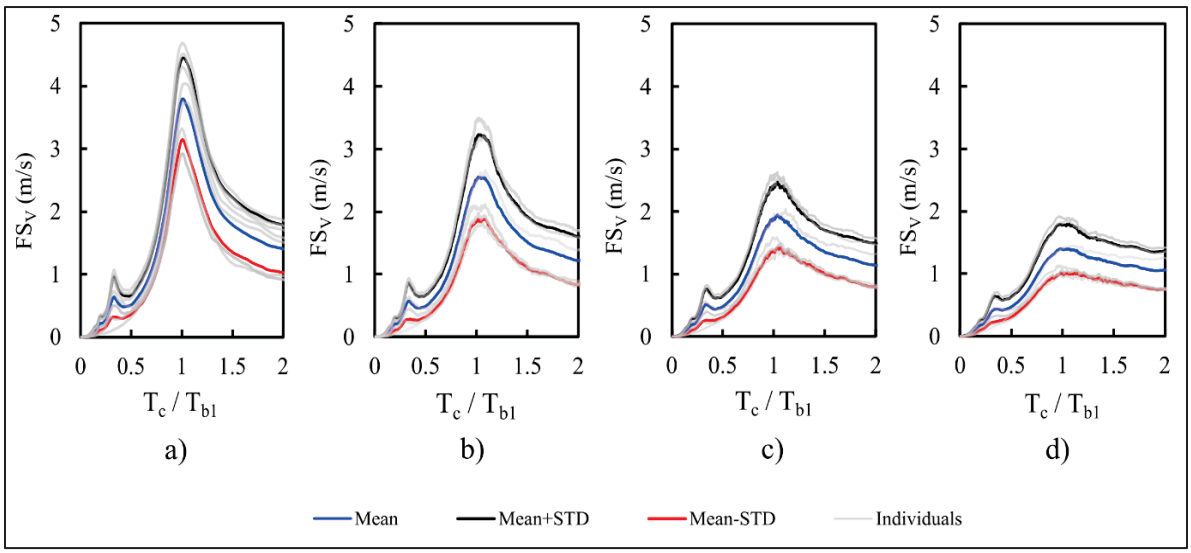

Figure 2.14 FS_v floor values of archetype buildings for various ductility levels: (a) μ_{comp}=1, (b) μ_{comp}=1.25, (c) μ_{comp}=1.5, (d) μ_{comp}=2, considering an earthquake scenario with a 2% probability of exceedance in 50 years

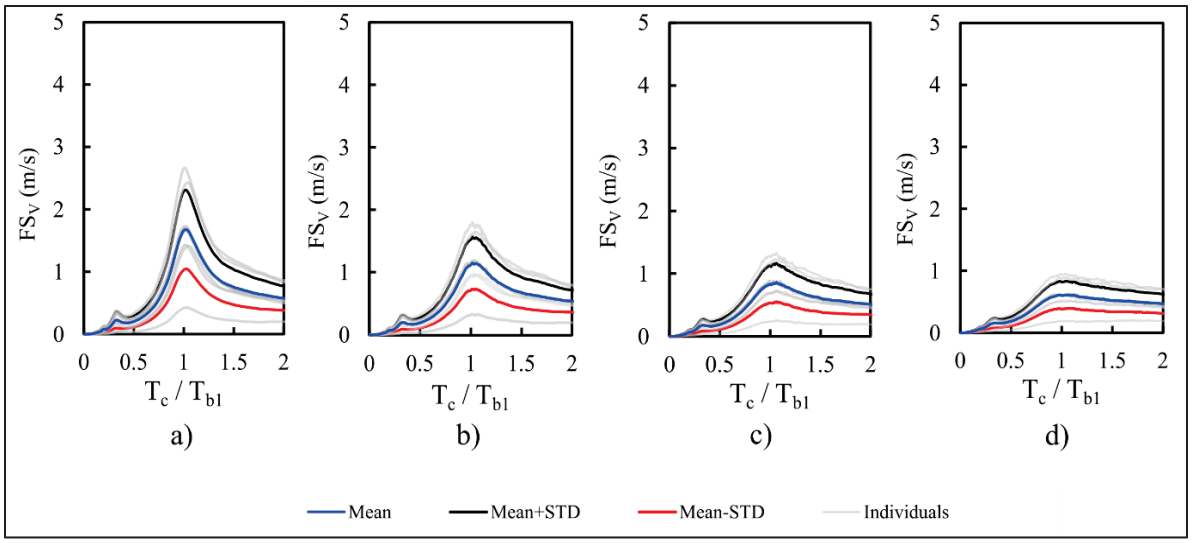

Figure 2.15 FS_v floor values of archetype buildings for various ductility levels: (a) μ_{comp}=1, (b) μ_{comp}=1.25, (c) μ_{comp}=1.5, (d) μ_{comp}=2, considering an earthquake scenario with a 10% probability of exceedance in 50 years

Figure 2.14 and Figure 2.15 indicate that the building height does not significantly influence the variability of FS_V values, as evidenced by the small standard deviations in both the roof and intermediate floor responses. This conclusion is supported by the analyses in Figure 2.10 to Figure 2.13 and by the previous observations in Section 2.3.1.3. In addition, in Figure 2.14 and Figure 2.15, for m_{comp} =1, representing an elastic response, the peak in the velocity spectra is the sharpest, indicating that elastic NSCs are likely to experience higher velocity demands during their resonance. Also, a spectral broadening was noted as the ductility of NSCs increased. With increased building height, the impact of higher vibration modes on the FS_V values becomes more pronounced, leading to the presence of two peaks. It is shown that when ductile NSCs are in resonance, they experience a notable decrease in seismic demands. Specifically, around the fundamental natural period (T_1), there is a noticeable decrease in FS_V values. The maximum FS_V values decreased by about 34% for m_{comp} = 1.25, 51% for m_{comp}= 1.5, and there was a significant 61% decrease in FS_V values for components m_{comp}= 2.

Figure 2.16 and Figure 2.17 illustrate the FS_V values for ground-level responses from all earthquakes, considering ductility levels of μ_{comp} = 1, 1.25, 1.5, and 2. Figure 2.16 and Figure 2.17 contain mean values with standard deviations of the FS_V values from all earthquake records.

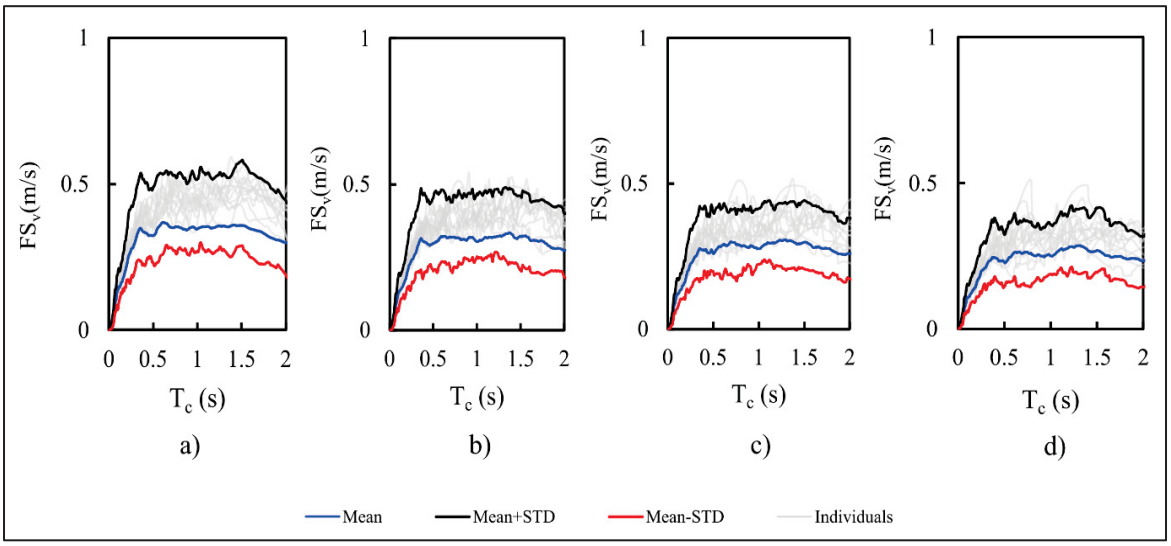

Figure 2.16 FS_v ground values of archetype buildings for various ductility levels: (a) μ_{comp}=1, (b) μ_{comp}=1.25, (c) μ_{comp}=1.5, (d) μ_{comp}=2, considering an earthquake scenario with a 2% probability of exceedance in 50 years

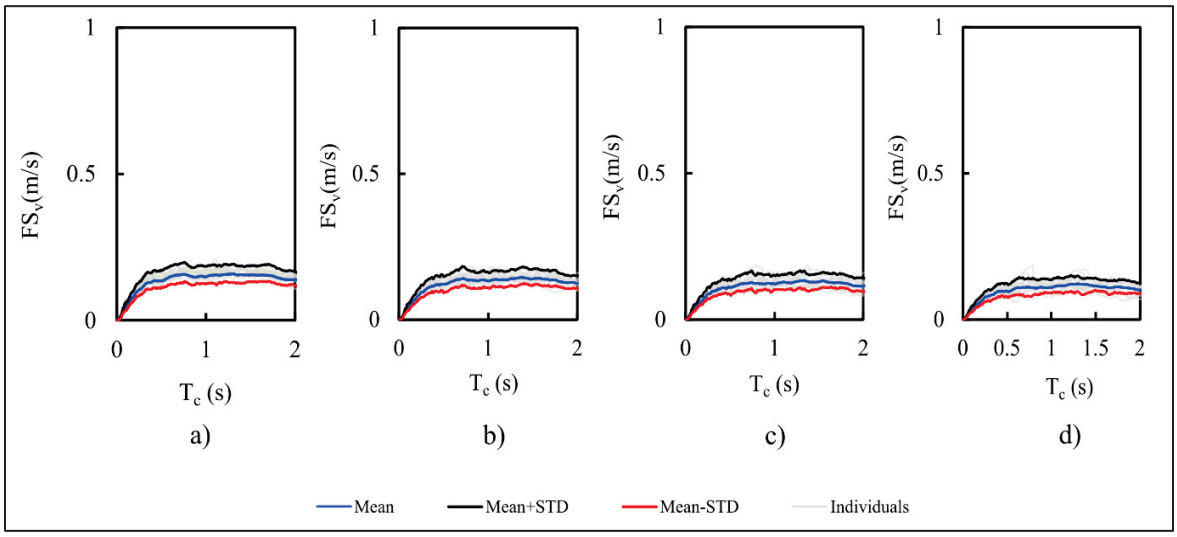

Figure 2.17 FS_v ground values of archetype buildings for various ductility levels: (a) μ_{comp}=1, (b) μ_{comp}=1.25, (c) μ_{comp}=1.5, (d) μ_{comp}=2, considering an earthquake scenario with a 10% probability of exceedance in 50 years

Figure 2.16 and Figure 2.17 illustrate the broadband flat velocity spectra curve at ground level for components ranging from low to high ductility, indicating the absence of amplification

effects on FS_V values at this level. Additionally, Figure 2.16 and Figure 2.17 demonstrate that the impact of ductility is less significant at ground level compared to elevated floors. It is concluded that the reductions in peak FS_V values for low, moderate, and high ductility components are approximately 8%, 16%, and 25%, respectively. Notably, Figure 2.12, Figure 2.13, Figure 2.15, and Figure 2.17 representing FS_V corresponding to earthquake scenario with a 10% probability of exceedance in 50 years, exhibit average values approximately 45% lower than those in Figure 2.10, Figure 2.11, Figure 2.14, and Figure 2.16 respectively, which correspond to scenarios with a 2% probability of exceedance in 50 years.

2.3.2.4 Proposed IVR Values Based on Obtained Results

The sensitivity analysis presented in Figure 2.18 offers an in-depth analysis of the effects of varying damping ratios (1%,2%,3%, calculated using Equation 2.1 on the IVR ratios in comparison to the default 5%, thereby further justifying the selection of the proposed IVR values.

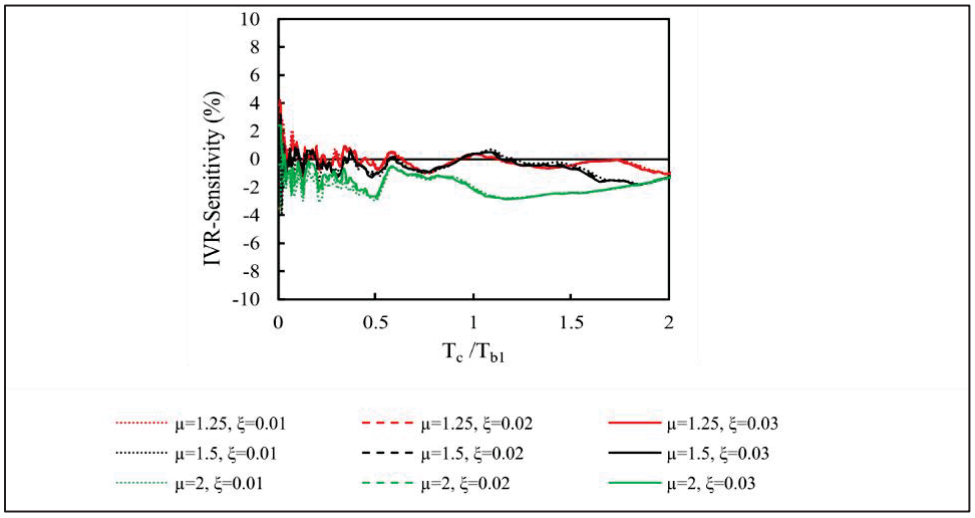

Figure 2.18 Sensitivity analysis of IVR values to damping ratios (1%, 2%, 3%) varying from the default 5%, averaged across roof, intermediate, and ground levels for earthquake scenarios with 2% and 10% probabilities of exceedance in 50 years

Table 2.5 presents IVR values derived from the analysis of roof, intermediate, and ground levels, based on data from Figure 2.9. The mean analysis values for each level were obtained using the Mean curve. To ensure a conservative design, Table 2.5 also includes proposed IVR values and the associated STD values for floor and ground levels, which are obtained from Figure 2.9. For the "Roof and Elevated Levels" row, the rounded average of the Mean+STD curves (Figure 2.9a and b) at the roof and intermediate level was used. For the "Ground Level" row, the Mean+STD rounded value of the ground level Mean curve (Figure 2.9c) was used. Also, the Figure 2.18 illustrates that the sensitivity analysis reveals minimal impact across all ductility levels, with changes in damping ratio resulting in less than 4% variation. Thus, the proposed IVR factors in Table 2.5 remain robust and require no modifications based on these sensitivity analysis results.

Table 2.5 Inelastic Velocity Ratio average values of all case studies

			Computed Mean Values	**STD**	**Proposed Values**
Level of component	μ_{comp}	**Specific Location**	**IVR**	**IVR**	**IVR**
Ground level	1		1	0	1
	1.25		1.1	0.002	1.1
	1.5		1.22	0.05	1.15
	2		1.37	0.07	1.3
Roof and elevated levels	1	Intermediate level	1	0	1
		Roof level	1		
	1.25	Intermediate level	1.27	0.001	1.2
		Roof level	1.37		
	1.5	Intermediate level	1.56	0.07	1.7
		Roof level	1.92		
	2	Intermediate level	2	0.15	2.1
		Roof level	2.5		

According to the data in Table 2.5, the mean and proposed values for the IVR values at the ground level consistently remained below 1.5. However, for the roof level, the IVR exceeded 2 for components with high ductility.

The IVR values provided in Table 2.5 allow engineers to estimate inelastic velocity demands for NSCs, clarifying how components with varying ductility behave under seismic loads. This supports the design of critical velocity-sensitive components, such as freestanding or suspended NSCs, to avoid damage during significant ground motions. Incorporating these factors into seismic design practices enables a more accurate representation of NSC demands. Additionally, using ductility-based factors for highly ductile components can yield more economical anchorage designs, reducing material consumption while ensuring adequate performance. Most importantly, accurate IVR values enable proper design of velocity-sensitive components by establishing appropriate velocity limits, thus preventing damage or failure from excessive velocities during seismic events, contributing to safer buildings that maintain functionality after an earthquake.

2.3.3 Mean Displacement at Different Ductility Levels

The seismic displacement demand results are presented in this section, divided into four distinct subsections. The first subsection explores the Inelastic Displacement Ratio, which is obtained by considering multiple ductility levels and employing both Historical and Synthetic ground motion data. This section examines the relationship between ductility levels and their corresponding effect on 1/IDR values. The second subsection investigates the floor spectral displacement (FS_D) response of NSCs across various periods. The third part explores the effect of the ductility levels on the FS_D responses across all earthquake records for the case study buildings. In the final subsection, a sensitivity analysis assesses how variations in damping ratios affect the IDR values. Subsequently, Table 2.6 presents a comprehensive summary of the IDR factors at various ductility levels and component locations.

2.3.3.1 Inelastic Displacement Ratio (IDR)

The Inelastic Displacement Ratio is defined as the ratio between the maximum displacement response of an elastic system (μ_{comp} =1) and an inelastic system μ_{comp} (A. K. Chopra & Chintanapakdee, 2004) within the specific range of the first tuning mode ($0.5 \leq T_c / T_{b1} \leq 1.5$). Figure 2.18 represents the peak 1/IDR values as a function of ductility of the components at the roof, intermediate floors, and ground level of the studied buildings subjected to historical earthquakes, synthetic earthquakes, and combined records across earthquake scenarios (2% and 10% probability of exceedance in 50 years). By presenting the data as 1/IDR, the correlation between seismic velocity demands and ductility becomes clearer, while the IDR values are listed in Table 2.6. Additionally, the graphs show the mean values of these datasets, along with the standard deviation (both above and below the mean).

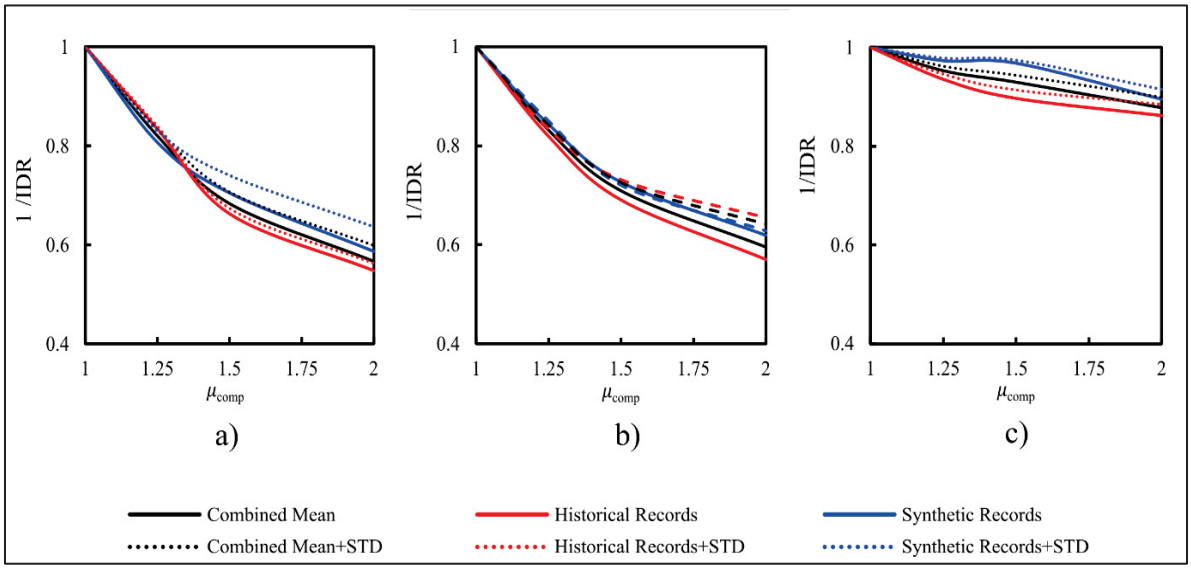

Figure 2.19 Reduction in Mean FS_D response for components with varying target ductilities at different levels: a) roof, b) intermediate, and c) ground

The graphs presented in Figure 2.18 show that as displacement demands shift from elastic to highly ductile components, a notable decrease is observed, averaging around 40% at higher levels and 15% at the ground level.

Also, it can be concluded that the effect of ductility is most pronounced at moderate ductility levels, with a steep decline in IDR values as μ_{comp} increases from 1 to about 1.5. Beyond this point, the rate of decline diminishes.

Therefore, designing NSCs with moderate ductility levels ($\mu_{comp} \approx 1.5$) is recommended for displacement-sensitive components, as is also observed in the acceleration and velocity sections, to optimize the seismic performance and maintain cost-effective designs. Furthermore, the effect of ductility on the IDR is observed to be much less pronounced at the ground level as compared to the elevated floors, indicating that the influence of ductility on the seismic response becomes more significant at higher elevations within the building.

As a result, the mean ground motion results, which reliably represent both historical and synthetic datasets across earthquake scenarios (2% and 10% probability of exceedance in 50 years), were the basis for the combined analysis displayed in Table 2.6. In Figure 2.19 to Figure 2.22, however, the mean results for the historical and synthetic datasets are shown separately, enabling a direct comparison between the two types of ground motion inputs for both earthquake scenarios.

2.3.3.2 Floor Spectral Displacement (FSD)

The floor spectral displacement response of NSCs to seismic events is presented in Figure 2.19 to Figure 2.22, illustrating four graphs (a, b, c, and d) that display the mean FS_D values at different levels, with each graph comprising four curves that examine the response in relation to the component period and ductility characteristics of NSCs, with μ_{comp} ranging from 1 to 2. These graphs also display the first three periods of the building.

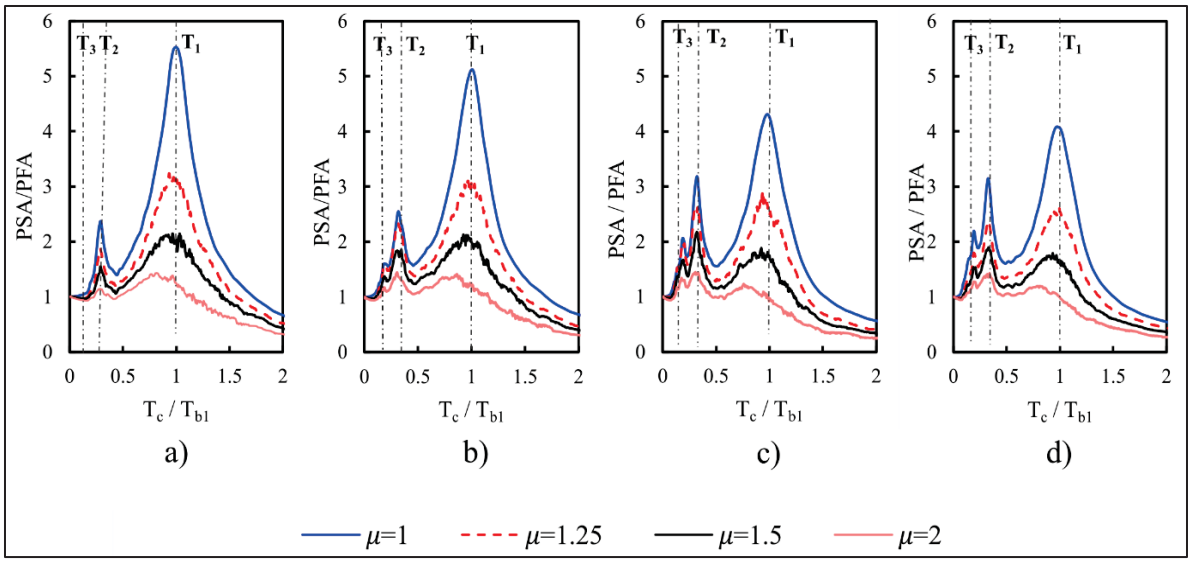

Figure 2.20 Mean floor spectral displacement of the intermediate floors of archetype buildings for various ductility levels: (a) 3-storey, (b) 6-storey, (c) 9-storey, (d) 12-storey, considering an earthquake scenario with a 2% probability of exceedance in 50 years

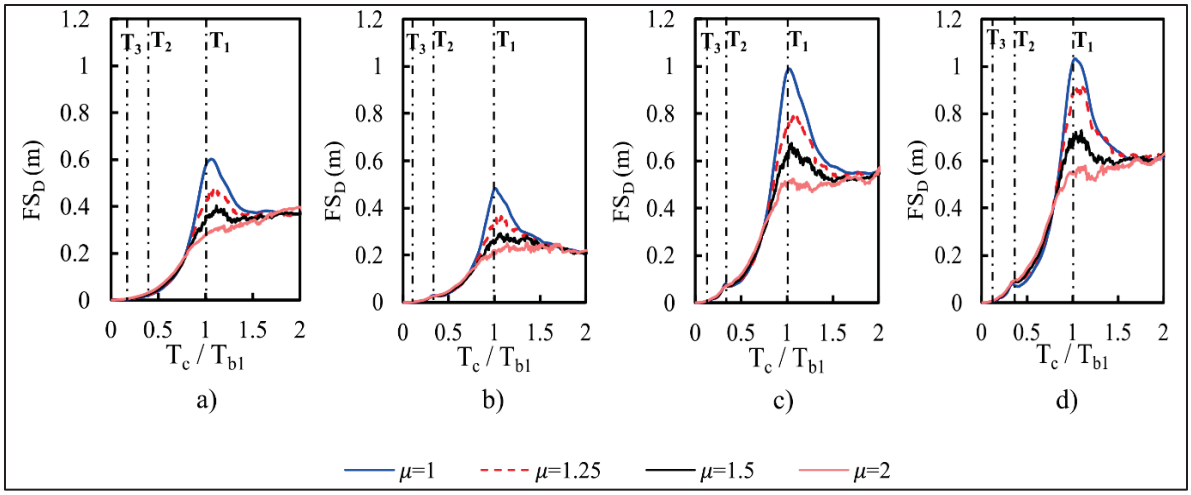

Figure 2.21 Mean floor spectral displacement of the roof level of archetype buildings for various ductility levels: (a) 3-storey, (b) 6-storey, (c) 9-storey, (d) 12-storey, considering an earthquake scenario with a 2% probability of exceedance in 50 years

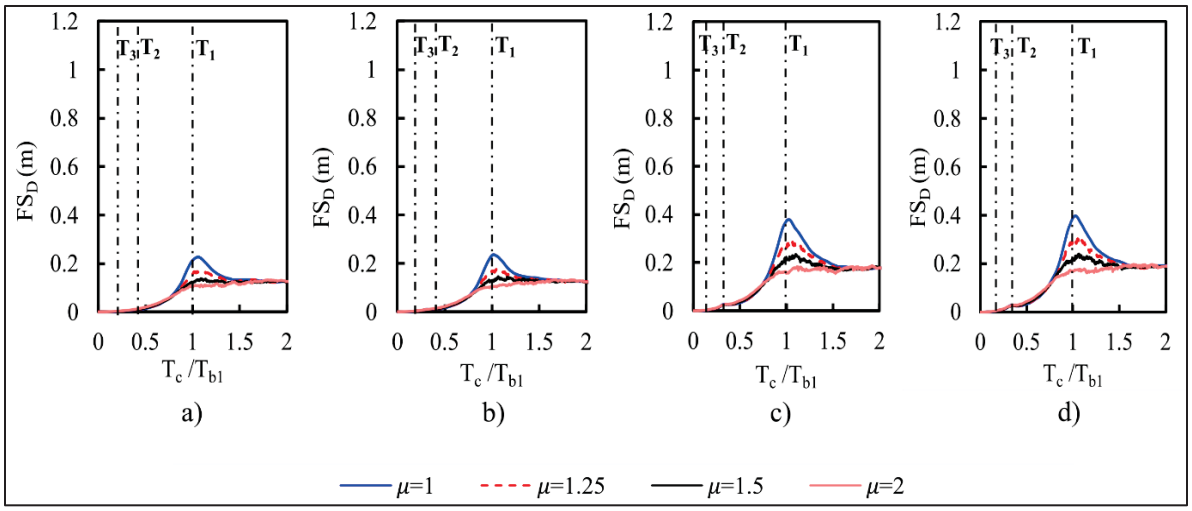

Figure 2.22 Mean floor spectral displacement of the intermediate floors of archetype buildings for various ductility levels: (a) 3-storey, (b) 6-storey, (c) 9-storey, (d) 12-storey, considering an earthquake scenario with a 10% probability of exceedance in 50 years

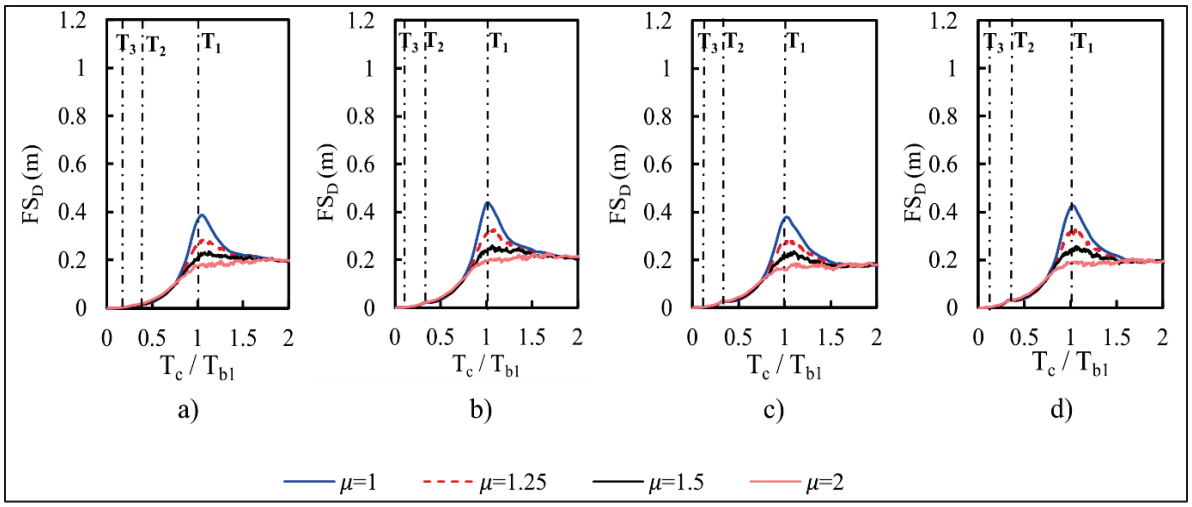

Figure 2.23 Mean floor spectral displacement of the roof level of archetype buildings for various ductility levels: (a) 3-storey, (b) 6-storey, (c) 9-storey, (d) 12-storey, considering an earthquake scenario with a 10% probability of exceedance in 50 years

The observed similarity in peak values, shapes, and FS_D values between Figure 2.20 to Figure 2.23 suggests that FS_D values are consistent across intermediate floors and at the roof level. Figure 2.20 to Figure 2.23 illustrate that FS_D values in components with elastic to highly ductile behavior, within a $0.5 \leq T_c / T_{b1} \leq 1.5$ period range, are considered to be in the main

resonance range, and are more likely to experience amplification. It is also observed that the displacement responses for NSCs mainly experience one peak around the first fundamental mode and have less pronounced spectral displacements around higher modes (T_2 and T_3). Thus, components with a period range of $T_c / T_{b1} > 1.5$ or $T_c / T_{b1} < 1.5$ is categorized as being in the out-of-resonance range, where resonance is less probable, and displacement demands remain relatively constant. Nevertheless, it is also observed that components with a period range of $0.4 \leq T_c / T_{b1} \leq 0.7$, a slightly reversed trend occurs, meaning that as the ductility is increased, the displacement demands increase as well. These findings are consistent with the studies by Anajafi et al. (2020) and Obando et al. (2018).

2.3.3.3 Ductility Effect on FS_D Values at Floor and Ground Levels

Figure 2.24 and Figure 2.25 illustrate the FS_D values for various ductility levels (μ_{comp} = 1, 1.25, 1.5, and 2) at elevated floors, as well as mean FS_D values and standard deviations for both roof and intermediate floors, incorporating data from all case studies and earthquake records.

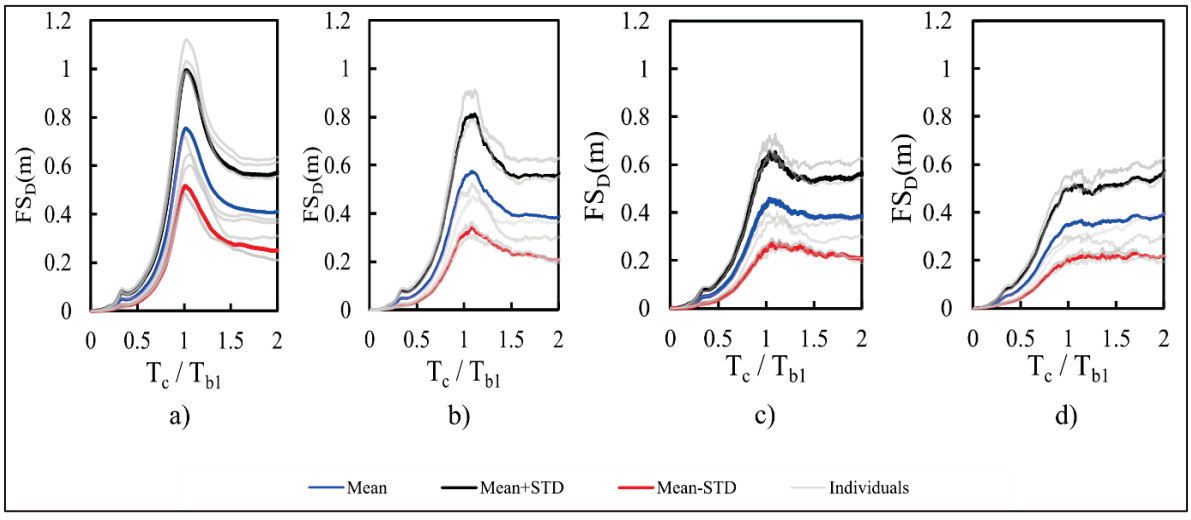

Figure 2.24 FS_D floor values of archetype buildings for various ductility levels: (a) μ_{comp}=1, (b) μ_{comp}=1.25, (c) μ_{comp}=1.5, (d) μ_{comp}=2, considering an earthquake scenario with a 2% probability of exceedance in 50 years

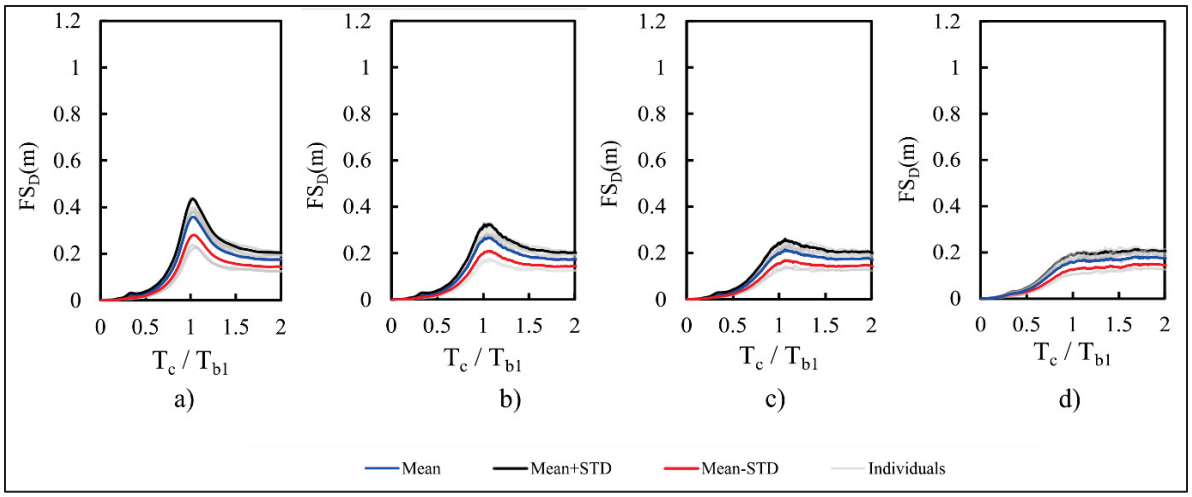

Figure 2.25 FS_D floor values of archetype buildings for various ductility levels: (a) μ_{comp}=1, (b) μ_{comp}=1.25, (c) μ_{comp}=1.5, (d) μ_{comp}=2, considering an earthquake scenario with a 10% probability of exceedance in 50 years

The information provided in Figure 2.24 and Figure 2.25 highlights the impact of the building height on FS_D values, indicating that the latter may not greatly influence the variability of these values. This is supported by the relatively small standard deviations observed in both roof and intermediate floor responses. This observation is also borne out by previous findings in Figure 2.20 to Figure 2.23, and Sections 2.3.1.3 and 2.3.2.3. It is typically observed that the FS_D values decrease with increasing ductility. This appears to contradict the behavior of the primary structures, which show an increase in structure displacement as they become more ductile. At the elevated floors in the fundamental resonance range, the displacement spectra for components with low ductility were reduced by approximately 22% as compared to the elastic case. For components with moderate ductility, the reduction was around 32%, while for highly ductile components, a 45% decrease in displacement spectral values was experienced.

Figure 2.26 and Figure 2.27 illustrate the FS_D values for various ductility levels (μ_{comp} = 1, 1.25, 1.5, and 2) at ground level, as well as mean FS_D values and standard deviations of earthquake records.

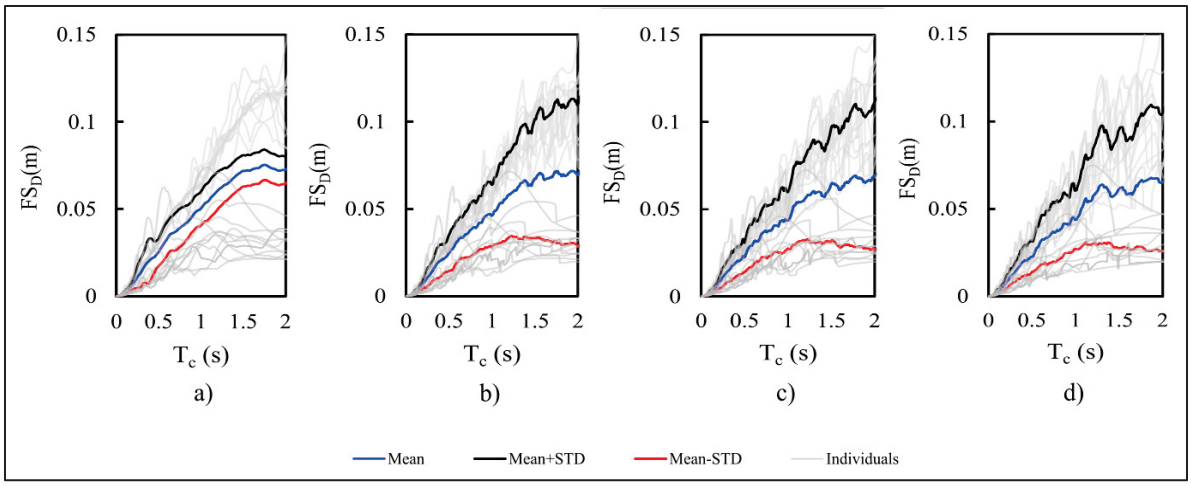

Figure 2.26 FS_D ground values of archetype buildings for various ductility levels (a) μ_{comp}=1, (b) μ_{comp}=1.25, (c) μ_{comp}=1.5, (d) μ_{comp}=2, considering an earthquake scenario with a 2% probability of exceedance in 50 years

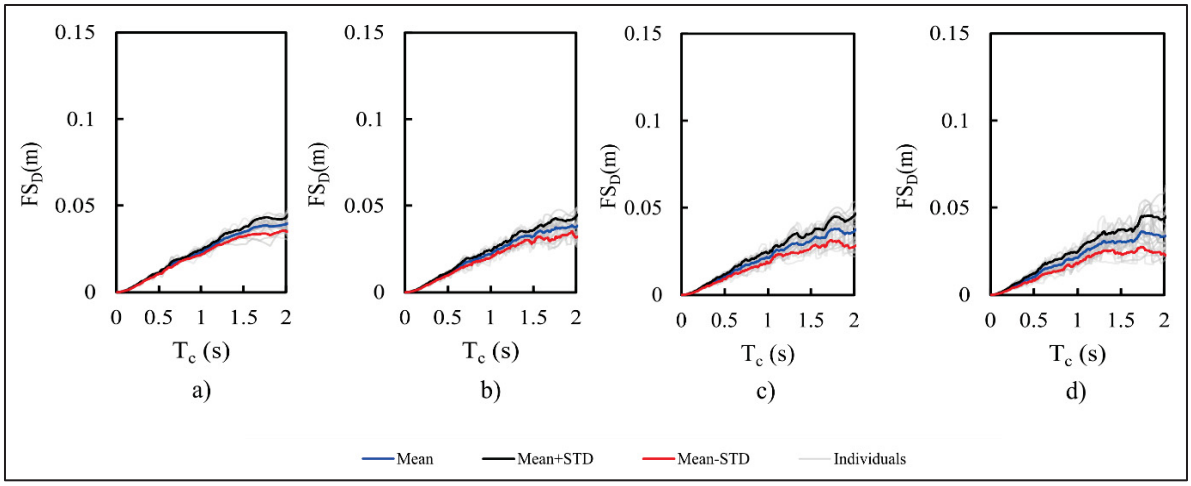

Figure 2.27 FS_D ground values of archetype buildings for various ductility levels (a) μ_{comp}=1, (b) μ_{comp}=1.25, (c) μ_{comp}=1.5, (d) μ_{comp}=2, considering earthquake scenarios with a 10% probability of exceedance in 50 years

Figure 2.26 and Figure 2.27 illustrate that while FS_D values at ground level show an increasing trend up to T_c = 1.5, the rate of increase slows down significantly beyond this point, resulting in a nearly flat trend. It is also observed that at ground level, the impact of component ductility was less significant than at elevated floors. Low ductility components showed only a 5% reduction in displacement response spectra compared to elastic components at this location.

Moderately ductile components experienced a 10% decrease, while highly ductile components resulted in a 13% reduction in displacement spectra at ground level.

It is worth noting that Figure 2.22, Figure 2.23, Figure 2.25, and Figure 2.27, which represent earthquake scenarios with a 10% probability of exceedance in 50 years, display values averaging 55% lower than those in Figure 2.20, Figure 2.21, Figure 2.24, and Figure 2.26 respectively, which correspond to scenarios with a 2% probability of exceedance in 50 years.

2.3.3.4 Proposed IDR Values Based on Obtained Results

The sensitivity analysis given in Figure 2.28 provides a detailed examination of the impacts of varied damping ratios (1%,2%,3%, calculated using Eq. 1) on the IDR ratios compared to the default 5%, further validating the selection of the recommended IDR values.

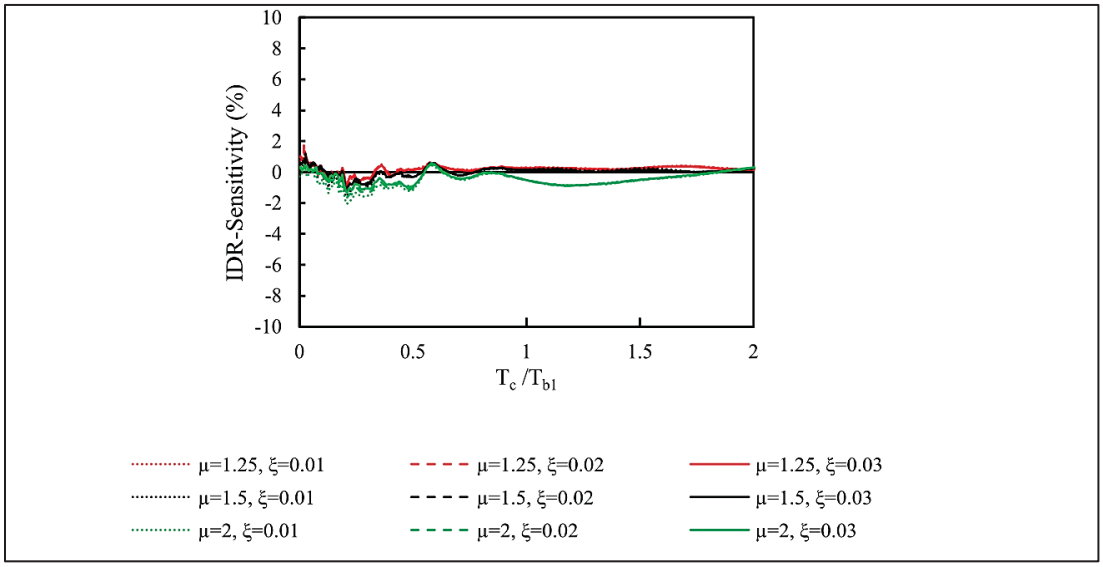

Figure 2.28 Sensitivity analysis of IDR values to damping ratios (1%, 2%, 3%) varying from the default 5%, averaged across roof, intermediate, and ground levels for earthquake scenarios with 2% and 10% probabilities of exceedance in 50 years

Table 2.6 presents a summary of IDR values obtained by analyzing data from different levels of a structure, specifically the roof, intermediate levels, and ground level (as shown in Figure 2.19). The Mean Analysis Values for each level were calculated using the Mean curve. To

ensure a conservative design, Table 2.6 also proposed IDR values and the associated STD values for both floor and ground levels, obtained from Figure 2.19. For the "Roof and Elevated Levels" row, the average of the Mean+STD curves for the roof and intermediate levels (Figure 2.19a and b) was used. The "Ground Level" row, on the other hand, used the Mean+STD curve values from the ground level (Figure 2.19c).

In addition, Figure 2.28 illustrates that the sensitivity analysis reveals minimal impact across all ductility levels, with changes in damping ratio resulting in less than 2% variation. Thus, the proposed IVR factors in Table 2.6 remain robust and require no modifications based on these sensitivity analysis results.

Table 2.6 Inelastic Displacement ratio average values of all case studies

			Computed Mean Values	**STD**	**Proposed Values**
Level of component	μ_{comp}	**Specific Location**	**IDR**	**IDR**	**IDR**
Ground level	1		1	0	1
	1.25		1.06	0.02	1.04
	1.5		1.1	0.03	1.05
	2		1.14	0.03	1.1
Roof and elevated levels	1	Intermediate level	1	0	1
		Roof level	1		
	1.25	Intermediate level	1.17	0.02	1.15
		Roof level	1.2		
	1.5	Intermediate level	1.4	0.025	1.5
		Roof level	1.47		
	2	Intermediate level	1.66	0.12	1.6
		Roof level	1.78		

According to the data in Table 2.6, the mean and proposed IDR values at ground level consistently remained below 1.2. However, at the roof level, components with high ductility exhibited IDR values as high as 2.

The IDR values in Table 2.6 can predict inelastic displacement demands for NSCs, providing engineers with insights into how components with varying ductility levels respond to seismic loads. This understanding is crucial for designing displacement-sensitive elements, such as partition walls and piping systems, to prevent damage during significant ground motions. By integrating these modification factors into seismic design methodologies, engineers can accurately represent anticipated seismic demands on NSCs. Additionally, applying ductility-based factors for ductile components can lead to cost-effective anchorage designs, reducing material use while ensuring adequate seismic performance. Precise IDR values also help prevent excessive drift in displacement-sensitive NSCs, mitigating the risk of significant damage or failure. This focused approach enhances building safety and ensures functionality after an earthquake.

2.4 Conclusion

The study provides an improved and reliable A_r/R_p, IVR, and IDR values that characterize the ductile behavior of NSCs at the elevated floor and ground levels, through THA performed on four archetype RC buildings (3, 6, 9, and 12 storeys) subjected to 24 earthquake records (12 historical and 12 synthetic) matched to Montreal's UHS scenarios (2% and 10% probability of exceedance in 50 years). In addition, a sensitivity analysis on damping ratio variations (1%, 2%, and 3%) confirmed the robustness of these factors, with notable impacts observed for elastic components.

The analysis was conducted using a MATLAB script employing the step-by-step Newmark integration method for solving the governing equations of motion. The key findings of this research are summarized as follows:

- Although the A_r/R_p, IVR, and IDR values presented in this study offer an improved understanding of seismic demands on non-structural components, the current analysis is based on four archetype buildings and 24 earthquake records. These values are intended as a first step toward more refined design guidelines, and not as immediate recommendations for design standards. Future studies should extend the scope to include a wider variety of building typologies and ground motion records, thereby

enhancing the applicability and robustness of the proposed values. Additionally, in order to implement these factors in design codes like NBC 2020 and for the development of future guidelines, different building configurations, seismic zones, and local soil conditions should be considered to ensure broad applicability and relevance.

- The analysis outcomes presented in this paper demonstrate a small standard deviation in seismic demand results. This reduced variability stems from the tight alignment of the selected records with the target UHS. While using the UHS for scaling provides a conservative estimate of seismic demands, it also inherently limits the variability in the results by minimizing the deviations between individual records and the target spectrum across all periods. This low standard deviation, resulting from the conservative scaling to UHS, adds robustness to the analysis and strengthens the confidence in the validity of the proposed factors for NSCs. Future studies can expand on this by incorporating CMS or other ground motion selection techniques to capture greater seismic variability.
- An analysis of the acceleration, velocity, and displacement responses reveals consistent trends between historical and synthetic ground motions, with the Mean curve typically lying between them. While historical inputs result in slightly higher A_r/R_p, IVR, and IDR factors across both 2% and 10% exceedance scenarios compared to synthetic inputs, the differences are minor. This suggests that the choice of ground motion input has a limited impact on the seismic design and performance of NSCs, even at higher ductility levels, consistent with previous findings by Galasso et al. (2012).
- The R_p values derived from this study align well with the theoretical formula proposed by Chopra (2011), validating the precision of this study's approach in capturing the ductility behavior of components.
- The seismic response, in terms of peak acceleration, velocity, and displacement demands, was observed to be dependent on the ductility of NSCs and on the resonance period range. Acceleration responses exhibited three distinct peaks, indicating significant amplifications during the fundamental mode and higher modes, with the fundamental mode playing a dominant role in NSCs' acceleration demands. In contrast, displacement and velocity demands were primarily governed by the fundamental mode,

as evidenced by a single peak in their responses. Within the resonance period range, higher ductility NSCs can better accommodate amplified demands, whereas lower ductility ones face excessive seismic demands. Outside the resonance period range, the influence of ductility on these demands diminishes.

- The A_r/R_p for elastic components located at the roof level is more likely to exceed the NBC-specified value of 2.5, which is associated with an R_p of 1. However, ground level components typically exhibit A_r/R_p values below 2.5, suggesting that the standard's design limit provides adequate safety for these ground level components.
- The impact of changing ductility has a greater significance on floor accelerations versus its effect on floor displacement and velocity.

In summary, this study contributes to the understanding of the effect of the level of ductility of NSCs on their seismic demands in a bid to improve the reliability of seismic analysis. The proposed ductility-based approach for estimating seismic demands demonstrates important refinements over code-prescribed factors. The results suggest that considering the component ductility, location, and resonance in the design process is crucial for ensuring the assumed seismic performance of NSCs.

FOREWORD TO CHAPTER 3

To support the interpretation of the results presented in this chapter, five technical clarifications are provided regarding the ground motion scaling, numerical modeling approach, and interpretation of results:

1. **Ground Motion Scaling and IDA Procedure:** It is important to clarify that the ground motion records were first spectrally matched to the Montreal Uniform Hazard Spectrum (UHS). Subsequently, to perform the Incremental Dynamic Analysis (IDA), these matched records were scaled by factors ranging from 0.1 to 4.0 times the design spectral acceleration. This scaling approach allows for the assessment of structural performance at intensities varying from a fraction of the design earthquake (linear range) up to four times the design intensity (collapse level). The adequacy of this upper limit is demonstrated by the IDA curves presented in ANNEX IV, which confirm that acceleration saturation from structural yielding occurs between 3.0g and 4.0g input intensity for all case study buildings, ensuring that all damage states are captured within the scaling range
2. **Numerical Modeling Strategy (Section 3.3):** A clarification regarding the modeling approach described in Section 3.3 is provided to resolve potential confusion regarding the use of 'stick models' versus 'plastic hinges'. The modeling strategy implemented in this study followed a two-step calibration process:
    - **Detailed Model Calibration (ETABS):** First, detailed finite element models were constructed in ETABS, with material nonlinearity represented by concentrated plastic hinges at beams and columns, and defined according to ASCE 41-23 (ASCE, 2023). Nonlinear static (pushover) analyses were performed to derive the nonlinear force-deformation relationship and yield displacement at each story.
    - **Simplified Dynamic Model (MATLAB):** Second, the story-level yield displacements and force-deformation relationships derived from the ETABS pushover analyses were used to define the properties of the simplified Multi-

Degree-of-Freedom (MDOF) 'stick models'. These computationally efficient models were implemented in MATLAB (The MathWorks Inc., 2023) to perform the extensive nonlinear time-history analyses.

Therefore, the mention of 'plastic hinges' refers to the detailed modeling phase in ETABS, while the 'stick model' refers to the computationally efficient model used for the final dynamic simulations in MATLAB.

3. Effect of Component Damping (Page 120): The text mentions that the effect of non-structural damping was found to be minimal. It is important to clarify that this observation is specific to the ductile (inelastic) component response investigated in this chapter. While damping is a critical parameter for controlling demands on elastic components (reducing resonant amplification), its relative influence diminishes for ductile components where hysteretic energy dissipation dominates. Therefore, the stated conclusion regarding minimal damping effects applies strictly to the yielding components analyzed and should not be generalized to an EDP utilized in this chapter, which is Peak Component Acceleration (PCA), also referred to as the component Peak Spectral Acceleration (PSA), rather than the Peak Floor Acceleration (PFA). This distinction has two major implications for the interpretation of the chapter:

- **Interpretation of Results (Section 3.6.1):** The reported acceleration values decrease as component ductility increases. This is because PCA represents the response of the component, yielding acts as a fuse, limiting the inertial forces that can be generated within the NSC.
- **Application of Hazus Thresholds (**Table 3.4, Figure 3.5**, and** Figure 3.6): It is acknowledged that the damage thresholds in Table 3.4 references damage thresholds derived from Hazus-MH 2.1 are adopted from Hazus-MH 2.1, which standardly defines limits in terms of PFA. However, this study intentionally applies these thresholds to PCA to explicitly account for dynamic amplification and resonance effects, factors that a PFA-based assessment would neglect. Although the horizontal axis in Figure 3.5 and Figure 3.6 retains the standard Hazus nomenclature ("PFA") consistent with the published manuscript, the plotted demand values represent the computed PCA.

6. Uncoupled Analysis Procedure: To clarify the 'uncoupled' analysis framework utilized in this study, which assumes the mass of the NSC is small relative to the supporting structure such that dynamic interaction is negligible, the computational workflow proceeds in two distinct, sequential phases:

- **Phase 1 (Structural Analysis):** The supporting structure (MDOF stick model) is subjected to ground motion time-histories. The absolute acceleration response at each floor is recorded, generating a database of Floor Acceleration Time-Histories.

- **Phase 2 (Component Analysis):** These recorded floor accelerations are then applied as the input motion to the independent Single-Degree-of-Freedom (SDOF) component models. The response of the component is calculated to determine Peak Spectral Accelerations (PSA) and displacements.

CHAPTER 3

PROBABILISTIC ASSESSMENT OF SEISMIC ACCELERATION DEMANDS OF DUCTILE LIGHT NSCS IN MODERATELY DUCTILE RC FRAME BUILDINGS

Majid Mehrjoo[a] and Rola Assi[b]

[a,b] Department of construction engineering, École de technologie supérieure (ÉTS), Montreal, Quebec, H3C 1K3, Canada

Paper published in Engineering Structures[2], Special Issue: "VSI: Nonstructural Elements in Buildings and Seismic Resilience, July 2025
https://doi.org/10.1016/j.engstruct.2025.120347

Abstract

This study investigates how the seismic demands of non-structural components (NSCs) are influenced by both their attachment ductility and the nonlinear behavior of supporting structures. The research focuses on acceleration demands at various building elevations and evaluates component damage states according to Hazus guidelines.

Incremental dynamic analysis (IDA) was applied to evaluate both linear and nonlinear structural responses of four archetype reinforced concrete moment-resisting frame buildings. Ground motions, consisting of historical and synthetic records, were scaled to match Montreal's uniform hazard spectrum for Site Class 'C' with a 2% probability of exceedance per 50 years. NSC responses were assessed using an uncoupled analysis approach, implemented through iterative Newmark integration. Key findings demonstrate that increasing the ductility

---

[2] Mehrjoo, M., & Assi, R. (2025). Probabilistic Assessment of Seismic Acceleration Demands of Ductile Light NSCs in Moderately Ductile RC Frame Buildings. Engineering Structures, 335, 120347. **https://doi.org/10.1016/j.engstruct.2025.120347**

of NSC attachments reduces their acceleration demands by up to 140% in elastic structures. When accounting for structural nonlinearity, acceleration demands decrease by 110%, highlighting the conservative nature of elastic analysis assumptions commonly used in current design practices. These reductions are most pronounced for components with periods corresponding to the structure's fundamental mode, with the effect diminishing for higher modes. The research provides practical design implications by quantifying the relationship between attachment ductility, structural behavior, and component damage thresholds. The results indicate that a moderately ductile ($\mu \approx 1.5$) NSC attachment provides optimal performance benefits while minimizing the risk of NSC damage, offering valuable insights for the performance-based design of NSCs.

Keywords: non-structural components, ductile behavior, component attachments, Iterative Newmark integration, dynamic analysis, peak component factors

3.1 Introduction

This study provides a comprehensive probabilistic examination of the impact of the extent of ductility of attachment of acceleration-sensitive non-structural components (NSCs) on their seismic demands. Examples of such NSCs include water heaters, chillers, antennas, chimneys, and parapets (Adam & Fotiu, 2000; ATC, 2018a; Igusa, 1990; Toro et al., 1989; Villaverde, 2006; Vukobratović & Fajfar, 2017). Accurate evaluation of these acceleration demands is critical for the design, performance, and fragility analysis of these NSCs (Ghasemof et al., 2022; Mehrjoo & Aval, 2024).

Research has shown that the ductility of NSCs' attachments plays a crucial role in reducing seismic demands, particularly within the resonance range of a building's fundamental period (Anajafi et al., 2020; Filiatrault et al., 2018; A. K. Kazantzi et al., 2020a; Obando & Lopez-Garcia, 2018; Vukobratović & Fajfar, 2017). Various numerical approaches have been employed to investigate the impact of the ductile behavior of NSCs attachments on their seismic demands. These approaches may be generally categorized into three main types:

advanced numerical simulations, simplified analytical techniques, and empirical code-based procedures.

Advanced numerical approaches that integrate seismic probabilistic assessment methods are necessary for a more comprehensive and accurate evaluation of NSCs' seismic demands. In this context, two prominent methodologies stand out: Incremental Dynamic Analysis (IDA) and Multiple-Stripe Analysis (MSA). IDA provides a comprehensive simulation framework to assess seismic demands across a continuous range of earthquake intensities by applying scaled accelerograms to the building model. MSA offers a complementary approach by analyzing structural response at discrete intensity levels using ground motion sets specifically selected for each intensity level (Banerjee et al., 2016). In this study, IDA was selected as it enables the generation of continuous fragility curves to evaluate component performance corresponding to different damage states (D'Altri et al., 2020; D'Ayala et al., 2015; Roca et al., 2010). On the other hand, simplified analytical techniques such as the nonlinear static analysis or the floor response spectra (FRS) are used to provide a preliminary assessment of the influence of the ductility of attachment of NSCs on the seismic demands of these components (Nardin et al., 2022). On the other hand, these techniques have limitations in capturing the nonlinear responses of structures and NSCs because of the oversimplification of complex behaviors such as material nonlinearity of the structural components and the ductile behavior of NSC attachments, which creates challenges in accounting for cumulative damage effects and may result in an overestimation of seismic demands (Moon et al., 2016, 2018; Olivo et al., 2020; Rahman et al., 2019). Additionally, empirical methods, which form the basis of most seismic design codes, tend to use simplified equations and assumptions to estimate the seismic demands on NSCs (Anajafi, 2018; Villaverde, 2006). Specifically, the National Building Code of Canada (NBC) suggests a force-based approach for the design of NSCs, incorporating parameters such as the component response modification factor (Rp) to account for the ductility at NSC's attachment (NRC 2020). Specifically, current analytical approaches in NBC provision primarily focus on the elastic behavior of the NSCs and the supporting structure, thereby potentially overestimating seismic demands. (Kawakatsu et al., 1979; Lin & Mahin, 1985; Soong et al., 1993; Viti et al., 1981) Despite their usefulness in simplifying the design procedures, empirical methods require improvement to more accurately represent the level of

ductility of NSCs' attachment (ASCE, 2017; Anajafi, 2018; ATC, 2018a; A. Kazantzi et al., 2018; Miranda et al., 2018; Villaverde, 2006; Vukobratović & Fajfar, 2017; T. Wang et al., 2021).

To address the nonlinear behavior of NSCs and their supporting structures, advanced analytical approaches have been employed to overcome the limitations of code-simplified methods. Notably, studies by Lin and Mahin (1985) and Taghavi and Miranda (2012) demonstrated that inelastic structural responses can either amplify or attenuate floor accelerations compared to linear models, depending on factors such as building height, lateral system flexibility, and NSC period. Recent work by Ruggieri and Vukobratović (2024) also emphasizes that accounting for nonlinear behavior can reduce acceleration demands by up to 40%, compared to elastic analysis predictions, particularly when considering energy dissipation through structural ductility and irregularities in mass and stiffness. Clayton and Medina (2012) proposed a probabilistic method to estimate acceleration demands for NSCs in shear wall structures based on the three NSCs (T_C) period ranges, rigid region ($T_C \rightarrow 0$), short-period region ($0 < T_C < 0.5T_{B1}$), and fundamental-period region ($0.5T_{B1} < T_C < 2.0T_{B1}$). IDA and site-specific ground-motion hazard data were used to develop hazard curves and component uniform hazard spectra (CUHS) considering various structural and NSC characteristics. The study found that component location, period ratios, and damping ratios are critical factors in estimating component responses.

Another key aspect in understanding NSC behavior is their fragility response to seismic loads. In this context, D'Angela et al. (2024) conducted a comprehensive study of the seismic fragility of NSCs modeled as nonlinear single-degree-of-freedom systems. The research utilized IDA to evaluate the seismic response of a range of NSC frequencies, including medical equipment, suspended ceiling systems, and museum objects. The various damage states and performance levels for each NSC category were evaluated in the analysis, which resulted in the production of fragility curves that are valuable in the seismic design and vulnerability assessment of NSCs. The results showed that as the rigidity of the NSCs increased, the probability of exceeding damage states tended to decrease. Conversely, fragility dispersion exhibited the opposite trend, which will decrease as the rigidity of NSCs increases. Gautam et al. (2021) investigated the seismic fragility of structural and NSCs in RC buildings in Nepal, using detailed vulnerability

assessments of school buildings after the 2015 Gorkha Earthquake (M_w 7.8). This assessment provides insights into their seismic demands and highlights the urgent need for strengthening the NSCs and beam-column connections.

While previous research has established the importance of NSC seismic behavior and provided valuable insights into their performance under different levels of ground motion intensity and structural configurations, there remains a critical need to understand the combined effects of NSC attachment ductility and structural nonlinearity on component seismic demands and damage states. Additionally, while the impact of structural ductility on seismic response has been well-documented, the relationship between NSC attachment ductility and acceleration demands across different floor levels and damage states remains insufficiently explored. (Abou-Elfath et al., 2018; Güner & Topkaya, 2020; Jamshidi Avanaki, 2019)

To address the existing knowledge gaps, this research focuses on three key objectives: (1) quantifying the relationship between NSC attachment ductility and seismic demands through probabilistic assessment, (2) evaluating the combined influence of structural nonlinearity and NSC ductility on component acceleration demands, and (3) developing practical design recommendations for optimal NSC attachment ductility levels that balance performance and damage control to support performance-based design of NSC attachments. To achieve these goals, this study employs IDA to evaluate the seismic demands of acceleration-sensitive NSCs and develop fragility curves. The analysis is based on three elevation levels along the building height (roof, intermediate, and ground) for four multi-story archetype reinforced concrete moment-resisting frame buildings subjected to 24 earthquake records matching Montreal's uniform hazard spectrum (UHS). Advanced numerical approaches were used to establish a correlation between four ductility levels and the damage states, slight, moderate, and extensive, specified in the Hazus manual (FEMA, 2012a). The use of the Hazus classification approach provides a foundation for a broader analysis of NSCs while recognizing the inherent limitations of creating specific fragility curves for all component types in different regions (FEMA, 2012a). The methodology employs multi-degree-of-freedom (MDOF) vibration systems in both elastic and elasto-plastic archetype-building models. Elasto-plastic behavior is used as a simplifying assumption to capture the essential nonlinear characteristics of the building while maintaining computational efficiency. (Asadpour et al., 2022; A. K. Chopra, 2011; Obando &

Lopez-Garcia, 2018) This analysis considers the NSCs with periods that match the first three periods for each case study building.

3.2 Selection and Scaling of Input Ground Motion Data

This study employs a total of 24 ground motion recordings, which include a suite of 12 historical ground motions and 12 synthetic ground motions, to accurately estimate the mean structural response quantities (ASCE, 2016; Hancock et al., 2008). The selected ground motions are representative of Montreal's seismic hazard characteristics, characterized by low-to-moderate seismicity. Historical ground motions were chosen to reflect regional tectonic settings, while synthetic motions were included to account for scenarios that may not be adequately represented in the historical dataset. This approach ensures comprehensive coverage of potential seismic hazards while maintaining consistency with Montreal's UHS (Panza et al., 2002). It is acknowledged, however, that synthetic records may exhibit certain properties, such as increased energy content or a higher number of cycles, potentially influencing the seismic demands on structures (Piscal A. & López-Almansa, 2018). To address this, frequency domain matching (Fahjan & Ozdemir, 2008) was employed through a MATLAB script to match synthetic and historical earthquakes with Montreal's target UHS for Site Class 'C', based on a 2% probability of exceedance in 50 years and a damping ratio of 5%. This Frequency domain matching involves defining the response spectra for the given accelerogram, defining the modification factors, and applying the frequency domain amplitude correction through the Fast Fourier Transform (FFT) algorithm to minimize the disparities in the spectral values. An inverse FFT is then performed to obtain the scaled time history records. This technique preserves the inherent features of seismic ground motions while ensuring that the energy distribution and spectral characteristics of the records are consistent with the target design spectrum, thereby minimizing potential biases in seismic demand estimation (Gascot & Montejo, 2014). While this study’s methodology focused on Montreal's Site Class 'C', it can be extended to other site classes and regions with varying seismic hazard zones. Such applications would broaden the scope of the research and enhance the understanding of NSC ductile behavior and seismic demands under a broader range of seismic conditions.

3.2.1 Historical Ground Motions

A collection of 12 far-field ground motions from the PEER NGA-East database was chosen, as shown in Table 3.1 and Figure 3.1, based on the following criteria: (FEMA, 2015; NRC, 2020; Reyes, 2009)

1. Moderate earthquake magnitudes (M_w) were considered, ranging from 3.5 to 6.
2. Far-field records were chosen with epicentral distances ranging between 20 - 100 km.
3. The strike-slip fault mechanism was selected (Rosset & Chouinard, 2009).
4. Average shear-wave velocities in the range of 360 to 760 cm/sec in the top 30 meters of soil (V_s-30) were chosen to represent very dense soil known as Site Class 'C' in the NBC 2020.

Far-field ground motions, which dominate Montreal's seismic environment, were selected (Chouinard et al., 2004; Ghofrani et al., 2015).

Table 3.1 Details of selected historical ground motions

No	Event/Station	Date/Time	Mw
1	Saguenay/Site 2, Quebec, PQ	1988-11-25	5.9
2	FtPayne_2003-04-29/Sewanee	2003-04-29 8:59	4.62
3	MtCarmel_2008-04-18a/Olney Central College Olney, IL	2008-04-18 15:14	4.64
4	MtCarmel_2008-04-18a/Univ. of Southern Indiana, Evansville, IN	2008-04-18 15:14	4.64
5	Slaughterville_2010-10-13/Jones High School	2010-10-13 14:06	4.36
6	Slaughterville_2010-10-13/Wilshire Boulevard- Harrah	2010-10-13 14:06	4.36
7	Arcadia_2010-11-24/Meyer Ranch, Chandler, OK	2010-11-24 22:48	3.96
8	Arcadia_2010-11-24/Bridge Creek, Tuttle, OK	2010-11-24 22:48	3.96
9	Sparks_2011-11-05/Pawnee, OK	2011-11-05 7:12	4.73
10	Sparks_2011-11-05/Meyer Ranch, Chandler, OK	2011-11-05 7:12	4.73
11	Sparks_2011-11-06/Jones High School	2011-11-06 3:53	5.68
12	Sparks_2011-11-06/Wilshire Boulevard- Harrah	2011-11-06 3:53	5.68

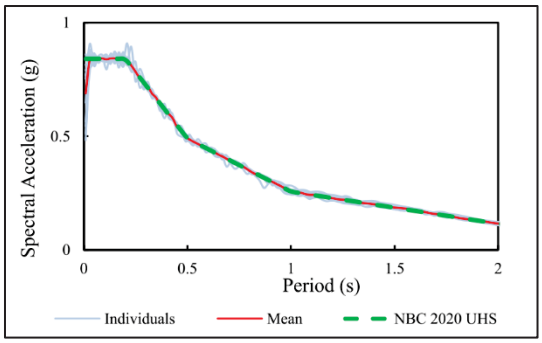

Figure 3.1 Mean and individual spectra of scaled historical ground motion and NBC 2020 UHS with a 2% possibility of exceedance per 50 years in Montreal

3.2.2 Synthetic Ground Motions

A collection of 12 synthetic accelerograms was extracted from the database developed by Atkinson (2009) and made available through the Engineering Seismology Toolbox website (www.seismotoolbox.ca). For the selection process, six records were considered for each magnitude-distance (M-R) scenario and were subsequently scaled to be compatible with Montreal UHS for Site class ‘C’ with a 2475-year return period. The properties of the selected accelerograms are detailed in Table 3.2, and their response spectra, along with Montreal’s UHS, are depicted in Figure 3.2.

Table 3.2 Details of the synthetic ground motions

M_w	R	Record	Duration(s)	Time step(s)	PGA(g)
6.0	15	E6c1_43	43.598	0.002	0.607
		E6c1_4			0.368
		E6c1_21			0.493
	30	E6c2_17	47.530		0.522
		E6c2_37			0.419
		E6c2_15			0.338
7.0	25	E7c1_18	51.126	0.002	0.395
		E7c1_30			0.285
		E7c1_40			0.538
	100	E7c2_12	57.352		0.213
		E7c2_4			0.329
		E7c2_36			0.178

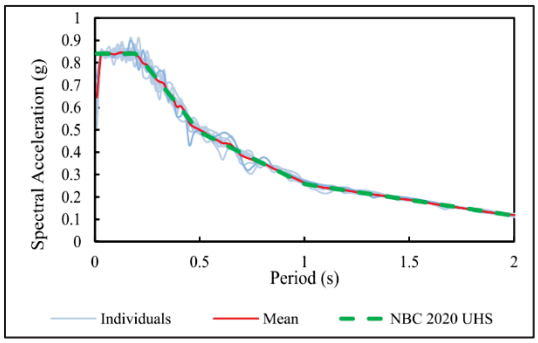

Figure 3.2 Mean, individual spectra of scaled synthetic records, and NBC 2020 UHS with 2% possibility of exceedance per 50 years in Montreal

3.3 Description of the Case Study Buildings and their Modeling Assumptions

The present investigation focused on a set of symmetric and regular 3-, 6-, 9-, and 12-story reinforced concrete moment-resisting frame (MRF) structures with limited ductility and a normal importance category. The buildings share a common layout, consisting of three bays, each spanning 7 meters in both the north-south (N-S) and east-west (E-W) directions, with a standard floor height of 3 meters, as shown in Figure 3.3. The structures were designed

following the guidelines specified in NBC 2015 (NRC, 2015) and CSA A23.3-14 (CSA, 2014a), with the design details addressed in the research of Mazloom and Assi (2022). The fundamental periods for these case studies are shown in Table 3.3.

The buildings were represented by stick models with lumped mass and stiffness at each floor, enabling the creation of matrices to analyze the MDOF system with 5% modal damping.

The stiffness of each level of the buildings modeled in the ETABS software (CSA, 2017) was determined using the flexibility method, which involves applying a unit force to each degree of freedom individually, calculating the resulting displacements, assembling these displacements into a flexibility matrix, and finally obtaining the stiffness matrix by inverting the flexibility matrix (Basset Salom, 2019; Georgioudakis & Plevris, 2018).

In order to determine the building's nonlinear floor acceleration responses, the governing equations of motion were solved using the Newmark integration technique.

The method was implemented in a MATLAB (The MathWorks Inc., 2023) script, using the yield displacement of each floor derived from pushover analysis, which provides insight into structural nonlinear behavior. In order to perform the pushover analysis in ETABS, concentrated plastic hinges were used to represent material nonlinearity at specific points in beams and columns, following the acceptance criteria outlined in ASCE 41-17 (ASCE, 2017). The nonlinear behavior characterization of these plastic hinges follows a standardized force-deformation relationship, as illustrated in Figure 3.4, where key behavioral points denote: 'a' (effective yield), 'b' (peak strength), and 'c' (residual strength). The analysis incorporates three critical performance levels: IO (Immediate Occupancy), LS (Life Safety), and CP (Collapse Prevention), which define the progressive degradation of structural capacity. Based on this behavioral framework, two-moment plastic hinges were assigned near the rigid zones at the ends of element, allowing for plastic hinge formation close to the joint faces. The beams were modeled with pure bending hinges while column hinges were modeled with axial force-bending moment interaction as introduced in Table-A II-1. The analyses continued until the displacement of the roof matched the predetermined target displacement, calculated using Equation 3.1 from ASCE 41-17 (ASCE, 2017) and presented in Table-A II-1. The yield displacement for each story, as outlined in Table-A II-1, is derived from an evaluation of the displacement-step curve of each storey obtained through pushover analysis in ETABS. This

yield displacement is subsequently used to conduct a nonlinear analysis of the MDOF structures in MATLAB.

Although stick models and elasto-plastic behavior offer significant computational efficiency and capture essential nonlinear characteristics for evaluating NSC demands in regular, symmetric buildings, they have limitations in capturing higher-order effects. The models may underestimate torsional effects and local deformations. Since the elasto-plastic assumption may not fully account for strain hardening, cyclic degradation, or P-delta effects, future studies should incorporate more realistic nonlinear behavior models beyond bilinear representations and explore a broader range of building case studies to strengthen the findings.

$$\delta_t = C_0 C_1 C_2 S_a \frac{T_e^2}{4\pi^2} g \tag{3.1}$$

In Equation 3.1, $\mathbf{C_0}$ represents the ratio of the roof displacement of the building to the maximum displacement of the equivalent single degree of freedom (SDOF) system, while $\mathbf{C_1}$ denotes the ratio of the maximum inelastic displacements of a bilinear elastic-perfectly plastic equivalent SDOF system to the displacements calculated for the linear elastic response of the same SDOF system. $\mathbf{C_2}$ accounts for the influence of pinched hysteretic shape, stiffness, and strength degradation on maximum displacement response. $\mathbf{S_a}$ represents the response spectrum acceleration, $\mathbf{T_e}$ denotes the elastic fundamental period of the bilinear approximation of the system, and **g** represents gravitational acceleration.

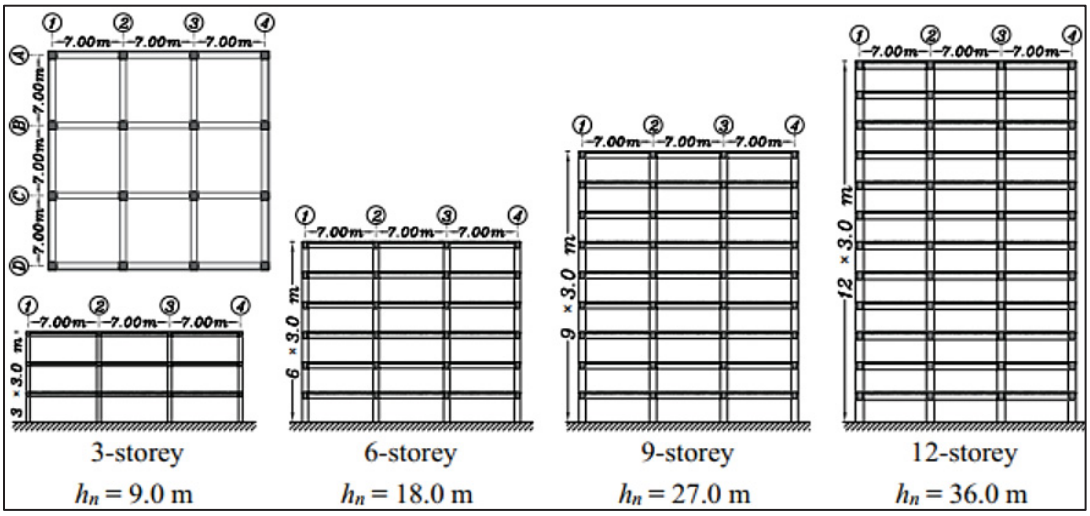

Figure 3.3 Plan and elevation views of the archetype reinforced concrete moment-resisting

Taken from Mazloom (2023, p. 62)

Table 3.3 The first three periods of the case study buildings

Case study	T_1(s)	T_2(s)	T_3(s)
3 Storey	0.973	0.279	0.182
6 Storey	1.014	0.321	0.189
9 Storey	1.354	0.441	0.261
12 Storey	1.468	0.279	0.182

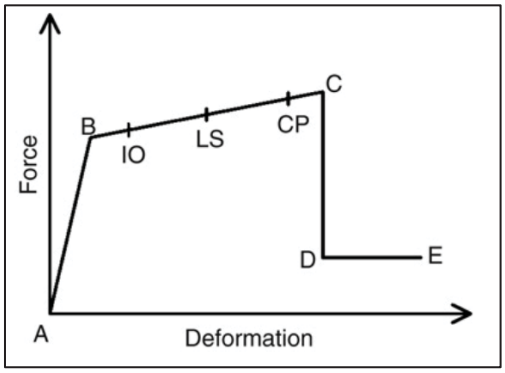

Figure 3.4 Force–deformation relationship of a typical plastic hinge
Taken from Wang et al. (2020, p. 5)

3.4 Description of the NSCs and their Modeling Assumptions

Light components with a mass less than 0.1% of the overall mass of the supporting structures (ranging from 303 to 3211 tonnes) were considered for uncoupled analysis (ASCE, 2000; Amin et al., 1971; Cunha et al., 2014; FEMA, 2013; A. Singh & Ang, 1974; Taghavi & Miranda, 2008).

The analyzed NSCs, presented as single-degree-of-freedom systems, are categorized into three groups corresponding to the fundamental periods (T_1, T_2, and T_3) of the archetype buildings,

as shown in Table 3.3, and are assumed to be attached at the rooftop, intermediate, and ground levels.

Aligning NSC periods with the building's fundamental modes (ranging from 0.97s to 1.47s) aims to maximize the seismic response amplification through resonance effects, thereby ensuring a conservative design analysis. This strategy captures realistic and frequently encountered scenarios in buildings, including tall storage rack systems(C. K. Chen et al., 1980), flexibly-mounted equipment such as medical devices, and suspended architectural or mechanical elements (Huang et al., 2013; Magliulo & D'Angela, 2024; Setareh, 2010; M. P. Singh et al., 2006).

For ground-level NSCs, structural amplification effects are negligible due to direct ground motion transmission. Accordingly, the period of 0.2 seconds was selected based on the NBC provisions S(0.2) for the seismic analysis of NSCs. An elasto-plastic behavior model was adopted for NSCs due to its computational efficiency and ability to capture essential nonlinear characteristics. This simplification is expected to slightly overestimate the seismic response of NSCs, providing conservative results for design purposes (A. K. Chopra & Chintanapakdee, 2004; Oropeza et al., 2010). Future studies should investigate more complex hysteretic models for NSCs to better capture their actual nonlinear behavior under seismic loading. In this analysis, four ductility levels were considered: elastic (μ_{comp}=1); low ductility (μ_{comp}=1.25); moderate ductility (μ_{comp}=1.5), and high ductility (μ_{comp}=2). These ductility levels were defined as the ratio of the maximum displacement of a bilinear elastoplastic system relative to its yield displacement ($\mu_{comp} = u_m/u_y$). To implement this, the equations of motion governing the dynamic response were solved numerically at each time step using the Newmark integration method with the linear acceleration approach (A. K. Chopra, 2011), employing parameters γ = 1/2 and β = 1/6, within a MATLAB script. This method was selected since it is widely recognized for its robustness in solving dynamic equations of motion. The equilibrium iterations were carried out to converge the displacement responses at each time increment, considering stiffness degradation and yield limits. Tangent stiffness was adjusted during the iterations to capture the changes from the linear to the nonlinear range. This approach aims to estimate the yield strength and ductility, thereby ensuring the most accurate acceleration demands possible. The discrepancies between obtained and target values of yield strength and

ductility were calculated across all iterations, serving as a quantitative measure for validating the analytical accuracy.

A modal damping ratio of 5% was adopted for all analyses. Previous investigations by Mehrjoo and Assi (2024) concluded that the sensitivity of seismic demands on NSC to variations in the damping ratio is minimal, confirming the reliability and robustness of the adopted approach.

3.5 Fragility Analyses and Performance Objectives of NSCs

The 24 earthquake recordings described in Section 3.2 are employed to perform nonlinear dynamic analyses. The IDA process involves scaling each record across a range of intensity levels, from 0.1g to 4.0g with increments of 0.1g. This is achieved by uniformly multiplying the entire accelerogram time history by a scale factor, thereby increasing all spectral ordinates while preserving the spectral shape of the records.

Given the study's focus on acceleration-sensitive NSCs, the damage index used in the IDA is determined based on the maximum absolute acceleration demands experienced by the NSCs within the archetype structures. Then, the evaluations and extraction of fragility curves for NSCs are conducted following Hazus guidelines, with four performance levels: slight, Moderate, Extensive, and complete damage levels (FEMA, 2012a). The fragility curve of a system represents the likelihood of exceeding a specified limit state (LS) at a given level of the seismic Intensity Measure (IM), as expressed in the Equation 3.2.

$$\text{Fragility} = P[\text{DM} \geq \text{LS} \mid \text{IM}] \tag{3.2}$$

Estimating the probability associated with a specific Intensity Measure (IM) value, denoted as IM = x, as expressed in Equation 3.2, can be achieved by utilizing a substantial number of earthquake simulations and analyses (Nsim) and determining the number of occurrences that lead to exceeding the considered limit state or capacity (N_{fail}), as outlined in the Equation 3.3.

$$P[\text{DM} \geq \text{LS} \mid \text{IM} = x] \cong \frac{N_{\text{fail}}}{N_{\text{sim}}} \tag{3.3}$$

Typically, a log-normal function is fitted to the resulting numerical fragility data to obtain the fragility curve, as illustrated in the Equation 3.4.

$$[\mathrm{DM} \geq \mathrm{LS} \mid \mathrm{IM} = x] = \Phi\left(\frac{\ln(x/\theta)}{\beta}\right) \tag{3.4}$$

In the aforementioned relationship, Φ() represents the standard normal cumulative distribution function, θ denotes the median of the fragility function, and β is the standard deviation of ln (IM = x). The lognormal distribution parameters were estimated using Maximum Likelihood Estimation (MLE), a widely adopted statistical method that optimizes probability distribution fit by maximizing the likelihood function. MLE was selected for this analysis due to its proven efficiency in parameter estimation for lognormal distributions, particularly for large datasets, as demonstrated in previous statistical studies (Basak et al., 2009; Cohen & Whitten, 1980). Table 3.4 presents the specified performance levels and corresponding acceleration thresholds for acceleration-sensitive NSCs.

Table 3.4 Peak floor accelerations used to define median values of damage to acceleration-sensitive NSCs

Taken from Hazus-MH 2.1 (2012a, pp. 15–68)

Seismic design level	**Floor acceleration at the threshold of nonstructural damage (g)**			
	Slight	**Moderate**	**Extensive**	**Complete**
Moderate	0.25	0.50	1.00	2.00

3.6 Computation of NSC Seismic Acceleration Demands at Different Ductility Levels

The section investigates the influence of ductility and the resonance condition on PFA (g), particularly focusing on resonance with the first three fundamental modes of the structures, when using $T_c/T_1=1$, $T_c/T_2=1$, and $T_c/T_3=1$. The probability of exceeding specific damage states is evaluated in terms of PFA intensity. The seismic demands on acceleration-sensitive NSCs were computed using both historical and synthetic ground motion records. Results are provided for the roof, and ground levels, as well as selected intermediate floors: level 6 in the 12-storey building, levels 4 and 5 in the 9-storey building, and level 3 in the 6-storey building. The first subsection investigates how the attachment ductility and resonance conditions influence the fragility curves of NSCs attached to elastic structures while the second subsection

focuses on the nonlinear structures. The fragility curves, shown in Figure 3.5 and Figure 3.6, present the probability of exceeding the specific damage states as a function of PFA intensity. Each subplot displays 16 curves corresponding to four distinct ductility levels (μ_{comp}=1, 1.25, 1.5, 2) across the four damage states of slight, moderate, extensive, and complete. Finally, Table 3.5 and Table 3.6 present the mean values of PFA (g) for a probability of exceedance of 50% on elevated floors, alongside the average ratios of nonlinear/linear PFA (g) values. Additionally, Table 3.7 provides the mean values of Sa (g) for the same probability of exceedance at the ground level across the four considered damage states.

3.6.1 Fragility Curves and Damage States of Acceleration-Sensitive NSCs Mounted on Elastic Structures

Figure 3.5 (a-f) presents the fragility curves for NSCs mounted on elastic structures. Subplots Figure 3.5 (a), 3-5 (c), and 3-5 (e) show responses at the roof level, while Subplots 3-5 (b), 3-5 (d), and 3-5 (f) represent the responses at intermediate levels. Each subplot corresponds to resonance with the building's first three modes, specifically T_c/T_1=1, T_c/T_2 =1, and T_c/T_3=1, respectively. In addition, Figure 3.5 includes the ground-level responses for NSCs with a spectral period of 0.2s.

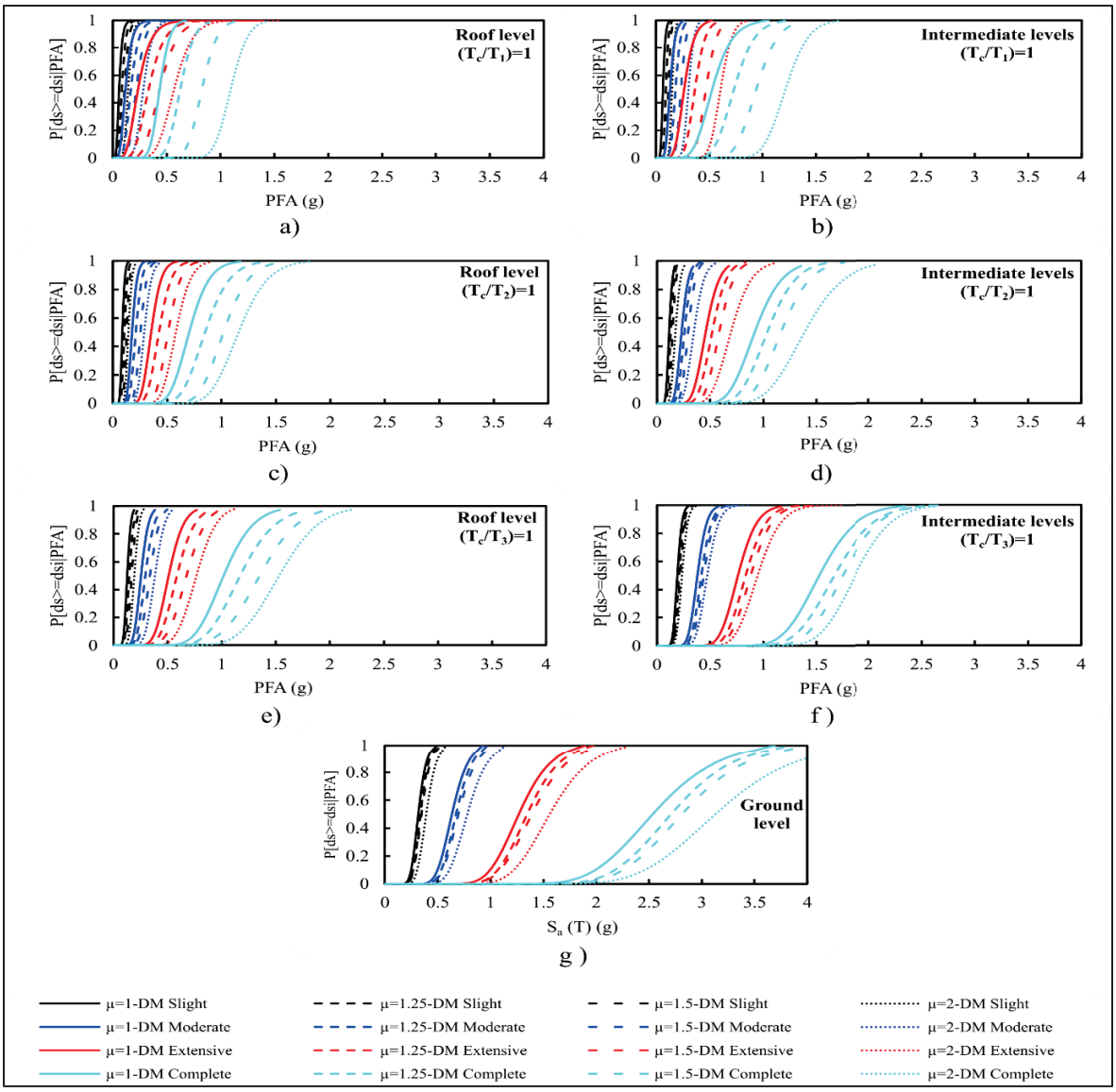

Figure 3.5 Seismic fragility curves for NSCs across various ductility levels and damage states under different resonance conditions in elastic structures: a) roof level (T_c/T_1=1), b) intermediate level (T_c/T_1=1), c) roof level (T_c/T_2=1), d) intermediate level (T_c/T_2=1), e) roof level (T_c/T_3=1), f) intermediate level (T_c/T_3=1), and g) at ground level

Figure 3.5 (a,b) shows that the probability of exceeding a given damage state is, on average, 10% higher at roof levels compared to intermediate levels, indicating a greater vulnerability of NSCs located at higher levels. As the resonance periods shift from T_1 in Figure 3.5 (a,b) to T_2 in Figure 3.5 (c,d), the PFA demand for a specific probability of exceeding a given damage state increases, on average, by 40% for intermediate levels and by 11% for roof levels.

Additionally, when resonance periods shift from T_2 to T_3 (Figure 3.5 (e,f)), the PFA demand to exceed a damage state increases by about 50% for both roof and intermediate levels. These trends indicate that the probability of exceeding a given damage state decreases at higher resonance periods. This is particularly noticeable at roof levels, where acceleration demand to exceed a damage state increases substantially (11% to 50%), compared to intermediate levels (40% to 50%).

Comparatively, Figure 3.5 (g) illustrates that at ground level, the acceleration demand to exceed a damage state increases on average by 80% compared to the T_3 resonance range and by 100% compared to the T_2 resonance range. This further emphasizes the influence of elevation on increasing acceleration demands under seismic loading. When considering the effect of ductility levels of attachment of NSCs on their performance, Figure 3.5 reveals another trend across different resonance ranges. For the T_1 resonance range at the roof level, the peak floor acceleration demand to exceed a given damage state increases on average by 144% when moving from elastic NSCs behavior to high ductility NSCs behavior, while at the intermediate level, the average increase is 130%. This trend is consistently observed across all damage states. For the T_2 resonance range at the roof level, the peak floor acceleration demand to exceed a given damage state increases on average by 130% when moving from an elastic NSC behavior to a high ductility NSC behavior. On the other hand, at intermediate levels within the T_2 resonance range, peak floor acceleration demand increases by 50% across all damage states. For the T_3 resonance range, transitioning from elastic to high ductility NSCs behavior results in more modest increases in the peak floor acceleration demand required to exceed a given damage state, averaging 50% at the roof levels and 20% at the intermediate levels. At ground level, transitioning from elastic to high ductility NSCs behavior leads to an average 20% increase in spectral acceleration demand across all damage states. Overall, these findings indicate that while higher ductility levels of NSCs increase the acceleration demand required to exceed a given damage state, this effect becomes less pronounced as the resonance range shifts from T_1 to T_2 and T_3. Additionally, as observed in Figure 3.5 (a,b), the fragility curves of highly ductile NSCs at the slight damage state align closely with those for elastic NSCs at the moderate damage state, highlighting the beneficial impact of ductility in reducing damage likelihood under comparable seismic intensities.

This correlation also holds for the fragility curves of highly ductile NSCs in the moderate damage state, which resemble those of elastic NSCs in the extensive damage state. Furthermore, the fragility curves of highly ductile NSCs in the extensive damage state align with those of elastic NSCs in the complete damage state. The slope of fragility curves, also referred to as cumulative distribution functions (CDFs), at any specific point corresponds to the probability density function (PDF). As the probability density increases, the likelihood of a specific peak floor acceleration value triggering the respective damage state becomes higher. In this context, the fragility curves exhibit steeper slopes for the slight and moderate damage states, particularly within the T_1 and T_2 resonance ranges. Conversely, as we progress to the extensive and complete damage states, the fragility curves flatten, particularly in the T_3 resonance range and at the ground level.

In conclusion, while higher ductility levels in the attachments of NSCs enhance energy dissipation, they also increase the likelihood of potential damage to these components.

3.6.2 Fragility Curves and Damage States of Acceleration-Sensitive NSCs for Acceleration Mounted on Nonlinear Structures

Figure 3.6 (a-f) illustrates the fragility curves for NSCs mounted on nonlinear structures, showing the relationship between peak floor acceleration demand and damage states across various ductility levels and resonance periods (T_1, T_2, T_3). Ground-level NSCs are not included here, as their response is independent of the building's structural behavior and was already presented in Figure 3.5 (g). Subplots Figure 3.6 (a), Figure 3.6 (c), and Figure 3.6 (e) show responses at the roof level, while subplots Figure 3.6 (b), Figure 3.6 (d), and Figure 3.6 (f) represent intermediate levels corresponding to resonance with the building's first three modes.

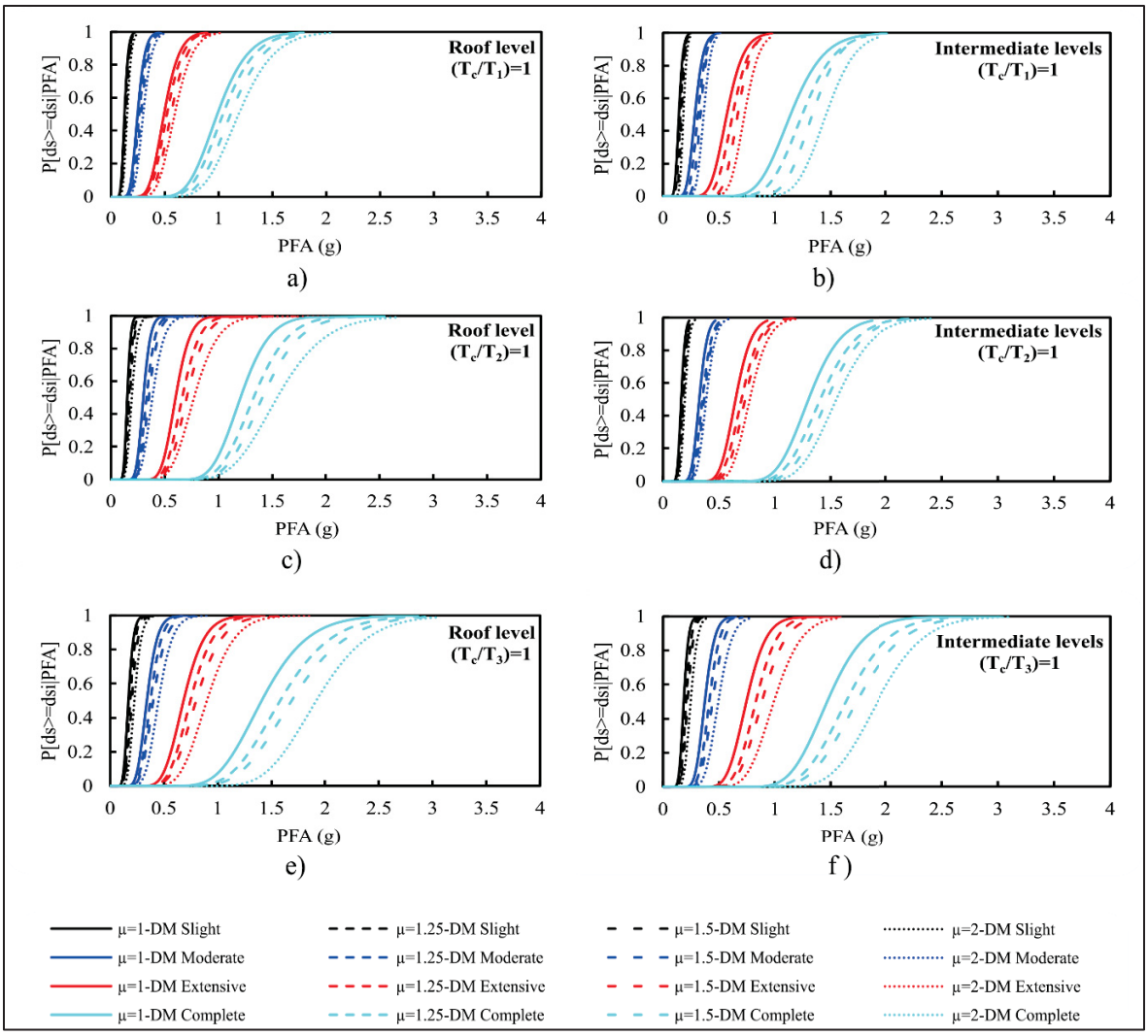

Figure 3.6 Seismic fragility curves for NSCs across various ductility levels and damage states under different resonance conditions in the nonlinear structures: a) roof level (T_c/T_1=1), b) intermediate level (T_c/T_1=1), c) roof level (T_c/T_2=1), d) intermediate level (T_c/T_2=1), e) roof level (T_c/T_3=1), f) intermediate level (T_c/T_3=1)

These fragility curves show a higher probability of exceeding damage states at the roof levels than at the intermediate levels. In addition, the fragility curves for nonlinear structure in Figure 3.6 (a,b) show a reduced probability of exceeding damage states at the roof and intermediate levels compared to those of the elastic structure as seen in Figure 3.5. This comparison emphasizes the significance of considering the actual nonlinear behavior of supporting structures in the probabilistic analysis of NSCs. The peak floor acceleration demand for a

specific probability of exceeding a given damage state exhibits a distinct pattern as the system transitions from resonance periods T_1 to T_3, particularly for nonlinear structures (Figure 3.6) compared to their elastic counterparts (Figure 3.5). For nonlinear structures, the peak floor acceleration demand decreases by 14% from T_1 to T_2 resonance range for intermediate floors and by 21% for the roof. In contrast, for elastic counterparts, the decrease is more pronounced, 40% for intermediate floors and 11% for the roof.

However, shifting from T_2 to T_3 resonance range shows a smaller increase for the peak floor acceleration demand to exceed a damage state for nonlinear structures (14%) compared to elastic ones (50%). This finding further confirms that the probability of exceeding damage states decreases at higher resonance periods for NSC attached to nonlinear structures.

A key observation from the fragility curves corresponding to nonlinear structures presented in Figure 3.6 is that they exhibit flatter curves compared to the elastic structures shown in Figure 3.5. Despite this overall flattening, the slopes of the fragility curves for the slight and moderate damage states are steeper than those for extensive and complete damage states shown in Figure 3.6 for nonlinear structures. This indicates that, even in the case of nonlinear structures, there is a higher probability density associated with the peak floor acceleration values corresponding to the slight and moderate damage levels. Consequently, this suggests an increased likelihood of these NSCs reaching damage states when subjected to given peak floor accelerations. The peak floor acceleration demand required to exceed a damage state in nonlinear structures gradually increases as the NSCs shift from elastic to highly ductile. Specifically, for the T_1 resonance range, the NSCs at the roof and intermediate levels exhibit an average increase in peak floor acceleration demand to exceed a damage state by 20% and 28%, respectively, significantly lower than the 144% and 130% observed in their elastic counterpart. The T_2 resonance range follows a similar trend, with the NSCs experiencing increases in peak floor acceleration demand to exceed a damage state by an average of 16% at the roof level and 26% at the intermediate level, notably lower than the 130% and 50% increases seen in the elastic structure. In the T_3 resonance range, peak floor acceleration demand to exceed a damage state increases by an average of 35% for NSCs at both roof and intermediate levels in the nonlinear structure, while the elastic structure saw increases of 50% at the roof and 20% at the intermediate level. These findings for nonlinear structures reinforce the previously observed

trend in elastic structures, where increasing the ductility levels of NSCs increases peak floor acceleration demand to exceed a damage state, with this effect decreasing as the resonance range shifts from T_1 to T_2 and T_3.

3.6.3 Comparison of the mean acceleration demands for different damage states in Elastic and nonlinear Structures

To assess the impact of nonlinear structural behavior on the seismic demands of NSCs across different damage states, and how this deviates from the elastic behavior typically assumed in design codes, the mean peak floor acceleration values, PFA(g)(T), for a 50% exceedance probability of each damage state (slight, moderate, extensive, and complete) are presented in Table 3.5 and Table 3.6, derived from Figure 3.5 and Figure 3.6. Additionally, Table 3.5 and Table 3.6 include a factor representing the average ratios of nonlinear/linear PFA (g), which quantifies the difference between linear and nonlinear structure models for each ductility level and damage state.

Table 3.5 Mean values of PFA (g)(T_c/T_{1-3}=1) IM at 50% possibility of exceedance of the slight and moderate damage state (DS) in elevated floors

			Slight DS			**Moderate DS**		
Resonance range (T)	**μ_{comp}**	**Specific location level**	Elastic structure	Nonlinear structure	Average nonlinear/ linear	Elastic structure	Nonlinear structure	Average nonlinear/ linear
T_1	1	Intermediate	0.066	0.143	2.16	0.13	0.29	2.16
		Roof	0.059	0.126		0.12	0.25	
	1.25	Intermediate	0.092	0.156	1.65	0.18	0.32	1.66
		Roof	0.083	0.133		0.17	0.26	
	1.5	Intermediate	0.12	0.167	1.34	0.24	0.33	1.32
		Roof	0.11	0.142		0.22	0.28	
	2	Intermediate	0.15	0.182	1.15	0.3	0.37	1.14
		Roof	0.14	0.151		0.28	0.298	
T_2	1	Intermediate	0.115	0.16	1.83	0.23	0.33	1.85
		Roof	0.066	0.15		0.132	0.3	
	1.25	Intermediate	0.13	0.176	1.6	0.26	0.35	1.57
		Roof	0.092	0.17		0.183	0.33	
	1.5	Intermediate	0.146	0.18	1.38	0.29	0.37	1.39
		Roof	0.118	0.18		0.235	0.35	
	2	Intermediate	0.174	0.19	1.17	0.35	0.39	1.2
		Roof	0.152	0.19		0.304	0.39	
T_3	1	Intermediate	0.191	0.186	1.155	0.38	0.37	1.17
		Roof	0.127	0.17		0.25	0.34	
	1.25	Intermediate	0.2	0.207	1.16	0.41	0.41	1.12
		Roof	0.146	0.187		0.3	0.37	
	1.5	Intermediate	0.22	0.22	1.09	0.44	0.44	1.14
		Roof	0.17	0.2		0.34	0.4	
	2	Intermediate	0.23	0.25	1.15	0.47	0.5	1.12
		Roof	0.19	0.23		0.38	0.45	

Table 3.6 Mean values of PFA (g) (T_c/ T_{1-3}=1) IM at 50% possibility of exceedance of the extensive and complete damage state(DS) in elevated floors

			Extensive DS			**Complete DS**		
Resonance range (T)	**μ_{comp}**	**Specific location level**	Elastic structure	Nonlinear structure	Average nonlinear/ linear	Elastic structure	Nonlinear structure	Average nonlinear/ linear
T_1	1	Intermediate	0.26	0.57	1.78	0.53	1.14	2.085
		Roof	0.23	0.49		0.43	0.99	
	1.25	Intermediate	0.37	0.62	1.63	0.73	1.25	1.91
		Roof	0.33	0.52		0.63	1.04	
	1.5	Intermediate	0.47	0.67	1.36	0.94	1.33	1.26
		Roof	0.43	0.56		0.83	1.11	
	2	Intermediate	0.61	0.73	1.24	1.21	1.46	1.03
		Roof	0.57	0.59		1.1	1.19	
T_2	1	Intermediate	0.46	0.65	2.03	0.92	1.3	1.79
		Roof	0.264	0.6		0.528	1.2	
	1.25	Intermediate	0.519	0.7	1.63	1.04	1.4	1.63
		Roof	0.367	0.66		0.733	1.32	
	1.5	Intermediate	0.584	0.73	1.34	1.17	1.47	1.41
		Roof	0.471	0.7		0.941	1.41	
	2	Intermediate	0.697	0.77	1.24	1.39	1.55	1.2
		Roof	0.608	0.77		1.22	1.55	
T_3	1	Intermediate	0.76	0.74	1.11	1.52	1.47	1.22
		Roof	0.51	0.68		1	1.41	
	1.25	Intermediate	0.83	0.83	1.01	1.66	1.64	1.2
		Roof	0.59	0.75		1.17	1.58	
	1.5	Intermediate	0.88	0.88	1.17	1.74	1.74	1.14
		Roof	0.68	0.8		1.35	1.69	
	2	Intermediate	0.94	0.99	1.065	1.87	1.92	1.23
		Roof	0.77	0.9		1.53	1.92	

The results from Table 3.5 and Table 3.6 indicate a trend across various ductility levels for different damage states. Specifically, as the ductility of NSCs increases, the average nonlinear/linear ratio tends to decrease for all periods within the resonance range. Notably, this trend remains consistent across all damage states, suggesting that the transition from elastic to nonlinear structural behavior has a relatively uniform impact across the resonance ranges (T_1, T_2, and T_3). This observed trend for the average nonlinear/linear ratio across all damage states is particularly pronounced in the T_1 range, where it decreases from 2.1 to 1.1 as the ductility of attachment of NSCs shifts from elastic to highly ductile. A similar trend is observed in the T_2 range, where the factor drops from 1.88 to 1.2 as the ductility of attachment of NSCs shifts from elastic to highly ductile. In the T_3 range, the decrease is less pronounced, with the average nonlinear/linear ratio dropping slightly from 1.16 to 1.14 as the ductility of attachment of NSCs shifts from elastic to highly ductile. It is worth noting that while this study mainly focuses on

the influence of the first three fundamental modes (T_1, T_2, T_3), it is important to recognize that higher modes may play a more significant role in taller buildings or structures with different dynamic characteristics. Nevertheless, the observed trends in this study, such as the diminishing impact of higher modes (T_2 and T_3) compared to T_1 and the decreasing nonlinear/linear ratios at these modes, suggest that modes beyond T_3 are likely to contribute less significantly to the considered reinforced concrete building models.

Overall, low to moderate NSC ductility levels are most effective, while further increases in ductility yield minimal reductions in peak floor acceleration demands.

Moreover, the influence of ductility on the seismic demands of NSCs is more pronounced at the first fundamental resonance period and the observed impact tends to diminish for higher modes. This trend has important implications for how NSCs should be designed, particularly when considering seismic demand reduction and ductility requirements. The observed reduction in acceleration demands due to structural nonlinearity has significant implications for current code provisions. The NBC 2020 and similar international codes typically employ elastic analysis assumptions when determining NSC design forces. This assumption simplifies the complex structural response during seismic events but does not capture the potential inelastic deformations that may occur in real-world scenarios. The findings of this study demonstrate that this approach can lead to conservative design requirements, particularly for components with periods matching the structure's fundamental modes.

Analysis of the average nonlinear/linear ratios across different damage states reveals that elastic code assumptions may result in overestimation of seismic demands by factors ranging from 1.1 to 2.1 (Table 3.5 and Table 3.6). This overestimation is most pronounced in the following scenarios:

- Components with periods matching T_1, where elastic assumptions overestimate demands by up to 115% for elastic NSCs (μ_{comp}=1).
- Upper floor installations, particularly at roof levels, where the difference between elastic and nonlinear predictions is most pronounced.
- Lower ductility components, where the disparity between elastic code predictions and actual nonlinear behavior is most significant.

These overestimations can lead to over-designed and potentially more expensive NSC installations, as the design forces derived from elastic analysis are generally higher than those experienced in a nonlinear structure. However, these findings complement, rather than contradict, current code approaches by providing deeper insight into the actual behavior of designed structures under seismic loading. Similarly, to assess the impact of ductility on the seismic demands of NSCs at the ground level, across different damage states, the mean spectral acceleration values, Sa(g)(T), corresponding to a 50% exceedance probability of a damage state (slight, moderate, extensive, and complete) are presented in Table 3.7. These values are derived from Figure 3.5 (g).

Table 3.7 Mean values of Sa(g)(T) IM at 50% possibility of exceedance of all damage state(DS) at the ground level

μ_{comp}	Slight DS	Moderate DS	Extensive DS	Complete DS
1	0.317	0.64	1.27	2.55
1.25	0.338	0.67	1.35	2.71
1.5	0.349	0.698	1.39	2.82
2	0.39	0.78	1.56	3.13

These observations further underscore the importance of considering the nonlinear behavior of buildings when evaluating the seismic demands on NSCs, as they provide a more accurate representation of the seismic force demands exerted on NSCs under varying levels of ductility and damage states.

3.7 Conclusion

This study provides a detailed analysis of the fragility of NSCs subjected to seismic loading, investigating the effects of ductility levels of NSC attachments and resonance period ranges (T_1, T_2, T_3) on their performance. Also, it examines the impact of the nonlinear behavior of the supporting structures on the probability of exceeding specific damage states for NSCs. The key findings of this research are summarized as follows:

- **Effect of Height:** NSCs at roof levels are significantly more vulnerable to seismic damage compared to those at intermediate or ground levels.
- **Impact of Resonance Periods:** As resonance shifts from the fundamental resonance period T_1 to higher ones (T_2, T_3), the seismic behavior of NSCs changes significantly. This shift results in reduced sensitivity to structural nonlinearity and attachment ductility, particularly in taller buildings.
- **Attachment Ductility:** While increased ductility levels reduce seismic forces, they may also increase the risk of localized damage to NSCs and their attachments. Therefore, achieving an optimal balance between ductility and acceptable damage levels is critical in NSC seismic design.
- **Structural Nonlinearity:** Accounting for the nonlinear behavior of the supporting structure is essential for improving the accuracy of probabilistic seismic assessments of NSCs. This consideration affects acceleration demands consistently across damage states and resonance ranges, simplifying seismic design provisions for NSCs.

To bridge the gap between current code provisions and the actual seismic performance of NSCs, it is essential to refine the component-specific response modification factor (Rp), that reflects the level of ductility of NSC attachments. Additionally, considering the nonlinear behavior of supporting structures would additionally enhance the accuracy of seismic demand predictions.

Extending performance-based design principles to NSCs and embedding fragility-based performance objectives into building codes represents a transformative approach to improving post-earthquake functionality and resilience. This approach links damage states to ductility levels, thereby enhancing the reliability of seismic design and performance predictions and ensures that NSCs are better equipped to withstand real-world seismic events. For acceleration-sensitive NSCs, adopting moderate ductility levels ($\mu_{comp} \approx 1.5$) provides an effective design target. This approach offers a well-balanced solution that reduces seismic demands while ensuring cost efficiency and resilience, avoiding both excessive over-design and undue risk of failure.

FOREWORD TO CHAPTER 4

To support the interpretation of the results presented in this chapter, the following methodological assumptions and specific limitations are provided. These points contextualize the scope and applicability of the derived loss estimates:

1. **Ground Motion Variability:** The use of ground motions spectrally matched to the Uniform Hazard Spectrum (UHS) reduces record-to-record variability compared to methods like Conditional Mean Spectrum (CMS) selection. While consistent with NBC 2020 design practice, this approach may underestimate the dispersion (uncertainty) in the resulting seismic demands and loss estimates.
2. **Idealized Component Modeling:** The parametric NSC models represent idealized frequency-ductility combinations. They do not account for installation-specific irregularities (e.g., uneven grid spacing in ceilings or imperfect anchorage installation), which could introduce additional failure modes observed in field reconnaissance reports.
3. **Structural Modeling Simplification:** The buildings are simulated using lumped-mass "stick models" with bilinear hysteretic behavior. While sufficient for capturing global displacement and acceleration profiles, this approach does not capture local element-level failures (e.g., beam-column joint shear) that could locally alter floor accelerations.
4. **Economic Assumptions:** The repair cost ratios and replacement values used in the consequence functions are adopted from the FEMA P-58 normative data (PACT database), adjusted for inflation and applicability to the Montreal, Quebec, context where necessary. It is assumed that repair costs for the studied components (suspended ceilings and chillers) are not affected by the extent of structural damage, an assumption valid for the design-level performance targeted in this study, where the moderately ductile RC frames are expected to undergo controlled yielding without structural collapse, and NSC damage is governed by floor accelerations rather than structural drift.

CHAPTER 4

SEISMIC VULNERABILITY ASSESSMENT OF DUCTILE LIGHT NSCS IN MODERATELY DUCTILE RC FRAME BUILDINGS

Majid Mehrjoo[a] and Rola Assi[b]

[a,b] Department of construction engineering, École de technologie supérieure (ÉTS), Montreal, Quebec, H3C 1K3, Canada

Paper submitted for publication in Journal of Urban Resilience and Earthquake Engineering[3], January 2026

Abstract

This study evaluates the seismic vulnerability of acceleration-sensitive non-structural components (NSCs), specifically suspended ceilings and chillers, in four moment-resisting buildings. Incremental Dynamic Analysis was performed with scaled ground-motion records and the FEMA P-58 framework was applied to estimate NSC losses.

Enhanced NSC configurations demonstrated improved seismic performance: wire-braced suspended ceilings increased damage-initiation thresholds by 3–5 times, and seismically restrained chillers achieved 1.3 times higher thresholds. Repair costs for suspended ceilings were reduced by up to 95% and those for chillers by 17%. Moderate-ductility variants further reduced repair costs by 30% relative to low-ductility variants. Results highlight the role of ductility in performance-based seismic design.

Keywords: non-structural components, attachment ductility, performance-based seismic assessment, incremental Dynamic Analysis, fragility function, FEMA P-58 loss assessment

---

[3] Submission ID: 258722354.R1

4.1 Introduction

Non-structural components (NSCs) account for the majority of a building's investment cost, representing approximately 70% of the total construction costs (Miranda & Taghavi, 2005; Rojas et al., 2023). These components can be classified into three main groups (Assi et al., 2016; CSA, 2014c): (1) architectural components (e.g., suspended ceilings, external cladding, and partition walls), (2) building services components (e.g., mechanical, plumbing, electrical, and telecommunication devices), and (3) building content (e.g., furniture and office equipment).

Despite their significant economic value, NSCs have proven to be particularly vulnerable during seismic events. Post-earthquake reconnaissance has consistently documented NSC vulnerability across major seismic events, beginning with the systematically documented 1971 San Fernando earthquake and extending through the 1994 Northridge, 1995 Kobe, 2010 Maule (Chile), and 2023 Turkey-Syria earthquakes (Esper & Tachibana, 1998; Lew et al., 1971; Miranda et al., 2012; Naeim, 2004; Tapia-Hernández et al., 2025). These investigations have shown that NSCs sustain damage at lower ground motion intensities than the main structural system, often resulting in occupant injuries, obstructed egress routes, and delayed rescue efforts.

Such losses are not limited to poorly designed structures; even in code-compliant buildings, the failure of NSCs has driven substantial repair costs and business interruptions (Goulet et al., 2007). For instance, Zeng et al. (2016) documented that exterior walls, partition systems, and ceiling installations suffered loss ratios of approximately 35% (repair cost/replacement cost of the building) across various case study buildings. Similarly, Anwar et al. (2018) reported that, although only 3.5–11% of NSCs in a tall building located in Manila and 2.7–4.7% in a similar building in Bangkok were damaged, the affected components were operation-critical, resulting in repair costs and functional disruptions that far exceeded their small share of the overall inventory. These findings highlight the need to quantify floor-level acceleration demands on NSCs as a prerequisite for performance-based design and for identifying the components most susceptible to failure (Assi et al., 2016; CSA, 2014c; Ghasemof et al., 2022; Mehrjoo & Aval, 2024).

The seismic response and associated economic losses of NSCs are primarily governed by two key parameters: natural frequency and component attachment ductility (Fierro et al., 2011; Magliulo & D'Angela, 2024; Zeng et al., 2016).

Nevertheless, many studies have assumed that suspended ceilings, mechanical equipment, and other NSCs exhibit similar ductility and frequency response characteristics, despite their fundamentally different attachment configurations, dynamic properties, and failure mechanisms (Kawakatsu et al., 1979; Lin & Mahin, 1985; Soong et al., 1993; Viti et al., 1981). Current design approaches partially account for ductility through the component response modification factor (R_P), which reduces design forces for components with ductile attachments. However, these code-prescribed R_P values have significant limitations: they do not reflect actual component ductility, fail to differentiate between different types of NSC, and do not account for the complex nonlinear behavior that governs damage progression and repair costs (ASCE, 2023; Anajafi, 2018; ATC, 2018b; A. Kazantzi et al., 2018; Miranda et al., 2018; Villaverde, 2006; Vukobratović & Fajfar, 2017; T. Wang et al., 2021).

Highlighting these limitations, recent studies have shown that components with moderate to high attachment ductility consistently experience 40–60% less damage, and consequently lower repair costs, compared to components with elastic attachments, particularly under resonance conditions (ASCE, 2022; Lin & Mahin, 1985; Mehrjoo & Assi, 2024; NRC, 2015; Taghavi & Miranda, 2012).

In addition, experimental and analytical studies have demonstrated that measures such as additional bracing, internal gaps, and energy-dissipating connections can significantly reduce damage to components such as suspended ceilings and mechanical equipment (Bianchi et al., 2019; Brandolese et al., 2019; Ciurlanti et al., 2022; Dhakal et al., 2016; Gallo et al., 2018; Pürgstaller et al., 2020; Rojas et al., 2023; Ryu & Reinhorn, 2019). However, important knowledge gaps remain. Although enhanced detailing has been shown to reduce seismic demands and failure probabilities by 30–40%, the combined effects of attachment ductility, enhanced connection details, and structural nonlinearity on financial losses in code-conforming buildings remain insufficiently understood (Ciurlanti et al., 2022; Preti & Bolis, 2017).

Among NSCs, suspended ceilings and rooftop chillers were selected for this study due to their fundamentally different risk profiles (life-safety hazards from falling ceiling components versus functionality risks from HVAC shutdowns) and their significant involvement in seismic building damage (ASCE, 2022; ATC, 2012; Dhakal et al., 2016; OSHPD, 2020; Pourali et al., 2014; Qi et al., 2023; Rezvani et al., 2022; Schultz et al., 2003).

Suspended ceilings endanger occupants through falling tiles and grid components that can cause injuries, obstruct egress routes, and disrupt operations, with failures documented at peak floor accelerations as low as 0.3-0.6g during the Canterbury and Northridge earthquakes (Brandolese et al., 2019; Dhakal et al., 2016; Pourali et al., 2017; Soroushian et al., 2016).

In contrast, rooftop chillers rarely cause direct occupant injuries but can shut down HVAC systems, render buildings inoperable, and force costly evacuations, particularly in critical facilities such as hospitals or data centers. This impact was evidenced during the Northridge earthquake, where nonstructural damage, including mechanical system failures, was the primary evacuation reason in eight of 91 hospitals (ASCE, 2022; OSHPD, 2020; Schultz et al., 2003).

The study of these two components offers valuable insights into cost-effective attachment strategies that ensure occupant safety and continuous building functionality.

Consequently, this study expanded the existing literature by investigating the influence of attachment ductility and frequency characteristics on the seismic vulnerability of acceleration-sensitive NSCs. The specific objectives were to (a) quantify variations in repair costs across different levels of attachment ductility and frequency ranges under varying seismic intensities, (b) establish performance-based selection criteria that correlate ductility-frequency combinations with expected damage reduction, and (c) develop cost-benefit frameworks for comparing conventional versus enhanced attachment systems.

The investigation employed nonlinear dynamic analysis combined with the FEMA P-58 methodology to quantify seismic vulnerability and associated repair costs for acceleration-sensitive NSCs. The assessment was conducted using four archetype multi-story reinforced concrete (RC) buildings subjected to 24 ground motion records, scaled to Montreal's Uniform Hazard Spectrum. By focusing on financial loss outcomes rather than solely on engineering

demand parameters (EDPs), this approach provides practical insights for performance-based seismic design decisions (FEMA, 2012b, FEMA, 2018a).

While this study focused on direct NSC repair costs, it is acknowledged that indirect losses, such as business downtime and loss of building functionality, may substantially contribute to total economic impacts. However, these aspects were beyond the scope of this investigation.

Fig. 1 presents a flowchart outlining the comprehensive methodology employed in this study, from building modeling through seismic performance loss assessment.

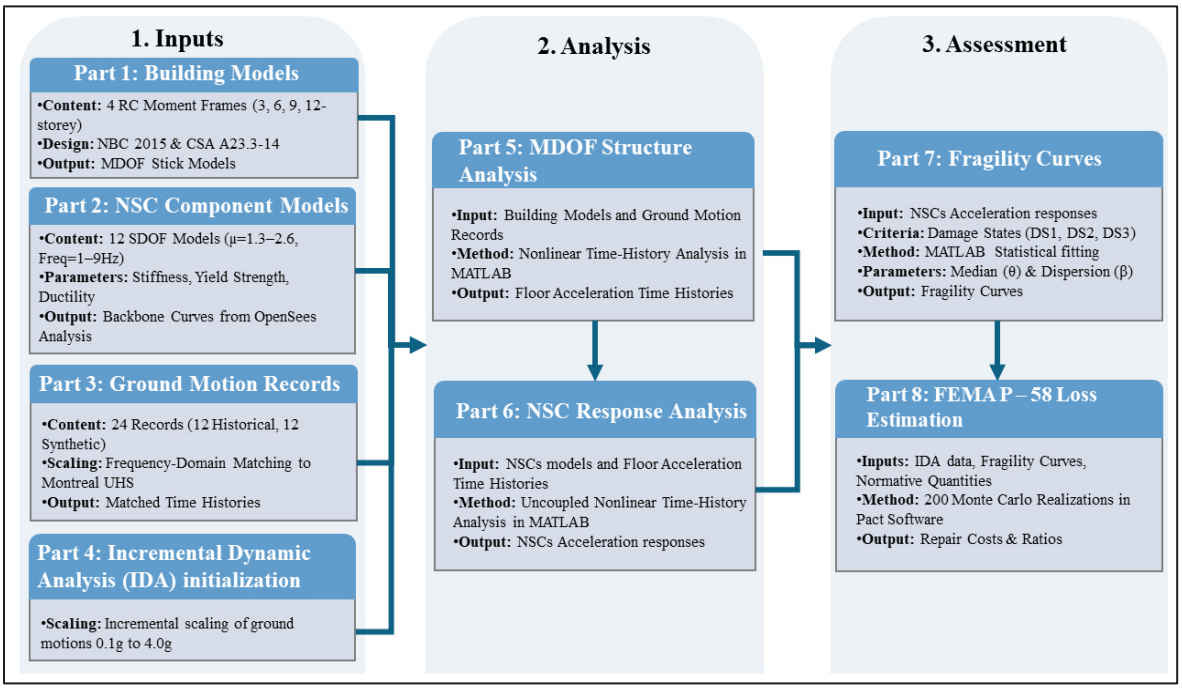

Figure 4.1 Methodology Framework for the seismic vulnerability analysis of the NSCs

4.2 Selection and scaling of input ground motion data

Twenty-four ground motion records were utilized for nonlinear dynamic analysis, consisting of 12 historical records selected from the PEER NGA-East database and 12 synthetic accelerograms sourced from Atkinson's database (2009). All records were spectral-matched to Montreal's Uniform Hazard Spectrum (UHS) for very dense soil and soft rock (NBC Site Class C) corresponding to a 2,475-year return period.

Spectral matching was performed using a frequency-domain method (Fahjan & Ozdemir, 2008). This was selected because it preserves the non-stationary characteristics of the original records (phase, duration, pulse content) while achieving close agreement with the target spectrum (Gascot & Montejo, 2014).

UHS matching was adopted for consistency with NBC 2020 seismic design practice. While this approach reduces record-to-record variability compared to Conditional Mean Spectrum (CMS) selection, it ensures that all NSC variants experience consistent spectral content. For comparative assessment of frequency-ductility effects, this consistency isolates the parameters of interest and ensures that observed performance differences are attributable to component characteristics rather than ground motion variability. Further details on the selection criteria, hazard characterization, and spectral matching procedures were provided in Mehrjoo and Assi (2025a).

Incremental Dynamic Analysis (IDA) was employed to develop fragility curves and assess the seismic capacity of acceleration-sensitive NSCs, as shown in ANNEX IV. In the IDA procedure, each ground motion record was incrementally scaled from 0.1g to 4.0g in steps of 0.1g. The scaling involved multiplying the entire accelerogram by a constant factor, ensuring uniform increases in spectral ordinates without altering the spectral shape. The upper limit of 4.0g was determined iteratively to ensure that even the most seismically resistant components (specifically the M4c model) at the top and intermediate floors, where the NSCs are located in this study (see Figure 4.2), reached complete failure probabilities (100% probability of exceeding the highest damage state). As floor acceleration responses approach horizontal asymptotes in the 3.0g–4.0g range due to structural yielding (see ANNEX IV, Figure-A IV-1–Figure-A IV-4), this upper-bound input intensity was necessary to capture the full failure probability of the high-capacity components.

4.3 Description of the case study buildings and their modeling assumptions

This study examined four moderately ductile RC moment-resisting frames (3-, 6-, 9-, and 12-stories) with symmetric configuration, featuring three 7-meter bays in both directions and 3-meter story heights. The buildings were designed according to NBC 2015 (NRC, 2015) and

CSA A23.3-14 (CSA, 2014b) specifications, as documented in Mazloom and Assi (2022). The corresponding structural properties and modeling parameters are summarized in Table-A I-1 (ANNEX I).

The nonlinear modeling approach adopted for this research utilized a lumped-mass multi-degree-of-freedom (MDOF) stick model. First, pushover analysis was performed using the ETABS software (CSI 2017) to characterize the story-level capacity curves, assuming bilinear elastoplastic behavior with concentrated plastic hinges at beam and column locations following ASCE 41-23 (ASCE 2023) acceptance criteria. The specific plastic hinge properties (including yield moments, backbone parameters, and story yield displacements) were adopted from Appendix A of Mehrjoo and Assi (2025a). Story-specific yield displacements obtained from these analyses were subsequently integrated into a bilinear elastoplastic MDOF dynamic model implemented via a MATLAB (The MathWorks Inc., 2023) script that employs Newmark Linear Acceleration for time integration and Newton-Raphson iteration for nonlinear system solution, as detailed in Mehrjoo and Assi (2025a).

The utilised MDOF formulation with N degrees of freedom inherently captures all N modal contributions through direct time-history integration (A. Chopra, 2016), including higher-mode effects that influence floor acceleration demands. This capability was validated in the authors' previous study, where floor spectral responses exhibited distinct amplification peaks at the first three natural periods (Mehrjoo & Assi, 2024).

This MDOF stick modeling approach captures the "structural fuse" mechanism where peak floor acceleration (PFA) is limited by the structural system’s lateral force capacity. Once a story yields, it limits the transmission of inertial forces to upper levels (Vukobratović & Fajfar, 2016). The utilized bilinear elastoplastic model explicitly captures the yield plateau (which limits force transmission) based on the detailed capacity curves derived from the ETABS pushover analysis.

Furthermore, the bilinear assumption provides a conservative estimate of acceleration demands compared to degrading fiber-based models. While real reinforced concrete members typically exhibit cyclic strength degradation (reduced transmitted acceleration), the bilinear model maintains the structural capacity at the yield level. This provides an upper-bound envelope of the demand, accounting for global dynamic amplification and higher-mode effects without

relying on strength-degrading parameters that might underestimate the acceleration transmission (Sankaranarayanan & Medina, 2007). Figure 4.2 illustrates the building configurations and identifies the specific floor elevations where non-structural components were evaluated throughout this study.

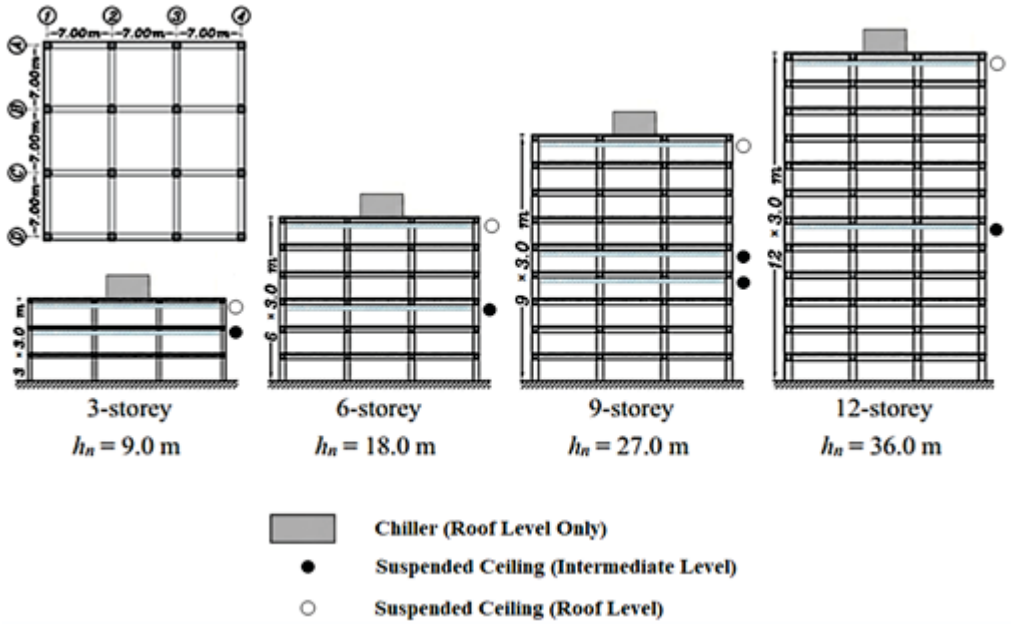

Figure 4.2 Elevation and typical plan views of the 3-, 6-, 9-, and 12-storey archetype buildings (adapted from Mazloom and Assi (2022)), indicating the specific locations of the investigated non-structural components: chillers (roof level only) and suspended ceilings (intermediate floors 2, 3, 4-5, and 6 for the 3-, 6-, 9-, and 12-storey buildings, respectively, plus all rooftop levels).

4.4 Description of the NSCs and their modeling assumptions

Twelve NSC models were adopted from recent studies by D'Angela and Magliulo (2024; 2025), who developed them as SDOF cantilevers to quantify nonlinear capacity and component amplification factors (CAF). The models span natural frequencies of 1.0–9.0 Hz and ductility ratios μ = 1.34–2.6, where $\mu = \theta c/\theta y$ represents the ratio of capping rotation to yield rotation, characterizing the deformation capacity of the NSC attachment system. These frequency–ductility ranges are representative of common acceleration-sensitive NSCs, including the suspended ceilings and rooftop chillers investigated in this study.

The original geometric properties (hollow square steel sections with varying width-to-thickness ratios), material characteristics (S275 steel with yield strength $F_y = 275$ MPa), natural frequencies, and reference IDs were retained from the source study to enable direct cross-checking.

The SDOF cantilever idealization is justified by: (1) NSC masses (m = 0.04–0.35 tonnes) representing less than 1% of the supporting structure's mass (303–3211 tonnes), satisfying the mass ratio criterion for dynamic uncoupling defined by Chen and Soong (1988); (2) the cantilever configuration with concentrated mass ensuring first-mode dominance; and (3) the widely validated applicability of this approach for acceleration-sensitive NSCs where behavior is governed by attachment flexibility (Magliulo & D'Angela, 2024). Consequently, the subsequent MATLAB analysis was treated as fully uncoupled (ASCE, 2000; Amin et al., 1971; FEMA, 2018a; Pinkawa et al., 2014; A. Singh & Ang, 1974).

The uncoupled IDA in MATLAB required the backbone curve parameters: initial stiffness (K_o), yield moment (M_γ), yield rotation (θ_γ), capping rotation (θ_c), residual rotation (θ_r), and ultimate rotation (θ_u). These parameters define the nonlinear force-deformation relationships for the equation of motion as expressed in Equation 4.1:

$$m\ddot{u} + c\dot{u} + f(u,\dot{u}) = -ma_x(t) \tag{4.1}$$

where $a_x(t)$ represents the floor acceleration time history. This equation of motion was solved using the Newmark-β integration method ($\gamma = 0.5$, $\beta = 0.25$) with time steps matching the ground motion record sampling intervals and convergence tolerance of 1×10^{-6} (A. Chopra, 2016).

The NSC models were reproduced and validated in OpenSees (McKenna et al., 2000) to extract the essential nonlinear properties. Each NSC model was represented by a zero-length rotational spring element (Node 1 to Node 2) connected to an elastic beam-column element (Node 2 to Node 3) with lumped mass (m) concentrated at the free node, as shown in Figure 4.3(a). The nonlinear behavior was captured using the IMKPeakOriented material, which implements the modified Ibarra-Medina-Krawinkler (IMK) deterioration model (Ibarra et al., 2005). A displacement-controlled, amplitude-increasing cyclic procedure was applied to obtain full hysteresis and the monotonic backbone**,** following standard IMK calibration practice (with

rotation steps of approximately 0.01 rad up to θ_u) (Ibarra et al., 2005). The resulting hysteretic responses and extracted backbone curves are presented in Figure-A III-1 (ANNEX III).

The normalized axial force ratio was set to zero since the cantilevered NSCs experienced negligible axial loads relative to lateral seismic forces (Magliulo & D'Angela, 2024). A residual strength ratio of $\kappa = 0.25$ and a strain hardening ratio of $\alpha_s = 0.03$ were adopted based on Lignos and Krawinkler (2010) and Kecman (1983). A uniform modal damping ratio (ξ = 5%) was assigned for all models, consistent with previous sensitivity analysis, which demonstrated negligible effects (<4% variation) of damping-ratio changes on the responses of NSCs with moderate-to-high attachment ductility (Mehrjoo & Assi, 2024). The complete numerical modeling approach, including the element scheme, IMK model, backbone parameterization, and calibrated curves, is summarized in Figure 4.3.

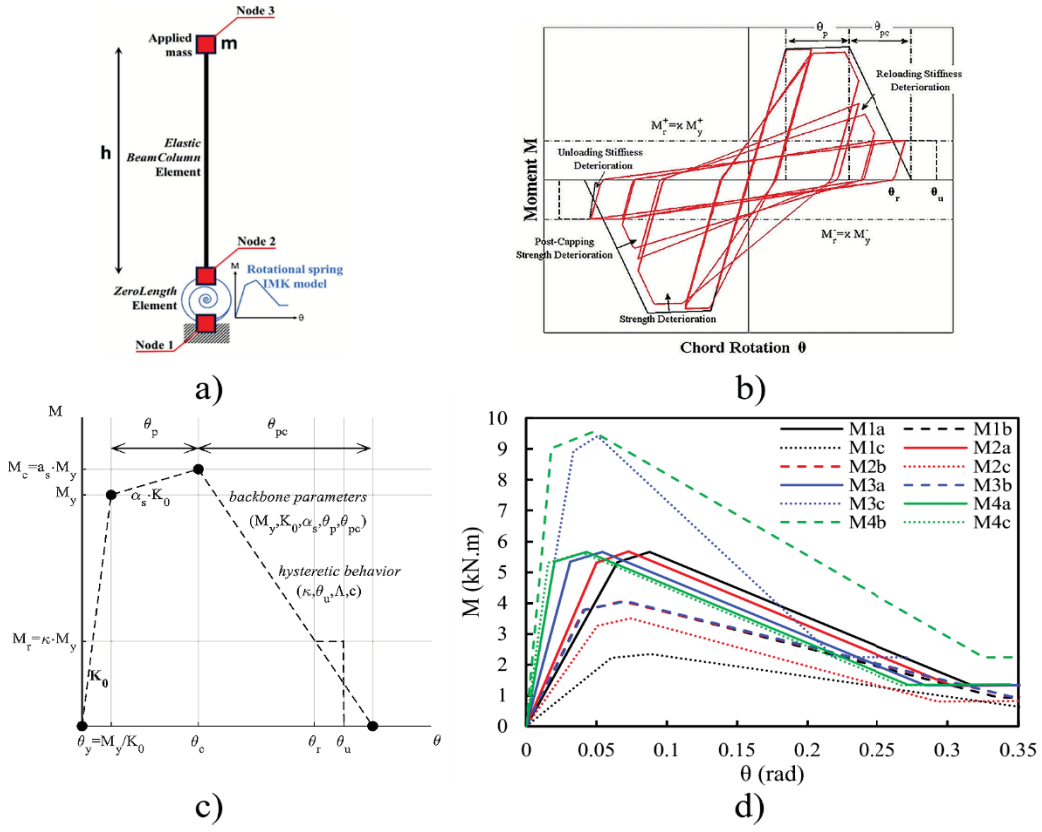

Figure 4.3 The numerical modeling approach: a) cantilever NSC modeling scheme; b) the IMK constitutive model with its schematic cyclic response as implemented in OpenSees; c) schematic backbone curve; d) backbone curves for all SDOF models derived from the OpenSees analysis from Figure-A III-1

Taken and adapted from Magliulo and D'Angela (2024, p. 1424)

The backbone curves in Figure 4.3(d) highlight varying ductility-dependent behavior: low ductility models (μ ≈ 1.3-1.5) exhibited limited post-yield deformation capacity but maintained relatively high residual strength; moderate ductility models (μ ≈ 1.6-2.1) showed balanced strain hardening and post-capping degradation; and high ductility models (μ ≈ 2.4-2.6) demonstrated significant deformation capacity but more pronounced strength degradation after reaching their capping point.

Based on these characteristics, the models were classified into four frequency ranges (I–IV: ≈1.0 Hz to >3.0 Hz) and were further categorized by ductility ratio as low (L) (μ ≈ 1.3-1.5), moderate (M) (μ ≈ 1.6-2.1), or high (H) (μ ≈ 2.4-2.6) ductility, as shown in Table 4.1.

Table 4.1 Backbone Curve Parameters for Nonlinear NSC Models derived from Figure 4.3(d)

Frequency	Model	μ = (θc/θy)	f (Hz)	Ko (kN-m) My/ θy	θ_y (rad)	M_Y (kN-m/rad)	θ_c (rad)	M_c (kN-m/rad)	θ_r (rad)	M_r (kN-m/rad)	θ_u (rad)	M_u (kN-m/rad)	θ_p (θc- θy) (rad)	θ_{pc} (θu- θc) (rad)
Range I (~1.0 Hz)	**M1a**	1.34(L)	1.02	82.31	0.065	5.35	0.087	5.64	0.32	1.33	0.39	1.33	0.022	0.303
	M1b	1.67(M)	1.03	90.95	0.042	3.82	0.07	4.07	0.34	0.96	0.43	1	0.028	0.36
	M1c	1.41(L)	1.13	36.07	0.061	2.2	0.086	2.35	0.36	0.55	0.45	0.55	0.025	0.36`
Range II (~1.5 Hz)	**M2a**	1.46(L)	1.48	106.8	0.05	5.34	0.073	5.65	0.3	1.33	0.375	1.35	0.023	0.302
	M2b	1.66(M)	1.52	90.95	0.042	3.82	0.07	4.07	0.34	0.96	0.43	1	0.028	0.36
	M2c	1.46(L)	1.52	65	0.05	3.25	0.073	3.47	0.295	0.82	0.36	0.84	0.023	0.287
Range III (~3.0 Hz)	**M3a**	1.76(M)	2.97	172.26	0.031	5.34	0.054	5.65	0.28	1.35	0.36	1.33	0.023	0.306
	M3b	1.67(M)	3.04	90.95	0.042	3.82	0.07	4.07	0.34	0.96	0.43	1	0.028	0.36
	M3c	1.54(L)	3.06	268.79	0.033	8.87	0.051	9.44	0.22	2.2	0.27	2.24	0.018	0.219
Range IV (>3.0 Hz)	**M4a**	2.15(M)	5.86	250	0.02	5.3	0.043	5.64	0.27	1.36	0.34	1.34	0.023	0.294
	M4b	2.42(H)	7.34	473.68	0.019	9	0.046	9.54	0.32	2.25	0.41	2.25	0.027	0.364
	M4c	2.6(H)	9.02	354.67	0.015	5.32	0.039	5.65	0.26	1.32	0.344	1.32	0.024	0.305

The classification facilitated correlation with FEMA P-58 Performance Assessment Calculation Tool (PACT) components based on natural frequency compatibility, as summarised in Table 4.2. Specifically, M1 and M3 were mapped to suspended ceiling systems

(unbraced vs. four-way diagonal wire braced) based on the study of McCormick et al. (2012), and were evaluated at both top-floor and intermediate-floor elevations. Similarly, M2 and M4 were mapped to chiller systems (unrestrained vs. seismically restrained) following ASCE 7-22 (ASCE, 2022) specifications, and were evaluated at the roof level, consistent with common mechanical system placement. Component-specific damage assessment was performed using FEMA P-58 fragility functions that capture actual failure mechanisms.

Table 4.2 Mapping of the 12 NSC models used in this study to their corresponding PACT identifiers and component descriptions

Components	**Corresponding PACT Identifier**	**Corresponding PACT NSC model**
M1a, M1b, M1c	C3032.001d	Unbraced suspended ceiling, SDC A, B, C, Area (A): A > 2500, Vertical support only
M2a, M2b, M2c	D3031.012a	Unrestrained vibration-isolated chiller, Capacity: < 100 Ton, Vibration isolated equipment that is not snubbed or restrained - Anchorage fragility only
M3a, M3b, M3c	C3032.003d	Four-way diagonal wire-braced suspended ceilings, SDC D, E (Ip=1.0), Area (A): A > 2500, Vertical & Lateral support
M4a, M4b, M4c	D3031.013d	Seismically restrained chillers, Capacity: 100 to <350 Ton, Equipment that is either hard anchored or is vibration isolated with seismic snubbers/restraints, Anchorage fragility only

The ductility parameters are physically grounded in specific inelastic mechanisms. For suspended ceilings (M1, M3), nonlinearity is localized at grid-to-perimeter connections (seismic clips and closure angles), which undergo slip and plastic deformation before hanger wires yield, controlling the unseating failure mode documented in post-earthquake reconnaissance (ASTM E580, 2022; CISCA, 2004; Dhakal et al., 2016; Soroushian et al., 2016). For chillers (M2, M4), the ductility parameter represents the deformation capacity of the seismic restraint assembly. The high-ductility category (M4, $\mu \approx 2.4–2.6$) corresponds to seismic snubbers with steel housings and elastomeric pads that absorb energy through nonlinear deformation, with ductile steel yielding precluding brittle concrete failure modes (Hoehler & Eligehausen, 2008; Mason Industries, 2019; Rieder, 2009; ASHRAE, 2012). The

low-ductility category (M2, $\mu \approx 1.5$) reflects unrestrained vibration isolators without seismic snubbers.

4.5 Vulnerability Assessment Framework and Damage State Definition

The vulnerability assessment followed the FEMA P-58 methodology, incorporating: (i) component quantity estimation using normative methods based on gross floor area, (ii) damage state characterization using fragility functions, and (iii) repair cost calculation.

Component quantities were obtained by dividing the building floor area (441 m^2 = 4747 square feet (SF)) by the normative coverage area specified in FEMA P-58-2 (FEMA, 2018b) for each component type. The normative coverage areas represent the typical floor area served by each component unit in standard buildings. Thus, the suspended ceiling quantity was calculated as 4747 SF divided by 2500 SF per unit, resulting in 1.89 units per floor, applied uniformly to every storey as a unitless demand multiplier. For rooftop chillers, a fixed quantity of one per building was assigned according to FEMA P-58-2 (FEMA, 2018b) normative specifications.

Economic loss metrics were defined in terms of total building replacement values and maximum component repair costs. Building replacement costs were derived from the FEMA P-58/BD-3.7.15 cost example, selected for its compatibility with the studied archetype buildings; with adjustments made to account for differences in building area and occupancy (FEMA, 2013). The component-level maximum repair costs were obtained from the consequence functions associated with the highest damage state (DS) in the PACT database (e.g., C3032.001d for M1a) and multiplied by their corresponding non-directional quantities. All values were converted from the original 2011 USD estimates to Canadian dollars using an exchange rate of 1 USD = 1.4 CAD, and then adjusted to 2025 price levels using a cumulative Canadian inflation factor of 1.4 (“World Bank Open Data,” 2025). The adjusted building replacement costs, expressed in Canadian dollars (CAD), were $7,190,000 (3-storey), $14,380,000 (6-storey), $21,570,000 (9-storey), and $28,739,000 (12-storey). For suspended ceilings, the maximum repair cost was $267,000 for all unbraced models (M1a–M1c) and $446,000 for the four-way diagonal wire-braced models (M3a–M3c). For chillers, the

unrestrained group (M2a–M2c) had a maximum repair cost of $191,000, while that of the seismically restrained group (M4a–M4c) were $343,000.

Furthermore, the damage classification for suspended ceilings and chillers was derived from FEMA P-58/BD-3.9.4 (DHS, 2011). For suspended ceilings, three damage states (DS) (slight DS1, moderate DS2, and extensive DS3) were defined based on the proportion of ceiling panels that collapsed: (1) DS1 at the elastic limit (≈70% of yield capacity, representing 5% panel collapse), (2) DS2 at yield initiation (representing 30% panel collapse), and (3) DS3 at the capping point (representing 50% panel collapse). These thresholds correspond to assumed key points on the force–deformation backbone curves shown in Figure 4.3, and align with performance-based seismic design principles (Bianchi & Pampanin, 2022; King & Fronk, 2004; Lagomarsino & Giovinazzi, 2006).

For chillers, fragility evaluation uses a single lognormal function with PFA as the EDP. The damage state threshold was defined at the capping point of the anchorage system's force-deformation backbone curve (Figure 4.3). When the computed PFA exceeded the median fragility threshold, the PACT algorithm allocated the component to one of two mutually exclusive damage states: DS1 (anchorage failure only, 70% probability) or DS2 (anchorage plus mechanical/electrical damage, 30% probability). These branching probabilities are specified in the FEMA P-58 fragility database and were derived from expert judgment, corroborated by post-earthquake performance data (Cremen & Baker, 2019; Porter, 2009).

The complete IDA scatter data from all 24 earthquake records for each case study building (3-, 6-, 9-, and 12-storey) are presented in ANNEX IV (Figure-A IV-1-Figure-A IV-4), showing the ground motion spectral acceleration (Sa) versus peak floor acceleration relationships for all floor levels. NSC fragility curves were developed for each case study, then combined using median statistics, following the detailed methodology in Mehrjoo and Assi (2025a). The resulting curves for M1 and M3 suspended ceilings are presented in Figure-A V-1, and the M2 and M4 chiller curves are presented in Figure-A V-2 in ANNEX V.

These IDA-derived fragility curves, characterized by median and dispersion parameters that account for variability from ground motion records, building configurations, and floor elevations, were subsequently used to replace the default fragility parameters in PACT for the corresponding component identifiers listed in Table 5.2.

This approach integrated the component-specific dynamic and inelastic properties (frequency and ductility) into the fragility parameters, while retaining FEMA P-58's established consequence functions (repair costs, repair times, and repair actions) for cost estimation.

4.6 Seismic performance assessment of NSCs: comparative analysis of repair costs, loss ratios, and repair ratios

This section examines the seismic performance of the studied NSCs as a function PFA, considering the influence of component type and floor elevation. PFA was adopted as the EDP because acceleration-sensitive NSCs respond to floor-level demands rather than ground motions directly. The analysis focuses on the comparative assessment of three key performance metrics that provide complementary perspectives on seismic vulnerability:

(i) Repair costs quantify the economic impact of seismic damage by translating physical damage states into monetary terms and were calculated using the FEMA P-58 methodology implemented in PACT software (FEMA, 2012b) through the following steps: (1) Building model setup with replacement costs and occupancy parameters, (2) modification of component-specific fragility functions with IDA-derived fragility parameters for the PACT component identifiers, (3) assignment of component quantities per floor, (4) importing IDA results represented by 24 PFA demand parameters, where floor-specific PFA values were assigned to components at their respective elevations to capture the vertical demand distribution, (5) performing 200 Monte Carlo realizations to ensure statistical convergence (Magsalay, 2025) and convolution of fragility curves with consequence functions to generate repair costs by weighting each damage state's repair cost by its probability of occurrence.

(ii) Loss ratios are defined as repair costs normalized by total building replacement value and indicate the relative contribution of individual component damage to overall building economic losses, enabling assessment of component criticality relative to total building value.

(iii) Repair ratios are defined as repair costs normalized by component replacement value and represent the extent of component-level damage, providing insight into whether repair or replacement strategies are more cost-effective.

These metrics were evaluated for each case study building (3-, 6-, 9-, and 12-storey). PACT outputs repair costs for all floor levels simultaneously within a single analysis per building.

For this study, specific floor elevations were selected for detailed presentation and analysis: roof levels for all buildings, plus representative intermediate floors (level 2 for 3-storey, level 3 for 6-storey, levels 4-5 for 9-storey, and level 6 for 12-storey buildings). Results were averaged across all case studies and evaluated as functions of PFA to establish vulnerability relationships. It should be noted that no adjustments were made to FEMA P-58 consequence functions based on floor elevation; all performance differences between roof and intermediate floors result from differences in seismic demand (PFA).

The following performance evaluation is organized into three parts. The first subsection investigates the seismic vulnerability of suspended ceiling systems by examining how different attachment configurations affect performance metrics of repair costs, loss ratios, and repair ratios under increasing spectral acceleration levels, with results comparing roof and intermediate floor elevations presented in Figure 4.4. The second subsection evaluates the seismic performance of chiller systems, examining these same performance metrics across various design variants, as shown in Figure 4.5. Finally, the comparative analysis identifies how component type, frequency, and ductility govern vulnerability patterns and establishes design implications.

4.6.1 Seismic vulnerability assessment of suspended ceiling groups

Figure 4.4 shows the comparative seismic performance metrics for M1 and M3 suspended ceiling groups at the top and intermediate floor elevations. Subplots (a, c, e) correspond to the M1 group, while Subplots (b, d, f) correspond to the M3 group. For both groups, the top row shows repair costs, the middle row shows loss ratios, and the bottom row shows repair ratios.

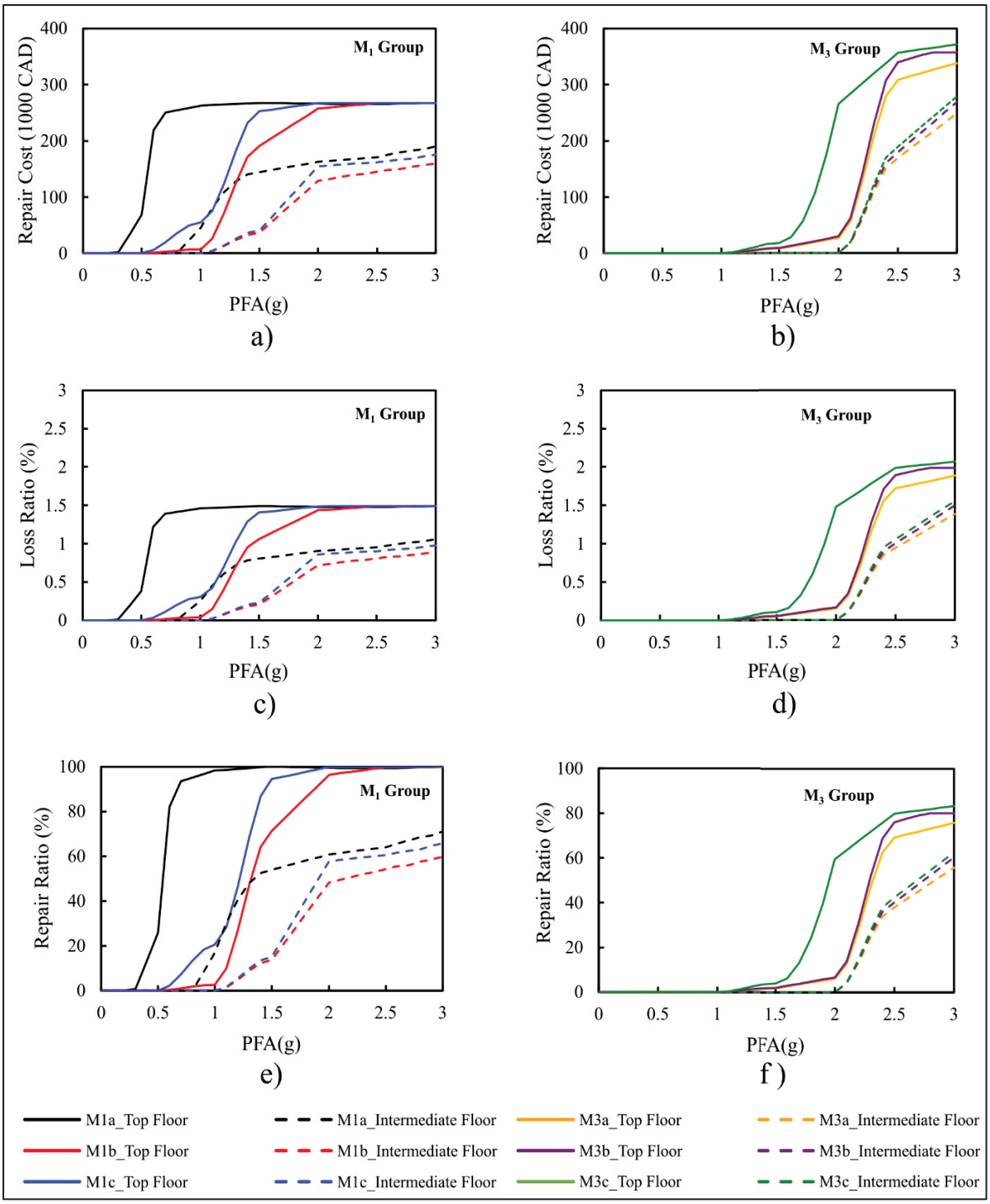

Figure 4.4 Comparison of seismic vulnerability metrics for M1 and M3 suspended ceiling groups at top and intermediate floor elevations: repair costs (top), loss ratios (middle), and repair ratios (bottom) as functions of PFA

In subplots (a, b), the repair cost curves demonstrate distinct damage initiation thresholds between the two ceiling systems, with notable variations based on floor elevation. M1 group, representing unbraced configurations of suspended ceiling, showed early damage initiation at the top floor (0.3-1.0g PFA depending on ductility) and intermediate floor (1.0-1.1g PFA). This early failure is consistent with experimental observations (Dhakal et al., 2016) that lack of lateral stiffness allows large relative displacements that trigger perimeter failures even at low intensities. In contrast, the M3 group, representing wire-braced configurations of suspended ceiling**,** remained undamaged until PFA exceeded 1.5g for both elevations, highlighting their superior seismic resilience. This aligns with experimental evidence (Brandolese et al., 2019) showing that four-way diagonal bracing limits these displacements and redistributes seismic forces to the building structure, thereby preventing unseating of ceiling components until significantly higher acceleration levels are reached.

Beyond initiation thresholds, both groups exhibited rapid cost escalation, with top-floor installations consistently more vulnerable. At PFA = 3.0g, the M1 group reached identical maximum costs of $267,400 at the top floor, while costs at intermediate floors varied between $160,000 and $190,000. In contrast, the M3 ceiling group showed greater cost variability, with top-floor costs ranging from $338,000 to $372,000 and intermediate-floor costs between $249,000 and $279,000. These patterns confirmed that higher ductility consistently reduced repair cost across both floor elevations, with the M3 group maintaining similar top-to-intermediate floor differentials of approximately 33-36%.

In subplots (c, d), the loss ratio curves reflect trends similar to repair costs. For the M1 group, loss ratios at the top floor were notably higher, approaching 1.1-1.5%, compared to 0.2-0.8% at the intermediate floor for PFA ≈ 1.5g. In contrast, M3 group maintained negligible loss ratios at both elevations until PFA ≈ 1.5g, after which they demonstrated a ductility-dependent increase: M3c reached the highest values (2.1% top, 1.6% intermediate), followed by M3b (2.0% top, 1.5% intermediate), and M3a (1.9% top, 1.4% intermediate) at PFA = 3.0g.

In subplots (e, f), M1 group reached repair ratios of approximately 100% at top floor compared to 60-71% at intermediate floor, while the M3 group demonstrated ductility-dependent progression with M3c showing the highest values (83% top, 63% intermediate), followed by M3b (80% top, 60% intermediate), and M3a (76% top, 56% intermediate) at PFA = 3.0g.

4.6.2 Seismic vulnerability assessment of chiller system groups

Figure 4.5 compares the seismic performance of chiller systems over a range of PFA values. Subplots (a, c, e) present the repair cost functions for the M2 group, while Subplots (b, d, f) show the corresponding results for the M4 group. For both groups, the top row shows repair costs, the middle row shows loss ratios, and the bottom row shows repair ratios.

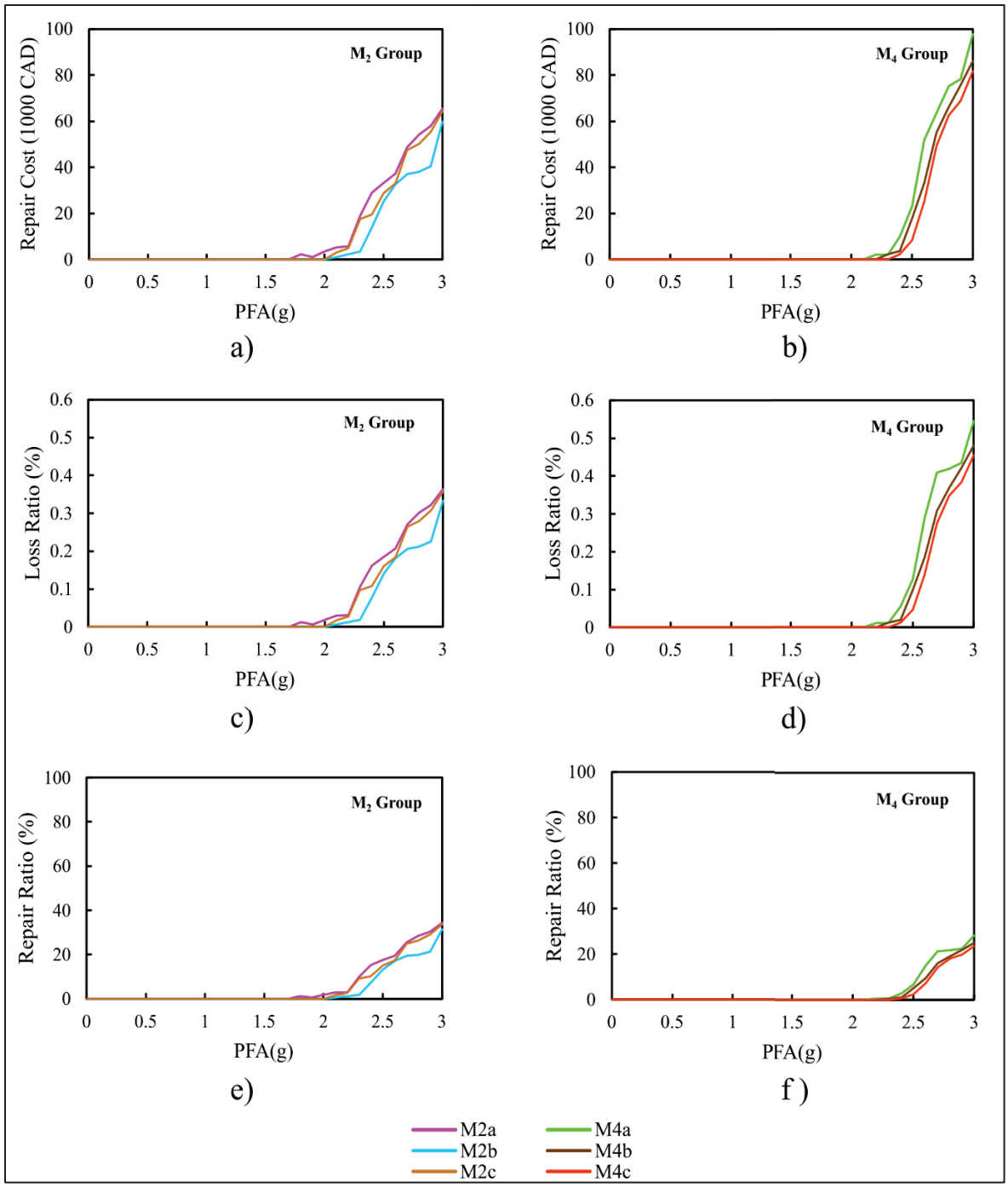

Figure 4.5 Seismic performance comparison of M2 and M4 Chiller groups showing repair cost, loss ratio, and repair ratio as functions of PFA

In subplots (a, b), the repair cost curves indicate that both M2 and M4 chiller groups remained highly resilient at lower PFAs, with minimal costs incurred until PFA exceeded ≈ 1.5 g for M2

and ≈ 2.0 g for M4. This higher damage initiation threshold in the M4 group reflects their superior seismic resilience relative to the M2 group. Beyond these thresholds, both groups showed rapid cost escalation with distinct ductility-dependent patterns. At PFA = 3.0 g, M2b's repair cost was about 7–9% (≈ $4,500–$5,600) lower than those of M2a and M2c, while high-ductility M4b and M4c showed 12–17% lower costs than M4a. At this intensity, total repair costs reached ≈ $60,000–$65,000 for the M2 group and ≈ $82,000–$100,000 for the M4 group. The high resilience of the M4 group, representing seismically restrained chillers, is consistent with the protective function of seismic snubbers documented in experimental studies (ASCE 2022; Porter, 2009), which act as displacement limiters that absorb energy through controlled impact and prevent the chiller from exceeding the anchorage capacity. In contrast, the M2 group, representing unrestrained configurations, exhibits vulnerability patterns consistent with systems that rely solely on the limited shear capacity of vibration isolation mounts, making them susceptible to anchorage failure at lower acceleration levels.

In subplots (c, d), the loss ratios for both chiller groups remained below 0.55%, significantly lower than those of architectural NSCs and consistent with Bradley et al. (2009), who reported that mechanical equipment generally contributes less to total building losses than architectural components. Loss ratio patterns revealed clear frequency-dependent characteristics between the M2 and M4 groups. For the M2 group, ratios began to rise gradually beyond PFA ≈ 1.5g, reaching a maximum of about 0.35% at PFA = 3.0g. In contrast, the M4 group maintained negligible loss ratios until PFA ≈ 2.0g, after which they increased more rapidly, peaking at roughly 0.55% at PFA = 3.0g.

In subplots (e, f), the repair ratios revealed variability among configurations within each group. M2a exhibited the highest repair ratio (35% at PFA = 3.0g), while moderate-ductility variant M2b showed more controlled progression (30%). The M4 group displayed more pronounced ductility effects, with high ductility variants M4b and M4c exhibiting 12–17% lower values than M4a.

4.6.3 Comparison of performance and design implications

A cross-typology comparison of Figure 4.4 and Figure 4.5 reveals that vulnerability is governed by a combination of component type, frequency, attachment ductility, and elevation. Regarding component type, suspended ceilings are significantly more vulnerable than chillers, with repair costs at PFA = 3.0g being three to five times higher (≈ $270,000–$370,000 vs. ≈ $60,000–$100,000). This disparity reflects the suspended ceilings' broad spatial distribution and greater sensitivity to acceleration, evidenced by their lower damage thresholds and steeper cost escalation, which aligns with findings by Dhakal et al. (2016).

Across both component types, higher-frequency configurations consistently exhibited delayed damage initiation. The lowest frequency ceiling group (M1; Range I, ≈1.0 Hz) was the first to have damage initiation (PFA ≈ 0.3g), while the highest frequency chiller group (M4; Range IV, >3.0 Hz) was the last to have damage initiation (PFA ≈ 2.0g).

This frequency-fragility relationship translates directly to repair cost reduction. At PFA = 1.5g, higher-frequency M3 ceilings ($f > 3.0$ Hz) incurred essentially zero repair costs while lower-frequency M1 ceilings ($f \approx 1.0$ Hz) reached $120,000–$270,000 depending on floor elevation and ductility. The frequency effect is similarly evident for chillers: M4 ($f > 3.0$ Hz) exhibited delayed damage initiation with minimal costs until PFA exceeded 2.0g, while M2 ($f \approx 1.5$ Hz) began accumulating damage at PFA ≈ 1.5-1.7g. At PFA = 3.0g, the frequency increase from M1 to M3 resulted in maximum repair costs increasing from $267,000 to $338,000-$372,000 (27-39% increase) despite the enhanced system's higher replacement value, while M2 to M4 showed costs rising from $40,000-65,000 to $80,000-100,000 (54-100% increase when comparing same ductility levels). The underlying mechanism is that higher-frequency components experience reduced floor acceleration amplification due to detuning from the building's fundamental period, resulting in delayed damage initiation and lower cumulative damage at equivalent ground motion intensities.

Within each frequency range, ductility proved to be an important mitigation factor. The improvements were particularly pronounced in the low-frequency M1 group, where the moderate-ductility M1b variant ($\mu = 1.67$) delivered ≈30% lower repair costs than M1a and ≈6% lower than M1c at PFA = 1.5g. Based on these analysis results, moderate ductility ($\mu \approx$

1.6–1.7) offers a practical target for improving performance. While the benefits were smaller in higher frequency ranges (e.g., a 12–17% repair ratio reduction in Range IV), the positive impact of enhanced ductility was consistent across all components.

A central finding is the important impact of component location. The consistently higher damage and costs at top-floor elevations compared to intermediate floors, particularly for suspended ceilings, confirm that vertical placement is a critical driver of vulnerability due to amplified seismic demands.

In addition, both component types present distinct risk profiles. Although suspended ceilings contribute a relatively small share of the total building replacement value (1.5-2%), their broad distribution can trigger significant indirect economic losses through building closure and business interruption in addition to the high direct repair costs quantified in this study. Conversely, despite their low direct repair costs, chiller failures can severely impact building functionality by disrupting critical HVAC systems, potentially rendering facilities like hospitals or data centers unusable and forcing costly evacuations (Alassafi et al., 2024; Myrefelt, 2008; Zhanwei Wang et al., 2024), though such indirect costs were beyond the scope of this study.

Therefore, these findings support a comprehensive performance-based design approach. Optimizing for higher-frequency configurations (via bracing/restraint) and enhanced attachment ductility, combined with strategic component placement, emerges as a robust strategy for mitigating both direct costs and the risk of systemic failure from non-structural components.

4.7 Conclusion

This study provides a comprehensive assessment of the seismic vulnerability of suspended ceiling and chiller systems using three complementary metrics: repair cost, loss ratio, and repair ratio, revealing that performance is driven by a combination of attachment ductility, component configuration, and elevation within a building.

The key findings demonstrate that enhanced, higher-frequency components (M3 ceilings, M4 chillers) significantly outperform standard designs by raising damage initiation thresholds.

Suspended ceilings proved far more vulnerable than chillers, incurring three to five times higher repair costs due to their broader spatial distribution and greater sensitivity to acceleration. Furthermore, component location was an important factor, with top-floor ceilings experiencing substantially higher damage and costs due to amplified seismic demands.

The study also quantified the economic benefits of ductility, confirming it as an important mitigation tool. Moderate ductility enhancements ($\mu \approx 1.6–1.7$) significantly reduced repair costs for both component types compared to their low-ductility counterparts.

Based on this study's findings, an integrated approach that combines enhanced attachment ductility with strategic placement delivers consistent performance improvements.

Several limitations should be acknowledged. First, the use of UHS-matched ground motions reduces response variability compared to unscaled or CMS ground motion selection, potentially underestimating dispersion in seismic demands; future studies could investigate CMS-based scaling for a more realistic representation of response variability. Second, future research should adopt more sophisticated nonlinear modeling approaches for buildings that go beyond simple bilinear representations and examine a wider variety of buildings, including different structural systems, configurations, and material properties, to enhance the robustness of the conclusions. Third, the parametric models represent idealized frequency-ductility combinations and do not capture installation-specific details such as ceiling grid irregularities or site-specific anchorage conditions. Fourth, the study focuses on horizontal accelerations and does not explicitly address vertical accelerations, which may be significant for NSCs with vertically-oriented support systems, such as pendant-mounted equipment, long-span suspended ceilings, and components where anchorage capacity is governed by vertical uplift forces. Despite these limitations, the approach enables systematic comparison of frequency-ductility effects on seismic vulnerability of the studied acceleration-sensitive components (suspended ceilings and chillers), providing valuable insights into the relative performance of different attachment strategies.

FOREWORD TO CHAPTER 5

To support the interpretation of the results presented in this chapter, two technical clarifications are provided regarding the data presentation and the comparison with building codes:

1. **Data Presentation (Figure 5.2):** A clarification is provided regarding the data points displayed in Figure 5.2, which compares the simplified method against reference numerical models. It is clarified that each of the 12 data points represents the arithmetic mean of the peak response quantities calculated across the entire dataset, encompassing both the four archetype buildings (3, 6, 9, and 12 stories) and the full suite of ground motion records utilized in the time-history analyses. This aggregation method was selected to capture the central tendency of the component responses across varying structural periods and ground motion records.
2. **Interpretation of NBC 2025 Provisions:** The manuscript observes that the design equations adopted for the 2025 edition of the National Building Code of Canada (NBC) yield seismic forces lower than the elastic analysis results derived in this study. It is acknowledged that these code provisions, along with ASCE 7-22 and ATC-120, are calibrated based on a minimum inherent component ductility **(**$\mu = 1.25$**)**(Fazileh et al., 2025), even for nominally elastic components. In contrast, the analysis presented in this chapter assumes a strictly elastic response ($\mu = 1.0$). Therefore, the discrepancy reported in this chapter highlights the difference between the theoretical elastic demand calculated in this study and the component ductility-based design targets inherent in the new code provisions.

CHAPTER 5

PROPOSED DUCTILITY-BASED FORCE FACTORS FOR ACCELERATION-SENSITIVE LIGHT NON-STRUCTURAL COMPONENTS

Majid Mehrjoo[a] and Rola Assi[b]

[a,b] Department of construction engineering, École de technologie supérieure (ÉTS), Montreal, Quebec, H3C 1K3, Canada

Paper accepted to appear in the Proceedings of the 6th International Workshop on Seismic Performance of Non-Structural Elements (SPONSE 2026)[4], October 2025

Abstract

This study examines the impact of the combined ductility of structural systems and non-structural components (NSCs) on the seismic demands placed on NSCs in moment-resisting frame buildings. The National Building Code of Canada (NBC 2020) estimates the NSC design forces based on elastic building response, using elastic spectral accelerations and a component force factor (S_P), which includes an empirical response modification factor (R_P) to account for NSC ductility. While recent proposed NBC provisions incorporate building period and structural ductility-related factors, both current and proposed approaches still do not explicitly account for the actual level of ductility of NSC attachment.

To address these limitations, nonlinear analyses were conducted on four moderately ductile frame buildings (3-, 6-, 9-, and 12-story) subjected to 24 ground motions matched to Montreal's Uniform Hazard Spectrum for very dense soil and soft rock. The NSCs were modelled with varying ductility capacities (μ_{comp} = 1.0, 1.25, 1.5, and 2.0) using elasto-plastic behavior, and their response was evaluated via time-history analyses with the Newmark

---

[4] Paper ID: 26050

integration method. The resulting component force factor (PSA/PGA) curves were validated against 12 detailed NSC models whose backbone parameters were identified in OpenSees with the IMK peak-oriented hysteretic model and implemented in the MATLAB time-history analyses.

The results indicate that structural nonlinearity substantially reduces seismic demands compared to elastic analyses, with reductions of 67–78% for components with elastic attachments and 9–64% for components with ductile attachments. The magnitude of the reduction generally diminishes as attachment ductility increases. The benefits of NSC attachment ductility are most evident when component periods are tuned to the building's fundamental period, where moderate ductility levels ($\mu_{comp} \approx 1.5$) achieve the best balance between performance and practical feasibility. These findings underscore the necessity of developing refined force modification models that capture both structural and non-structural nonlinear behavior.

Keywords: nonstructural components, ductility, nonlinear response, dynamic analysis, elasto-plastic behavior.

5.1 Introduction

Non-structural components (NSCs) account for approximately 70% of building investment costs and play a crucial role in ensuring building functionality and occupant safety during seismic events (Miranda & Taghavi, 2005; T. Wang et al., 2021). These components encompass architectural components (e.g., suspended ceilings, external cladding, and partition walls), building services components (e.g., mechanical, plumbing, electrical, and telecommunication devices), and building contents (e.g., furniture, office equipment)(CSA 2014c). Post-earthquake reconnaissance has consistently documented NSC vulnerability across major seismic events, beginning with the systematically documented 1971 San Fernando earthquake and extending through the 1994 Northridge, 1995 Kobe, 2010 Maule, and 2023 Turkey-Syria earthquakes. These investigations have consistently demonstrated that

NSCs sustain damage before the main structural system, creating life-safety hazards, blocking escape routes, and causing substantial economic losses (Esper & Tachibana, 1998; Lew et al., 1971; Mehrjoo & Aval, 2024; Miranda et al., 2012; Naeim, 2004; D. Perrone et al., 2019; Tapia-Hernández et al., 2025).

The seismic design of NSCs has evolved significantly, yet significant limitations persist in current code approaches. The National Building Code of Canada (NRC 2020) relies on simplified linear acceleration amplification based on elastic building response, while recent proposed provisions (CBHCC, 2024) introduce more sophisticated formulations incorporating building dynamics. However, both approaches share a fundamental limitation: they fail to capture the combined actual nonlinear behavior of supporting structures and varying NSC attachment ductility levels under seismic conditions (Anajafi, 2018; ATC, 2018a; A. Kazantzi et al., 2018).

Recent research has shown that the ductility of NSC attachments can substantially reduce seismic demands, particularly within the resonance range of a building's fundamental period, and lower repair costs compared to components with elastic attachments. Specifically, components with moderate to high attachment ductility can experience 40–60% less damage (Anajafi et al., 2020; Filiatrault et al., 2018; Mehrjoo & Assi, 2024, 2025a; Obando & Lopez-Garcia, 2018). However, most of these findings are based on studies that assume elastic structural behavior, raising questions about their applicability when supporting structures undergo inelastic deformations. Previous research has established that inelastic structural responses can either amplify or attenuate floor accelerations compared to linear models, depending on factors such as building height, lateral system flexibility, and NSC period (Ruggieri & Vukobratović, 2024; Taghavi & Miranda, 2012). The main shortcoming is that the combined effects of structural nonlinearity and component ductility on seismic demands remain insufficiently quantified for NSCs, particularly since the effectiveness of ductility varies with both the resonance ratio between component and structure and the extent of structural yielding.

Building upon the authors' previous work on elastic structural assumptions (Mehrjoo & Assi, 2024), this study investigates these limitations through nonlinear dynamic analysis of four archetype reinforced concrete moment-resisting frame buildings (3, 6, 9, and 12 stories)

subjected to ground motions matched to Montreal's Uniform Hazard Spectrum for very dense soil and soft rock conditions. The analyses quantify how structural yielding modifies floor accelerations and, in turn, how NSC-attachment ductility affects the component force factor (S_P), which accounts for the in-structure amplification of ground motion and the component's dynamic properties. Based on these findings, the study proposes revised S_P values calibrated to performance-based design applications.

5.2 Case study buildings, ground motion selection, and modelling assumptions

This study examined four reinforced concrete moment-resisting frame structures (3, 6, 9, and 12 stories) with limited ductility, symmetric layouts, three 7 m bays in both directions, and uniform 3 m floor heights. The buildings were designed following the NBC 2015 (NRC, 2015) and CSA A23.3-14 (CSA, 2014a) provisions, with full design details available in the study by Mazloom and Assi (2022). The buildings were idealized as one-dimensional stick models with lumped mass and equivalent stiffness concentrated at each floor level, enabling the formulation of mass, damping, and stiffness matrices for the multi-degree-of-freedom (MDOF) systems. The equivalent floor stiffness was computed in ETABS software (CSI, 2024) using the flexibility method, which involves applying unit forces to each degree of freedom and inverting the resulting flexibility matrix. Pushover analyses performed with discrete plastic hinge elements at beam-column interfaces per ASCE/SEI 41-23 standard (ASCE, 2023), provided story-level yield displacements. The governing equations of motion for the MDOF system were then solved using the step-by-step Newmark integration method ($\gamma = 1/2$, $\beta = 1/6$) implemented in MATLAB (The MathWorks Inc., 2023), with story yield displacements incorporated to capture structural nonlinearity.

For the dynamic analysis, 24 ground motion records were used, comprising 12 historical accelerograms from the PEER NGA-East database (Goulet et al., 2021) and 12 synthetic records from Atkinson's database (Atkinson, 2009). These motions were spectrally matched to the Montreal Uniform Hazard Spectrum (UHS) for very dense soil and soft rock conditions (NBC Site Class C), with return periods of 475 years and 2,475 years. Detailed selection

methodology, spectral matching procedures, and complete modelling details are available in the studies by Mehrjoo and Assi (2024, 2025a).

5.3 Description of the NSCs and their modelling assumptions

Light NSCs with masses less than 0.1% of the supporting structures (303–3211 tonnes) were examined, enabling uncoupled analysis (Amin et al., 1971). For the parametric study, the NSCs were modeled as single-degree-of-freedom (SDOF) systems positioned at the roof and intermediate floor levels with periods ranging from 0.01 to 2.0 s. Four distinct ductility levels were investigated to develop reliable component force factors: elastic behavior ($\mu_{comp} = 1.0$), low ductility ($\mu_{comp} = 1.25$), moderate ductility ($\mu_{comp} = 1.5$), and high ductility ($\mu_{comp}=2.0$). Ductility was defined as the ratio of maximum to yield displacement ($\mu_{comp} = u_m/u_y$). A bilinear elasto-plastic model was employed for computational efficiency in the parametric analyses while capturing essential nonlinear characteristics of NSCs.

To ensure the reliability of the proposed component force factors, 12 detailed NSC models with varying frequencies (1.0-9.0 Hz) and ductility ratios ($\mu_{comp} = 1.34$-2.6) were adopted from the studies of D'Angela and Magliulo (2024 a; 2025; 2024 b). These NSC models were used for comprehensive validation using advanced nonlinear models that incorporate realistic cyclic behavior. These advanced models include explicit deterioration mechanisms covering stiffness degradation (post-capping softening and cyclic degradation of unloading/reloading stiffness), strength deterioration, and rotation-capacity deterioration. These models represent cantilever-type NSCs with hollow square steel sections (S275 steel, Fy = 275 MPa), covering four frequency ranges and three ductility categories, as detailed in Table 5.1 and illustrated by their backbone curves in Figure 5.1(d). These models were reproduced in OpenSees (McKenna et al., 2000) using the modified Ibarra–Medina–Krawinkler (IMK) peak-oriented hysteretic formulation to extract the backbone-curve parameters for the subsequent MATLAB-based uncoupled analysis (Figure 5.1(a-c)). Each NSC was modeled using zero-length rotational spring elements connected to elastic beam-column elements, with backbone curve parameters, initial stiffness (K_0), yield moment (M_γ), yield rotation (θ_γ), capping rotation (θ_c), residual rotation (θ_r), and ultimate rotation (θ_u).

A uniform modal damping ratio of 5% was adopted for all analyses, consistent with previous sensitivity studies that demonstrated minimal influence of damping variations on NSC seismic demands (Mehrjoo & Assi, 2024, 2025a).

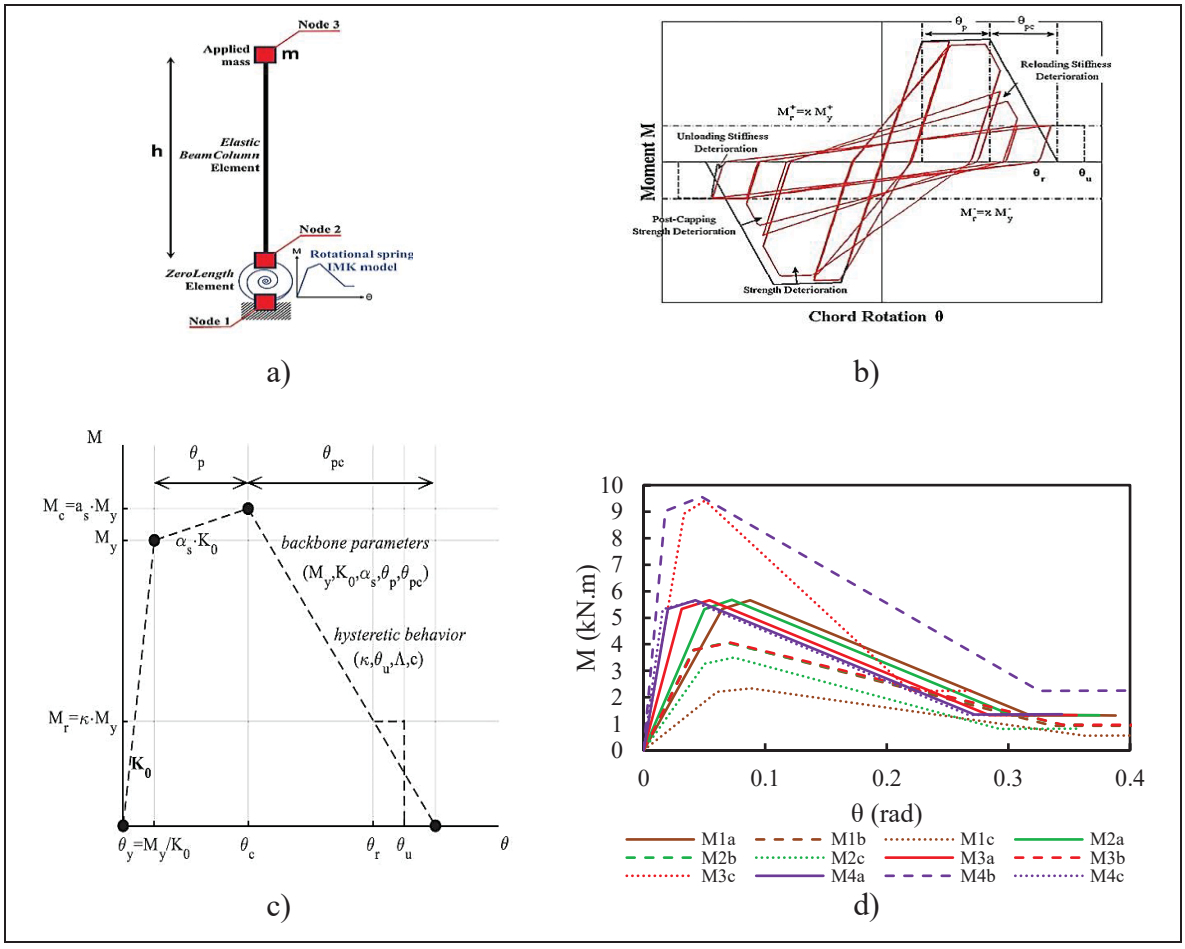

Figure 5.1 The numerical model includes: a) cantilever NSC modeling scheme; b) the IMK constitutive model with its schematic cyclic response as implemented in OpenSees; c) schematic backbone curve; d) backbone curves for all SDOF models derived from the OpenSees analysis from Figure-A III-1

Taken and adapted from Magliulo and D'Angela (2024, p. 1424)

Table 5.1 Used NSC models: frequency and ductility parameters across four frequency ranges

Taken and adapted from Magliulo and D'Angela (2024, p. 1424)

Frequency	Range I (~1.0 Hz)			Range II (~1.5 Hz)			Range III (~3.0 Hz)			Range IV (>3.0 Hz)		
Model	M1a	M1b	M1c	M2a	M2b	M2c	M3a	M3b	M3c	M4a	M4b	M4c
f (Hz)	1.02	1.03	1.13	1.48	1.52	1.52	2.97	3.04	3.06	5.86	7.34	9.02
μ_{comp} $=(\theta c/\theta y)$	1.34	1.67	1.41	1.46	1.66	1.46	1.76	1.67	1.54	2.15	2.42	2.6

Based on their natural-frequency characteristics, the 12 NSC models fall into two primary NBC (2020) categories: M1 and M3 groups correspond to suspended ceilings, light fixtures, and other ceiling attachments (McCormick et al., 2012), classified as NBC Category 7, while M2 and M4 groups represent machinery, fixtures, equipment, and tanks with contents (ASCE, 2022), classified as NBC Category 12.

5.4 NSC seismic demand

This section presents the NSC seismic demands at the roof and intermediate floor levels, extending the elastic structural response analysis of Mehrjoo and Assi (2024) to incorporate structural nonlinearity effects. The intermediate floors considered are level 6 in the 12-storey building, levels 4 and 5 in the 9-storey building, level 3 in the 6-storey building, and level 2 in the 3-storey building. The analysis focuses on the mean response across all records and case studies and is organized into two parts. The first examines current NBC provisions for calculating S_P factors, evaluating both the existing NBC 2020 method and the alternative formulation recommended for future editions. The second analysis focuses on the S_P force factor, examining how structural nonlinearity and component ductility influence the component force factor (PSA/PGA) across the entire period range considered. The computed mean response curves are validated against individual data points from 12 detailed NSC models (M1a -M4c), as illustrated in Figure 5.2. The resulting analysis forms the basis for the proposed NSC force factors presented in Section 5.5.

5.4.1 According to the NBC provisions

In the NBC, the seismic design force for NSCs is determined using a formula in which the S_P factor plays a central role in defining the peak seismic demand on the component. The S_P factor is expressed by Equation 5.1:

$$S_P = \frac{C_P A_r A_x}{R_P} \tag{5.1}$$

Where C_p (element/component factor), A_r (element/component force amplification factor), R_p (element/component response modification factor), and A_x (height factor) are as defined in the NBC, with C_p, A_r, and R_p values specified in Table 4.1.8.18.

For the machinery components (Category 12), the NBC specifies C_P = 1.50, A_r = 1.00, R_P = 1.25 for rigid connections, and C_P = 1.50, A_r = 2.50, R_P = 2.50 for flexible connections. For suspended ceiling components (Category 7), the NBC specifies C_P = 1.00, A_r = 1.00, and R_P = 2.50. The S_P factor is constrained to be not less than 0.7 and not greater than 4.0. The NBC offers two approaches for calculating the height factor A_X of the S_P formulation:

1. **NBC 2020 Method ($S_P(1)$):** The current code uses a simplified, linear amplification factor based on the component's relative height in the structure, as shown in Equation 5.2:

$$A_X = 1 + 2\frac{h_x}{h_n} \tag{5.2}$$

This approach, designated as $S_P(1)$ in this study, assumes that the A_x factor increases linearly from the base to the roof, reaching a maximum value of 3.

2. **Alternative Code Method ($S_P(2)$):** A new, more detailed formulation has been recommended for future NBC editions (CBHCC, 2024) to better capture the dynamic response of buildings, as shown in Equation 5.3:

$$A_X = \frac{1+\frac{1}{T_{ao}}\left(\frac{h_x}{h_n}\right)+\left(1-\left(\frac{0.4}{T_{ao}}\right)^2\right)\left(\frac{h_x}{h_n}\right)^{10}}{\sqrt{\frac{1.1R_{do}}{I_E}}} \tag{5.3}$$

This method, designated as $S_P(2)$ in this study, incorporates the building's fundamental period (T_{ao}), structural ductility-related modification factor (R_{do}), and the importance factor for the building (I_E), aiming for a more realistic demand prediction. However, while $S_P(2)$ incorporates R_{do} to reduce demands based on structural ductility capacity, it relies on empirical fundamental

period formulas (T_{ao}) that are calibrated to elastic structural behavior and do not capture the dynamic characteristic changes that occurs when structures respond nonlinearly under strong seismic loading.

To evaluate these code provisions against the proposed factors from this study (Section 5.5, Table 2.4), Table 5.2 compares the S_P values computed using both NBC methods across different building heights and component categories:

Table 5.2 Comparison of S_P values for NSC categories across building heights using two NBC calculation methods

			3 Storey		6 Storey		9 Storey		12 Storey	
Component Category	Specific Component	Specific Elevation	S_P (1)	S_P (2)	S_P (1)	S_P (2)	S_P (1)	S_P (2)	S_P (1)	S_P (2)
Suspended ceilings, light fixtures, and other attachments to ceilings		Intermediate level	0.7	0.7	0.7	0.7	0.7	0.7	0.7	0.7
		Roof level	1.4	1.43	1.4	1.05	1.4	0.92	1.4	0.86
Machinery, fixtures, equipment, and tanks (including contents)	Flexibly connected	Intermediate level	1.55	1.57	1.42	1.25	1.42	1.19	1.42	1.15
		Roof level	3.5	3.57	3.5	2.61	3.5	2.3	3.5	2.15
	Rigidly connected	Intermediate level	1.25	1.26	1.13	1.003	1.13	0.95	1.13	0.92
		Roof level	2.8	2.85	2.8	2.09	2.8	1.85	2.8	1.72

Analysis of Table 5.2 for the studied NSC categories (suspended ceilings and machinery components) reveals three key patterns. At intermediate floors, both NBC methods produce similar results: ceiling components reach the minimum S_P value of 0.7, while machinery components show only minor differences between $S_P(1)$ and $S_P(2)$, with $S_P(2)$ being slightly lower in most cases. At roof levels, $S_P(1)$ remains constant regardless of the building height (1.4 for ceilings, 3.5 for flexible machinery, 2.8 for rigid machinery), whereas $S_P(2)$ decreases as building height increases. The largest differences occur in tall buildings at the roof level: for the 12-storey building, $S_P(2)$ predicts substantially lower values than $S_P(1)$, with ceiling components dropping from 1.4 to 0.86, flexible machinery from 3.5 to 2.15, and rigid machinery from 2.8 to 1.72, representing approximately 40% reductions. These patterns

establish the baseline for comparison with the nonlinear analysis results presented in Section 5.4.2.

5.4.2 Component force factor (S_P)

The results are presented as a function of the component-to-building period ratio (T_c/T_{b1}), where T_{b1} is the fundamental period of the building and T_C is the component period, as illustrated in Figure 5.2.

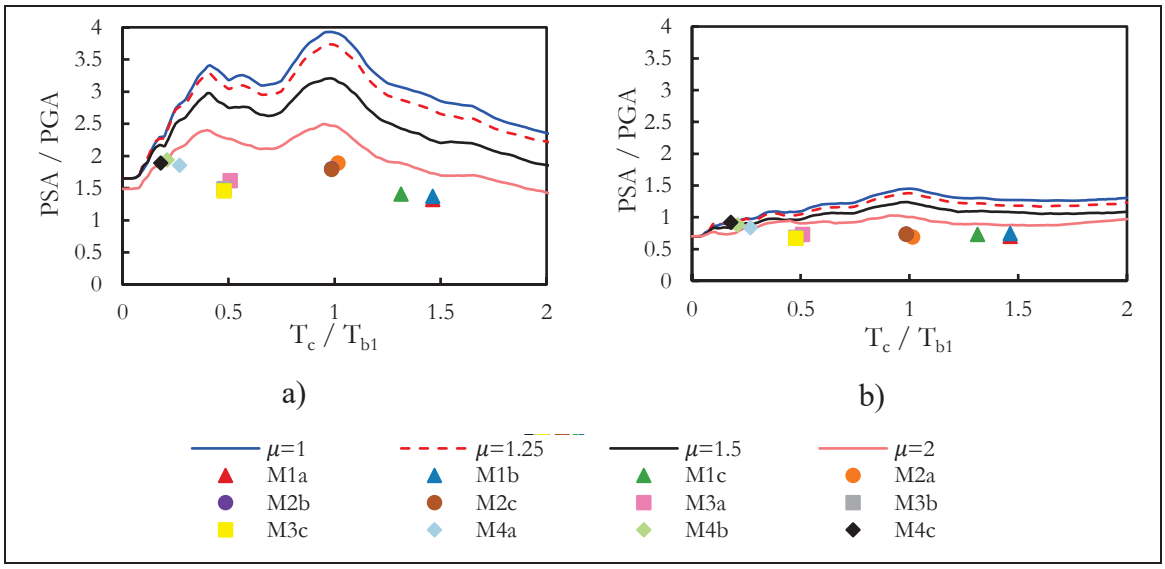

Figure 5.2 Mean PSA/PGA values of archetype buildings at two building elevations: (a) roof, (b) Intermediate

Figure 5.2 reveals distinct elevation-dependent response patterns across all ductility levels, with roof-level NSCs experiencing significantly higher amplification than those at intermediate floors. At the roof level (Figure 5.2a), the PSA/PGA spectra exhibit a distinct amplification, with PSA/PGA ratios of 3.5-4.0 in the resonant period range ($T_c/T_{b1} \approx 0.5$-1.5), showing a pronounced peak that gradually declines at longer periods. In contrast, intermediate floors (Figure 5.2b) demonstrate markedly different behavior with significantly lower amplification (peak ratios of 1.5-2.0) and flatter response spectra that remain stable across the period range. Beyond $T_c/T_{b1} \approx 1.5$, intermediate floors responses converge toward ratios of

approximately 0.95-1.2, while roof levels maintain higher amplification (1.4-2.2), indicating off-resonance dominance.

Another key finding is that the building nonlinearity substantially reduces seismic demands compared to elastic building assumptions (Mehrjoo & Assi, 2024), as summarized in Table 5.3. For elastic components ($\mu_{comp} = 1$), incorporating building nonlinearity reduces seismic demands by 67% at the roof level (from 11.9 to 3.92) and 78% at intermediate floors (from 6.46 to 1.45). This demonstrates that traditional elastic building assumptions noticeably overestimate NSC demands.

Beyond the effects of building nonlinearity, component ductility provides further reductions, primarily at the roof level. Increasing component ductility from elastic behavior ($\mu_{comp} = 1$) to moderate levels ($\mu_{comp} = 1.5$) decreased predicted S_P values at the roof by 15% (from 4.0 to 3.4), while high ductility ($\mu_{comp} = 2$) achieves an additional 21% reduction (from 3.4 to 2.7). In contrast, these ductility-related benefits are minimal at intermediate floors, where values remain relatively constant regardless of component behavior.

The analytical mean-response curves are validated by 12 NSC models (M1a-M4c), represented as individual data points distributed across the period ratio range ($T_c/T_{b1} \approx 0.2$ to 1.5) in Figure 5.2. Most points fall below the mean analytical curves at both elevations, confirming the conservative nature of the mean-response curves. The greater vertical variation at the roof level (Figure 5.2a) reflects a stronger influence of component characteristics such as attachment flexibility, mass distribution, and modal properties, while the reduced spread at intermediate floors (Figure 5.2b) confirms their lower sensitivity.

Evaluation of the nonlinear analysis results against current NBC provisions in Table 5.2 reveals considerable shortcomings in the code formulations. For flexibly connected equipment at the roof of the 12-storey building, $S_P(1)$ yields 3.5, which is below the 3.92 obtained from nonlinear analysis for components with elastic behavior ($\mu_{comp} = 1$). The alternative method, $S_P(2)$, exhibits an even more pronounced underestimation, calculating an S_P of only 2.15 for the same configuration, nearly 45% below the nonlinear analysis value of 3.92. Similarly, for rigidly connected equipment, $S_P(2)$ predicts only 1.72 compared to 3.92 from the nonlinear analysis. The results demonstrate that current code provisions inadequately capture the nonlinear dynamic amplification effects observed in this study. This conclusion aligns with

recent research showing that current code provisions, which rely on linear formulations, tend to underestimate NSC amplification factors and fail to reliably predict peak acceleration responses (Challagulla et al., 2023; Pürgstaller et al., 2020). In particular, Fazileh et al. (2025) reached similar conclusions for Canadian RC moment-resisting frames when assessing the NBC 2025 equations against floor-response-spectrum demands.

5.5 Proposed factors based on obtained results

This section presents the proposed S_P factors that incorporate both structural nonlinearity and component ductility effects, providing a realistic representation of seismic demands compared to traditional elastic assumptions. Table 2.4 presents both the computed mean and proposed S_P values, which are conservatively defined as the mean plus one standard deviation (Mean + STD). For comparison, the "Linear building" column shows S_P values from previous analysis assuming elastic building behavior (Mehrjoo & Assi, 2024).

Table 5.3 Computed mean S_P values for linear and nonlinear buildings with proposed design values for intermediate and roof levels

μ_{comp}	Specific Elevation	Linear building	Nonlinear building	STD	Proposed Values
1	Intermediate level	6.46	1.45	0.39	1.9
	Roof level	11.9	3.92	0.18	4
1.25	Intermediate level	3.8	1.38	0.39	1.8
	Roof level	7.0	3.73	0.18	3.9
1.5	Intermediate level	2.4	1.23	0.3	1.5
	Roof level	4.5	3.2	0.21	3.4
2	Intermediate level	2.15	1.0	0.2	1.2
	Roof level	2.7	2.47	0.19	2.7

In Table 5.3, the small standard deviations (0.18-0.39) indicate high consistency across all building heights and ground motion records, confirming the reliability of the mean predictions. Consequently, the proposed values introduce only a minimal conservative margin, for instance, 4.0 versus 3.92 at the roof for elastic components, thereby ensuring safety without excessive conservatism.

For design purposes, S_p factors should be selected based on the attainable ductility of attachment. For components with standard rigid connections, the values in the $\mu_{comp} = 1$ row are recommended ($S_P = 4.0$ at the roof, 1.9 at the intermediate floors). Where reliable ductile detailing can be implemented, the moderate ductility level ($\mu_{comp} = 1.5$) is recommended as the optimal design target, providing justified reductions ($S_P = 3.4$ at the roof) that translate directly to reduced installation and repair costs. Higher ductility levels ($\mu_{comp} = 2$) offer minimal additional benefit and are generally not recommended due to increased detailing complexity and uncertainty in nonlinear response.

5.6 Conclusion

This study investigates the influence of structural nonlinearity and component ductility on the component force factor (S_P) for acceleration-sensitive NSCs. The analysis validated using the responses of 12 detailed NSC models, which showed excellent agreement with the computed mean response curves, yields key findings that provide quantitative evidence of substantial inaccuracies in current NBC provisions. These findings point toward more refined design approaches, particularly for taller buildings.

First, this study quantifies the combined effects of structural nonlinearity and component ductility on NSC demands, demonstrating reductions of 15-34% compared to traditional elastic analysis, depending on component ductility levels.

Second, a moderate component ductility of $\mu_{comp} \approx 1.5$ emerges as the optimal design target, reducing the roof-level S_P value substantially from 4.0 (elastic) to 3.4. This level of ductility offers considerable benefit while avoiding the complex and less predictable responses observed at higher ductility levels.

Third, component elevation is an important factor, with roof-level NSCs experiencing S_P demands that are 111-127% higher than those at intermediate floors. Moreover, the beneficial effects of component ductility are also most significant at the roof level.

Fourth, comparison with current NBC provisions indicates that both approaches are unconservative for mid- to high-rise buildings. The NBC 2020 approach ($S_P(1)$) is inaccurate because its assumed linear acceleration amplification profile does not to represent the true

dynamic response of nonlinear structures. The alternative NBC approach ($S_P(2)$) becomes particularly unconservative at the roof level, underestimating seismic demands by over 35% in some cases, owing to its reliance on empirical fundamental period formulas that fail to capture structural nonlinear behavior under seismic loading. Furthermore, neither NBC approaches explicitly accounts for the level of ductility of NSC attachments (μ_{comp}) in the S_P calculation, overlooking the considerable potential for reducing seismic demands through controlled component nonlinearity.

CONCLUSION

This thesis demonstrated the significant role of NSC attachment ductility in seismic design and performance assessment for reinforced concrete buildings in a moderate seismicity region (Montreal, Canada). The research addressed four specific objectives, yielding the following key findings:

Objective I: Ductility-Based Modification Factors

The first objective established improved and reliable acceleration response factors (A_r/R_p), inelastic velocity ratios (IVR), and inelastic displacement ratios (IDR) that characterize the ductile behavior of NSCs at elevated floor and ground levels. The following key outcomes were obtained:

- Consistent trends exist between historical and synthetic ground motions. While historical inputs result in slightly higher A_r/R_p, IVR, and IDR factors across both 2% and 10% exceedance scenarios compared to synthetic inputs, the differences are minor. This suggests that the choice of ground motion input has a limited impact on the seismic design and performance of NSCs, even at higher ductility levels, consistent with previous findings by Galasso et al. (2012).
- The R_p values derived from this study align well with the theoretical formula proposed by Chopra (2011), validating the accuracy of this study's approach in capturing the ductility behavior of NSCs.
- The seismic response, in terms of peak acceleration, velocity, and displacement demands, is dependent on the ductility of NSCs and on the resonance period range. Acceleration responses exhibited three distinct peaks, indicating significant amplifications during the fundamental mode and higher modes, with the fundamental mode playing a dominant role in NSCs' acceleration demands. In contrast, displacement and velocity demands were primarily governed by the fundamental mode, as evidenced by a single peak in their responses. Within the resonance period range, increased ductility effectively mitigates amplification effects, whereas components

with limited ductility remain subject to significantly higher seismic demands. Outside the resonance period range, the influence of ductility on these demands diminishes.

- The A_r/R_p for elastic components located at the roof level is more likely to exceed the NBC-specified value of 2.5, which is associated with an R_P of 1. However, ground-level components typically exhibit A_r/R_p values below 2.5, suggesting that the standard's design limit provides adequate safety for these ground-level components.
- The impact of changing ductility has a greater significance on floor accelerations than its effect on floor displacement and velocity.

Objective II: Fragility Assessment and Optimal Ductility Levels

The second objective evaluated the fragility of NSCs subjected to seismic loading, investigating the effects of ductility levels of NSC attachments and resonance period ranges (T_1, T_2, T_3) on their performance. The following main findings were concluded:

- NSCs at roof levels are significantly more vulnerable to seismic damage compared to those at intermediate or ground levels, confirming the height-dependent amplification effects observed in the first phase of this research.
- As resonance shifts from the fundamental resonance period T_1 to higher ones (T_2, T_3), the seismic behavior of NSCs changes significantly. This shift results in component acceleration demands becoming less sensitive to structural nonlinearity and attachment ductility, particularly in taller buildings.
- While increased ductility levels reduce seismic forces, they may also increase the risk of localized damage to NSCs and their attachments. Therefore, achieving an optimal balance between ductility and acceptable damage levels is critical in NSC seismic design.
- Incorporating the nonlinear behavior of the supporting structure demonstrated that structural yielding generally attenuates floor acceleration demands, thereby reducing the seismic demands imposed on NSCs across damage states and resonance ranges.
- For acceleration-sensitive NSCs, adopting moderate ductility levels ($\mu_{comp} \approx 1.5$) emerges as the optimal design target. As shown in Table 3.5 and Table 3.6, the incremental PFA reduction per unit increase in ductility remains substantial between

μ_{comp} = 1.0 and μ_{comp} = 1.5 but decreases markedly beyond μ_{comp} = 1.5, indicating that the performance gains from additional ductility become progressively less efficient. This trend is more pronounced for nonlinear structures, where structural yielding already reduces floor demands, leaving less margin for further improvement through component ductility alone.

Objective III: Economic Impact of Component Ductility and Detailing

The third objective assessed the seismic vulnerability of suspended ceiling and chiller systems using three complementary metrics: repair cost, loss ratio, and repair ratio. The following conclusions were derived from the obtained results:

- Enhanced, higher-frequency components (M3 ceilings, M4 chillers) significantly outperform standard designs by raising damage initiation thresholds, demonstrating the economic value of improved component detailing and design.
- Suspended ceilings proved far more vulnerable than chillers, incurring three to five times higher repair costs due to their broader spatial distribution and greater sensitivity to acceleration demands.
- Component location was identified as an important factor, with top-floor ceilings experiencing substantially higher damage and costs due to amplified seismic demands at elevated levels, consistent with the height-dependent vulnerability patterns identified in the first and second phases of this research.
- Moderate ductility enhancements ($\mu_{comp} \approx 1.6–1.7$) provide significant economic benefits, reducing expected repair costs by approximately 30% for suspended ceilings and 7–9% for chillers compared to their standard low-ductility counterparts. This reduction is primarily driven by the attenuation of peak acceleration demands through component nonlinearity, which delays the onset of damage states associated with costly repairs.
- An integrated approach that combines enhanced attachment ductility with strategic placement delivers consistent performance improvements across different building configurations. These findings align with the conclusions of Ciurlanti et al. (2022) and Gallo et al. (2018), who reported that enhanced connection details reduce NSC damage in experimental testing.

Objective IV: Component Force Factors Accounting for Structural Nonlinearity

The fourth objective quantified the combined effects of structural nonlinearity and NSC attachment ductility on seismic force demands. The following key findings were obtained:

- Structural yielding substantially reduces floor accelerations compared to elastic assumptions, with reductions of 67-78% for components with elastic attachments (μ_{comp} = 1.0) and 9-64% for components with ductile attachments. The magnitude of reduction decreases as NSC attachment ductility increases.
- The derived component force factors (S_P) quantify the force reduction benefits of ductility, showing that moderate component ductility ($\mu_{comp} \approx 1.5$) lowers the roof-level S_P factor from 4.0 (elastic) to 3.4. Increasing ductility further to μ_{comp} = 2.0 reduces S_P to 2.7. This corresponds to a ~20% reduction in demand for a ductility increase of 0.5 (from μ_{comp} = 1.5 to 2.0), compared to a 15% reduction observed over the smaller ductility increase of 0.25 (from μ_{comp} = 1.25 to 1.5). In other words, beyond μ_{comp} = 1.5, the rate of S_P reduction with respect to ductility decreases by approximately 50%. Moreover, NIST GCR 18-917-43 (ATC, 2018a) documents that achieving ductility levels of μ_{comp} = 2.0 in typical acceleration-sensitive components imposes severe detailing requirements, such as tripling anchor density and substantially reducing storage capacity, that limit practical implementation. The moderate ductility target of $\mu_{comp} \approx 1.5$, therefore, provides the most favorable balance between force reduction and constructability.
- Comparison with NBC 2020 provisions reveals important shortcomings in current code approaches. The current NBC 2020 approach underestimates demands by failing to capture nonlinear dynamic amplification, while the NBC 2025 formulation (referred to as the alternative formulation in Chapter 5) underestimates roof-level accelerations by over 35% due to its reliance on empirical period formulas that cannot accurately represent structural yielding.

  Specifically, the NBC 2025 height factor (Equation 1.3) uses the empirical elastic period T_{ao} as input, which remains constant regardless of seismic intensity. Under strong ground motions, it is expected that structural yielding causes period elongation

and stiffness degradation that shift the building's dynamic characteristics away from their elastic values(Fazileh et al., 2025). Significantly, neither NBC approach explicitly accounts for NSC attachment ductility (μ_{comp}), missing opportunities for substantial demand reduction through controlled component nonlinearity.

RECOMMENDATIONS FOR FUTURE STUDIES

Extensive efforts were made in the present thesis to emphasize the importance of accounting for the ductility levels of non-structural component (NSC) attachments in seismic design and performance assessment. However, further analytical studies are required to confirm and expand the observations obtained in this study. Therefore, the following research directions are recommended for future work:

- Perform time history analysis on different building types, including steel moment-resisting frames, shear wall systems, braced frames, and dual systems to establish A_r/R_P, IVR, and IDR values for a broader range of structural systems beyond the four RC moment-resisting frame buildings analyzed in this study.
- Perform comparative analyses using ground motion records selected to match the Conditional Mean Spectrum (CMS), which represents hazard-consistent spectral shapes conditioned on magnitude, distance, and epsilon, versus the UHS scaling employed in this study, to evaluate the impact of ground motion spectral variability on the proposed Ar/Rp, IVR, and IDR design factors.
- Extend the analysis to different seismic zones across Canada, including Western Canada, and compare the obtained A_r/R_p, IVR, and IDR values with those from Montreal to establish region-specific factors that account for varying seismicity levels and ground motion characteristics.
- Conduct parametric studies to evaluate the effect of different site classes (A, B, D, E) on the A_r/R_P, IVR, and IDR values, expanding beyond the Site Class C considered in this research to provide comprehensive design factors for various soil conditions.
- Validate and refine the proposed A_r/R_p and S_P factors through experimental testing. This work should also seek to expand its applicability by investigating a broader range of component ductility levels (e.g., μ_{comp} = 1.75, 2.5, 3.0), extending beyond the values analyzed in this study (μ_{comp} = 1, 1.25, 1.5, 2).
- Investigate the fragility of NSCs under combined horizontal and vertical acceleration demands to assess the multi-directional effects on damage states and incorporate these findings into performance-based seismic assessment frameworks.

- Broaden the economic vulnerability assessment to include additional NSC types such as piping systems, medical equipment, fire protection systems, and building facades to create a comprehensive database of repair costs, loss ratios, and repair ratios for performance-based design.
- Investigate the effects of soil-structure interaction and foundation flexibility on NSC seismic demands by incorporating compliant foundation modeling, moving beyond the fixed-base assumption employed in this study.
- Extend the assessment to structures with plan asymmetries and vertical irregularities. While this study derived design factors based on translational floor motions in symmetric buildings, irregular structures produce torsional responses that create coupled translational-torsional floor demands with distinct spectral characteristics. Future research should investigate whether the proposed ductility-based factors (A_r/R_P, IVR, and IDR) remain applicable under these coupled floor motions or if adjustments are required to account for the modified dynamic amplification patterns generated by structural torsion. Such an investigation would require three-dimensional (3D) structural models capable of capturing coupled translational-torsional response at each floor level.

ANNEX I

STRUCTURAL PROPERTIES OF CASE STUDY BUILDINGS

This annex summarizes the structural properties and member dimensions of the four case study reinforced concrete moment-resisting frame buildings (3-, 6-, 9-, and 12-storey) used throughout this thesis. Table-A I-1 (a) presents the common configuration, material properties, and modeling parameters shared by all buildings, while Table-A I-1 (b) lists the building-specific beam and column cross-sectional dimensions. These archetype buildings, originally designed according to NBC 2015 (NRC, 2015) and CSA A23.3-14 (CSA, 2014a) for moderately ductile RC frame construction, were adopted from Mazloom (2023) and serve as mand analyses presented in Chapters 2 through 5.

Table-A I-1 Structural properties of the four case study RC moment-resisting frame buildings (adapted from Mazloom (2023))

(a) Common Properties (All Buildings)

BUILDING CONFIGURATION	MATERIAL PROPERTIES	MODELING PARAMETERS
Story height: 3.0 m	**Concrete mean strength (f'_c):** 35 MPa	**Effective stiffness of Beams:** 0.40 EIg
Bay spacing: 3 x 7.0 m	**Concrete modulus (E_c):** 30.5 GPa	**Effective stiffness of Columns:** 0.70 EIg
Slab thickness: 140 mm	**Concrete unit weight:** 24 kN/m³	**Effective stiffness of Slabs:** 0.20 EIg
	Steel yield strength (f_y): 400 MPa	**Damping ratio:** 5% (Rayleigh)
	Steel ultimate strength (f_u): 440 MPa	**Hysteretic model:** ASCE 41-23 Concentrated plastic hinges (see ANNEX II, Table-A II-1)
	Steel modulus (E_s): 200 GPa	

(b) Building-Specific Member Dimensions (mm)

Building	3-Storey	6-Storey	9-Storey	12-Storey
Columns (b×h) mm	400×400	600×600	700×700	800×800
Beams (b×h) mm	350×400	400×600	500×650	600×750

The Detailed floor-by-floor reinforcement layouts (including flexural and shear reinforcement specifications for all beams and columns) are provided in Mazloom (2023), Appendix IV, Tables A IV-1 through A IV-16. Additional structural and dynamic characteristics of these

buildings could be found in Mazloom (2023), Mazloom and Assi (2022), and Mehrjoo and Assi (2024, 2025a).

ANNEX II

REQUIRED INPUT AND OUTPUT DATA FOR THE PUSHOVER ANALYSIS IN ETABS

This annex presents the input parameters and output results from pushover analyses in ETABS for the four archetype buildings (3, 6, 9, and 12-storey). Table-A II-1 summarizes plastic hinge properties (PHB: beams, PHCE: columns), including yield moment capacities (M_y), backbone curve parameters (a, b, c), and performance level rotation limits (IO, LS, CP) per ASCE 41-23 (ASCE, 2023). Target roof displacement was calculated using Equation 3.1 in CHAPTER 3, while yield displacement was obtained from pushover results.

Table-A II-1 Required input and output data for the pushover analysis

		Hinge properties used in ETABS									Output	
Case study	Target disp (m)	Hinge name	My (kN-m)		a	b	c	IO	LS	CP	Storey level	Yield disp(m)
			+	-								
3 Storey	0.72	PHB01	284.6	284.6	0.025	0.05	0.2	0.01	0.025	0.05	1st	0.05
		PHB02	227.4	266	0.025	0.05	0.2	0.01	0.025	0.05	2nd	0.071
		PHB03	222.2	222.2	0.025	0.05	0.2	0.01	0.025	0.05		
		PHB04	154.1	205.5	0.025	0.05	0.2	0.01	0.025	0.05	3rd	0.091
		PHCE01	-	-	0.038	0.078	0.2	0.005	0.039	0.05		
6 Storey	0.84	PHB01	651.5	651.5	0.02	0.03	0.2	0.005	0.02	0.03	1st	0.032
		PHB02	762.5	762.5	0.02	0.02	0.2	0.005	0.02	0.03	2nd	0.057
		PHB03	325.1	252.3	0.019	0.029	0.2	0.005	0.0193	0.029	3rd	0.098
		PHB04	250.2	176.3	0.019	0.029	0.2	0.005	0.0193	0.029	4th	0.102
		PHCE01	-	-	0.041	0.058	0.2	0.005	0.029	0.04	5th	0.122
		PHCE02	-	-	0.047	0.068	0.2	0.005	0.034	0.048	6th	0.133
9 Storey	1.5	PHB01	1076	865.6	0.01	0.015	0.2	0.0015	0.01	0.015	1st	0.036
		PHB02	1267	1190	0.01	0.015	0.2	0.0015	0.01	0.015	2nd	0.075
		PHB03	1106	997.7	0.01	0.015	0.2	0.0015	0.01	0.015	3rd	0.109
		PHB04	933.1	730.3	0.01	0.015	0.2	0.0015	0.01	0.015	4th	0.125
		PHB05	690.1	455.1	0.01	0.015	0.2	0.0015	0.01	0.015	5th	0.14
		PHB06	772.4	371.7	0.02	0.03	0.2	0.005	0.2	0.03	6th	0.186
		PHB07	370.4	370.4	0.02	0.03	0.2	0.005	0.2	0.03	7th	0.202
		PHCE01	-	-	0.041	0.041	0.2	0.005	0.018	0.026	8th	0.213
		PHCE02	-	-	0.046	0.046	0.2	0.005	0.025	0.035	9th	0.22
12 Storey	1.77	PHB01	1729	1441	0.01	0.015	0.2	0.0015	0.01	0.015	1st	0.016
		PHB02	2094	2033	0.01	0.015	0.2	0.0015	0.01	0.015	2nd	0.038
		PHB03	1593	1438	0.01	0.015	0.2	0.0015	0.01	0.015	3rd	0.06
		PHB04	1793	1673	0.01	0.015	0.2	0.0015	0.01	0.015	4th	0.082
		PHB05	1593	1438	0.01	0.015	0.2	0.0015	0.01	0.015	5th	0.102
		PHB06	1321	1052	0.02	0.03	0.2	0.005	0.02	0.03	6th	0.12
		PHB07	1171	885.6	0.02	0.03	0.2	0.005	0.02	0.03	7th	0.134
		PHB08	1535	1209	0.02	0.03	0.2	0.005	0.02	0.03	8th	0.145
		PHB09	656.5	754	0.02	0.03	0.2	0.005	0.02	0.03	9th	0.156
		PHB10	559.9	751.1	0.02	0.03	0.2	0.005	0.02	0.03	10th	0.164
		PHCE01	-	-	0.04	0.04	0.2	0.005	0.01	0.014	11th	0.169
		PHCE02	-	-	0.045	0.045	0.2	0.005	0.022	0.031	12th	0.173

For completeness, Figure-A II-1 presents the corresponding pushover curves (base shear versus roof displacement) generated by ETABS, illustrating the progressive yielding behavior and the extraction points for yield displacements listed in Table-A II-1.

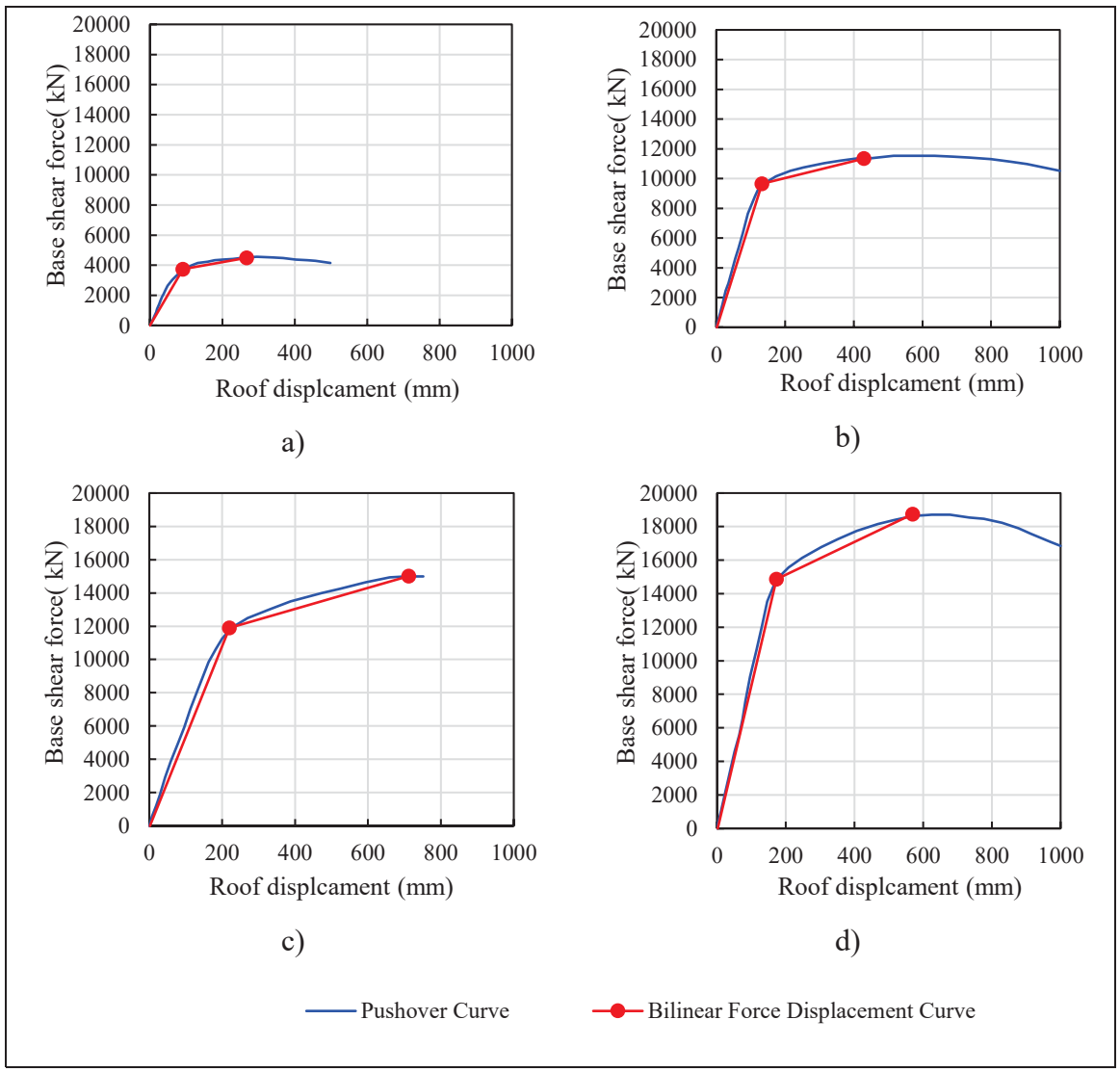

Figure-A II-1 ETABS pushover curves and FEMA 356 bilinear idealization for archetype buildings

ANNEX III

BACKBONE CURVES AND CYCLIC RESPONSE OF NSC MODELS

This annex documents the hysteretic response of the twelve nonlinear NSC models used in this study. All models employ the modified Ibarra–Medina–Krawinkler (IMK) peak-oriented deterioration formulation (OpenSees IMKPeakOriented). The complete backbone curve parameters $\left(\mathrm{K_0}, \mathrm{M_y}, \theta_\mathrm{y}, \alpha_\mathrm{s}, \mathrm{M_c}, \theta_\mathrm{p}, \mathrm{K_c}, \mathrm{M_r}, \theta_\mathrm{r}, \theta_\mathrm{u}\right)$ are presented in Table 4.1 (CHAPTER 4); the additional IMK-specific parameters (b/t, Λ) required for the cyclic deterioration formulation are summarized in Table-A III-1. Figure-A III-1 displays the cyclic moment-rotation relationships obtained from displacement-controlled analyses in OpenSees, where M represents the applied moment (kN·m), and θ represents the rotation (rad).

- **Modeling summary: Initial stiffness and yield strength**

The NSC rotational spring is defined with an elastic stiffness and yield strength as mentioned in Equations A III.1, A III.2, and A III.3.

$$K_0 = (2\pi f_a)^2 m \tag{A III.1}$$

where f_a is the target natural frequency (Hz) and m is the lumped mass at the degree of freedom. The yield moment is computed from section properties.

$$M_y = F_y S \tag{A III.2}$$

$$M_p = F_y Z \tag{A III.3}$$

with $\mathbf{F_y}$ the steel yield stress, **S** the elastic section modulus, and **Z** the plastic section modulus. Post-yield hardening is modeled by Equation A III.4.

$$K_p = \alpha K_0 \tag{A III.4}$$

with a hardening ratio $\alpha = 0.03$.

- **IMK backbone and cyclic deterioration parameters**

The backbone parameters governing pre-capping rotation (θ_p), post-capping rotation (θ_{pc}), and cyclic deterioration (Λ) were obtained from the published IMK peak-oriented calibrations to steel cyclic tests (Ibarra et al., 2005; Lignos & Krawinkler, 2013), as mentioned in Equation A III.5.

$$X = a(b/t)^b\left(1 - N/N_y\right)^c\left(C\sigma_y/380\right)^d \quad \text{(A III.5)}$$

with $X \in \{\theta_p, \theta_{pc}, \Lambda\}$, and the variables are defined as:

- b/t: Section slenderness (section dimension b over thickness t);
- N/N_y: The axial-load ratio. This is taken as **0** for the acceleration-sensitive NSCs in this study (e.g., ceilings, anchored equipment, cabinets) that do not carry sustained axial force in the modeled degree of freedom;
- σ_y: Yield strength of S275 steel (275 MPa);
- C: Stress conversion coefficient (1.0 for σ_y in MPa);
- {a, b, c, d}: Coefficient sets from IMK literature for peak-oriented hysteresis.

Substituting each model's ($b, t, \sigma_y, N/N_y$) yields θ_p, θ_{pc}, and Λ. Together with $\left(K_0, M_y, \alpha_s\right)$, and the residual strength ratio M_r/M_y (denoted κ in this section), these define the OpenSees IMKPeakOriented material for each NSC.

It is worth noting that the cyclic deterioration parameter Λ (summarized in **Error! Reference source not found.**) is distinct from the residual strength ratio κ (κ=0.25 was used); in the OpenSees input, the latter is specified as the ratio M_r/M_y, while the λ-parameters control deterioration.

Table-A III-1 Section slenderness b/t and cyclic deterioration parameter Λ for the twelve NSC models

Model ID	**M1a**	**M1b**	**M1c**	**M2a**	**M2b**	**M2c**	**M3a**	**M3b**	**M3c**	**M4a**	**M4b**	**M4c**
b/t	23.33	20	20	23.33	20	24	23.33	20	30	23.33	20	23.33
Λ (× 10^6)	2.22	1.26	1.26	2.22	1.26	2.52	2.22	1.26	5.92	2.22	1.26	2.22

- **Cyclic analyses and backbones**

The displacement-controlled cyclic analyses in OpenSees produce the symmetric hysteretic loops shown in Figure-A III-1 . The backbone for each model is obtained by enveloping the cyclic response; all backbones are plotted together in Figure 4.3(d), and the corresponding parameters $\left(K_0, M_y, \theta_y, \alpha_s, M_c, \theta_p, K_c, M_r, \theta_r, \theta_u\right)$ are listed in Table 4.1.

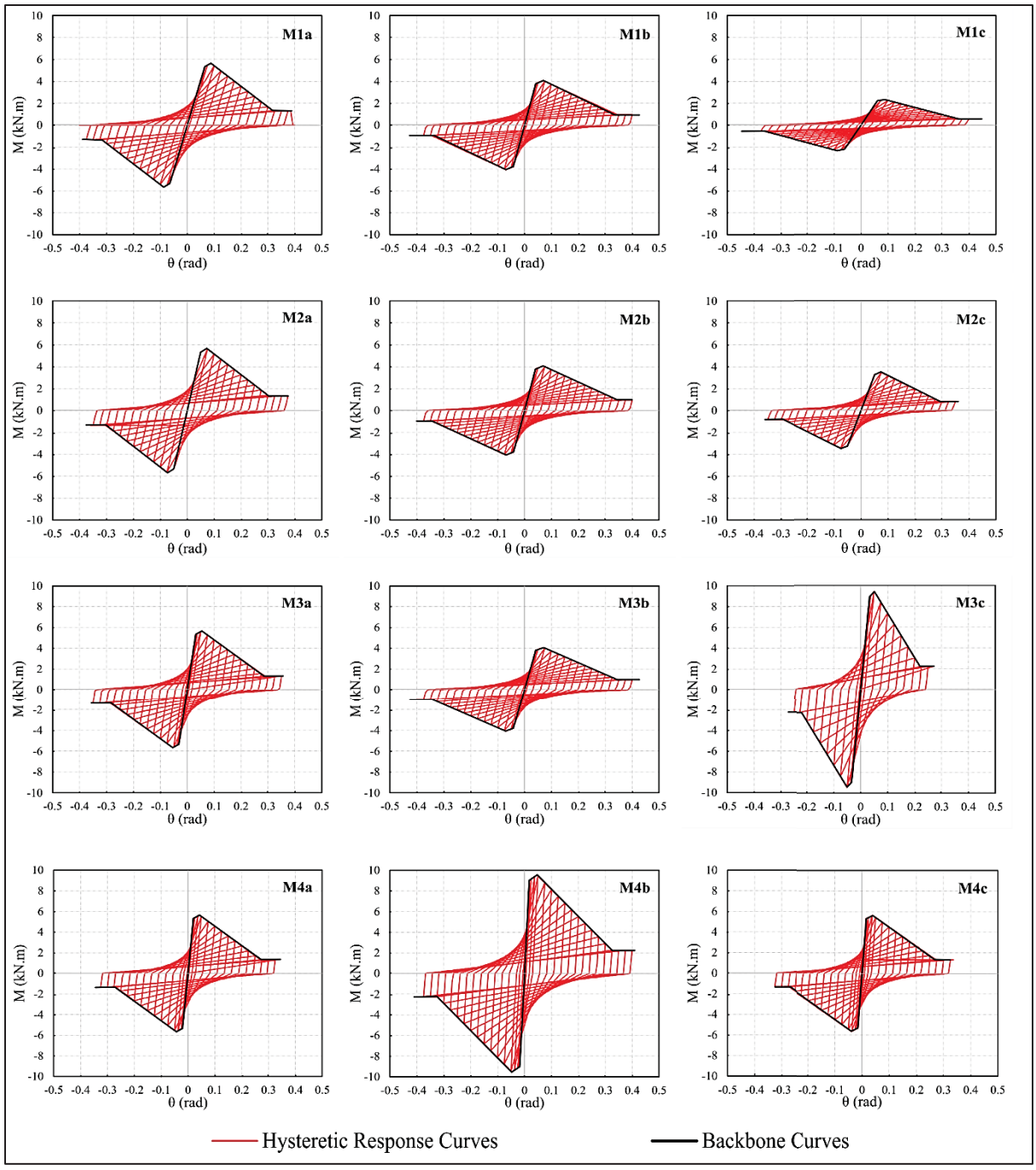

Figure-A III-1 Hysteretic response curves and backbone parameters for the twelve investigated NSC models, generated through displacement-controlled cyclic analyses in OpenSees

ANNEX IV

INCREMENTAL DYNAMIC ANALYSIS (IDA) CURVES FOR ALL CASE STUDIES AT ALL FLOOR LEVELS

This annex presents the floor-by-floor IDA results for all case study buildings (3-, 6-, 9-, and 12-storey). The 24 UHS-matched ground motion accelerograms were incrementally scaled from 0.1g to 4.0g in 0.1g increments (vertical axis, denoted as Sa (g)), and the resulting peak floor acceleration (PFA) responses were computed at each floor level (horizontal axis). In each subplot, gray lines represent individual earthquake record responses; the bold red line indicates the median response used for fragility derivation presented in Chapter 4.

Two distinct behaviors are observed: (1) lower floors exhibit steeper curves because their response closely follows the ground motion input, and (2) upper floors display flatter curves due to dynamic amplification effects. The curves approach horizontal asymptotes at input intensities between 3.0 and 4.0g, demonstrating acceleration saturation from structural yielding, confirming that the 4.0g upper limit captures all damage states.

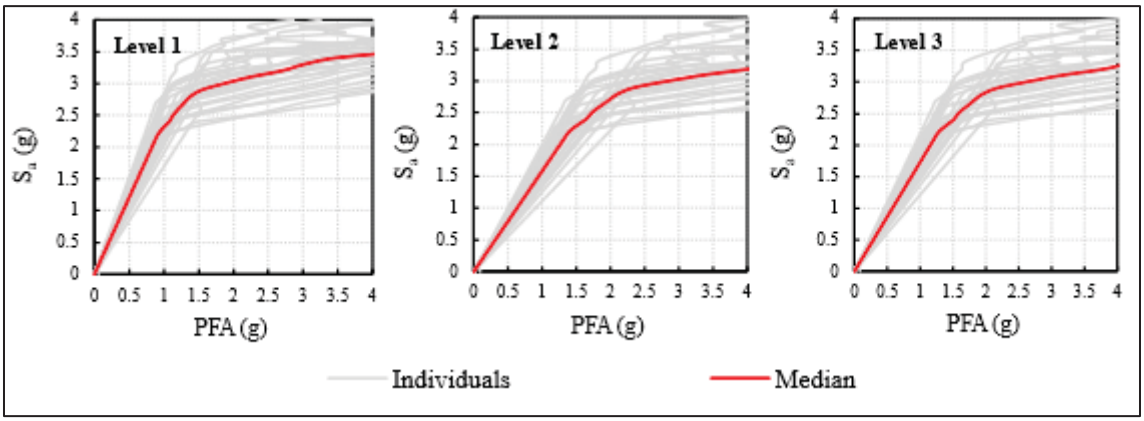

Figure-A IV-1 Floor-by-floor IDA curves for 3-storey building showing ground motion intensity measure Sa versus peak floor acceleration (PFA) response at each level

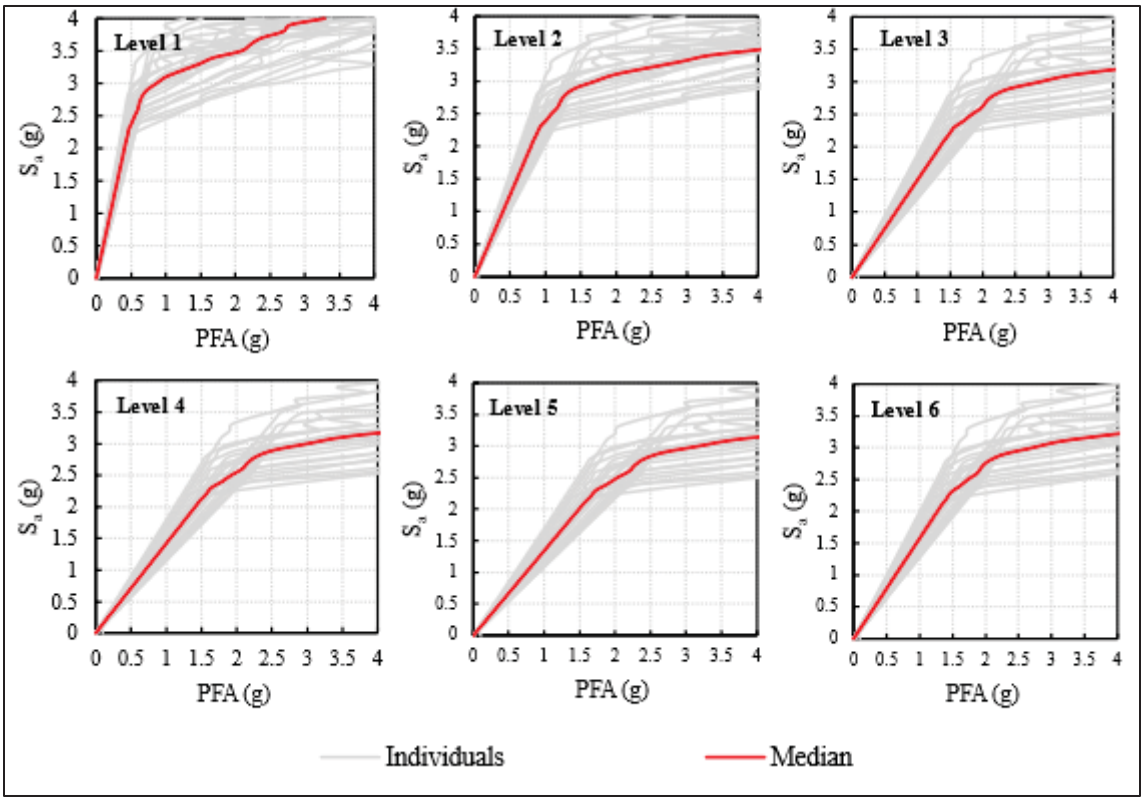

Figure-A IV-2 Floor-by-floor IDA curves for 6-storey building showing ground motion intensity measure Sa versus peak floor acceleration (PFA) response at each level

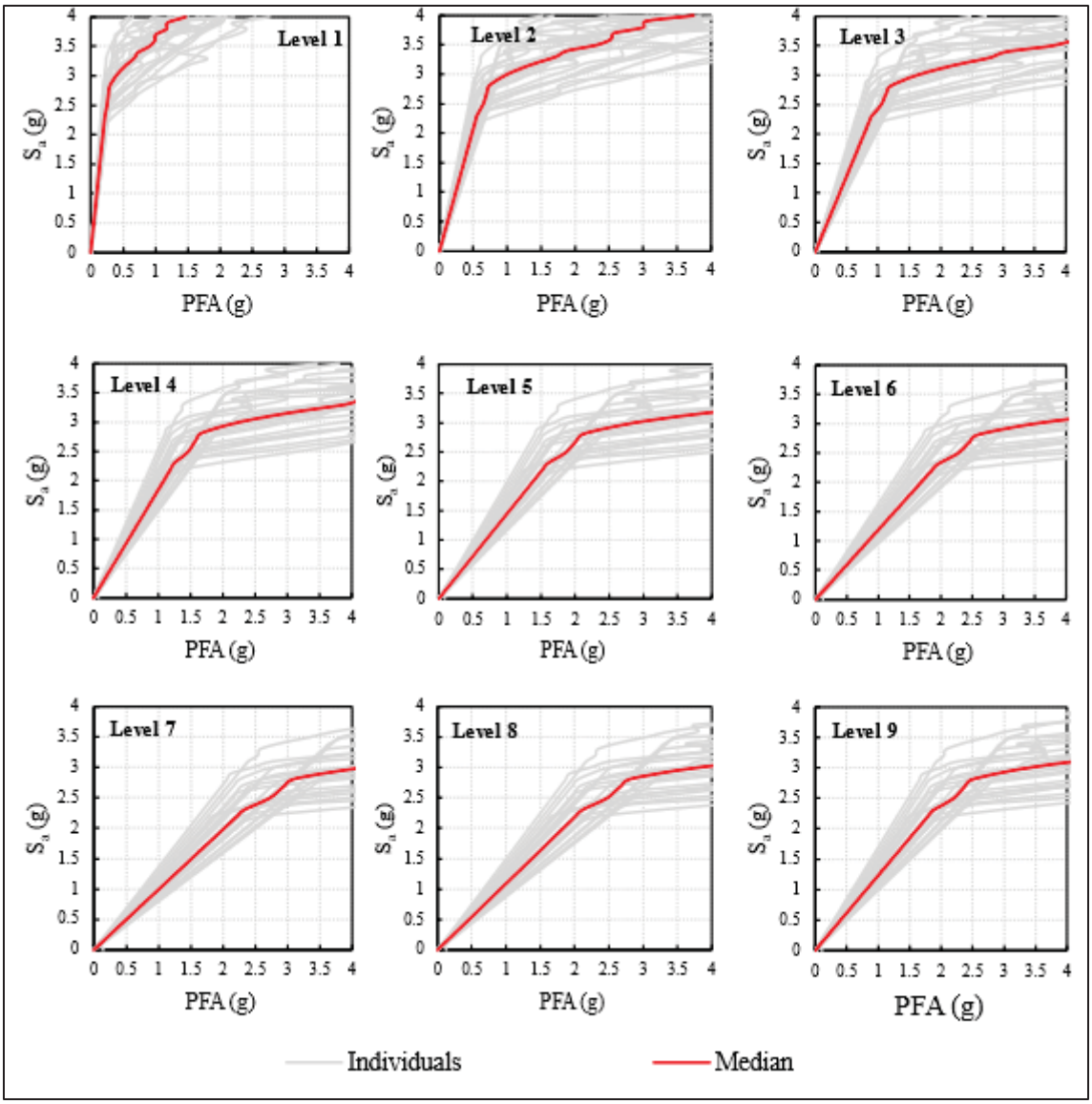

Figure-A IV-3 Floor-by-floor IDA curves for 9-storey building showing ground motion intensity measure Sa versus peak floor acceleration (PFA) response at each level

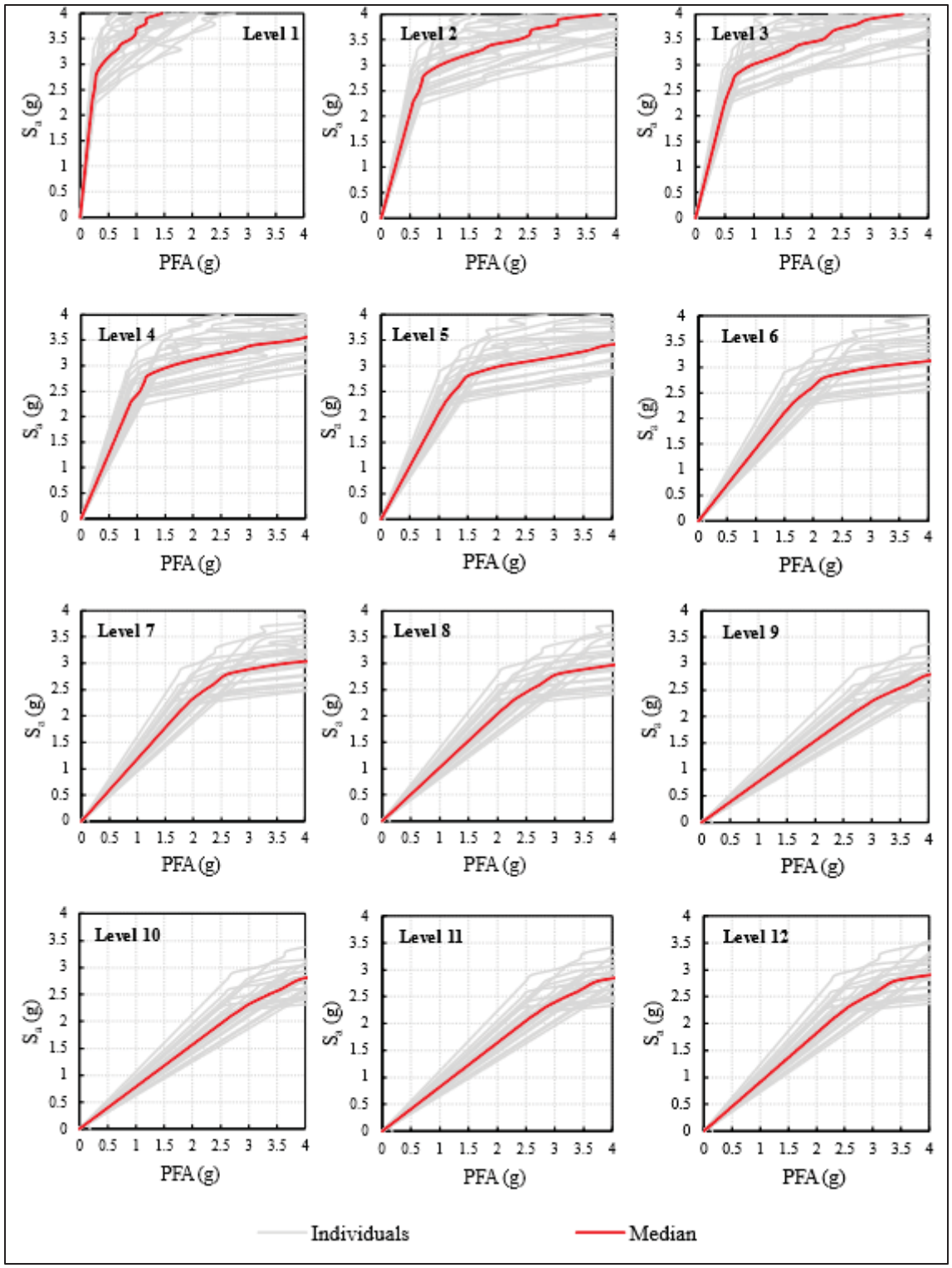

Figure-A IV-4 Floor-by-floor IDA curves for 12-storey building showing ground motion intensity measure Sa versus peak floor acceleration (PFA) response at each level

ANNEX V

FRAGILITY CURVES OF SUSPENDED CEILING AND CHILLER NSCS MODELS

This annex presents median-based fragility curves for NSCs models analyzed in Chapter 4. The assessment focuses on two primary component types:

- Suspended ceilings (M1: standard, M3: enhanced) with three damage states (DS1, DS2, DS3)
- Chillers (M2: standard, M4: enhanced) with a single damage state per FEMA P-58 guidelines

Fragility Assessment Methodology and PACT Implementation

To ensure consistency with the FEMA P-58 performance-based framework, the NSC models analyzed in this study were mapped to specific component classifications within the Performance Assessment Calculation Tool (PACT) database. The component identifiers, connection details, and fragility descriptions used are summarized below:

1. Suspended Ceiling Systems

- Standard Configuration (M1): Mapped to PACT ID C3032.001d.
    - Description: "Unbraced suspended ceiling, SDC A, B, C; Area > 2500 sq.ft."
    - Connection Detail: Vertical support only. Fragility is governed by the failure of vertical hanger connections or tile dislodgment.
- Enhanced Configuration (M3): Mapped to PACT ID C3032.003d.
    - Description: "Four-way diagonal wire-braced suspended ceilings, SDC D, E; Area > 2500 sq.ft."
    - Connection Detail: Vertical & Lateral support. Fragility accounts for the enhanced capacity provided by splay wires and compression posts.
    - Quantity Estimation: 1.89 units per floor (derived from 4,747 sq. ft. floor area / 2,500 sq. ft. normative unit area).

2. Chiller Systems

- Standard Configuration (M2): Mapped to PACT ID D3031.012a.
    - Description: "Unrestrained vibration-isolated chiller, Capacity < 100 Ton."

- Connection Detail: Vibration isolated equipment (not snubbed). Fragility is defined strictly by anchorage failure.

- Enhanced Configuration (M4): Mapped to PACT ID D3031.013d.
  - Description: "Seismically restrained chillers, Capacity 100 to <350 Ton."
  - Connection Detail: Seismic snubbers/restraints. Fragility is defined by the capacity of the restraint anchorage or hard anchors.
  - Quantity Estimation: 1 unit per building (rooftop installation).

Analysis Procedure

Nonlinear dynamic analyses were performed using 24 ground motions described in Chapter 4, scaled from 0.1g to 4.0g in 0.1g increments. For each record-scale pair, the PFA at the component location was extracted, and damage state exceedance was evaluated.

Fragility Function Development

Empirical exceedance probabilities were computed at each intensity level IM=x (with IM≡PFA), as mentioned in Equation A V.1.

$$P[\mathrm{DM} \geq \mathrm{LS} \mid \mathrm{IM} = x] \cong \frac{N_{\mathrm{fail}}}{N_{\mathrm{sim}}} \quad \text{(A V.1)}$$

Lognormal fragility functions were then fitted using maximum likelihood estimation (MATLAB fitdist) to obtain the parameters of ln (IM) as mentioned in Equation A V.2:

$$P[DM \geq LS \mid IM = x] = \Phi\left(\frac{\ln\left(x/\theta\right)}{\beta}\right) \quad \text{(A V.2)}$$

where:

- $\theta_i=\exp(\mu_i)$ is the median capacity (50% exceedance probability)
- $\beta_i=\sigma_i$ is the logarithmic dispersion
- Φ is the standard normal cumulative distribution function

Loss Assessment Metrics

The probabilistic loss assessment was conducted within PACT using a Monte Carlo simulation process with 200 realizations per intensity level, a count selected to ensure statistical convergence of the loss estimates consistent with the methodology of Magsalay (2025). The analysis convolved the custom fragility functions with the consequence functions to calculate three economic metrics:

- **Repair Cost:** The absolute economic impact (in CAD).
- **Loss Ratio:** Repair cost normalized by the total building replacement cost.
- **Repair Ratio:** Repair cost normalized by the component's replacement value.

Component-Specific Implementation

Suspended Ceilings (M1, M3)

Three separate fragility curves were developed corresponding to damage states DS1 (Slight), DS2 (Moderate), and DS3 (Extensive) as defined in Chapter 4. These curves quantify the progression of damage from minor tile dislodgment to grid collapse. The fitted lognormal parameters (θ_i, β_i) derived from the incremental dynamic analysis results ANNEX IV and fitted using maximum likelihood estimation (Equation 3.4) for each damage state and configuration are presented in Figure-A V-1 .

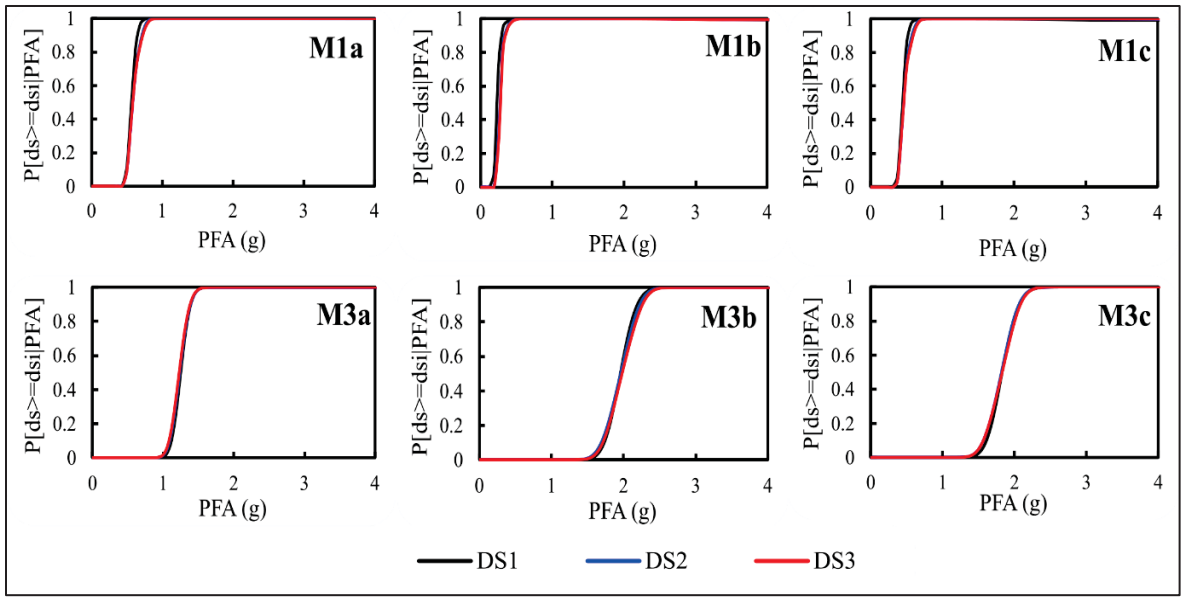

Figure-A V-1 Median-based fragility curves for the M1 and M3 NSC models

Chillers (M2, M4)

Following FEMA P-58 methodology for mechanical equipment, a single lognormal fragility threshold was developed using PFA as the intensity measure. Unlike suspended ceilings, which employ three separate fragility curves for progressive damage states (DS1–DS3), the chiller fragility is defined by a single threshold corresponding to the capping point of the anchorage system's force-deformation backbone curve. When this threshold is exceeded, PACT allocates the component to one of two mutually exclusive damage states, DS1 (anchorage failure only, 70% probability) or DS2 (anchorage plus mechanical/electrical damage, 30% probability), using the branching probabilities specified in the FEMA P-58 fragility database. The resulting fragility curves and their fitted parameters are presented in Figure-A V-2 .

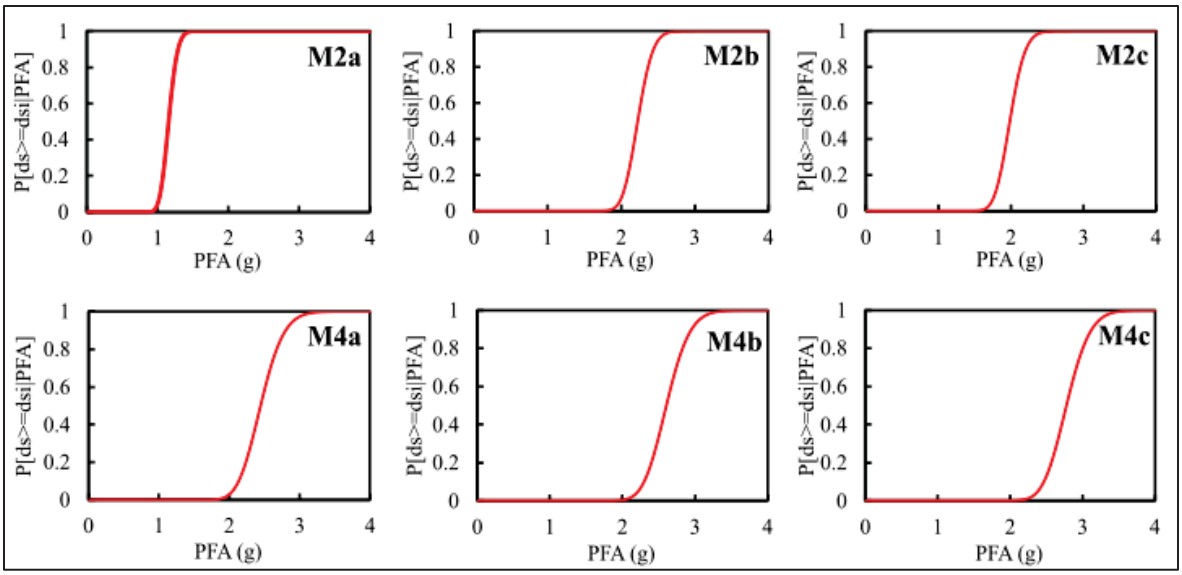

Figure-A V-2 Median-based fragility curves for the M2 and M4 NSC models

ANNEX VI

FREQUENCY DOMAIN MATCHING TECHNIQUE

This study employed frequency domain matching (Fahjan & Ozdemir, 2008) implemented through a MATLAB script to match both synthetic and historical earthquake records with Montreal's target Uniform Hazard Spectrum (UHS) for Site Class C. This approach is explicitly recognized in Section 4.2 of NBC 2015 Commentary J as an acceptable method for scaling ground motions, provided that the nonstationary amplitude–phase characteristics, energy measures (e.g., PGA/PGV/PGD and Arias intensity), and significant duration of acceleration, velocity, and displacement traces are carefully preserved. The frequency domain matching technique was selected for its ability to preserve the intrinsic characteristics of seismic ground motions, closely match the target spectrum, and optimize the computation time required for the spectral matching process (Gascot & Montejo, 2014).

The frequency domain matching procedure implemented in the MATLAB script involves the following steps:

1. **Computation of Original Response Spectrum**: The response spectrum of the original accelerogram is computed for the specified period range and damping ratio.
2. **Determination of Modification Factors**: Modification factors (*P_MODIF*) are calculated as the ratio between the target UHS spectral accelerations (*Sa_design_interp*) and the original response spectrum values (*Sa*) at each period (*P_MODIF(1,:) = Sa_design_interp ./ Sa(1,:)*).
3. **Fast Fourier Transform (FFT)**: The original acceleration time history is transformed to the frequency domain using FFT (*Y = fft(y, NFFT) / L*). The parameter *NFFT = 2^nextpow2(L)* sets the FFT length to the next power of two greater than or equal to the record length L. This zero-padding to a power-of-two length optimizes computational efficiency by allowing the FFT algorithm to run in a radix-2 configuration, and provides a finer, uniformly spaced frequency grid without altering the original time samples or their content.

4. **Frequency Domain Amplitude Adjustment**: The modification factors are interpolated to match the frequency values obtained from the FFT, and the Fourier coefficients are multiplied by these factors (*Y_modif(j-1,:) = Y * MODIF_Y(j-1,:)*), with special attention paid to aliasing by ensuring symmetric modification factors across the frequency spectrum.
5. **Inverse FFT**: The modified Fourier coefficients are transformed back to the time domain using inverse FFT (*y_recomposto_modif_aux = real(ifft(Y_modif(j-1,:)) * L)*).
6. **Iterative Refinement**: The process is repeated iteratively (*N_iter iterations*) to minimize spectral discrepancies between the scaled record and the target spectrum. A tapering function is applied at the beginning and end of the record to smooth transitions and preserve acceleration pulse characteristics.
7. **Scale Factor Computation**: A common scale factor is computed for each iteration to ensure that the mean response spectrum of the suite does not fall below 90% of the target spectrum across all periods (*SCALE_factor(j,:) = sum(P_MODIF(j,:)) / length(P_MODIF(j,:))*).

The above procedure was implemented in the MATLAB function F_AAG as follows:

Algorithm-A VI-1 MATLAB function F_AAG for FFT-based accelerogram matching

```
% INPUTS
%   original_accel = [time; acceleration; velocity; displacement]
%   N_iter         = number of FFT-matching iterations
%   Sa_elastic     = [T; Sa_target(T)] (UHS at damping z)
%   T              = period vector
%   z              = damping ratio (e.g., 0.05)
%   sfac           = pre-match PGA downscale factor
% OUTPUTS
%   Final_accelerogram = [time; acc; vel; disp] after matching
%   Sa                 = spectra at each iteration (rows)
function
[Final_accelerogram,Sa]=F_AAG(original_accel,N_iter,Sa_elastic,T,z,sfac)

% ---- TARGET & PRE-MATCH SCALING (SCALING STAGE #1) ----
ag              = Sa_elastic(2,1);              % target PGA anchor (g)
freq_spectra    = 1./T;                         % map periods to freq
Sa_design_interp = interp1(Sa_elastic(1,:),Sa_elastic(2,:),T);

% Pre-match PGA normalization with sfac (places record near target)
original_accel(2,:)=
original_accel(2,:)*ag/max(abs(original_accel(2,:)))*sfac;
```

Algorithm-A VI-1 MATLAB function F_AAG for FFT-based accelerogram matching (continued)

```
% ---- PREPARE TIME SERIES & CONTAINERS ----
time  = original_accel(1,:);
y     = original_accel(2,:);                    % acceleration (g)
dt    = time(2)-time(1);
Sa    = zeros(N_iter,length(T));

% Cosine taper to suppress Gibbs artifacts on IFFT
L         = length(y);
aux_var_1 = [0, 0.05, 0.95,1; 0, 1, 1,0];
aux_var_2 = interp1(aux_var_1(1,:),aux_var_1(2,:),0:1/(L-1):1);

P_MODIF      = zeros(N_iter,length(T));   % period-wise multipliers
SCALE_factor = zeros(N_iter,1);           % centering scalars

% ---- BASELINE SPECTRUM (iteration 1) ----
S_aux        = ARS([time;y],z,T);
Sa(1,:)      = S_aux(4,:);
P_MODIF(1,:) = Sa_design_interp ./ max(Sa(1,:), eps);
SCALE_factor(1)= mean(P_MODIF(1,:));          % SCALING STAGE #2 (init)
P_MODIF(1,:)   = P_MODIF(1,:) / SCALE_factor(1);

% ---- FFT PREP ----
Fs   = 1/dt;
NFFT = 2^nextpow2(L);                          % efficient zero-padding
Y    = fft(y,NFFT)/L;                          % base spectrum
f    = Fs*linspace(0,1,NFFT);

% Containers for iterative shaping
MODIF_Y = zeros(N_iter-1,NFFT);
Y_modif = zeros(N_iter-1,NFFT);
V_modif = zeros(N_iter-1,NFFT);
D_modif = zeros(N_iter-1,NFFT);
y_aux   = zeros(N_iter,L);  v_aux = zeros(N_iter,L);  d_aux =
zeros(N_iter,L);
y_aux(1,1:L)= original_accel(2,:);
v_aux(1,1:L)= original_accel(3,:);
d_aux(1,1:L)= original_accel(4,:);


% ---- ITERATIVE FREQUENCY-DOMAIN SHAPING (SCALING STAGE #2 each iter) --
--
for j=2:N_iter
    % Period-wise multipliers and centering scalar
    P_MODIF_aux = P_MODIF(j-1,:) .* SCALE_factor(j-1);

    % Interpolate multipliers to frequency grid, band-limited to
[fmin,fmax]
    for jj=1:(NFFT/2)
        if f(jj)>=freq_spectra(end) && f(jj)<=freq_spectra(1)
            MODIF_Y(j-1,jj)= interp1(freq_spectra, P_MODIF_aux, f(jj));
        else
            MODIF_Y(j-1,jj)= 1;    % no shaping outside target band
        end
    end
```

Algorithm-A VI-1 MATLAB function F_AAG for FFT-based accelerogram matching (continued)

```
    % Enforce conjugate symmetry to keep time series real-valued
    MODIF_Y(j-1,NFFT:-1:(NFFT/2+1)) = MODIF_Y(j-1,1:(NFFT/2));

    % Accumulate shaping in frequency domain
    if j==2
        Y_modif(j-1,:) = Y .* MODIF_Y(j-1,:);
    else
        Y_modif(j-1,:) = Y_modif(j-2,:) .* MODIF_Y(j-1,:);
    end

    % Velocity/Displacement spectra (handle DC safely)
    V_modif(j-1,:) = Y_modif(j-1,:) ./ (1i*2*pi*f);
    D_modif(j-1,:) = -Y_modif(j-1,:) ./ (2*pi*f).^2;
    V_modif(j-1,1) = 0;  D_modif(j-1,1) = 0;

    % IFFT back to time domain + taper
    y_rec  = real(ifft(Y_modif(j-1,:))*L);
    v_rec  = real(ifft(V_modif(j-1,:))*L);
    d_rec  = real(ifft(D_modif(j-1,:))*L);
    y_aux(j,:) = y_rec(1:L) .* aux_var_2;
    v_aux(j,:) = v_rec(1:L);
    d_aux(j,:) = d_rec(1:L) - d_rec(1);

    % Update spectra and multipliers
    S_aux        = ARS([time; y_aux(j,1:L)], z, T);
    Sa(j,:)      = S_aux(4,:);
    P_MODIF(j,:) = Sa_design_interp ./ max(Sa(j,:), eps);
    SCALE_factor(j)= mean(P_MODIF(j,:));
    P_MODIF(j,:) = P_MODIF(j,:) / SCALE_factor(j);
end

% ---- FINAL MATCHED RECORD ----
Final_accelerogram = [time; y_aux(N_iter,1:L); v_aux(N_iter,1:L);
d_aux(N_iter,1:L)];
end
% ================= END F_AAG ============================
```

Suite Adequacy Validation

Following the spectral matching process, the ground motion suite was validated to ensure compliance with NBC 2020 requirements, which specify that the mean response spectrum of the suite should not fall below 90% of the target spectrum across all periods. This validation was performed using the following MATLAB function:

Algorithm-A VI-2 MATLAB validation code for suite adequacy

```
% art_spec : Neq x Nt matrix of final Sa(T) for matched records
% Sa_T(2,:) : 1 x Nt target UHS Sa(T)
muSa       = mean(art_spec, 1, 'omitnan');
ratio_mean = muSa ./ max(Sa_T(2,:), eps);
if any(ratio_mean < 0.90)
    warning('Suite mean < 0.90*UHS at some T. Min ratio =
%.3f',min(ratio_mean));
end
```

ANNEX VII

NEWMARK INTEGRATION METHOD FOR NONLINEAR DYNAMIC ANALYSIS

The equations of motion for MDOF structural systems with bilinear hysteresis are integrated by a nonlinear Newmark method in which the Newmark kinematic relations are embedded within a Full Newton–Raphson iteration at every time step. The Newmark integration scheme that utilizes implicit, second-order difference equations (Newmark, 1959) to compute the displacement, velocity, and acceleration vectors at each successive time step, while enforcing nonlinearity through iterative equilibrium with the current tangent stiffness. For reference, the Average Constant Acceleration (ACA) form ($\beta = 1/4$, $\gamma = 1/2$) is unconditionally stable for linear systems; the Linear Acceleration (LA) form used in this study ($\beta = 1/6$, $\gamma = 1/2$) is second-order accurate and exact for linearly varying acceleration over a step, with practical stability in the nonlinear analysis governed by the chosen time step and Newton–Raphson convergence (A. K. Chopra, 2011; Hughes, 2003).

- **Mathematical Formulation**

The equations of motion are written in base-excited (relative) form as:

$M\,\ddot{u}(t) + C\,\dot{u}(t) + F_s(u, \dot{u}) = -M\,I\,\ddot{u}_g(t)$

Where M is the mass matrix, C is the damping matrix, F_s represents the nonlinear restoring force, I is the influence vector, and $\ddot{u}_g$ is the ground acceleration.

The Newmark integration formulas for a step from t to $t+\Delta t$:

$\dot{u}_{t+\Delta t} = \dot{u}_t + [(1-\gamma)\ddot{u}_t + \gamma\ddot{u}_{t+\Delta t}]\Delta t$

$u_{t+\Delta t} = u_t + \dot{u}_t\,\Delta t + [(0.5-\beta)\ddot{u}_t + \beta\ddot{u}_{t+\Delta t}]\Delta t^2$

In this study, the Linear Acceleration parameters are used (gamma= 0.5, beta= 1/6).

- Linear Elastic Implementation

For linear elastic systems ($F_s = Ku$), the method requires one matrix solve per time step. The following MATLAB function implements the linear Newmark method:

Algorithm-A VII-1 MATLAB implementation of the linear Newmark-β method for MDOF systems

```
function [U,V,A] = Newmark_MDOF_Linear(M,C,K,ag,dt_EQ,NMCase,Factor)
% Purpose: Linear MDOF Newmark-β-γ integrator with base excitation and
NMCase.
if nargin < 7, Factor = 1; end
ag = ag .* Factor;
switch NMCase
    case 1, beta=1/4; gamma=1/2;   % ACA
    case 2, beta=1/6; gamma=1/2;   % LA
    otherwise, error('NMCase must be 1 or 2.');
end
n  = size(M,1); nt = length(ag);
U = zeros(n,nt); V = zeros(n,nt); A = zeros(n,nt);
% initial acceleration: M*a + C*v + K*u = -M*1*ag
A(:,1) = M \ ( -M*ones(n,1)*ag(1) - C*V(:,1) - K*U(:,1) );
% effective matrices
a0 = 1/(beta*dt_EQ^2); a1 = gamma/(beta*dt_EQ); a2 = 1/(beta*dt_EQ);
a3 = 1/(2*beta) - 1;   a4 = gamma/beta - 1;     a5 =
(dt_EQ/2)*(gamma/beta - 2);
Keff = K + a1*C + a0*M;
for k = 1:nt-1
    Peff = -M*ones(n,1)*ag(k+1) ...
         + M*( a0*U(:,k) + a2*V(:,k) + a3*A(:,k) ) ...
         + C*( a1*U(:,k) + a4*V(:,k) + a5*A(:,k) );
    dU       = Keff \ Peff;
    U(:,k+1) = U(:,k) + dU;
    dV       = a1*dU - a4*V(:,k) - a5*A(:,k);
    dA       = a0*dU - a2*V(:,k) - a3*A(:,k);
    V(:,k+1) = V(:,k) + dV;
    A(:,k+1) = A(:,k) + dA;
end
end
```

- **Nonlinear Implementation with Newton-Raphson Iteration**

For structures with bilinear hysteretic behavior (characterized by initial stiffness k_hi, post-yield stiffness k_lo, and yield displacement u_y), the nonlinear restoring force F_s cannot be computed explicitly. A Full Newton–Raphson iteration is performed at each time step to enforce equilibrium (A. Chopra, 2016):

1. **Predictor Step:** Estimate displacement and velocity using Newmark formulas with acceleration from the previous step
2. **Newton-Raphson Correction:**
    - Evaluate the nonlinear restoring force F_s and tangent stiffness K_t at the current displacement
    - Compute the unbalanced force vector (residual) R:

$$R = -M\,\ddot{u}_{t+\Delta t} - C\,\dot{u}_{t+\Delta t} - F_s(u_{t+\Delta t}) + F_{ext}$$

- Solve for displacement correction: Δu
- Update kinematics using Newmark relations
- Check convergence: $\|R\| <$ tolerance (where tol = 1.0×10^{-6})

3. **Hysteretic State Update:** Update plastic displacement and determine the current position on the bilinear backbone curve
4. **Repeat** steps 2-3 until convergence ($\|R\| <$ tol) or maximum iterations (jmax = 200) are reached.

The nonlinear Newmark integration (consistent with NLDRHA_MDOF_1D used in this study) is implemented as:

Algorithm-A VII-2 MATLAB implementation of the nonlinear Newmark-β method with full Newton iterations for MDOF systems

```
function [U,V,A,info] =
Newmark_MDOF_Nonlinear(M,C,K0,ag,dt_EQ,NMCase,model,Factor,maxtol,jmax)
% Purpose: Nonlinear MDOF Newmark-β-γ integrator with base excitation and
Full Newton iterations.
% Nonlinearity enters through model.restoring(u,state) -> [Fs, Kt, state].
% Inputs:
%   M,C,K0 : mass, damping, initial elastic stiffness (matrices)
%   ag     : base acceleration time history (units per Factor)
%   dt_EQ  : time step (s)
%   NMCase : 1 -> ACA (β=1/4, γ=1/2), 2 -> LA (β=1/6, γ=1/2)
%   model  : struct with function handle:
%            [Fs,Kt,state] = model.restoring(u,state)  % bilinear, etc.
%   Factor : 1 if ag in m/s^2; 9.81 if ag in g  (default = 1)
%   maxtol : convergence tolerance on residual norm (default = 1e-2)
%   jmax   : max Newton iterations per step (default = 200)
%
% Outputs:
%   U,V,A  : displacement, velocity, relative acceleration time histories
%   info   : struct with iteration counts, flags

    if nargin < 8 || isempty(Factor), Factor = 1; end
    if nargin < 9 || isempty(maxtol), maxtol = 1e-2; end
    if nargin < 10 || isempty(jmax),   jmax   = 200; end
    ag = ag .* Factor;

    % Newmark parameters
    switch NMCase
        case 1, beta=1/4; gamma=1/2;   % ACA (unconditional for linear
systems)
        case 2, beta=1/6; gamma=1/2;   % LA   (second-order, conditional)
        otherwise, error('NMCase must be 1 (ACA) or 2 (LA).');
    end
```

Algorithm-A VII-2 MATLAB implementation of the nonlinear Newmark-β method with full Newton iterations for MDOF systems (continued)

```
    % Precompute Newmark scalars
    a0 = 1/(beta*dt_EQ^2);
    a1 = gamma/(beta*dt_EQ);
    a2 = 1/(beta*dt_EQ);
    a3 = 1/(2*beta) - 1;
    a4 = gamma/beta - 1;
    a5 = (dt_EQ/2)*(gamma/beta - 2);

    n  = size(M,1);
    nt = length(ag);

    U = zeros(n,nt);  V = zeros(n,nt);  A = zeros(n,nt);

    % Initial state
    state = model.init_state(n);  % user/model-defined (e.g., zeros for
plastic vars)
    Fs0 = K0 * U(:,1);
    A(:,1) = M \ ( -M*ones(n,1)*ag(1) - C*V(:,1) - Fs0 );
    info.iters     = zeros(1,nt);
    info.converged = true(1,nt);

    for k = 1:nt-1
        % --- Newmark predictors (trial kinematics) ---
        Uhat = U(:,k) + dt_EQ*V(:,k) + dt_EQ^2*(0.5 - beta)*A(:,k);
        Vhat = V(:,k) + dt_EQ*(1 - gamma)*A(:,k);

        % Start Newton with trial = predictors
        u  = Uhat;    v = Vhat;    a = zeros(n,1);

        % Evaluate restoring at trial and set tangent
        [Fs,Kt,state_trial] = model.restoring(u,state);

        % Effective stiffness (depends on Kt at current trial)
        Keff = Kt + a1*C + a0*M;

        % Effective RHS for base excitation (relative EOM form)
        Peff = -M*ones(n,1)*ag(k+1) ...
             + M*( a0*U(:,k) + a2*V(:,k) + a3*A(:,k) ) ...
             + C*( a1*U(:,k) + a4*V(:,k) + a5*A(:,k) );

        % Residual in displacement form
        r = Peff - Fs - Keff*(u - U(:,k));

        it = 0;  converged = false;
        while it < jmax
            it = it + 1;

            % Solve for displacement correction
            du = Keff \ r;
            u  = u + du;

            % Update velocities and accelerations from Newmark relations
            dv = a1*du - a4*V(:,k) - a5*A(:,k);
            da = a0*du - a2*V(:,k) - a3*A(:,k);
            v  = V(:,k) + dv;
            a  = A(:,k) + da;
```

Algorithm-A VII-2 MATLAB implementation of the nonlinear Newmark-β method with full Newton iterations for MDOF systems (continued)

```
            % Update restoring force & tangent at new u
            [Fs,Kt,state_new] = model.restoring(u,state_trial);

            % Rebuild effective stiffness with updated tangent
            Keff = Kt + a1*C + a0*M;

            % Recompute residual
            r = Peff - Fs - Keff*(u - U(:,k));

            if norm(r,2) <= maxtol
                converged = true;
                state = state_new;  % accept plastic state
                break
            end

            % prepare for next Newton iteration
            state_trial = state_new;
        end

        info.iters(k+1)     = it;
        info.converged(k+1) = converged;

        % Accept step
        U(:,k+1) = u;
        V(:,k+1) = v;
        A(:,k+1) = a;
    end
end
```

LIST OF BIBLIOGRAPHICAL REFERENCES

Abou-Elfath, H., Shamel Fahmy, A., & Mohamed Khalifa, K. (2018). Response Modification Factors of Buckling-Restrained Braced Frames Designed According to the Egyptian Code. *Alexandria Engineering Journal*, *57*(4), 2851–2864. https://doi.org/10.1016/j.aej.2018.07.001

Adam, C., & Fotiu, P. A. (2000). Dynamic Analysis of Inelastic Primary–Secondary Systems. *Engineering Structures*, *22*(1), 58–71.

Alassafi, H. T., Al-Gahtani, K. S., Almohsen, A. S., & Alsugair, A. M. (2024). HVAC Maintainability Risks in Healthcare Facilities: A Design Optimization Perspective. *Facilities*, *42*(15–16), 30–52. https://doi.org/10.1108/F-09-2022-0121

Alavi, E., Mahootchian, A., Yadegari, S., Shamsodin, M., Nouri, M. B., & Ordoubadi, B. (2018). Report of: M7. 3 Ezgele, Kermanshah, Iran Earthquake on November 12. *Earthquake Engineering Research Institute*, 1–22.

Aldeka, A. B. (2015). *Seismic Response of Acceleration-Sensitive Non-Structural Components Mounted on Irregular Multi-Storey Reinforced Concrete Buildings* (PhD Thesis). University of Birmingham.

American Concrete Institute (ACI). (2019, May). Building Code Requirements for Structural Concrete and Commentary. Farmington Hills, MI: American Concrete Institute.

American Society of Civil Engineers (ASCE). (2000, April 18). Seismic Analysis of Safety-Related Nuclear Structures and Commentary. Reston, VA. https://doi.org/https://doi.org/10.1061/9780784404331

American Society of Civil Engineers (ASCE). (2016). Minimum Design Loads and Associated Criteria for Buildings and Other Structures. Reston, VA: American Society of Civil Engineers. https://doi.org/10.1061/9780784414248

American Society of Civil Engineers (ASCE). (2017). *Seismic Evaluation and Retrofit of Existing Buildings* (41st ed.). Reston, VA: American Society of Civil Engineers. https://doi.org/10.1061/9780784414859

American Society of Civil Engineers (ASCE). (2022). Minimum Design Loads and Associated Criteria for Buildings and Other Structures. Reston, VA: American Society of Civil Engineers.

American Society of Civil Engineers (ASCE). (2023, November 30). Seismic Evaluation and Retrofit of Existing Buildings. Reston, VA: American Society of Civil Engineers. https://doi.org/10.1061/9780784416112

Amin, M., Hall, W. J., Newmark, N. M., & Kassawara, R. P. (1971). Earthquake Response of Multiply Connected Light Secondary Systems by Spectrum Methods. In *Proceedings of the 1st National Congress on Pressure Vessels and Piping, American Society of Mechanical Engineers, New York, NY* (pp. 103–129). San Francisco, California: American Society of Mechanical Engineers.

Anajafi, H. (2018). *Improved Seismic Design of Non-Structural Components (NSCs) and Development of Innovative Control Approaches to Enhance the Seismic Performance of Buildings and NSCs* (PhD Thesis). University of New Hampshire.

Anajafi, H., & Medina, R. A. (2019a). Damping Modification Factor for Elastic Floor Spectra. *Bulletin of Earthquake Engineering*, *17*(11), 6079–6108.

Anajafi, H., & Medina, R. A. (2019b). Lessons Learned from Evaluating the Responses of Instrumented Buildings in the United States: The Effects of Supporting Building Characteristics on Floor Response Spectra. *Earthquake Spectra*, *35*(1), 159–191.

Anajafi, H., Medina, R. A., & Adam, C. (2021). Evaluation of the Floor Acceleration Response Spectra of Numerical Building Models Based on Recorded Building Response Data. *Journal of Earthquake Engineering*, *0*(0), 1–25. https://doi.org/10.1080/13632469.2021.1927887

Anajafi, H., Medina, R. A., & Santini-Bell, E. (2020). Inelastic Floor Spectra for Designing Anchored Acceleration-Sensitive Nonstructural Components. *Bulletin of Earthquake Engineering*, *18*(5), 2115–2147.

Anwar, N., Toe, N. N. S., Aung, T. H., & Najam, F. A. (2018). Seismic Loss Estimation of Nonstructural Components Based on Actual Parameters In High-Rise RC Shear Wall Buildings. In *Proceedings of the Australian Structural Engineering Conference (2018: Adelaide, SA)* (pp. 356–364). Engineers Australia Barton, ACT.

Applied Technology Council (ATC). (2012, December). Reducing the Risks of Nonstructural Earthquake Damage – A Practical Guide. Federal Emergency Management Agency (FEMA).

Applied Technology Council (ATC). (2015). *NEHRP Recommended Seismic Provisions for New Buildings and Other Structures* (Report No. FEMA P-1050-1). Redwood City, CA: Applied Technology Council. Retrieved from https://www.fema.gov/media-collection/nehrp-recommended-seismic-provisions-new-buildings-and-other-structures-2015

Applied Technology Council (ATC). (2017). *Seismic Analysis, Design, and Installation of Nonstructural Components and Systems - Background and Recommendations for Future Work* (Report No. NIST GCR 17-917-38). Gaithersburg, MD: ATC Applied Technology Council. Retrieved from https://www.nist.gov/publications/seismic-analysis-design-and-installation-nonstructural-components-and-systems

Applied Technology Council (ATC). (2018a). *Recommendations for Improved Seismic Performance of Nonstructural Components* (Report No. NIST GCR 18-917-43). Gaithersburg, MD: National Institute of Standards and Technology. https://doi.org/10.6028/NIST.GCR.18-917-43

Applied Technology Council (ATC). (2018b). *Recommendations for improved seismic performance of nonstructural components* (Report No. NIST GCR 18-917-43). Gaithersburg, MD: National Institute of Standards and Technology. https://doi.org/10.6028/NIST.GCR.18-917-43

Aragaw, L., & Calvi, P. (2018). Floor Spectra in Hybrid Base-Rocking Wall Buildings. In *Proceedings of the 2018 European Conference on Earthquake Engineering* (pp. 4291–4302). Thessaloniki, Greece.

Archila, M., Ventura, C., Figueira, A., & Yang, Y. (2012). Modal Testing of Non-Structural Components for Seismic Risk Assessment. In J. Brownjohn & P. Fanning (Eds.), *Experimental Vibration Analysis for Civil Engineering Structures* (pp. 239–246). (S.l.): Springer. https://doi.org/10.1007/978-1-4614-2413-0_24

Asadpour, G., Asadi, P., & Hajirasouliha, I. (2022). Analysis of Bilinear Hysteretic Structures with Nonlinear Fluid Viscous Dampers Using Modified Stochastic Linearization Technique. *Engineering Structures*, *251*, 113555. https://doi.org/10.1016/j.engstruct.2021.113555

Assi, R., Mazloom, S., & Abouda, A. (2024). Effect of nonlinearity on seismic response of nonstructural components in a code-conforming RC shear wall building. *Canadian Journal of Civil Engineering*, *52*(1), 89–104.

Assi, R., Youance, S., Bonne, A., & Nollet, M.-J. (2016). Effect of Non-Structural Components on the Modal Properties of Buildings Using Ambient Vibration Testing. In *Proceedings of the 2016 CSCE International Conference on Civil Engineering* (pp. 2652–2661). London, ON, Canada.

ASTM International. (2022). *Standard Practice for Installation of Ceiling Suspension Systems for Acoustical Tile and Lay-in Panels in Areas Subject to Earthquake Ground Motions*. West Conshohocken, PA: ASTM International. Retrieved from https://www.astm.org/e0580_e0580m-22.html

Astroza, R., Pantoli, E., Selva, F., Restrepo, J. I., Hutchinson, T. C., & Conte, J. P. (2015). Experimental Evaluation of the Seismic Response of a Rooftop-Mounted Cooling Tower. *Earthquake Spectra*, *31*(3), 1567–1589. https://doi.org/10.1193/071513EQS205M

Atkinson, G. (2009). Earthquake Time Histories Compatible with the 2005 National Building Code of Canada Uniform Hazard Spectrum. *Canadian Journal of Civil Engineering*, *36*, 991–1000. https://doi.org/10.1139/L09-044

Banerjee, A. K., Pramanik, D., & Roy, R. (2016). Seismic Structural Fragilities: Proposals for Improved Methodology Per Spectral Matching of Accelerogram. *Engineering Structures*, *111*, 538–551. https://doi.org/10.1016/j.engstruct.2016.01.002

Basak, P., Basak, I., & Balakrishnan, N. (2009). Estimation for the Three-Parameter Lognormal Distribution Based on Progressively Censored Data. *Computational Statistics and Data Analysis*, *53*(10), 3580–3592. https://doi.org/https://doi.org/10.1016/j.csda.2009.03.015

Basset Salom, L. (2019, May 17). The Flexibility Method. València, Spain: Universitat Politècnica de València. Retrieved from http://hdl.handle.net/10251/120620

Bianchi, S., Ciurlanti, J., & Pampanin, S. (2019). Seismic vulnerability of non-structural components: from traditional solutions to innovative low-damage systems. In *Proceedings of the SECED 2019 Conference: Earthquake Risk and Engineering towards a Resilient World*. London, UK.

Bianchi, S., & Pampanin, S. (2022). Fragility Functions for Architectural Nonstructural Components. *Journal of Structural Engineering*, *148*(10), 03122005. https://doi.org/10.1061/(ASCE)ST.1943-541X.0003352

Bradley, B. A., Dhakal, R. P., Cubrinovski, M., MacRae, G. A., & Lee, D. S. (2009). Seismic Loss Estimation for Efficient Decision Making. *Bulletin of the New Zealand Society for Earthquake Engineering*, *42*(2), 96–110. https://doi.org/10.5459/bnzsee.42.2.96-110

Brandolese, S., Fiorin, L., & Scotta, R. (2019). Seismic Demand and Capacity Assessment of Suspended Ceiling Systems. *Engineering Structures*, *193*, 219–237. https://doi.org/10.1016/j.engstruct.2019.05.034

Buccella, N., Wiebe, L., Konstantinidis, D., & Steele, T. C. (2020). Demands on Nonstructural Components in Buildings With Controlled Rocking Braced Frames. *Earthquake Engineering & Structural Dynamics*. https://doi.org/10.1002/eqe.3385

Canadian Board for Harmonized Construction Codes (CBHCC). (2024). *Proposed Change 1901: Modification of the Requirements for Determining the Specified Lateral Earthquake Force*. Ottawa, Canada.

Canadian Standards Association (CSA). (2014a). Design of Concrete Structures. Mississauga, Ontario, Canada.

Canadian Standards Association (CSA). (2014b). *Design of concrete structures* (Sixth edition). (S.l.): CSA A23.3-14 (2014a).

Canadian Standards Association (CSA). (2014c). Seismic Risk Reduction of Operational and Functional Components (OFCs) of Buildings.

Ceilings and Interior Systems Construction Association (CISCA). (2004). *Guidelines for Seismic Restraint of Direct-Hung Suspended Ceiling Assemblies, Seismic Zones 3-4*. St. Charles, IL: Ceilings and Interior Systems Construction Association.

Challagulla, S. P., Kontoni, D.-P. N., Suluguru, A. K., Hossain, I., Ramakrishna, U., & Jameel, M. (2023). Assessing the Seismic Demands on Non-Structural Components Attached to Reinforced Concrete Frames. *Applied Sciences*, *13*(3), 1817. https://doi.org/10.3390/app13031817

Chaudhuri, S. R., & Villaverde, R. (2008). Effect of Building Nonlinearity on Seismic Response of Nonstructural Components: A Parametric Study. *Journal of structural engineering*, *134*(4), 661–670.

Chen, C. K., Scholl, R. E., & Blume, J. A. (1980). *Seismic Study of Industrial Steel Storage Racks.* (Report No. PB81142101). URS/John A. Blume and Associates, San Francisco, CA.; National Science Foundation, Washington, DC. Engineering and Applied.

Chen, Y., & Soong, T. T. (1988). Seismic Response of Secondary Systems. *Engineering Structures*, *10*(4), 218–228. https://doi.org/10.1016/0141-0296(88)90043-0

Chopra, A. (2016). *Dynamics of Structures* (5th edition). Hoboken, NJ: Pearson.

Chopra, A. K. (2011). *Dynamics of Structures* (4th edition). Upper Saddle River, N.J: Pearson.

Chopra, A. K., & Chintanapakdee, C. (2004). Inelastic Deformation Ratios for Design and Evaluation of Structures: Single-Degree-of-Freedom Bilinear Systems. *Journal of Structural Engineering*, *130*(9), 1309–1319. https://doi.org/10.1061/(ASCE)0733-9445(2004)130:9(1309)

Chouinard, L., Rosset, P., De La Puente, A., Madriz, R., Mitchell, D., & Adams, J. (2004). Seismic Hazard Analysis for Montreal. In *Proceedings of the 13th World Conference on Earthquake Engineering, Vancouver, Canada. Paper* (Vol. 7010).

Ciurlanti, J., Bianchi, S., Pürgstaller, A., Gallo, P. Q., Bergmeister, K., & Pampanin, S. (2022). Shake Table Tests of Concrete Anchors for Non-Structural Components Including Innovative and Alternative Anchorage Detailing. *Bulletin of Earthquake Engineering*, *20*(8), 3971–3993. https://doi.org/10.1007/s10518-022-01359-2

Clayton, J. S., & Medina, R. A. (2012). Proposed Method for Probabilistic Estimation of Peak Component Acceleration Demands. *Earthquake Spectra*, *28*(1), 55–75. https://doi.org/10.1193/1.3673623

Cohen, A. C., & Whitten, B. J. (1980). Estimation in the Three-Parameter Lognormal Distribution. *Journal of the American Statistical Association*, *75*(370), 399–404. https://doi.org/10.2307/2287466

Comite Europeen de Normalization. (2004). *Eurocode 8–Design of Structures for Earthquake Resistance–Part 1: General Rules, Seismic Actions and Rules for Buildings*. Brussels, Belgium: EN-1998-1.

Computers and Structures Inc. (CSI). (2017). ETABS-Building Analysis and Design (version 17.01) [Software]. California, USA.

Computers and Structures Inc. (CSI). (2024). ETABS-Building Analysis and Design (version 22) [Software]. California, USA: Computers and Structures Inc.

Cremen, G., & Baker, J. W. (2019). Improving FEMA P-58 Non-Structural Component Fragility Functions and Loss Predictions. *Bulletin of Earthquake Engineering*, *17*(4), 1961–1962. https://doi.org/10.1007/s10518-019-00565-9

Cunha, A., Caetano, E., Ribeiro, P., & Müller, G. (2014). A Critical Review of Current Approaches on the Determination of Seismic Force Demands on Nonstructural Components. In *Proceedings of the 9th European Conference on Structural Dynamics (EURODYN 2014)* (pp. 421–428). Porto, Portugal: EURODYN. Retrieved from https://publications.rwth-aachen.de/record/443918

D'Altri, A. M., Sarhosis, V., Milani, G., Rots, J., Cattari, S., Lagomarsino, S., … de Miranda, S. (2020). Modeling Strategies for the Computational Analysis of Unreinforced Masonry Structures: Review and Classification. *Archives of Computational Methods in Engineering*, *27*(4), 1153–1185. https://doi.org/10.1007/s11831-019-09351-x

D'Angela, D., & Magliulo, G. (2025). Methodological Guidance and Quantitative Measures Regarding Seismic Capacity and Safety of Freestanding and Inelastic Anchored Nonstructural Elements Housed in Ordinary and Critical Facilities. *Reliability Engineering & System Safety*, *260*, 111029. https://doi.org/10.1016/j.ress.2025.111029

D'Angela, D., Magliulo, G., Zito, M., & Calenzo, F. (2024). Seismic Fragility of Nonstructural Elements Modelled as Nonlinear Single-Degree-Of-Freedom Systems. In *Proceedings of the 18th World Conference on Earthquake Engineering (18WCEE)*. Milan, Italy.

D'Ayala, D., Meslem, A., Vamvatsikos, D., Porter, K., & Rossetto, T. (2015). *GEM Guidelines for Analytical Vulnerability Assessment of Low/Mid-Rise Buildings*. (S.l.): Global Earthquake Model. https://doi.org/10.13117/GEM.VULN- -MOD.TR2014.12

Dhakal, R. P., MacRae, G. A., Pourali, A., & Paganotti, G. (2016). Seismic Fragility of Suspended Ceiling Systems Used in NZ Based on Component Tests. *Bulletin of the New Zealand Society for Earthquake Engineering*, *49*(1), 45–63. https://doi.org/10.5459/bnzsee.49.1.45-63

Ding, X., Liapopoulou, M., & Elghazouli, A. Y. (2024). Seismic Response of Non-Structural Components in Multi-Storey Steel Frames. *Journal of Constructional Steel Research*, *213*, 108398. https://doi.org/10.1016/j.jcsr.2023.108398

Drake, R. M., & Bachman, R. E. (1994). NEHRP Provisions for 1994 for Nonstructural Components. *Journal of Architectural Engineering*, *2*(1), 26–31.

Esper, P., & Tachibana, E. (1998). Lessons from the Kobe Earthquake. *Geological Society, London, Engineering Geology Special Publications*, *15*(1), 105–116. https://doi.org/10.1144/GSL.ENG.1998.015.01.11

European Committee for Standardization. (2022a). *Eurocode 8: Design of structures for earthquake resistance – Part 1-2: Buildings*. Brussels, Belgium: European Committee for Standardization (CEN).

European Committee for Standardization. (2022b). *Eurocode 8: Design of structures for earthquake resistance – Part 4: Silos, tanks and pipelines, towers, masts and chimneys*. Brussels, Belgium: European Committee for Standardization (CEN).

Fahjan, Y., & Ozdemir, Z. (2008). Scaling of Earthquake Accelerograms for Non-Linear Dynamic Analyses to Match the Earthquake Design Spectra. In *Proceedings of the 14th World Conference on Earthquake Engineering (14WCEE)*. Beijing, China: International Association for Earthquake Engineering. Retrieved from https://www.iitk.ac.in/nicee/wcee/article/14_02-0165.PDF

Fajfar, P., & Vukobratović, V. (2022). Floor acceleration spectra: from research to seismic code provisions. In *Proceedings of the fifth international workshop on the seismic performance of non-structural elements (SPONSE)* (pp. 2–14).

Fan, X., Juang, C. H., Wasowski, J., Huang, R., Xu, Q., Scaringi, G., … Havenith, H.-B. (2018). What We Have Learned from the 2008 Wenchuan Earthquake and Its Aftermath: A Decade of Research and Challenges. *Engineering Geology*, *241*, 25–32.

Fazileh, F., Rodriguez, D., & Cai, Z. (2025). Evaluation of the seismic design equations for non-structural components specified in the National Building Code of Canada. *Journal of Building Engineering*, *114*, 114123. https://doi.org/10.1016/j.jobe.2025.114123

Federal Emergency Management Agency. (2009). *Quantification of Building Seismic Performance Factors*. Washington, D.C.: Federal Emergency Management Agency (FEMA).

Federal Emergency Management Agency (FEMA). (2003). NEHRP Recommended Provisions for Seismic Regulations for New Buildings and Other Structures. *Report FEMA-450 (Provisions), Federal Emergency Management Agency (FEMA), Washington*.

Federal Emergency Management Agency (FEMA). (2011). *Development of Seismic Fragilities for Acoustical Tile or Lay-in Panel Suspended Ceilings.* (Report No. FEMA P-58/BD-3.9.4). Washington, DC: Applied Technology Council. Retrieved from https://www.atcouncil.org/fema-p-58-background-documents

Federal Emergency Management Agency (FEMA). (2012a). *Hazus-MH 2.1: Earthquake Model Technical Manual*. Washington, DC: Department of Homeland Security, Federal Emergency Management Agency.

Federal Emergency Management Agency (FEMA). (2012b). *Seismic Performance Assessment of Buildings, Volume 3: Performance Assessment Calculation Tool (PACT) (Version 3.1.2)*. Washington, DC: Federal Emergency Management Agency (FEMA).

Federal Emergency Management Agency (FEMA). (2013). PACT Beta Test Example: Building C Reinforced Masonry Shear Wall Building. *FEMA P-58/BD-3.7.16*.

Federal Emergency Management Agency (FEMA). (2018a). *Seismic Performance Assessment of Buildings Volume 1-Methodology* (Report No. FEMA P-58-1). Washington, DC: Federal Emergency Management Agency.

Federal Emergency Management Agency (FEMA). (2018b). *Seismic Performance Assessment of Buildings Volume 2-Methodology* (Report No. FEMA P-58-2). Washington, DC: Federal Emergency Management Agency.

Fierro, E. A., Miranda, E., & Perry, C. L. (2011). Behavior of Nonstructural Components in Recent Earthquakes. In *AEI 2011: Building Integrated Solutions - Proceedings of the AEI 2011 Conference* (pp. 369–377). https://doi.org/10.1061/41168(399)44

Filiatrault, A., Lee, G. C., Aref, A. J., Bruneau, M., Constantinou, M. C., Reinhorn, A. M., & Whittaker, A. S. (2004). Recent Progress Towards the Seismic Control of Structural and Non-Structural Systems in Hospitals. In *Proceedings of the US-Japan 36th Technical Meeting of Panel on Wind and Seismic Effects, Washington, DC, USA* (pp. 17–22). National Institute of Standards and Technology (NIST). Retrieved from https://www.pwri.go.jp/eng/ujnr/joint/36/paper/25filiat.pdf

Filiatrault, A., Perrone, D., Merino, R. J., & Calvi, G. M. (2018). Performance-Based Seismic Design of Nonstructural Building Elements. *Journal of Earthquake Engineering*, *25*(2), 237–269. https://doi.org/10.1080/13632469.2018.1512910

Filiatrault, A., Uang, C.-M., Folz, B., Chrstopoulos, C., & Gatto, K. (2001). Reconnaissance Report of the February 28, 2001 Nisqually (Seattle-Olympia) Earthquake. *SSRP*, *2*.

Galasso, C., Zareian, F., Iervolino, I., & Graves, R. W. (2012). Elastic and Post-Elastic Response of Structures to Hybrid Broadband Synthetic Ground Motions. In *Proceedings of the 15th World Conference on Earthquake Engineering (15WCEE)*. Lisbon, Portugal. Retrieved from https://central.scec.org/publication/1684

Gallo, P. Q., Moghaddasi, M., Pampanin, S., & Bergmeister, K. (2018). Shake Table Tests of Post-Installed Anchors with Supplemental Damping. *ACI Structural Journal*, *115*(3), 595–606.

Gascot, R. L., & Montejo, L. A. (2014). Evaluation of Spectrum Compatible Earthquake Records and Its Effect on the Inelastic Demand of Civil Structures. In *Proceedings of the 10th U.S. National Conference on Earthquake Engineering (10NCEE)*. Retrieved from https://www.researchgate.net/publication/272829687_Evaluation_of_spectrum_compatible_earthquake_records_and_its_effect_on_the_inelastic_demand_of_civil_structures

Gautam, D., Adhikari, R., & Rupakhety, R. (2021). Seismic Fragility of Structural and Non-Structural Elements of Nepali RC Buildings. *Engineering Structures*, *232*, 111879. https://doi.org/10.1016/j.engstruct.2021.111879

Georgioudakis, M., & Plevris, V. (2018). A Combined Modal Correlation Criterion for Structural Damage Identification with Noisy Modal Data. *Advances in Civil Engineering*, *2018*. https://doi.org/10.1155/2018/3183067

Ghasemof, A., Mirtaheri, M., & Karami Mohammadi, R. (2022). Multi-Objective Optimization for Probabilistic Performance-Based Design of Buildings Using FEMA P-58 Methodology. *Engineering Structures*, *254*, 113856. https://doi.org/10.1016/j.engstruct.2022.113856

Ghofrani, H., Atkinson, G. M., Chouinard, L., Rosset, P., & Tiampo, K. F. (2015). Scenario Shakemaps for Montreal. *Canadian Journal of Civil Engineering*, *42*(7), 463–476. https://doi.org/10.1139/cjce-2014-0496

González, I., Silva, A., Macedo, L., Monteiro, R., & Castro, J. M. (2019). Critical Assessment of Estimation Procedures for Floor Acceleration Demands in Steel Moment-Resisting Frames. *Frontiers in Built Environment*, *5*, 139. https://doi.org/10.3389/fbuil.2019.00139

Goulet, C. A., Haselton, C. B., Mitrani-Reiser, J., Beck, J. L., Deierlein, G. G., Porter, K. A., & Stewart, J. P. (2007). Evaluation of the Seismic Performance of a Code-Conforming Reinforced-Concrete Frame Building—from Seismic Hazard to Collapse Safety and Economic Losses. *Earthquake Engineering & Structural Dynamics*, *36*(13), 1973–1997.

Goulet, C. A., Kishida, T., Ancheta, T. D., Cramer, C. H., Darragh, R. B., Silva, W. J., … Stewart, J. P. (2021). PEER NGA-East Database. *Earthquake Spectra*, *37*(1_suppl), 1331–1353.

Güner, T., & Topkaya, C. (2020). Performance Comparison of BRBFs Designed Using Different Response Modification Factors. *Engineering Structures*, *225*, 111281. https://doi.org/10.1016/j.engstruct.2020.111281

Hancock, J., Bommer, J. J., & Stafford, P. J. (2008). Numbers of Scaled and Matched Accelerograms Required for Inelastic Dynamic Analyses. *Earthquake Engineering & Structural Dynamics*, *37*(14), 1585–1607. https://doi.org/10.1002/eqe.827

Hatzigeorgiou, G. D., & Papagiannopoulos, G. A. (2012). Inelastic Velocity Ratio. *Earthquake Engineering & Structural Dynamics*, *41*(14), 2025–2041. https://doi.org/10.1002/eqe.2172

Hoehler, M. S., & Eligehausen, R. (2008). Behavior and testing of anchors in simulated seismic cracks. *ACI Structural Journal*, *105*(3), 348–357.

Hosseini, M., & Imagh-e-Naiini, M. R. (1999). A Quick Method for Estimating the Lateral Stiffness of Building Systems. *The Structural Design of Tall Buildings*, *8*(3), 247–260. https://doi.org/10.1002/(SICI)1099-1794(199909)8:3%3C247::AID-TAL126%3E3.0.CO;2-K

Huang, W.-C., Hussainzada, N., & Mcclure, G. (2013). Experimental Study on the Seismic Behaviour of Suspended Ceilings. *Proceedings, Annual Conference - Canadian Society for Civil Engineering*, *2*, 1526–1535.

Hughes, T. J. (2003). *The finite element method: linear static and dynamic finite element analysis*. (S.l.): Courier Corporation.

Ibarra, L. F., Medina, R. A., & Krawinkler, H. (2005). Hysteretic Models That Incorporate Strength and Stiffness Deterioration. *Earthquake Engineering & Structural Dynamics*, *34*(12), 1489–1511. https://doi.org/10.1002/eqe.495

Igusa, T. (1990). Response Characteristics of Inelastic 2-DOF Primary-Secondary System. *Journal of Engineering Mechanics*, *116*(5), 1160–1174. https://doi.org/10.1061/(ASCE)0733-9399(1990)116:5(1160)

International Code Council. (2012). IBC, International Building Code, Country Club Hills IL, USA.

Jamshidi Avanaki, M. (2019). Response Modification Factors for Seismic Design of Steel Fiber Reinforced Concrete Segmental Tunnels. *Construction and Building Materials*, *211*, 1042–1049. https://doi.org/10.1016/j.conbuildmat.2019.03.275

Kawakatsu, T., Kitade, K., Takemori, T., Kuwabara, Y., & Ogiwara, Y. (1979). *Floor Response Spectra Considering Elasto-Plastic Behaviour of Nuclear Power Facilities*. Netherlands: North-Holland Publishing Co.

Kazantzi, A. K., Karaferis, N. D., Melissianos, V. E., & Vamvatsikos, D. (2024). Seismic Reliability of Acceleration-sensitive Ancillary Elements in the New Generation of Eurocodes. In *18th World Conference on Earthquake Engineering, Milan, Italy*.

Kazantzi, A. K., Vamvatsikos, D., & Miranda, E. (2020a). Evaluation of Seismic Acceleration Demands on Building Nonstructural Elements. *Journal of Structural Engineering*, *146*(7), 04020118. https://doi.org/10.1061/(ASCE)ST.1943-541X.0002676

Kazantzi, A. K., Vamvatsikos, D., & Miranda, E. (2020b). The Effect of Damping on Floor Spectral Accelerations as Inferred from Instrumented Buildings. *Bulletin of Earthquake Engineering*, *18*(5), 2149–2164.

Kazantzi, A., Vamvatsikos, D., & Miranda, E. (2018). Effect of Yielding on the Seismic Demands of Nonstructural Elements. In *Proceedings of the 16th European conference on earthquake engineering, Thessaloniki, Greece* (pp. 1–12).

Kecman, D. (1983). Bending Collapse of Rectangular and Square Section Tubes. *International Journal of Mechanical Sciences*, *25*(9), 623–636. https://doi.org/10.1016/0020-7403(83)90072-3

King, A., & Fronk, R. (2004). An Overview of IEEE 693-IEEE Recommended Practice for the Seismic Design of Substations. In *Proceedings of the 13th World Conference on Earthquake Engineering (13WCEE)*. Vancouver, Canada: International Association for Earthquake Engineering.

Lagomarsino, S., & Giovinazzi, S. (2006). Macroseismic and Mechanical Models for the Vulnerability and Damage Assessment of Current Buildings. *Bulletin of Earthquake Engineering*, *4*, 415–443.

Lew, H. S., Leyendecker, E. V., & Dikkers, R. D. (1971). *Engineering Aspects of the 1971 San Fernando Earthquake* (Vol. 40). (S.l.): US National Bureau of Standards.

Lignos, D. G., & Krawinkler, H. (2010). A Steel Database for Component Deterioration of Tubular Hollow Square Steel Columns Under Varying Axial Load for Collapse Assessment of Steel Structures Under Earthquakes. In *Proc. 7th Int. Conf. on Urban Earthquake Engineering (7CUEE)* (Vol. 55, pp. 1481–1496). Tokyo, Japan: Center for Urban Earthquake Engineering, Tokyo Institute of Technology Tokyo.

Lignos, D. G., & Krawinkler, H. (2013). Development and Utilization of Structural Component Databases for Performance-Based Earthquake Engineering. *Journal of Structural Engineering*, *139*(8), 1382–1394. https://doi.org/10.1061/(ASCE)ST.1943-541X.0000646

Lima, C., & Martinelli, E. (2018). Seismic Response of Acceleration-Sensitive Non-Structural Components in Buildings. *Buildings*, *9*(1), 7.

Lin, J., & Mahin, S. A. (1985). Seismic Response of Light Subsystems on Inelastic Structures. *Journal of Structural Engineering*, *111*(2), 400–417. https://doi.org/10.1061/(ASCE)0733-9445(1985)111:2(400)

Lucchini, A., Mollaioli, F., & Bazzurro, P. (2014). Floor Response Spectra for Bare and Infilled Reinforced Concrete Frames. *Journal of Earthquake Engineering*, *18*(7), 1060–1082.

Magliulo, G., & D'Angela, D. (2024). Seismic Response and Capacity of Inelastic Acceleration-Sensitive Nonstructural Elements Subjected to Building Floor Motions. *Earthquake Engineering & Structural Dynamics*, *53*(4), 1421–1445. https://doi.org/10.1002/eqe.4080

Magsalay, R. J. M. (2025). Quantifying Central Limit Theorem Convergence: A Monte Carlo Simulation Approach to Minimum Sample Size. *International Journal of Research and Innovation in Social Science*, *IX*(VIII), 639–644. https://doi.org/10.47772/IJRISS.2025.908000050

Mason Industries. (2019). *Seismic Restraint Manual*. Hauppauge, NY: Mason Industries Inc. Retrieved from https://mason-ind.com/

Mazloom, S. (2023). *Evaluation of Vertical Ground and Floor Accelerations and Spectra in Elastic RC Frame Buildings Located in Eastern Canada*. PhD Thesis. École de technologie supérieure. Retrieved from https://espace.etsmtl.ca/id/eprint/3253/

Mazloom, S., & Assi, R. (2022). Estimate of V/H Spectral Acceleration Ratios for Firm Soil Sites in Eastern Canada. *Soil Dynamics and Earthquake Engineering*, *159*, 107350. https://doi.org/10.1016/j.soildyn.2022.107350

McCormick, J., Matsuoka, Y., Pan, P., & Nakashima, M. (2012). Evaluation of Non-Structural Partition Walls and Suspended Ceiling Systems Through a Shake Table Study, 1–10. https://doi.org/10.1061/41016(314)223

McKenna, F., Fenves, G. L., Filippou, F., Mazzoni, S., Scott, M., Elgamal, A., … McKenzie, P. (2000). *Open System for Earthquake Engineering Simulation (OpenSees)*. Berkeley, CA: University of California, Berkeley. Retrieved from http://opensees.berkeley.edu.

Medina, R. A., Sankaranarayanan, R., & Kingston, K. M. (2006). Floor Response Spectra for Light Components Mounted on Regular Moment-Resisting Frame Structures. *Engineering Structures*, *28*(14), 1927–1940.

Mehrjoo, M., & Assi, R. (2024). Proposed Reliable Peak Component Factors for Ductile Light NSCs Subjected to Horizontal Ground Motions. *Bulletin of Earthquake Engineering*, *23*(2), 693–726. https://doi.org/10.1007/s10518-024-02081-x

Mehrjoo, M., & Assi, R. (2025a). Probabilistic Assessment of Seismic Acceleration Demands of Ductile Light NSCs in Moderately Ductile RC Frame Buildings. *Engineering Structures*, *335*, 120347. https://doi.org/10.1016/j.engstruct.2025.120347

Mehrjoo, M., & Assi, R. (2025b). Seismic Vulnerability Assessment of Ductile Light NSCs in Moderately Ductile RC Frame Buildings. *Journal of Urban Resilience and Earthquake Engineering (under review)*.

Mehrjoo, M., & Assi, R. (2026). Proposed Ductility-Based Force Factors for Acceleration-Sensitive Light Non-Structural Components. In *Proceedings of the 6th International Workshop on Seismic Performance of Non-Structural Elements (SPONSE 2026)*. Suzukakedai Campus, Institute of Science Tokyo, Japan: International Association for the Seismic Performance of Non-Structural Elements (SPONSE).

Mehrjoo, M., & Aval, S. B. B. (2024). Proposing New Design and Retrofitting Objectives for Seismic Design of Hospital Structures: A Case Study of Imam Khomeini Hospital in Eslamabad-E Gharb. *Bulletin of Earthquake Engineering*. https://doi.org/10.1007/s10518-024-01892-2

Miranda, E. (1991). *Seismic Evaluation and Upgrading of Existing Buildings* (PhD Thesis). University of California, Berkeley, Berkeley, CA.

Miranda, E., & Bertero, V. V. (1994). Evaluation of Strength Reduction Factors for Earthquake-Resistant Design. *Earthquake Spectra*, *10*(2), 357–379.

Miranda, E., Kazantzi, A., & Vamvatsikos, D. (2018). Towards a New Approach to Design Acceleration-Sensitive Non-Structural Components. In *Proceedings of the 11th U.S. National Conference on Earthquake Engineering (11NCEE)*. Los Angeles, CA: Earthquake Engineering Research Institute. Retrieved from https://infoscience.epfl.ch/bitstreams/5e479b60-2e37-433e-ab5d-fc7aee66aab8/download

Miranda, E., Mosqueda, G., Retamales, R., & Pekcan, G. (2012). Performance of Nonstructural Components During the 27 February 2010 Chile Earthquake. *Earthquake Spectra*, *28*(S1), 453–471. https://doi.org/10.1193/1.4000032

Miranda, E., & Taghavi, S. (2005). Approximate Floor Acceleration Demands in Multistory Buildings. I: Formulation. *Journal of Structural Engineering*, *131*(2), 203–211. https://doi.org/10.1061/(ASCE)0733-9445(2005)131:2(203)

Mitchell, D., Tinawi, R., & Law, T. (1989). *The 1988 Saguenay Earthquake - a Site Visit Report* (Report No. 1999). https://doi.org/10.4095/130606

Moon, D.-S., Lee, Y., & Lee, S. (2016). Seismic Vulnerability Assessment of RC Frame Structures Using 3D Analytical Models. *Journal of the Korea Academia-Industrial Cooperation Society*, *17*(9), 724–731. https://doi.org/10.5762/kais.2016.17.9.724

Moon, D.-S., Lee, Y., & Lee, S. M. (2018). Fragility Analysis of Space Reinforced Concrete Frame Structures With Structural Irregularity in Plan. *Journal of Structural Engineering*, *144*(8). https://doi.org/10.1061/(asce)st.1943-541x.0002092

Myrefelt, S. (2008). Functional Availability of HVAC Systems. *International Journal of Ventilation*, *7*(1), 89–98. https://doi.org/10.1080/14733315.2008.11683802

Naeim, F. (2004). Impact of the 1994 Northridge Earthquake on the Art and Practice of Structural Engineering. *The Structural Design of Tall and Special Buildings*, *13*(5), 373–389. https://doi.org/10.1002/tal.280

Nardin, C., Bursi, O. S., Paolacci, F., Pavese, A., & Quinci, G. (2022). Experimental Performance of a Multi-Storey Braced Frame Structure with Non-Structural Industrial Components Subjected to Synthetic Ground Motions. *Earthquake Engineering & Structural Dynamics*, *51*(9), 2113–2136. https://doi.org/10.1002/eqe.3656

National Research Council Canada (NRC). (2015). National Building Code of Canada (NBCC).

National Research Council Canada (NRC). (2020). National Building Code of Canada (NBCC). National Research Council of Canada. https://doi.org/10.4224/W324-HV93

Newmark, N. M. (1959). A Method of Computation for Structural Dynamics. *Journal of the Engineering Mechanics Division, ASCE*, *85*(EM3), 67–94.

Newmark, N. M., & Hall, W. J. (1973). Procedures and Criteria for Earthquake-Resistant Design. In *Proceedings of the Selected Papers By Nathan M. Newmark: Civil Engineering Classics* (pp. 829–872). ASCE.

Obando, J. C., Arroyo, O., Lopez-Garcia, D., & Carrillo, J. (2022). Seismic Response of Acceleration-Sensitive Nonstructural Components in a Thin Lightly-Reinforced Concrete Wall (TLRCW) Mid-Rise Building. *Structures*, *45*, 1878–1901. https://doi.org/10.1016/j.istruc.2022.10.017

Obando, J. C., & Lopez-Garcia, D. (2018). Inelastic Displacement Ratios for Nonstructural Components Subjected to Floor Accelerations. *Journal of Earthquake Engineering*, *22*(4), 569–594. https://doi.org/10.1080/13632469.2016.1244131

Office of Statewide Health Planning and Development (OSHPD), Facilities Development Division. (2020). OSHPD Special Seismic Certification Preapproval (OSP). California Health and Human Services Agency. Retrieved from https://hcai.ca.gov/wp-content/uploads/2020/11/OSHPD-Special-Seismic-Certification-Preapproval.pdf

Olivo, M., Bortolozzi, M., Tessarolo, A., & Luise, F. (2020). A New Method for the Accurate Prediction of on-Load Power Factor in Two-Pole Induction Motors Considering Shaft Eddy Currents. *IEEE Transactions on Energy Conversion*, *35*(3), 1196–1207. https://doi.org/10.1109/tec.2020.2976617

Oropeza, M., Favez, P., & Lestuzzi, P. (2010). Seismic Response of Nonstructural Components in Case of Nonlinear Structures Based on Floor Response Spectra Method. *Bulletin of Earthquake Engineering*, *8*(2), 387–400. https://doi.org/10.1007/s10518-009-9139-0

Panza, G. F., Alvarez, L., Aoudia, A., Ayadi, A., Benhallou, H., Benouar, D., … Vaccari, F. (2002). Realistic Modeling of Seismic Input for Megacities and Large Urban Areas (the

UNESCO/IUGS/IGCP Project 414). *Episodes*, *25*(3), 160–184. https://doi.org/10.18814/epiiugs/2002/v25i3/002

Pavlou, E., & Constantinou, M. C. (2006). Response of Nonstructural Components in Structures with Damping Systems. *Journal of Structural Engineering*, *132*(7), 1108–1117. https://doi.org/10.1061/(ASCE)0733-9445(2006)132:7(1108)

Perrone, D., Calvi, P. M., Nascimbene, R., Fischer, E. C., & Magliulo, G. (2019). Seismic Performance of Non-Structural Elements During the 2016 Central Italy Earthquake. *Bulletin of Earthquake Engineering*, *17*(10), 5655–5677. https://doi.org/10.1007/s10518-018-0361-5

Perrone, Daniele, Rodriguez, D., Filiatrault, A., Brunesi, E., Beiter, C., & Piccinin, R. (2022). A Framework for the Quantification of Non-Structural Seismic Performance Factors. *Journal of Earthquake Engineering*, 1–27. https://doi.org/10.1080/13632469.2021.1991516

Pinkawa, M., Hoffmeister, B., & Feldmann, M. (2014). A Critical Review of Current Approaches on the Determination of Seismic Force Demands on Nonstructural Components. In A. Cunha, E. Caetano, P. Ribeiro, & G. Müller (Eds.), *Proceedings of the 9th International Conference on Structural Dynamics, EURODYN 2014* (pp. 421–428). Porto, Portugal: FEUP.

Piscal A., C. M., & López-Almansa, F. (2018). Generating Damping Modification Factors After Artificial Inputs in Scenarios of Local Records Scarcity. *Bulletin of Earthquake Engineering*, *16*(11), 5371–5396. https://doi.org/10.1007/s10518-018-0406-9

Porter, K. (2009). *Fragility of Chillers* (Report No. FEMA P-58/BD-3.9.15). Redwood City, CA: Applied Technology Council. Retrieved from https://www.atcouncil.org/fema-p-58-background-documents

Pourali, A., Dhakal, R., & MacRae, G. (2014). Seismic Performance of Suspended Ceilings: Critical Review of Current Design Practice. In *Proceedings of the New Zealand Society for Earthquake Engineering (NZSEE) Annual Technical Conference*. Auckland, New Zealand. Retrieved from https://db.nzsee.org.nz/2014/oral/68_Pourali.pdf

Pourali, A., Dhakal, R., MacRae, G. A., & Taşlıgedik, A. Ş. (2017). Fully Floating Suspended Ceiling System: Experimental Evaluation of Structural Feasibility and Challenges. *Earthquake Spectra*, *33*(4), 1627–1654. https://doi.org/10.1193/092916eqs163m

Preti, M., & Bolis, V. (2017). Masonry Infill Construction and Retrofit Technique for the Infill-Frame Interaction Mitigation: Test Results. *Engineering Structures*, *132*, 597–608. https://doi.org/10.1016/j.engstruct.2016.11.053

Pürgstaller, A., Quintana Gallo, P., Pampanin, S., & Bergmeister, K. (2020). Seismic Demands on Nonstructural Components Anchored to Concrete Accounting for Structure-

Fastener-Nonstructural Interaction (SFNI). *Earthquake Engineering & Structural Dynamics*, *49*(6), 589–606. https://doi.org/10.1002/eqe.3255

Qi, L., Luo, Z., Cao, Y., & Xue, J. (2023). Seismic Damage Mechanism and Performance Evaluation of Suspended Ceiling Systems. *Journal of Building Engineering*, *64*, 105595. https://doi.org/10.1016/j.jobe.2022.105595

Rahman, A., Khan, Q. uz Z., & Qureshi, M. I. (2019). Evaluation of Simplified Analysis Procedures for a High-Rise Reinforced Concrete Core Wall Structure. *Advances in Civil Engineering*, *2019*, 1–21. https://doi.org/10.1155/2019/1035015

Retamales, R., Davies, R., Mosqueda, G., & Filiatrault, A. (2013). Experimental Seismic Fragility of Cold-Formed Steel Framed Gypsum Partition Walls. *Journal of Structural Engineering*, *139*(8), 1285–1293. https://doi.org/10.1061/(ASCE)ST.1943-541X.0000657

Reyes, J. C. (2009). *Estimating Seismic Demands for Performance-Based Engineering of Buildings*. PhD Thesis. University of California, Berkeley, Berkeley, CA. Retrieved from https://escholarship.org/uc/item/9fp377cr

Rezvani, R., Soroushian, S., Zaghi, A. E., & Maragakis, M. (2022). Numerical Seismic Fragility Analysis for Suspended Ceilings with Various Geometries. *Journal of Building Engineering*, *54*, 104627. https://doi.org/10.1016/j.jobe.2022.104627

Rieder, A. (2009). *Seismic Response of Post-Installed Anchors in Concrete* (PhD Thesis). University of Natural Resources and Life Sciences, Vienna.

Roca, P., Cervera, M., Gariup, G., & Pela', L. (2010). Structural Analysis of Masonry Historical Constructions. Classical and Advanced Approaches. *Archives of Computational Methods in Engineering*, *17*(3), 299–325. https://doi.org/10.1007/s11831-010-9046-1

Rojas, D., Quintana Gallo, P., Pürgstaller, A., Bianchi, S., Ciurlanti, J., Pampanin, S., & Bergmeister, K. (2023). Influence of the Anchorage Shear Hysteresis on the Seismic Response of Nonstructural Components in RC Buildings. *Bulletin of Earthquake Engineering*, *21*(7), 3399–3432. https://doi.org/10.1007/s10518-023-01642-w

Rosset, P., & Chouinard, L. E. (2009). Characterization of Site Effects in Montreal, Canada. *Natural Hazards*, *48*(2), 295–308. https://doi.org/10.1007/s11069-008-9263-1

Ruggieri, S., & Vukobratović, V. (2024). The Influence of Torsion on Acceleration Demands in Low-Rise RC Buildings. *Bulletin of Earthquake Engineering*, *22*(5), 2433–2468. https://doi.org/10.1007/s10518-024-01873-5

Ryu, K. P., & Reinhorn, A. M. (2019). Experimental Study of Large Area Suspended Ceilings. *Journal of Earthquake Engineering*, *23*(6), 1001–1032. https://doi.org/10.1080/13632469.2017.1342294

Sadeghzadeh-Nazari, M., & Ghafory-Ashtiany, M. (2011). Influential Parameters for the Design of Nonstructural Components in Multi-Story Buildings. In *Proceedings of the 3rd ECCOMAS Thematic Conference on Computational Methods in Structural Dynamics and Earthquake Engineering (COMPDYN 2011)*. Corfu, Greece: ECCOMAS / CIMNE. Retrieved from https://congress.cimne.com/eccomas/proceedings/compdyn2011/compdyn2011_full/554.pdf

Sankaranarayanan, R., & Medina, R. A. (2007). Acceleration response modification factors for nonstructural components attached to inelastic moment-resisting frame structures. *Earthquake Engineering & Structural Dynamics*, *36*(14), 2189–2210. https://doi.org/10.1002/eqe.724

Schultz, C. H., Koenig, K. L., & Lewis, R. J. (2003). Implications of Hospital Evacuation After the Northridge, California, Earthquake. *New England Journal of Medicine*, *348*(14), 1349–1355. https://doi.org/10.1056/NEJMsa021807

Setareh, M. (2010). Vibration Serviceability of a Building Floor Structure. I: Dynamic Testing and Computer Modeling. *Journal of Performance of Constructed Facilities*, *24*(6), 497–507. https://doi.org/10.1061/(ASCE)CF.1943-5509.0000134

Shakeel, S. (2019). Effect of Architectural Non-Structural Components on Lateral Behaviour of CFS Structures: Shake-Table Tests and Numerical Modelling. In *Proceedings of International Conference on Computational Methods in Structural Dynamics and Earthquake Engineering (COMPDYN 2015)*.

Shang, Q., Li, J., & Wang, T. (2021). Floor Acceleration Response Spectra of Elastic Reinforced Concrete Frames. *Journal of Building Engineering*. https://doi.org/10.1016/j.jobe.2021.103558

Sheikhzadeh Shayan, R., & Assi, R. (2023). Assessment of Seismic Acceleration Demands on Nonstructural Components in Moderately Ductile RC Frame Buildings Designed According to NBC 2015. *Canadian Journal of Civil Engineering*, *50*(4), 335–347. https://doi.org/10.1139/cjce-2022-0222

Singh, A., & Ang, A.-S. (1974). Stochastic Prediction of Maximum Seismic Response of Light Secondary Systems. *Nuclear Engineering and Design*, *29*(2), 218–230.

Singh, M. P., Moreschi, L. M., Suárez, L. E., & Matheu, E. E. (2006). Seismic Design Forces. II: Flexible Nonstructural Components. *Journal of Structural Engineering*, *132*(10), 1533–1542. https://doi.org/10.1061/(ASCE)0733-9445(2006)132:10(1533)

Soong, T. T., Chen, G., Wu, Z., Zhang, R., & Grigoriu, M. (1993). *Assessment of the 1991 NEHRP Provisions for Nonstructural Components and Recommended Revisions* (Report No. NCEER-93-0003). Buffalo, NY: National Center for Earthquake

Engineering Research (NCEER), State University of New York at Buffalo. Retrieved from https://ubir.buffalo.edu/xmlui/bitstream/handle/10477/754/93-0003.pdf

Soroushian, S., Rahmanishamsi, E., Ryu, K. P., Maragakis, M., & Reinhorn, A. M. (2016). Experimental Fragility Analysis of Suspension Ceiling Systems. *Earthquake Spectra*, *32*(2). https://doi.org/10.1193/071514eqs109m

Soroushian, S., Zaghi, A. E., Maragakis, M., Echevarria, A., Tian, Y., & Filiatrault, A. (2015). Analytical Seismic Fragility Analyses of Fire Sprinkler Piping Systems with Threaded Joints. *Earthquake Spectra*, *31*(2), 1125–1155. https://doi.org/10.1193/083112EQS277M

Standards New Zealand. (2004). *Structural Design Actions – Part 5: Earthquake Actions – New Zealand – Commentary: Supplement to NZS 1170.5:2004*. Wellington, New Zealand: Standards New Zealand.

Sullivan, T. J., Calvi, P. M., & Nascimbene, R. (2013). Towards Improved Floor Spectra Estimates for Seismic Design. *Earthquakes and Structures*, *4*(1), 109–132. https://doi.org/10.12989/eas.2013.4.1.109

Surana, M., Singh, Y., & Lang, D. H. (2021). Effect of Structural Characteristics on Damping Modification Factors for Floor Response Spectra in RC Buildings. *Engineering Structures*, *242*, 112514. https://doi.org/10.1016/j.engstruct.2021.112514

Taghavi, S., & Miranda, E. (2003). *Response Assessment of Nonstructural Building Elements*. Berkeley: Pacific Earthquake Engineering Research Center.

Taghavi, S., & Miranda, E. (2008). Effect of Interaction Between Primary and Secondary Systems on Floor Response Spectra. In *Proceedings of the 14th World Conference on Earthquake Engineering (14WCEE)* (pp. 12–17). Beijing, China.

Taghavi, S., & Miranda, E. (2012). Probabilistic Study of Peak Floor Acceleration Demands in Nonlinear Structures. In *Proceedings of the 15th world conference on earthquake engineering (15WCEE), Lisbon, Portugal*.

Tapia-Hernández, E., Geneş, M. C., & Guerrero-Bobadilla, H. (2025). Structural Behavior of Hospitals During the Kahramanmaraş Earthquake of February 6, 2023. *Earthquake Spectra*, *41*(2), 1589–1615. https://doi.org/10.1177/87552930241298678

Tauby, J. R., Lloyd, R., Noce, T., & Tunnissen, J. (2012). *A Practical Guide to Seismic Restraint* (2nd ed.). Atlanta, GA: American Society of Heating, Refrigerating and Air-Conditioning Engineers (ASHRAE).

The MathWorks Inc. (2023). MATLAB (version R2023a) [Software]. Natick, Massachusetts: The MathWorks, Inc. Retrieved from https://www.mathworks.com/

Toro, G. R., McGuire, R. K., Cornell, C. A., & Sewell, R. T. (1989). *Linear and Nonlinear Response of Structures and Equipment to California and Eastern United States Earthquakes*. Electric Power Research Inst., Palo Alto, CA (USA); Risk Engineering, Inc ….

Vijayanarayanan, A. R., Goswami, R., & Murty, C. V. R. (2017). Estimation of Storey Stiffness in Multi-Storey Buildings. In *The 16th World Conference on Earthquake Engineering*.

Villaverde, R. (2006). Simple Method to Estimate the Seismic Nonlinear Response of Nonstructural Components in Buildings. *Engineering Structures*, *28*(8), 1209–1221.

Viti, G., Olivieri, M., & Travi, S. (1981). Development of Non-Linear Floor Response Spectra. *Nuclear Engineering and Design*, *64*(1), 33–38. https://doi.org/10.1016/0029-5493(81)90029-7

Vukobratović, V., & Fajfar, P. (2016). A Method for the Direct Estimation of Floor Acceleration Spectra for Elastic and Inelastic MDOF Structures. *Earthquake Engineering & Structural Dynamics*, *45*(15), 2495–2511. https://doi.org/10.1002/eqe.2779

Vukobratović, V., & Fajfar, P. (2017). Code-Oriented Floor Acceleration Spectra for Building Structures. *Bulletin of Earthquake Engineering*, *15*(7), 3013–3026. https://doi.org/10.1007/s10518-016-0076-4

Wang, D. Z., & Dai, J. W. (2014). Research Status for Nonstructural Components Under Severe Earthquake. *Applied Mechanics and Materials*, *477–478*, 1042–1045. https://doi.org/10.4028/www.scientific.net/AMM.477-478.1042

Wang, T., Shang, Q., & Li, J. (2021). Seismic Force Demands on Acceleration-Sensitive Nonstructural Components: A State-of-the-Art Review. *Earthquake Engineering and Engineering Vibration*, *20*(1), 39–62. https://doi.org/10.1007/s11803-021-2004-0

Wang, X., & Hutchinson, T. C. (2024). Elastic and Inelastic Acceleration Amplification of Nonstructural Components Characterized Using Recorded Building Responses. *Engineering Structures*, *302*, 117306. https://doi.org/10.1016/j.engstruct.2023.117306

Wang, Zhanwei, Xia, P., Zhou, S., Wang, L., Guo, J., Li, X., … Chen, J. (2024). Examining the Impact of Common Faults on Chiller Performance Through Experimental Investigation and Parameter Sensitivity Analysis. *Energy and Buildings*, *317*, 114389. https://doi.org/10.1016/j.enbuild.2024.114389

Wang, Zijun, Martinez-Vazquez, P., & Zhao, B. (2020). Pushover analysis of structures subjected to combined actions of earthquake and wind. *Engineering structures*, *221*, 111034.

Watkins, D. A. (2011). *Seismic Behavior and Modeling of Anchored Nonstructural Components Considering the Influence of Cyclic Cracks*. PhD Thesis. University of

California, San Diego, La Jolla, CA. Retrieved from https://escholarship.org/uc/item/3ds752n9

Watkins, D., Chiu, L., Hutchinson, T., & Hoehler, M. (2009). *Survey and Characterization of Floor and Wall Mounted Mechanical and Electrical Equipment in Buildings* (Report No. SSRP–2009/11).

Whittaker, A. S., & Soong, T. T. (2003). An Overview of Nonstructural Components Research at Three US Earthquake Engineering Research Centers. In *Proceedings of Seminar on Seismic Design, Performance, and Retrofit of Nonstructural Components in Critical Facilities, ATC*. Applied Technology Council.

World Bank Open Data. (2025). *World Bank*. Retrieved from https://data.worldbank.org

Zeng, X., Lu, X., Yang, T. Y., & Xu, Z. (2016). Application of the FEMA-P58 Methodology for Regional Earthquake Loss Prediction. *Natural Hazards*, *83*(1), 177–192. https://doi.org/10.1007/s11069-016-2307-z

Zhai, C.-H., Zheng, Z., Li, S., Pan, X., & Xie, L.-L. (2016). Seismic Response of Nonstructural Components Considering the Near-Fault Pulse-Like Ground Motions. *Earthquakes and Structures*, *10*(5), 1213–1232.

Zohrabi, A. (2017). Imam Khomeini Hospital, Kermanshah, Iran, after the 2017 earthquake. *Iranian Students' News Agency (ISNA)*.